Department of Civil and Environmental Engineering
Stanford University

MODELING OF EARTHQUAKE GROUND MOTION IN THE FREQUENCY DOMAIN

by
Hjörtur Thráinsson,
Anne S. Kiremidjian
and
Steven R. Winterstein

Report No. 134
June 2000

The John A. Blume Earthquake Engineering Center was established to promote research and education in earthquake engineering. Through its activities our understanding of earthquakes and their effects on mankind's facilities and structures is improving. The Center conducts research, provides instruction, publishes reports and articles, conducts seminar and conferences, and provides financial support for students. The Center is named for Dr. John A. Blume, a well-known consulting engineer and Stanford alumnus.

Address:

The John A. Blume Earthquake Engineering Center
Department of Civil and Environmental Engineering
Stanford University
Stanford CA 94305-4020

(650) 723-4150
(650) 725-9755 (fax)
earthquake @ce. stanford.edu
http://blume.stanford.edu

MODELING OF EARTHQUAKE GROUND MOTION IN THE FREQUENCY DOMAIN

by

Hjörtur Thráinsson
Anne S. Kiremidjian
and
Steven R. Winterstein

This research was partially supported
by
The John A. Blume Earthquake Engineering Center
The National Science Foundation Grant No. CMS-5926102
and
The Stanford University UPS Foundation Grant

The John A. Blume Earthquake Engineering Center
Department of Civil and Environmental Engineering
Stanford University, Stanford, CA 94305-4020

Report No. 134
May 2000

ABSTRACT

In recent years, the utilization of time histories of earthquake ground motion has grown considerably in the design and analysis of civil structures. It is very unlikely, however, that recordings of earthquake ground motion will be available for all sites and conditions of interest. Hence, there is a need for efficient methods for the simulation and spatial interpolation of earthquake ground motion. In addition to providing estimates of the ground motion at a site using data from adjacent recording stations, spatially interpolated ground motions can also be used in design and analysis of long-span structures, such as bridges and pipelines, where differential movement is important.

The objective of this research is to develop a methodology for rapid generation of horizontal earthquake ground motion at any site for a given region, based on readily available source, path and site characteristics, or (sparse) recordings. The research includes two main topics: (i) the simulation of earthquake ground motion at a given site, and (ii) the spatial interpolation of earthquake ground motion.

In topic (i), models are developed to simulate acceleration time histories using the inverse discrete Fourier transform. The Fourier phase differences, defined as the difference in phase angle between adjacent frequency components, are simulated conditional on the Fourier amplitude. Uniformly processed recordings from recent California earthquakes are used to validate the simulation models, as well as to develop prediction formulas for the model parameters. The models developed in this research provide rapid simulation of earthquake ground motion over a wide range of magnitudes and distances, but they are not intended to replace more robust geophysical models.

In topic (ii), a model is developed in which Fourier amplitudes and Fourier phase angles are interpolated separately. A simple dispersion relationship is included in the phase angle interpolation. The accuracy of the interpolation model is assessed using data from the SMART-1 array in Taiwan. The interpolation model provides an effective method to estimate ground motion at a site using recordings from stations located up to several kilometers away. Reliable estimates of differential ground motion are restricted to relatively limited ranges of frequencies and inter-station spacings.

ACKNOWLEDGMENTS

This report is based on the doctoral dissertation of Hjörtur Thráinsson. The research was partially supported by the John A. Blume Earthquake Engineering Center, the National Science Foundation Grant No. CMS-5926102, and the Stanford University UPS Foundation Grant. This support is gratefully acknowledged.

Several people contributed to this research. Feedback from participants in the annual meetings of the Reliability of Marine Structures Program at Stanford University was very helpful. Conversations with Bill Joyner at the U.S. Geological Survey in Menlo Park were also beneficial. Professor Greg Beroza, Department of Geophysics at Stanford University, reviewed the manuscript. The advice of these individuals is gratefully appreciated.

TABLE OF CONTENTS

LIST OF TABLES

LIST OF FIGURES

CHAPTER 1
INTRODUCTION

In recent years, the utilization of time histories of earthquake ground motion has grown considerably in the field of earthquake engineering. Ground motion time histories are, for example, used in the design and analysis of civil structures. Time histories are also used to correlate ground motion characteristics to structural and nonstructural damage. Reliable ground motion-damage relationships are essential for regional risk assessment and risk management purposes. In addition, emergency response personnel need reliable estimates of ground motion to assess the level of damage at critical facilities as soon as possible following an earthquake, in order to allocate resources in an efficient manner. It is very unlikely, however, that ground motion recordings will be available for all sites and conditions of interest. Hence, there is a need for efficient methods for the simulation and spatial interpolation of earthquake ground motion. Spatial interpolation can also be used in the design and analysis of long-span structures, such as bridges and pipelines, where differential movement is of importance.

1.1 Background

Several models exist in the literature for the numerical simulation and spatial interpolation of earthquake ground motion. The ground motion simulation models can be classified into two categories: geophysical models, and models based on stochastic processes. A ground motion model can also be based on both geophysical models and stochastic processes (e.g. McGuire et al., 1984; Suzuki and Kiremidjian, 1988).

Geophysical Ground Motion Models

In geophysical ground motion models, the ground motion at a site is obtained by a convolution of an earthquake source process and functions describing the wave propagation through the Earth's strata. Geophysical ground motion models are of two types: dynamic models and kinematic models. The dynamic models take into account the

tectonic and frictional forces that govern the earthquake process and solve the differential equations of motion to obtain the rupture process and the resulting ground motion. In kinematic models, the ground motion at the site is derived from the dislocation time history along the causative fault's surface, which is assumed to be known a priori.

Dynamic models of earthquake ground motion rigorously take into account the causative forces resulting in earthquakes. They require highly detailed information and complex and costly computation. For the most part, these models have been used to gain insight into the process of earthquake faulting, or to place constraints on kinematic models, rather than to generate ground motion time histories (Reiter, 1990).

Kinematic modeling of earthquake ground motion is physically less complete than dynamic modeling, but on the other hand, it is less costly. The earliest kinematic models were proposed by Aki (1968) and Haskell (1969). These early models assumed a simple, uniform dislocation traveling at a constant rupture velocity on a rectangular fault in an infinite and homogenous medium. More recent models allow for different fault configurations and locally varying slip and rupture velocity. A good summary and description of these models can be found in Spudich and Hartzell (1985).

Kinematic models have proved to be useful for the simulation of earthquake ground motion, especially at frequencies lower than 1 Hertz. For frequencies higher than 2-3 Hertz, however, they are not so useful. In addition, kinematic models – as do geophysical models in general – require relatively detailed information about the source, path, and site characteristics.

Geophysical ground motion models, both dynamic and kinematic models, depend on many uncertain or unknown parameters. These model parameters are often earthquake-specific. Therefore, geophysical models are not well suited for predicting the earthquake ground motion due to future events.

Stochastic Ground Motion Models

The earliest efforts in the stochastic modeling of earthquake ground motion were based on the interpretation of earthquake ground acceleration as a filtered white noise process or as a filtered Poisson process. More recently, models based on the spectral

representation of stochastic processes, and auto-regressive moving average processes, have become more popular (Shinozuka and Deodatis, 1988).

In the simplest form of the spectral representation method, the earthquake ground motion is expressed in terms of an amplitude modulated, stationary process:

$$f(t_k) = M(t_k) \cdot \sum_{j=1}^{N} A_j \cdot \sin(\omega_j \cdot t_k + \theta_j) \tag{1.1}$$

Here, $f(t_k)$ is the value of the ground motion time series at the k-th time point, $t_k = k \cdot \Delta t$, where Δt is the sampling interval, $M(t)$ is the amplitude modulating function (sometimes referred to as the intensity modulating function), A_j represents the amplitude of the j-th sinusoid, ω_j is the frequency (in rad/sec) of the j-th sinusoid, and θ_j is a phase angle, assumed to be uniformly distributed between 0 and 2π – or any other interval of size 2π. The frequency of the j-th sinusoid is given by:

$$\omega_j = j \cdot \Delta\omega \tag{1.2}$$

where $\Delta\omega$ is the incremental frequency. The amplitude of the j-th sinusoid can be inferred from:

$$A_j = \sqrt{2 \cdot S(\omega_j) \cdot \Delta\omega} \tag{1.3}$$

where $S(\omega)$ is the one-sided power spectral density of the underlying stationary stochastic process.

Time series that are generated using Equation (1.1) are stationary with respect to frequency content, i.e. the frequency content is controlled by the power spectral density function $S(\omega)$, which does not change with time. In recorded accelerograms, on the other hand, the high frequencies tend to be dominating at the beginning, but toward the end, the main portion of the energy shifts down to lower frequencies. This is mainly due to the fact that the high-frequency body waves travel faster than the low-frequency surface waves. To account for this time-varying frequency content, a modulation function has to

be applied to the frequency content as well as the intensity. Following Priestley's (1967) definition of evolutionary power spectral density, the time series

$$f(t_k) = \sum A_{kj} \cdot \sin(\omega_j \cdot t_k + \theta_j) \tag{1.4}$$

where

$$A_{kj} = \sqrt{2 \cdot M^2(t_k, \omega_j) \cdot S(\omega_j) \cdot \Delta\omega} \tag{1.5}$$

is nonstationary, both with respect to intensity and frequency content. In Equation (1.5) $M(t, \omega)$ is a time- and frequency dependent modulation function.

Earthquake ground motion models based on the spectral representation method have several drawbacks. For example, they require predefined modulation functions, including their shape and duration. Moreover, the phases θ_j are usually taken as uniformly distributed and independent of each other. This characterization of the phase angles is questionable. As shown by Kubo (1987), for example, the phase angles of the ground motion affect the response of a structure. It is therefore important to accurately reproduce the characteristics of the phase angles of recorded ground motions in simulated ground motions.

Auto-regressive moving average (ARMA) models are often used to simulate earthquake ground motion. Kozin (1988) gives a comprehensive summary of the application of ARMA models in earthquake ground motion modeling. ARMA models consist of a discrete, linear transfer function applied to a white noise process. The stationary ARMA model of order (p,q) – denoted by ARMA(p,q) – is given by:

$$f_k - a_1 \cdot f_{k-1} - \ldots - a_p \cdot f_{k-p} = e_k - b_1 \cdot e_{k-1} - \ldots - b_q \cdot e_{k-q} \tag{1.6}$$

where $f_k = f(k \cdot \Delta t)$ is the k-th value of the time series, $e_k = e(k \cdot \Delta t)$ is the k-th value of a zero-mean, white noise process with variance σ_e^2, $a_i; i = 1, \ldots p$ are the auto-regressive parameters, and $b_i; i = 1, \ldots q$ are the moving average parameters.

Since earthquake ground motion is a nonstationary process, the parameters of the ARMA models have to vary with time. A modulation function can be easily applied to the variance of the noise process, in order to account for the variation of intensity with time, but to account for the nonstationary frequency content provides for a complex and cumbersome procedure (Ellis et al., 1987; Westermo, 1992). Another shortcoming of the ARMA models is that except for the ARMA(2,1) model, the ARMA parameters do not lend themselves to physical interpretation (Conte et al., 1992).

Spatial Interpolation of Ground Motion

When the earthquake ground motion is to be evaluated over an extended spatial region, it is not feasible to simulate a time history at every site of interest. An alternative approach is to simulate the ground motion at predefined grid points, and use spatial interpolation techniques to estimate the ground motion in-between the grid points. Spatial interpolation can also be used to evaluate the ground motion time history between ground motion recording stations (rather than between simulation grid points).

The spatial interpolation of earthquake ground motion is generally performed applying specific models of spatial variability. The spatial variation of earthquake ground motion can be either modeled in the time domain or the frequency domain. In the time domain, the spatial variability is quantified by a correlation function, while in the frequency domain, it is described by a coherency function. The frequency domain approach is more convenient when dealing with wave motion (Zembaty and Krenk, 1993).

Consider the ground motion at two sites, X and Y, denoted by $X(t)$ and $Y(t)$. The separation distance between the sites, measured parallel to the direction of wave propagation, is *d*. Assuming the ground motion to be stationary, the coherency function for the two signals $X(t)$ and $Y(t)$ is given by:

$$\Gamma_{XY}(\omega, d) = \frac{S_{XY}(\omega, d)}{\sqrt{S_X(\omega) \cdot S_Y(\omega)}} \tag{1.7}$$

where $S_{XY}(\omega, d)$ is the cross spectral density, and $S_X(\omega)$ and $S_Y(\omega)$ are the power spectral densities of $X(t)$ and $Y(t)$, respectively. The coherency is, therefore, the cross spectral density normalized with respect to the product of the individual power spectral densities. The coherency function can be factored into its modulus and phase:

$$\Gamma_{XY}(\omega, d) = |\Gamma_{XY}(\omega, d)| \cdot \exp[i \cdot \varphi(\omega, d)] \tag{1.8}$$

The modulus of the coherency function is often referred to as the lagged coherency. It is a measure of the similarity of the signals $X(t)$ and $Y(t)$, excluding the effect of wave propagation. The effect of wave propagation is included in the phase of the coherency function. Assuming a plane wave propagating with the same apparent velocity for all frequencies, the phase term can be written as:

$$\varphi(\omega, d) = \frac{\omega \cdot d}{v} \tag{1.9}$$

where v is the apparent propagation velocity of the seismic waves.

Several coherency models for earthquake ground motion have been proposed in the literature. The most important consideration for the phase term is to properly select or estimate the apparent propagation velocity. The lagged coherency is usually modeled either by a single exponent (Harichandran and Vanmarcke, 1986) or a double exponent (Hao, 1989). Abrahamson et al. (1991) propose a lagged coherency model that better accounts for short distances between sites and high-frequency ground motion than previous models did. These models of the lagged coherency are all empirical. Der Kiureghian (1996) proposes a theoretical model for the coherency function, accounting for incoherence, wave passage, attenuation, and site effects. This theoretical model, however, has not been validated with observations. All the ground motion coherency models have one limitation in common: they assume the ground motion to be realizations of stationary processes. Another important drawback of the lagged coherency is its insensitivity to pure amplitude variation. That is to say, whether the signal $Y(t)$ is equal to, two times, or even five times the signal $X(t)$, does not matter. In every case, the lagged coherency is identically equal to one.

1.2 Objective and Scope

The objective of this research is to develop a methodology for rapid evaluation of horizontal earthquake ground motion at any site for a given region, based on readily available source, path and site characteristics, or (sparse) recordings. To accomplish this, the research is divided into two main topics: (1) the simulation of earthquake ground motion at a given site based on the magnitude and the location of the earthquake, and (2) the spatial interpolation of earthquake ground motion. In this study, the ground motion is characterized by digital acceleration time histories.

The ground motion simulation model has to be easy to use for the prediction of earthquake ground motion due to a future event, while providing results that are accurate enough for engineering purposes; i.e. analysis and design of civil structures. No assumptions concerning the Gaussianity of the earthquake ground motion, its stationarity, the form of the modulation functions or mutual independence of phases are made a priori. Only one parameter is chosen to characterize the source, path, and site, respectively. The magnitude of the earthquake is used to characterize the source, the path is described by the source to site distance, and the site characteristics are inferred from the local soil conditions. Recordings from recent California earthquakes are used to validate the simulation models that are developed in this study, and to estimate the parameters of the prediction formulas for the ground motion.

The model for the spatial interpolation of earthquake ground motion also does not rely on any assumptions regarding the stationarity or Gaussianity of the processes. The interpolation should work equally well for simulated ground motions as for recorded ground motions. Data from the SMART-1 array in Taiwan are used to assess the accuracy of the interpolation model.

1.3 Organization of the Report

This report is divided into four parts: (1) the discussion of the ground motion data and the data processing, (2) the formulation of the earthquake ground motion simulation method

for a given site, (3) the spatial interpolation of earthquake ground motion, and (4) a case study.

The earthquake ground motion database that is used to validate the ground motion simulation models and to develop prediction formulas for the model parameters is introduced in Chapter 2. The selection of the ground motion records is discussed and their processing is explained. In addition, the two-step regression procedure used to develop the prediction formulas is presented.

The components of the ground motion simulation models are presented in chapters 3, 4, and 5. In Chapter 3, the convention and notation used for the discrete Fourier transform are introduced and the general characteristics of the probability distributions of Fourier phase angles and phase differences are examined. Then, an empirical, parametric model of the phase differences is proposed, prediction formulas for the model parameters are developed, and the goodness of fit for the assumed phase difference distributions is assessed.

In the fourth chapter, an alternative method for the modeling of Fourier phase differences is developed, based on a frequency domain analogy to the method of envelopes for narrow band processes. After a brief review of the method of envelopes and description of the analogy, prediction formulas are developed for the model parameters and the quality of the Fourier phase difference model is assessed.

The phase difference models presented in Chapters 3 and 4 do not depend on a specific Fourier amplitude model. In Chapter 5, two common models of the Fourier amplitude spectrum are reviewed, followed by a simple alternative approach. The ground motion database is then used to develop prediction formulas for the parameters of the alternative approach.

The spatial interpolation of earthquake ground motion is addressed in Chapter 6. A simple interpolation model is developed for the amplitude and phase angle of the Fourier transform of an earthquake accelerogram. The model is validated using data from the SMART-1 array in Taiwan.

In Chapter 7, the simulation model is used to generate ground motion intensity maps for the 1994 Northridge, California earthquake, and the interpolation model is used to estimate the acceleration time history at the site of a collapsed highway bridge.

CHAPTER 2
DATA AND DATA PROCESSING

In this report, new methods for the modeling of earthquake ground motion are developed. In order to facilitate the application of those models, it is necessary to develop general formulations that can be used to predict the model parameters. The prediction formulas for the model parameters should be based on relevant and readily determined source, site, and path characteristics.

The source parameters considered in this study are the moment magnitude of the earthquake and the vertical projection of the seismogenic rupture on the Earth's surface. The path effects are characterized by the distance to the surface projection of the seismogenic rupture. The site characteristics are accounted for by using the site classification proposed by the National Earthquake Hazard Reduction Program.

This chapter describes the development of the prediction formulas for the model parameters. The prediction formulas are obtained using a two-step regression procedure and uniformly processed data from recent California earthquakes.

2.1 The Ground Motion Data Set

Uncorrected data from recent California earthquakes were obtained and were processed to produce a uniform ground motion database. In the following subsections, the ground motion database and the data processing are described.

2.1.1 Ground Motion Recordings

The earthquakes considered in this study are listed in Table 2.1 along with the number of stations from which records were obtained. Figure 2.1 shows the relationship between the source to site distance and the moment magnitude of the earthquake.

In this study, only records from recent California earthquakes are included. Raw data, i.e. uncorrected and unprocessed recordings of ground acceleration from these

earthquakes, are readily available in digital format and are easily accessible on the World Wide Web. More importantly, these recordings cover relatively wide range of magnitudes and they represent homogenous geologic and tectonic settings. Agencies such as the California Division of Mines and Geology (http://docinet3.consrv.ca.gov/csmip/), the United States Geological Survey (http://nsmp.wr.usgs.gov/data.html), and the Southern California Earthquake Center (http://smdb.crustal.ucsb.edu/) are among the most valuable data sources. The recording stations are listed in Appendix A.

Strong ground motion accelerographs trigger and start recording after they are subjected to ground motion levels above a certain pre-set threshold value. Therefore, strong ground motion data sets tend to be biased towards large magnitudes for long distances. The data set shown in Figure 2.1, however, is relatively complete for magnitudes between 6 and 7½ and distances up to 70 kilometers. The recordings are fewer for larger distances, but reasonably complete for magnitudes between 6½ and 7½ and distances up to 100 km.

This study includes only free field records, and records obtained from the ground floor of stiff, low-rise (at most 2-story high) buildings. Records from other man-made structures, such as those obtained at dam abutments or the base of bridge columns, are excluded in order to eliminate the effects of soil-structure interaction. Each station recorded two horizontal components, one of which (chosen at random) is used in the regression analyses.

Table 2.1: The California earthquakes and the number of ground motion recording stations that are used in this study.

Earthquake	**Date (GMT)**	**M_w**	**Type***	**Stations**
Coyote Lake	6-Aug-1979	5.8	S	9
Whittier Narrows	1-Oct-1987	5.9	R	35
Morgan Hill	24-Apr-1984	6.0	S	20
Parkfield	28-Jun-1966	6.1	S	5
North Palm Springs	8-Jul-1986	6.2	S	18
Imperial Valley	15-Oct-1979	6.5	S	35
San Fernando	9-Feb-1971	6.6	R	10
Northridge	17-Jan-1994	6.7	R	69
Loma Prieta	18-Oct-1989	6.9	S	45
Petrolia	25-Apr-1992	7.1	R	12
Landers	28-Jun-1992	7.3	S	22

* S denotes strike-slip, R represents reverse-slip

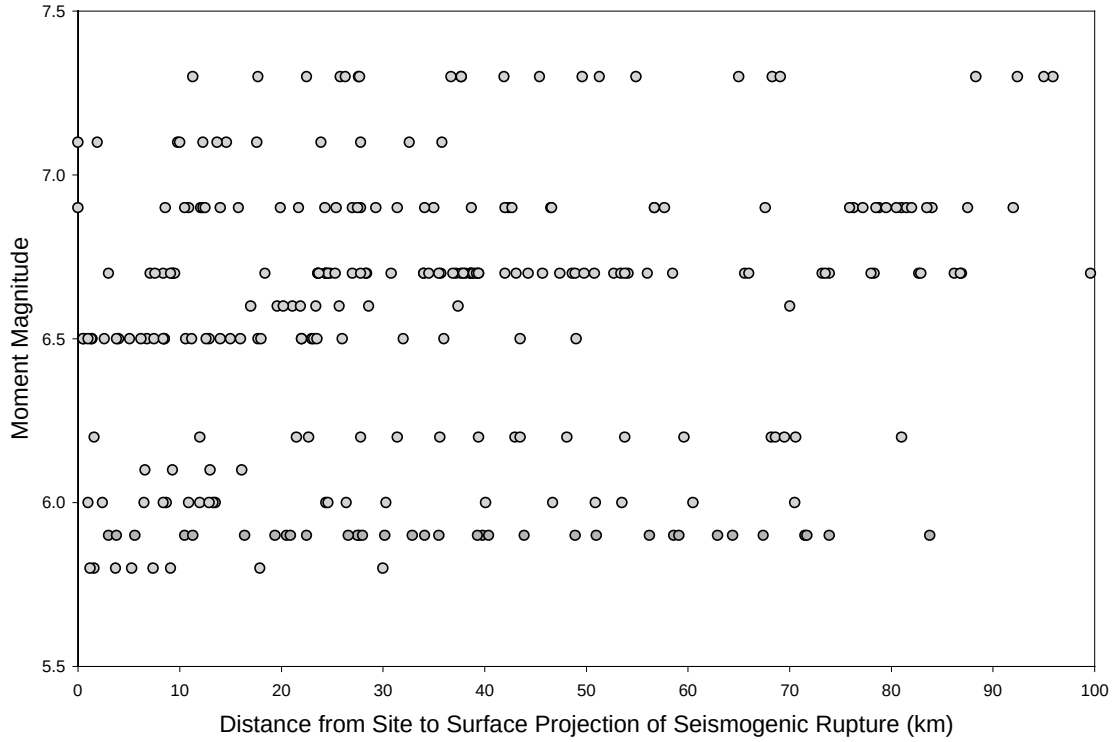

Figure 2.1: The magnitude-distance combination of the California strong motion records.

2.1.2 Data Processing

In order to develop a database that is uniformly processed, the uncorrected accelerograms are baseline and instrument corrected, as well as band-pass filtered. A sampling frequency of 50 Hz and a total duration of approximately 41 seconds (2048 points) is used for all the records. Shorter records are zero-padded, while longer records are truncated.

The filtering scheme employed in this data processing is similar to that used by the U.S. Geological Survey's strong ground motion program (Converse and Brady, 1992). The high-cut filter is a cosine half-bell between 23 Hz and 25 Hz, the latter being the Nyquist frequency. The low-cut filter is a second order bi-directional Butterworth filter with a corner frequency at 0.1 Hz. In some exceptional cases, however, the corner frequency can be as high as 0.15 Hz. The corner frequency is chosen after inspecting the Fourier amplitude spectrum of the raw time series. The gain function of the bi-directional low-cut Butterworth filter, or the squared magnitude of its transfer function, is given by:

$$\left|H_{LC}(f)\right|^2 = \frac{1}{1+(f_c/f)^{2N}} \tag{2.1}$$

where $\left|H_{LC}(f)\right|^2$ is the gain function, f denotes frequency, f_c is the corner frequency and N is the order of the filter. The gain function is shown graphically in Figure 2.2 as function of the normalized frequency, f/f_c, for N = 2. The gain function has a value of ½ at the corner frequency. The order of the filter controls the steepness of the gain function. The higher the order, the steeper is the gain function. The Butterworth filter is monotonic – i.e. there are no ripples in the gain function, neither in the pass-band nor in the stop-band. One disadvantage of the Butterworth filter is that its transition band is relatively wide. As can be seen on Figure 2.2, the gain function has reached approximately the value of 0.95 at twice the corner frequency and it is practically one at three times the corner frequency. The major drawback of the Butterworth filter is its phase distortion, which is most prominent around the corner frequency. However, the phase distortion can be eliminated by filtering the time history twice; from front to back, and from back to front.

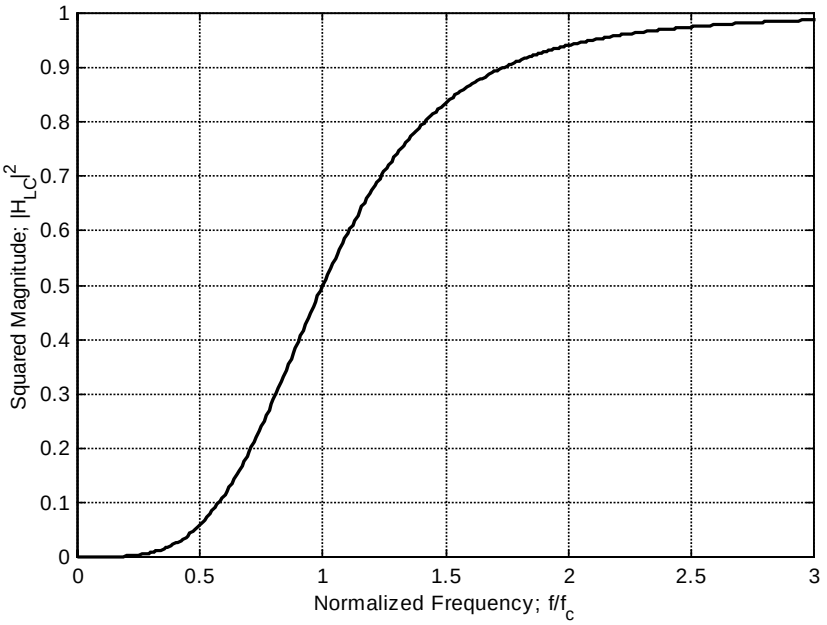

Figure 2.2: The gain function for a second order bi-directional Butterworth low-cut filter (roll-of parameter equal to 4).

Most filters with ideal amplitude response, i.e. flat pass- and stop-bands and a steep transition-band, have less than ideal phase response properties. The converse is also true, filters with perfectly linear phase response, i.e. no phase distortion, have usually rather poor amplitude characteristics. The bi-directional Butterworth filter is a good compromise of all the important features in filters (Marven and Ewers, 1996).

Due to the characteristics of the band-pass filtering discussed in this subsection, the results of this study are expected to be valid for acceleration in the frequency band between 0.4 Hz and 23 Hz. The results are not valid for frequencies lower than 0.2 Hz, and questionable for frequencies from 0.2 Hz to 0.4 Hz. These limitations should be kept in mind when interpreting the results of this study.

2.1.3 Site Classification According to Soil Conditions

Prior to the 1971 San Fernando, California, earthquake, no information was available on the effects of local soil conditions on earthquake ground motion. Since then, and especially since the 1985 Mexico earthquake, the importance and influence of local soil deposits on the characteristics and severity of ground motion has been emphasized numerous times.

In a very comprehensive study, Borcherdt (1994) summarizes the amplification effects of local geologic deposits on earthquake ground motion. In his paper, Borcherdt proposes a site classification method, which is incorporated with minor modifications in the building design provisions recommended by NEHRP, the National Earthquake Hazard Reduction Program (BSSC, 1994). The NEHRP site classification scheme is used in this study.

The recording sites are classified according to the shear wave velocity averaged over the uppermost 30 meters of the soil column at the site (see Table 2.2). Sites classified in either class A or B correspond roughly to “firm and hard rocks” as defined by Borcherdt (1994), and site class C corresponds to “gravely soils and soft to firm rocks” in Borcherdt’s paper. Site class D is similar to “stiff clays and sandy soils”, and site class E corresponds approximately to “soft soils” as defined in Borcherdt (1994).

Table 2.2: Definition of NEHRP Site Classes (BSSC, 1994).

Site Class	Shear Wave Velocity*
A	Greater than 1500 m/s
B	760 m/s to 1500 m/s
C	360 m/s to 760 m/s
D	180 m/s to 360 m/s
E	Less than 180 m/s

* Averaged over the uppermost 30 m

In this research the classification of recording sites is to a great extent based on the classification reported by Boore et al. (1993, 1994, 1997), since most sites used here were also used in their studies. Site classifications are further inferred from Borcherdt (1994), and from information in the Southern California Earthquake Center web site (http://smdb.crustal.ucsb.edu/ows-bin/owa/summary5.main) in conjunction with Park and Elrick (1998) and Tinsley and Fumal (1985). Prediction formulas for the model parameters are developed for all sites, as well as for different site classes. Due to limited data, classes A and B are combined in Site Class A&B (rock sites), and no prediction formulas are developed for Site Class E (soft soil sites).

2.2 The Regression Procedure

The magnitude of the earthquake and the source to site distance are the predictor variables, or the independent variables, selected for the prediction formulas of the model parameters. The magnitude scale used is the moment magnitude (Hanks and Kanamori, 1979). The moment magnitude is deemed the most suitable magnitude to represent the size of an earthquake, because it can be directly related to physical parameters of the earthquake process and it is not as prone to saturation as other magnitude scales.

Several different definitions of source to site distance have been used in the development of ground motion prediction relationships. The simplest and most common in early practice are the epicentral distance and the hypocentral distance. For large earthquakes, which rupture large areas, these distances can be very misleading, since the

site can be located directly above the fault, while the epicentral/hypocentral distance can be of the order of tens or even hundreds of kilometers. Therefore, other definitions have been proposed, such as the shortest distance from the site to the seismogenic rupture (Campbell, 1987) or the shortest distance from the site to the vertical projection of the seismogenic rupture on the surface of the Earth (Joyner and Boore, 1981). In this study, the Joyner and Boore source to site distance definition is used. This definition of the source to site distance is illustrated in Figure 2.3.

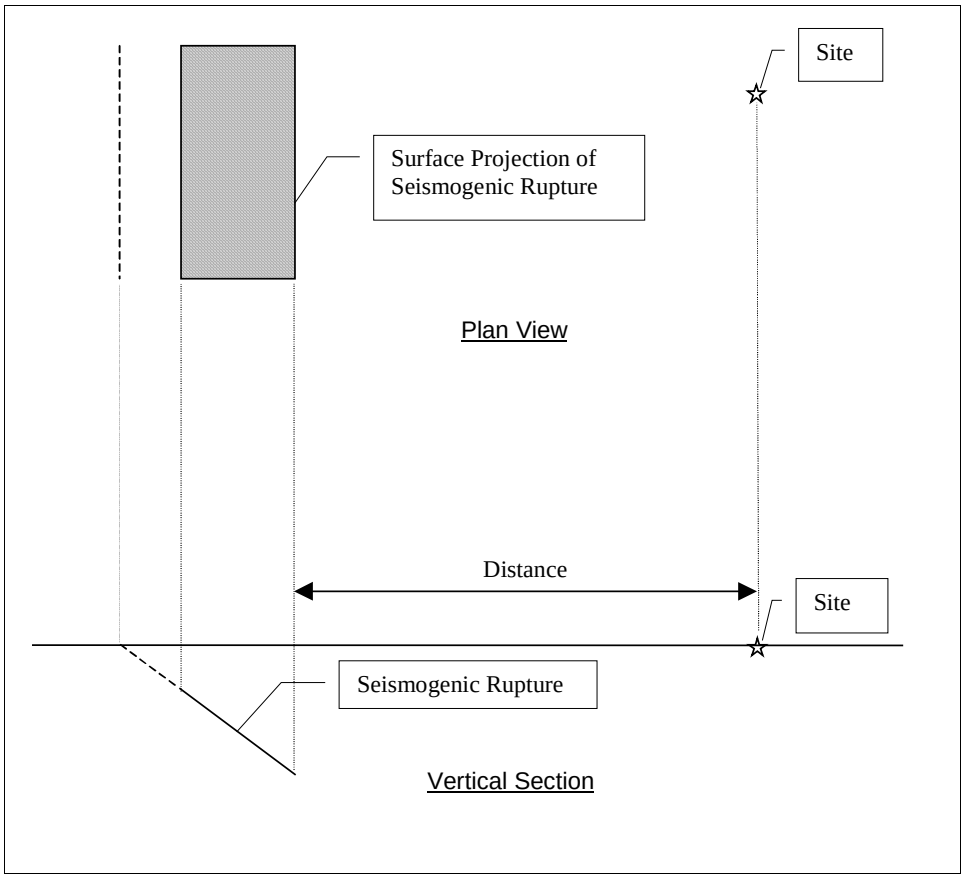

Figure 2.3: Shortest distance from site to vertical surface projection of seismogenic rupture.

For a given data set, the model parameters are estimated as function of distance and magnitude employing a two-step weighted least squares regression procedure, similar to the procedure described by Joyner and Boore (1988). In the first step, the distance dependence is determined along with a set of magnitude dependent scaling factors, one for each earthquake. In the second step, the scaling factors are regressed against

magnitude, using a weighted least squares regression, to obtain the magnitude dependence. The weights are proportional to the number of records in the data set for the given magnitude.

To explain the two-step regression procedure, consider the following example. Imagine that the distance dependence of the parameter *Y* is modeled by:

$$Y = c_1 + c_2 \cdot \exp\left(c_3 \cdot D^{c_4}\right) \tag{2.2}$$

where $c_i ; i \in \{1,2,3,4\}$ are regression parameters to be determined, and *D* is the distance. The data set under consideration includes joint observations of *Y* and *D* from *N* different earthquakes. In the first step of the two-step regression, the parameters $c_i ; i \in \{1,2,3,4\}$ and $\alpha_k ; k = 1,\ldots N$ are determined such that the sum of the squared errors:

$$SSE = \sum_{k=1}^{N} \sum_{j=1}^{n_k} I_k \cdot \left[\alpha_k \cdot Y_{kj} - \left(c_1 + c_2 \cdot \exp\left(c_3 \cdot D_{kj}^{c_4}\right)\right)\right]^2 \tag{2.3}$$

is minimized, using nonlinear optimization techniques. The optimization routine used in this study is based on the Nelder-Mead simplex search algorithm (Nelder and Mead, 1964). In Equation (2.3), the pair $\left(Y_{kj}, D_{kj}\right)$ is the j-th joint observation of *Y* and *D* for earthquake number k, n_k is the number of observations in the data set for the k-th earthquake, α_k is the scaling factor corresponding to the k-th earthquake, and I_k is an indicator variable, which is equal to one for the k-th earthquake but zero for all the other earthquakes.

In the second step of the regression procedure, the scaling factors, $\alpha_k ; k = 1,\ldots N$, are regressed against the magnitude, using a weighted least squares regression. If the scaling factors are, for example, believed to be linearly dependent on the magnitude, the parameters q_1 and q_2 are determined such that the sum of the weighted squared errors:

$$SWSE = \sum_{k=1}^{N} n_k \cdot \left[\alpha_k - \left(q_1 + q_2 \cdot M_k\right)\right]^2 \tag{2.4}$$

is minimized. In Equation (2.4), the parameter M_k represents the magnitude of the k-th earthquake.

The two-step regression procedure is illustrated graphically in Figure 2.4. In the first step, which is shown in Figure 2.4(a), the sum of the squared residuals is minimized by varying the shape of the regression curve representing the distance dependence (by varying the parameters c_i), and by shifting all the data points from the k-th earthquake by a scaling factor α_k. The data points from each earthquake are contained within a closed oval in the figure. In the second step, which is portrayed in Figure 2.4(b), the scaling factors are regressed against the magnitude, using weighted least squares regression.

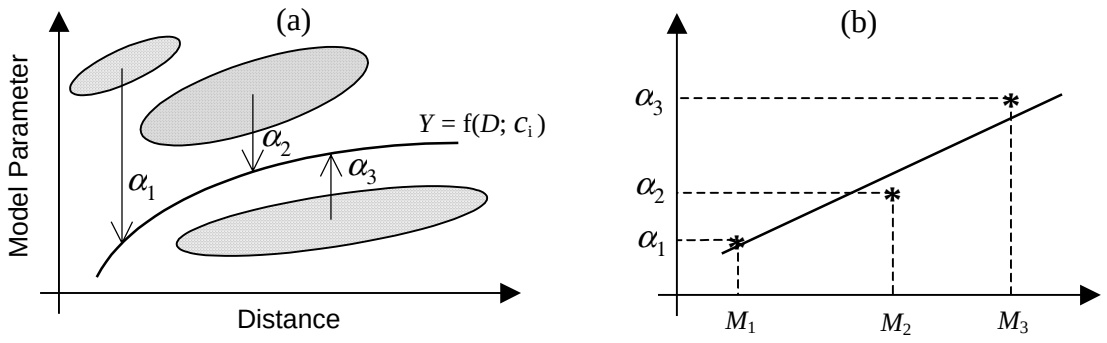

Figure 2.4: Schematic diagram of the two-step regression procedure. (a) Determination of the distance dependence and the magnitude scaling factors; (b) regression of the scaling factors against magnitude.

CHAPTER 3
MODELING OF PHASE DIFFERENCES: PARAMETRIC METHOD

In this study, the frequency-dependent characteristics of earthquake accelerograms are investigated using the discrete Fourier transform. In this chapter, an empirical method for the modeling of Fourier phase differences is presented. An alternative theoretical method is presented in the next chapter, and the modeling of the Fourier amplitude spectrum is discussed in Chapter 5.

In the first section of this chapter, the notational convention for the discrete Fourier transform is established. In the subsequent sections, an empirical phase difference distribution model is described, and prediction formulas for the model parameters are developed using the California ground motion database and the two-step regression procedure presented in Chapter 2. Finally, the quality of the fitted phase difference distributions is examined. The statistics on the phase difference distributions that are used in this chapter are tabulated in Appendix B.

3.1 The Discrete Fourier Transform

For digitally sampled time histories, both the time series, $f(t_k)$, and its Fourier transform, $F(\omega_j)$, are functions of a discrete argument (time and frequency, respectively). The discrete Fourier transform is defined here by:

$$F(\omega_j) = \frac{1}{N} \sum_{k=-N/2}^{N/2-1} f(t_k) \cdot \exp(-i \cdot \omega_j \cdot t_k); \quad j = -N/2, \ldots, N/2-1 \tag{3.1}$$

and the inverse discrete Fourier transform is given by:

$$f(t_k) = \sum_{j=-N/2}^{N/2-1} F(\omega_j) \cdot \exp(i \cdot \omega_j \cdot t_k); \quad k = -N/2, \ldots, N/2-1 \tag{3.2}$$

where $F(\omega_j)$ is the discrete Fourier transform evaluated at the j-th circular frequency, ω_j:

$$\omega_j = \frac{2\pi \cdot j}{T_d} = \frac{2\pi \cdot j}{N \cdot \Delta t}; \quad j = -N/2, \ldots, N/2 - 1 \tag{3.3}$$

In Equation (3.3), T_d is the total duration of the time series, Δt is the sampling interval, and N is the order of the discrete Fourier transform.

The discrete Fourier transform given by Equation (3.1) is a complex function that can be characterized by its amplitude and phase angle:

$$F(\omega_j) = A_j \cdot \exp(i \cdot \Phi_j) \tag{3.4}$$

where A_j is the Fourier amplitude corresponding to ω_j, and Φ_j is the phase angle. While the Fourier amplitudes of earthquake ground acceleration have been studied extensively, the phase angles have received little or no attention. Frequently, the phase angles are assumed to be independent of each other and uniformly distributed (e.g. Shinozuka and Deodatis, 1988). The validity of this independence and uniformity assumption is examined in the following section.

3.2 Characterization of Fourier Phase Differences

In earthquake ground motion modeling, the Fourier phase angles, Φ_j, are most frequently assumed to be independent, both of each other and the Fourier amplitude. In addition, the phase angles are typically assumed to be uniformly distributed between 0 and 2π or $-\pi$ and π. For a stationary Gaussian process, it can be shown that these are valid assumptions. The objective of this section is to demonstrate that these assumptions are not justifiable for a typical (nonstationary) ground motion record, and to propose an alternative model.

Figure 3.1 shows the results of an analysis of a typical recording of horizontal ground acceleration from a moderate size earthquake. The analysis involves taking a 2048 point discrete Fourier transform and evaluating the phase angles and the phase

differences, creating histograms of these quantities and plotting them as function of frequency as well as the Fourier amplitude.

The graphs on the left hand side of Figure 3.1 show the results of the analysis of the phase angles. Figure 3.1(a) shows a histogram of the phase angles for non-negative frequencies. The distribution is very close to uniform. In Figure 3.1(c), the phase angles are plotted versus frequency. The points appear to be uniformly scattered throughout the entire frequency-phase angle domain. In Figure 3.1(e), the phase angles are plotted as function of the Fourier amplitude. Once again, no systematic pattern is observed. For a given amplitude, the phase angles seem to be uniformly distributed between $-\pi$ and π. Therefore, one can justify the assumption that the phase angles follow a uniform distribution. It is, however, a different question whether the phase angles are independent of each other. That question can be answered by looking at the phase differences.

The right hand side of Figure 3.1 illustrates the results of analyses on the phase differences. The phase difference is defined as the difference in phase angles of adjacent, non-negative frequencies:

$$\Delta\Phi_j = \Phi_{j+1} - \Phi_j; \quad j = 0,1,\ldots, N/2-1 \tag{3.5}$$

A histogram of observed phase differences is shown in Figure 3.1(b). The histogram is clearly non-uniform. It should be noted that before constructing this histogram, the phase differences are unwrapped. The phase angle domain is $[-\pi, \pi]$ and hence the phase difference domain should be $[-2\pi, 2\pi]$. However, prior to further analyses, a factor of 2π is subtracted from the phase difference if it exceeds π, and 2π are added to the phase difference if it is less than $-\pi$. Therefore, the unwrapped phase difference domain becomes $[-\pi, \pi]$.

A scatterplot of the phase differences as function of frequency is displayed in Figure 3.1(d). As can be seen in this figure, the phase difference distribution appears to be independent of frequency. The independence assumption, however, seems no longer valid when the phase differences are plotted as function of the Fourier amplitude, as shown in Figure 3.1(f). While the mean phase difference does not appear to depend on amplitude, the dispersion around the mean decreases with increasing amplitude.

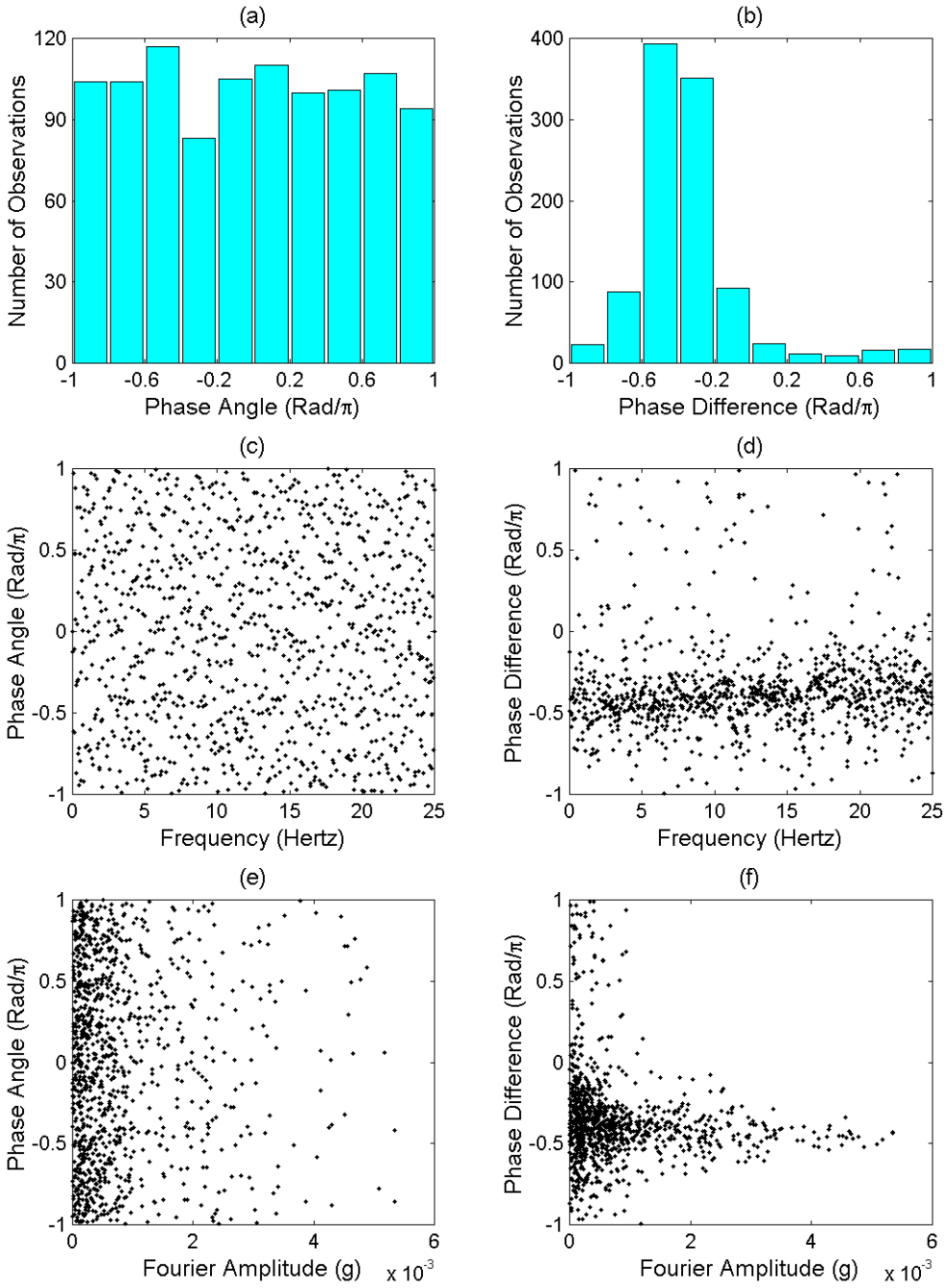

Figure 3.1: Observed phase angles and phase differences for the east-west component of the Santa Cruz record from the 1989 Loma Prieta, California earthquake. (a) Histogram of phase angles; (b) histogram of phase differences; (c) phase angles as function of frequency; (d) phase differences as function of frequency; (e) phase angles as function of amplitude; (f) phase differences as function of amplitude.

For a stationary stochastic process, the phase angles and the phase differences are independent, identically distributed and uniform. As shown in Figure 3.1, this is not the case for typical earthquake accelerograms. Therefore, the phase differences contain information on the non-stationarity of the process. By properly modeling this phenomenon, it is perhaps possible to simulate earthquake accelerograms in the frequency domain, invert the discrete Fourier transform, and obtain the nonstationary time series without employing any explicit modulation functions. This hypothesis is tested in this and the following chapter.

Several researchers have attempted to fit statistical distributions to the phase differences. Ohsaki (1979) performs statistical analysis on 49 Japanese accelerograms recorded on rock, and infers that the probability distribution is "normal or normal-like", after introducing a proper shift of the phase difference domain to account for the asymmetry. Kanda et al. (1983) simulate accelerograms using uniform distributions for the phase differences at different frequency bands. The width of the uniform distribution decreases with increasing frequency. Similarly, the mean phase difference decreases to ensure that the higher frequencies, in general, will occur before the lower frequencies in the simulated time series. Naraoka and Watanabe (1987) simulate accelerograms using a lognormal distribution for the phase differences. Matsukawa et al. (1987) fit a normal distribution to the phase differences, after a proper shift, and they find the fit to be "good" based on a chi-square test. Sigbjörnsson et al. (1994) develop probabilistic seismic hazard maps by simulating accelerograms using a normal distribution for the phase differences.

To capture the dependence of phase angle differences on Fourier amplitude, the amplitudes are classified into three categories in this chapter: small, intermediate and large. Statistical analyses are performed on the phase differences corresponding to each amplitude category. The 10% largest amplitudes are defined as *large*, the 55% smallest are defined as *small*, and the remaining are *intermediate*. Several other cut-off fractiles were examined, but based on analysis of many recorded time histories from different earthquakes, the two fractiles mentioned above (55% and 90%) yielded the most consistent results. An attempt was made to use only two Fourier amplitude categories, small and large, but the simulated accelerograms did not look realistic. In Section 3.4, it is shown that classifying the Fourier amplitudes into three categories yields sufficiently

good results. Therefore, finer discretization was not pursued. In the next chapter, the amplitude range is not discretized at all, but a Fourier phase difference distribution is developed where the parameters are continuous functions of the Fourier amplitude.

Phase difference histograms for an entire time history and for each amplitude category are displayed in Figure 3.2. The dispersion of the phase differences is considerably smaller for the large amplitudes than the small ones.

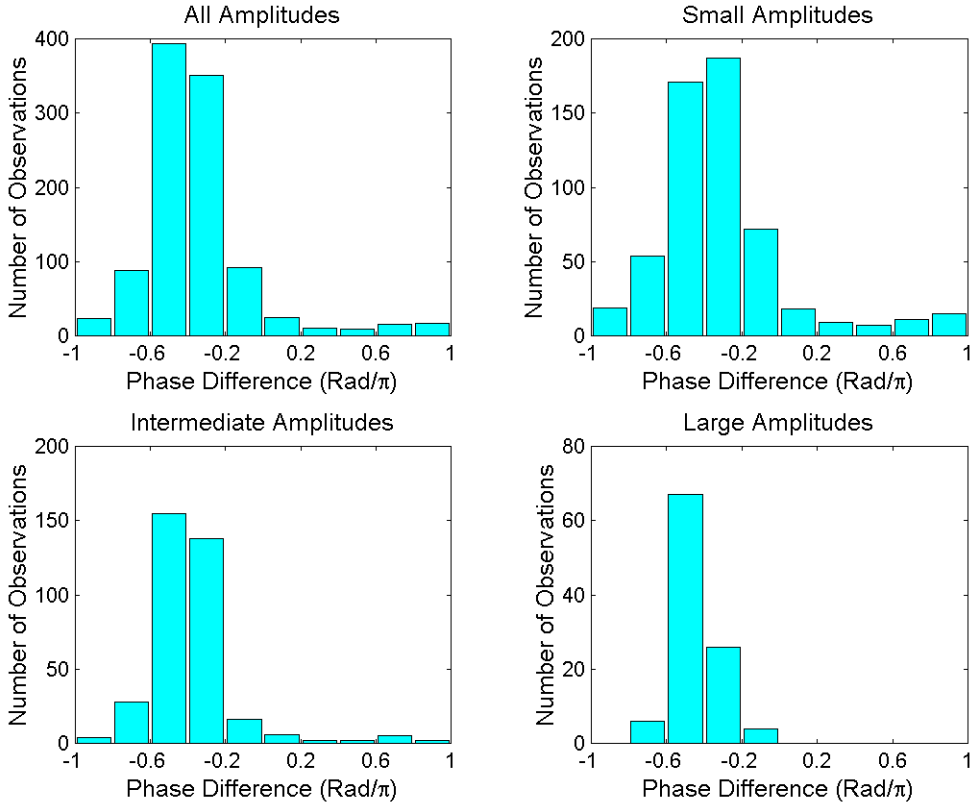

Figure 3.2: Histograms of phase differences for different amplitude categories. The east-west component of the UC Santa Cruz record from the 1989 Loma Prieta, California earthquake.

The distribution fitted to the phase differences should take into account the circular nature of the phase differences, i.e. the probability density should have the same value at $-\pi$ as at $+\pi$. The beta distribution appears to be an obvious choice for the large and the intermediate Fourier amplitudes. It describes the probability distribution of a bounded random variable, and if both its shape parameters are larger than one, the probability density function is unimodal and zero at both ends. For the small amplitudes, however, it is found useful to superimpose a beta on a uniform distribution. To facilitate

the use of the standardized beta distribution, the phase differences are first shifted from [-π, π] to [-1.4π, 0.6π] in order to obtain a unimodal distribution, and then the shifted phase differences are normalized to the interval [0,1].

The probability density function of a beta distributed random variable, *X*, which is bounded between zero and one, is given by:

$$f_X(x) = \frac{x^{r-1}(1-x)^{s-1}}{B(r,s)}; \quad 0 \le x \le 1; \tag{3.6}$$

where $r, s > 0$ are the shape parameters of the distribution, and the normalizing constant is given by:

$$B(r,s) = \int_0^1 u^{r-1}(1-u)^{s-1}\,du \tag{3.7}$$

The cumulative distribution function, which is sometimes referred to as the incomplete beta function, does not exist in a closed form for arbitrary values of *r* and *s*. The mean and the variance of the random variable *X* are related to the shape parameters according to:

$$\begin{aligned} \mu_X &= \frac{r}{r+s} \\ \sigma_X^2 &= \frac{r \cdot s}{(r+s)^2 \cdot (r+s+1)} \end{aligned} \tag{3.8}$$

where μ_X is the mean and σ_X^2 represents the variance.

An example of the fitted phase difference distributions is shown in Figure 3.3 for large, intermediate and small Fourier amplitudes. The parameters of the beta distribution for the different amplitude categories are estimated using the method of moments. The relative weight of the uniform distribution for small amplitudes is obtained as follows. First, the interval between zero and one is discretized into ten bins and the number of observed phase differences within each bin is determined. Then the numbers within the bins are scaled such that the total area of the histogram equals one. Finally, the relative weight of the uniform distribution is determined as the height of the smallest bar, after

scaling. In Figure 3.3, the fitted distributions are shown with black dashed lines, while the observed distributions are shown with gray solid lines.

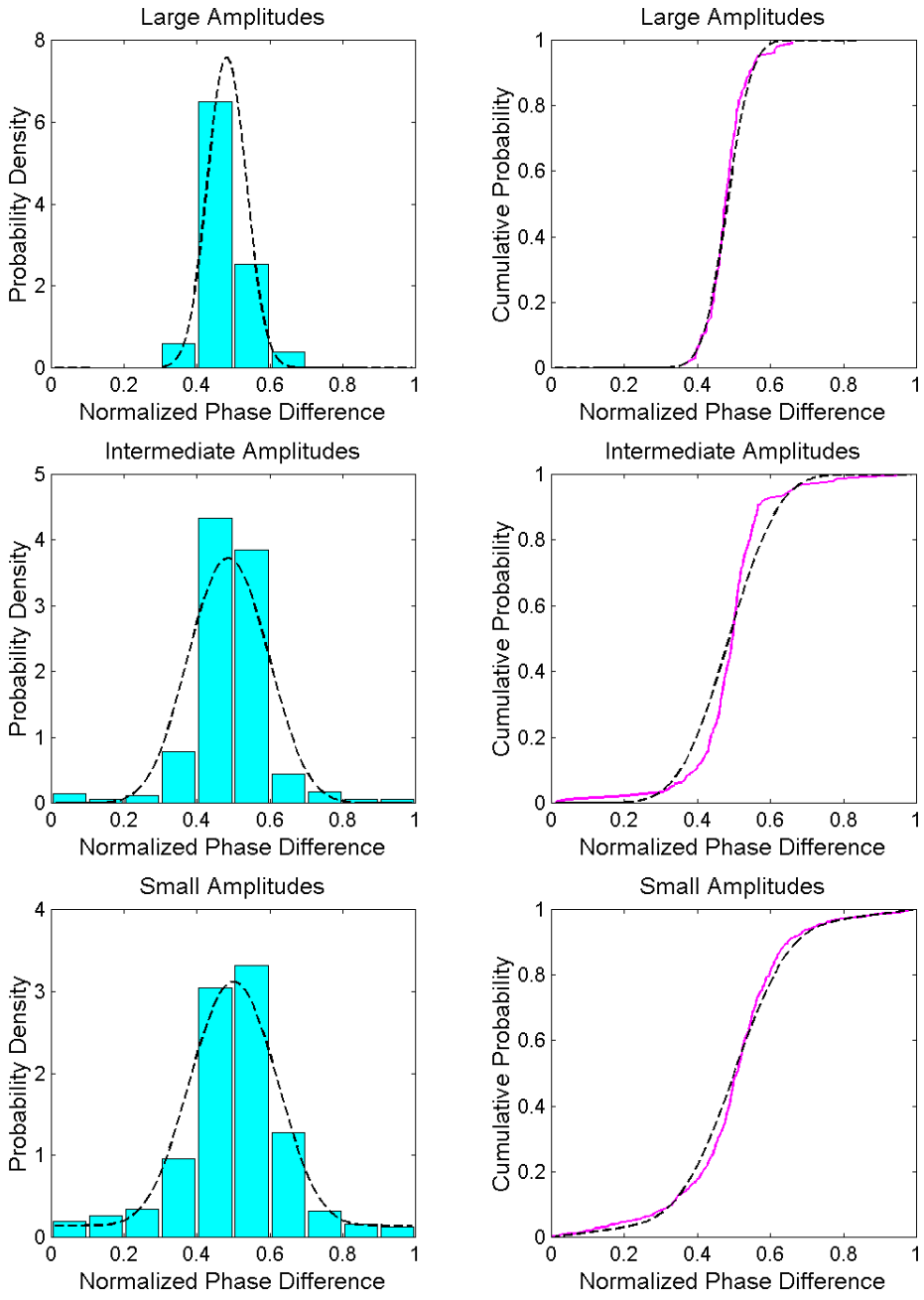

Figure 3.3: Fitted (dashed lines) and observed (bars, solid lines) conditional phase difference distributions. The east-west component of the UC Santa Cruz record from the 1989 Loma Prieta, California earthquake.

3.3 Model Parameters

A beta distribution can either be characterized by the mean and the variance of the random variable, or by the two shape parameters of the distribution. In this study, the means and the variances are used to define the beta distributions for normalized phase differences, because the sample means and variances are uncorrelated, while the estimates of the shape parameters are correlated.

The model of the phase differences described in the previous section requires seven parameters: the mean normalized phase difference and variance for small, intermediate, and large Fourier amplitudes, respectively, and the relative weight of the uniform distribution for small Fourier amplitudes. In this section, the dependency between the model parameters is examined, and prediction formulas are developed. Analyses of the ground motion data from California show that the seven phase difference parameters are not mutually independent. The relationship between the parameters is illustrated in Figures 3.4, 3.5 and 3.6.

In Figure 3.4(a) the mean normalized phase difference for intermediate Fourier amplitudes is plotted as a function of the mean phase difference for large amplitudes. A distinct linear trend is apparent. In Figure 3.4(b), the relationship between the mean phase difference for small amplitudes and the mean phase difference for large amplitudes is examined. As observed for the intermediate amplitudes, the mean phase difference for small amplitudes seems to be linearly related to the mean phase difference for large amplitudes. According to Figure 3.4, it is sufficient to develop prediction formulas based on magnitude and distance for the mean normalized phase difference for large Fourier amplitudes only. Once that has been determined, the mean values for intermediate and small Fourier amplitudes can easily be estimated using linear regression.

The relationships between the variances of the normalized phase differences are examined in Figure 3.5. The variance of phase differences for small amplitudes is taken as the independent variable and plotted on the horizontal axes. In Figures 3.5(a) and 3.5(c) the variance for large Fourier amplitudes is plotted on the vertical axes. In Figures 3.5(b) and 3.5(d) the variance for intermediate Fourier amplitudes is plotted on the vertical axes. The figures at the top, 3.5(a) and 3.5(b), are in linear space, while the

figures at the bottom, 3.5(c) and 3.5(d), are in logarithmic space. The scatterplots in Figures 3.5(c) and 3.5(d) reveal a linear trend where the dispersion around a potential regression line does not appear to depend on the independent variable, i.e. the logarithm of the variance for small Fourier amplitudes. Hence, the variance of the normalized phase difference for large and intermediate Fourier amplitudes, respectively, are regressed against the variance for small amplitudes in logarithmic space.

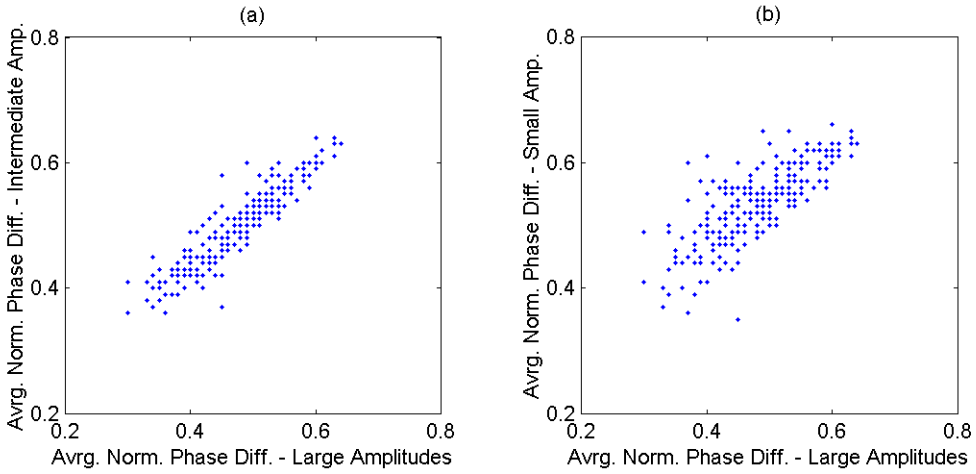

Figure 3.4: The relationship between average normalized phase differences for the California ground motion records. (a) Average normalized phase difference for intermediate Fourier amplitudes vs. average normalized phase difference for large Fourier amplitudes; (b) average normalized phase difference for small Fourier amplitudes vs. average normalized phase difference for large Fourier amplitudes.

A scatterplot of the relative weight of the uniform distribution versus the variance of normalized phase difference for small Fourier amplitudes is shown in Figure 3.6. Based on the linear trend revealed in this figure, the weight of the uniform distribution is determined from linear regression on the variance.

It can be concluded from Figures 3.4, 3.5, and 3.6 that information on only two phase difference parameters, i.e. the mean normalized phase difference for large amplitudes and the variance of normalized phase difference for small amplitudes, are generally sufficient to infer the values of the other five parameters. For the remainder of this report, the mean of the normalized phase difference for large Fourier amplitudes and the variance of normalized phase difference for small Fourier amplitudes are referred to

as the fundamental parameters, while the other five parameters are referred to as the secondary parameters. In the following subsections, the results of the regression analyses of the phase difference parameters are presented. First, prediction formulas for the fundamental parameters are developed, followed by regression analyses of the secondary parameters as function of the fundamental parameters. Prediction formulas are developed for the fundamental parameters for all sites, as well as different site classes (see Subsection 2.1.3 for the definition of site classes), while the local site conditions are not explicitly accounted for in the development of the prediction formulas for the secondary beta parameters. However, the site conditions are implicitly taken into account, since the secondary parameters are conditional on the fundamental parameters.

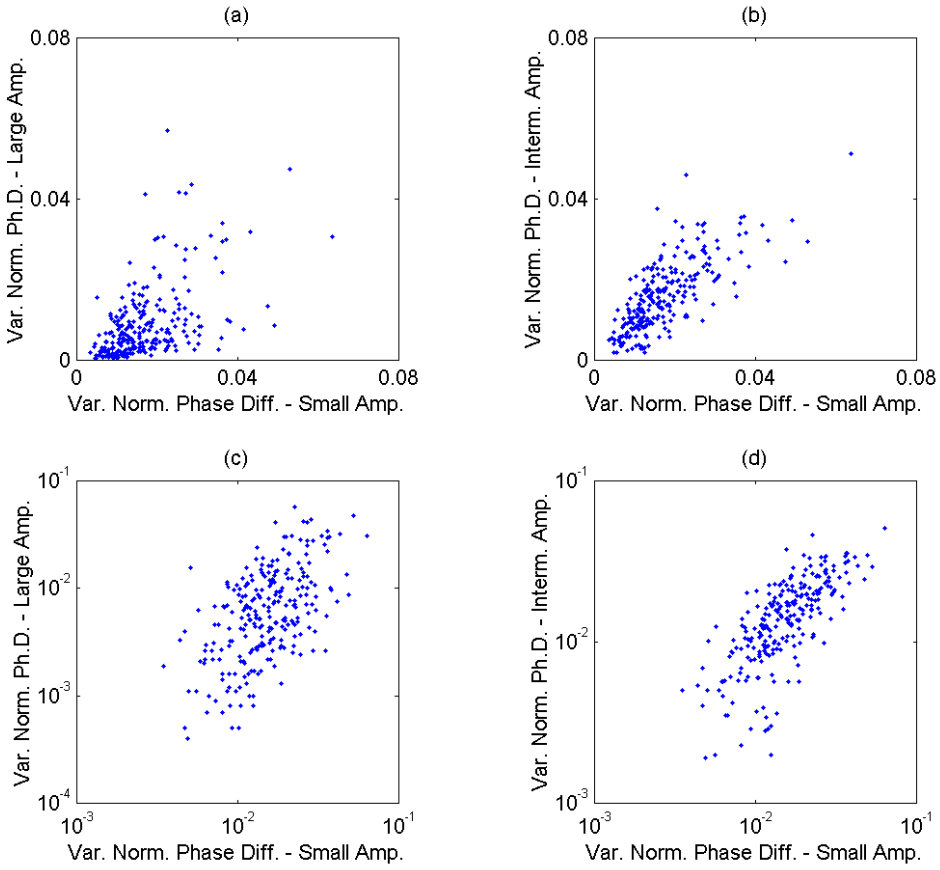

Figure 3.5: The relationship between the variance of normalized phase differences for the California ground motion records. (a) The variance for large amplitudes vs. the variance for small amplitudes on a linear scale; (b) the variance for intermediate amplitudes vs. the variance for small amplitudes on a linear scale; (c) the variance for large amplitudes vs. the variance for small amplitudes on a logarithmic scale; (d) the variance for intermediate amplitudes vs. the variance for small amplitudes on a logarithmic scale.

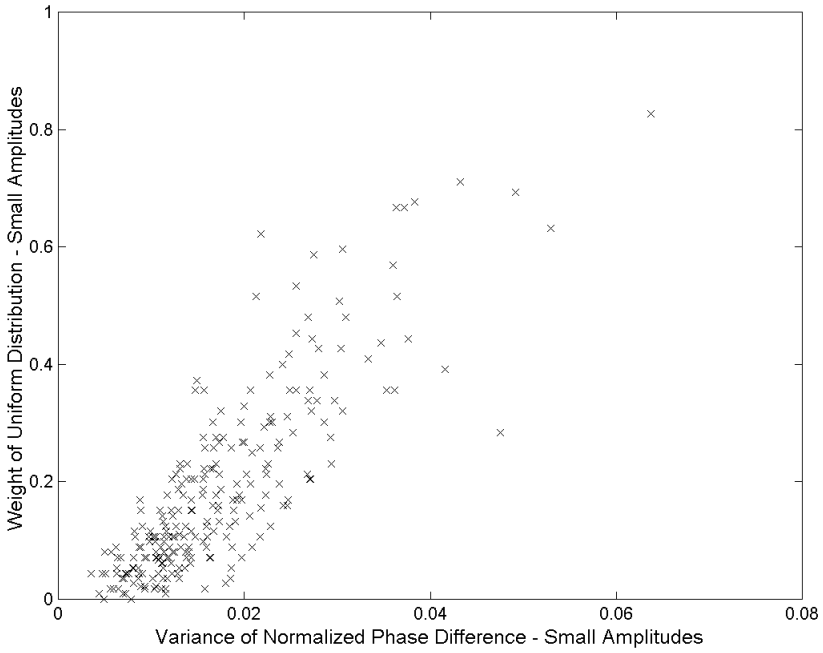

Figure 3.6: The weight of the uniform distribution as function of the variance of normalized phase difference for small amplitudes.

3.3.1 Fundamental Parameters

The fundamental parameters are the mean normalized phase difference for large Fourier amplitudes and the variance of the normalized phase difference for small amplitudes. The five secondary beta parameters can all be determined conditional on these two fundamental parameters, which is done in the following subsection. In this subsection, the two-step regression procedure described in Section 2.2 is used to obtain prediction formulas for the fundamental parameters, based on the magnitude of the earthquake and the source to site distance.

The Mean Normalized Phase Difference for Large Amplitudes

In Figure 3.7, the mean normalized phase difference for large Fourier amplitudes is plotted as function of distance for two earthquakes; the M_w = 5.9 1987 Whittier Narrows earthquake, and the M_w = 6.9 1989 Loma Prieta earthquake. Two trends are apparent from this scatterplot: (i) the mean normalized phase difference decreases with distance,

and (ii) the mean phase difference for the smaller earthquake tends to be slightly larger than the mean phase difference for the larger earthquake. Furthermore, the mean seems to decrease roughly linearly with distance.

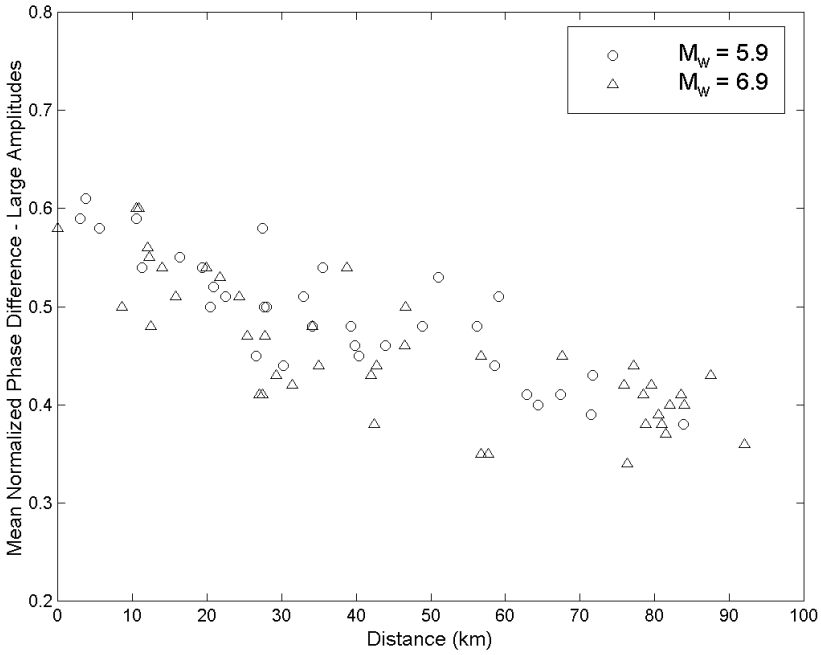

Figure 3.7: Mean normalized phase difference for large Fourier amplitudes as function of distance, for two different earthquake magnitudes.

With these two observations in mind, the following regression model is fitted to the data:

$$\mu_L = \frac{c_1 + c_2 \cdot D}{c_M(M_W)} \tag{3.9}$$

where μ_L is the mean normalized phase difference for large Fourier amplitudes, *D* is the distance of the site from the source, and c_1, c_2 and $c_M(M_W)$ are regression coefficients. The coefficients $c_M(M_W)$ are magnitude-dependent scaling factors. In the second step of the regression procedure, a linear model is fitted to the magnitude scaling factor:

$$c_M = q_1 + q_2 \cdot M_W \tag{3.10}$$

Here, q_1 and q_2 are regression coefficients, and M_W is the moment magnitude.

The results of the regression analysis described above are shown in Figure 3.8 for the entire ground motion data set. In Figure 3.8(a), the magnitude-scaled mean is plotted as function of distance (both the observed data points and the fitted line). The term "magnitude-scaled mean" refers to the quantity $\mu_L \cdot c_M(M_W)$, which according to the model in Equation (3.9) only depends on distance. The equation of the best-fit line is given at the top of the figure. In Figure 3.8(b), the residuals from the regression in (a) are plotted as function of distance, and the standard deviation of these residuals is given in the lower right hand corner. The residuals do not seem to be dependent on distance. A histogram of the standardized residuals is displayed in Figure 3.8(d). The coefficients of skewness and kurtosis are reported on the figure. The residuals exhibit a slight positive skewness. The results of the second step of the regression procedure are shown in Figure 3.8(c), where the magnitude scaling factor is regressed against the moment magnitude. A linear trend is revealed, where the scaling factor increases with magnitude. The line in 3.8(c) is not very steep, indicating only a mild magnitude dependence.

The two-step regression was repeated for Site Class A&B, Site Class C, and Site Class D. The model parameters from these analyses are recorded in Table 3.1, along with the parameters that were obtained using recordings from the entire data set. The parameter σ represents the standard error of the regression; it is the standard deviation of the difference between the observed and predicted magnitude-scaled normalized phase difference.

The results of the regression analyses summarized in Table 3.1 are displayed graphically in Figure 3.9. In Figure 3.9(a), the magnitude-scaled mean normalized phase difference is plotted as a function of distance for different site classes. The thick, solid line in Figure 3.9(a) is the same as the solid line in Figure 3.8(a). Even though the difference between the site classes is rather small, some systematic differences are apparent. The mean tends to be smaller for the softer sites than the stiffer ones, and it decreases faster with distance for the softest site class than the other site classes.

The magnitude dependency of the mean normalized phase difference is illustrated in Figure 3.9(b) for different site classes. The thick, solid line in Figure 3.9(b) is the same as the solid line in Figure 3.8(c). The scaling factor is more sensitive to the magnitude for the stiffest sites (Site Class A&B) than the other site classes. The magnitude scaling

factor for Site Class C is practically the same as the magnitude scaling factor for Site Class D.

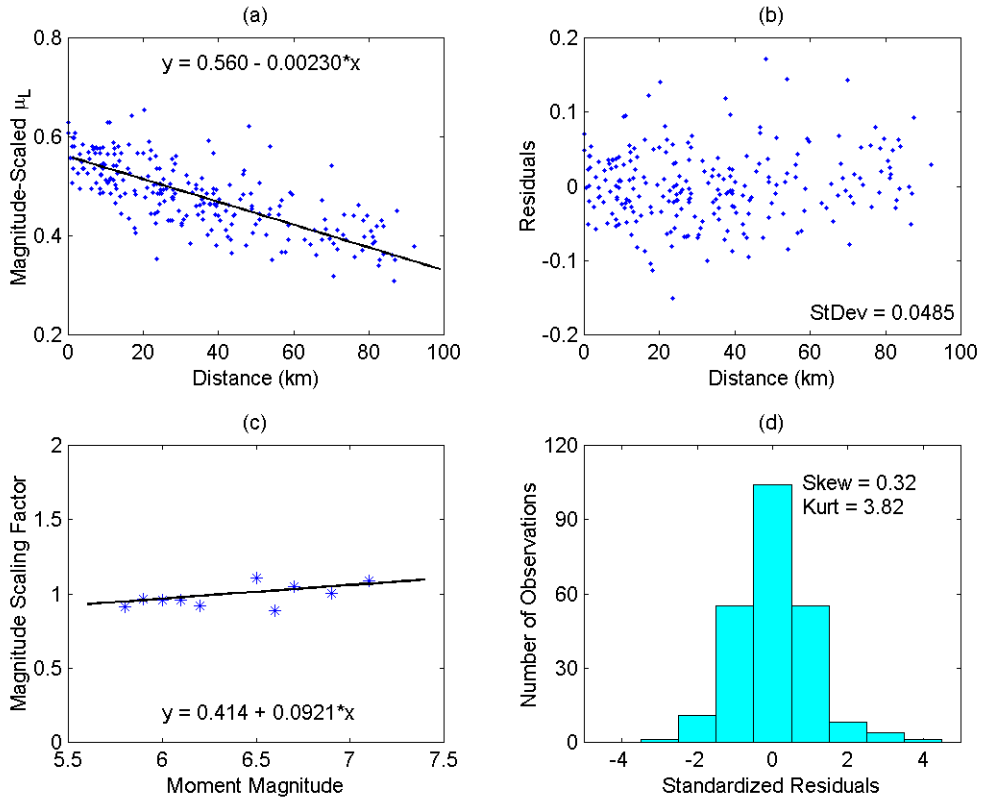

Figure 3.8: Results of a two step regression analysis for the mean normalized phase difference for large Fourier amplitudes and all site classes. (a) The distance dependence of the magnitude-scaled mean; (b) residuals from (a) as function of distance; (c) the magnitude dependent scaling factor; (d) histogram of the standardized residuals from (a).

Table 3.1: Regression results for μ_L.

Data Set	c_1	c_2	q_1	q_2	σ
All Sites	0.56	-0.0023	0.41	0.092	0.0485
Site Class A&B	0.60	-0.0023	-0.67	0.259	0.0386
Site Class C	0.55	-0.0021	0.40	0.094	0.0560
Site Class D	0.55	-0.0027	0.51	0.077	0.0397

Model: $\mu_L = \dfrac{c_1 + c_2 \cdot D}{q_1 + q_2 \cdot M_W}$

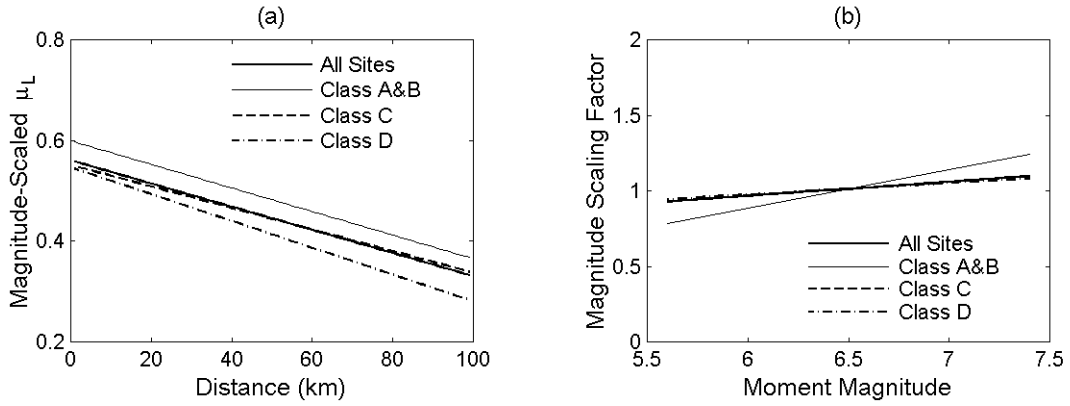

Figure 3.9: Results of a two step regression analysis for the mean normalized phase difference for large Fourier amplitudes and different site classes. (a) The distance dependence of the magnitude-scaled mean; (b) the magnitude dependent scaling factor.

The Variance of Normalized Phase Difference for Small Amplitudes

In Figure 3.10(a), the variance of the normalized phase difference for small Fourier amplitudes is plotted as a function of distance, while in Figure 3.10(b), the natural logarithm of the variance is plotted as function of distance. The scatterplot in Figure 3.10(a) might suggest a linear relationship. However, the linear model is not desirable, because the scatter increases significantly with distance. The scatter of the natural logarithm in Figure 3.10(b) does not seem to depend on distance. Therefore, the regression analysis is performed on the natural logarithm of the variance rather than the variance itself.

The following regression model for the small variance is fitted to the California ground motion data:

$$\ln\left(\sigma_S^2\right) = \frac{c_1 + c_2 \cdot \exp\left(c_3 \cdot D^{c_4}\right)}{c_M\left(M_W\right)} \tag{3.11}$$

where σ_S^2 is the variance of the normalized phase difference for small Fourier amplitudes, D is the distance from the site to the source, and c_1, c_2, c_3, c_4, and $c_M\left(M_W\right)$ are regression coefficients. This functional form is chosen because it conforms to the pattern of the data points in Figure 3.10(b). A linear regression is then performed on the magnitude scaling factors:

$$c_M = q_1 + q_2 \cdot M_W \tag{3.12}$$

where, q_1 and q_2 are regression coefficients, and M_W is the moment magnitude of the earthquake.

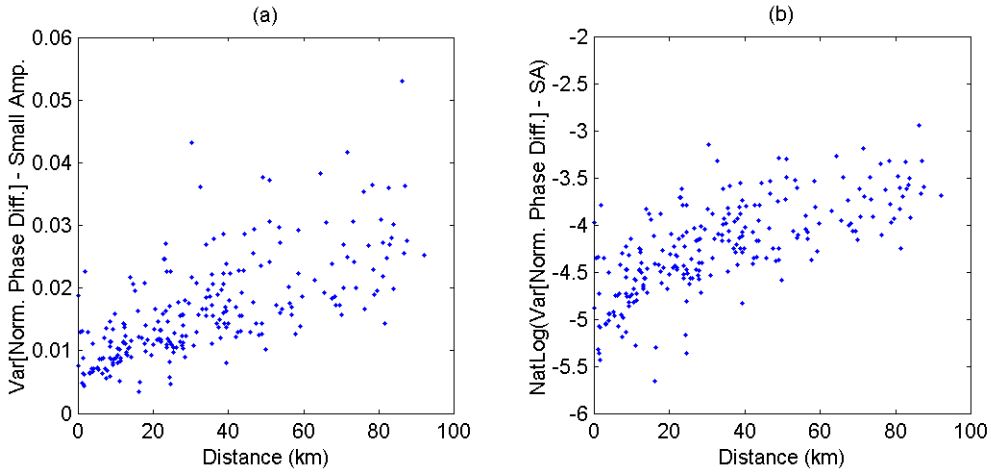

Figure 3.10: Variance of normalized phase difference for small Fourier amplitudes as function of distance. (a) The variance versus distance; (b) the natural logarithm of the variance as function of distance.

The results of the two-step regression analysis for the variance using the entire ground motion data set are shown in Figure 3.11. In Figure 3.11(a), the magnitude-scaled natural logarithm is plotted as function of distance; both the observed data points and the fitted curve. The equation of the best-fit curve is given at the top of the figure. In Figure 3.11(b), the residuals from the regression in (a) are plotted as function of distance, and the standard deviation of these residuals is given in the lower right hand corner. The residuals do not seem to be dependent on distance. A histogram of the standardized residuals is displayed in Figure 3.11(d). The coefficients of skewness and kurtosis are reported on the figure. The residuals exhibit a slight positive skewness. The results of the second step of the regression procedure are shown in Figure 3.11(c), where the magnitude scaling factor is regressed against the moment magnitude. The scaling factor – and hence, the variance – does not appear to depend on magnitude.

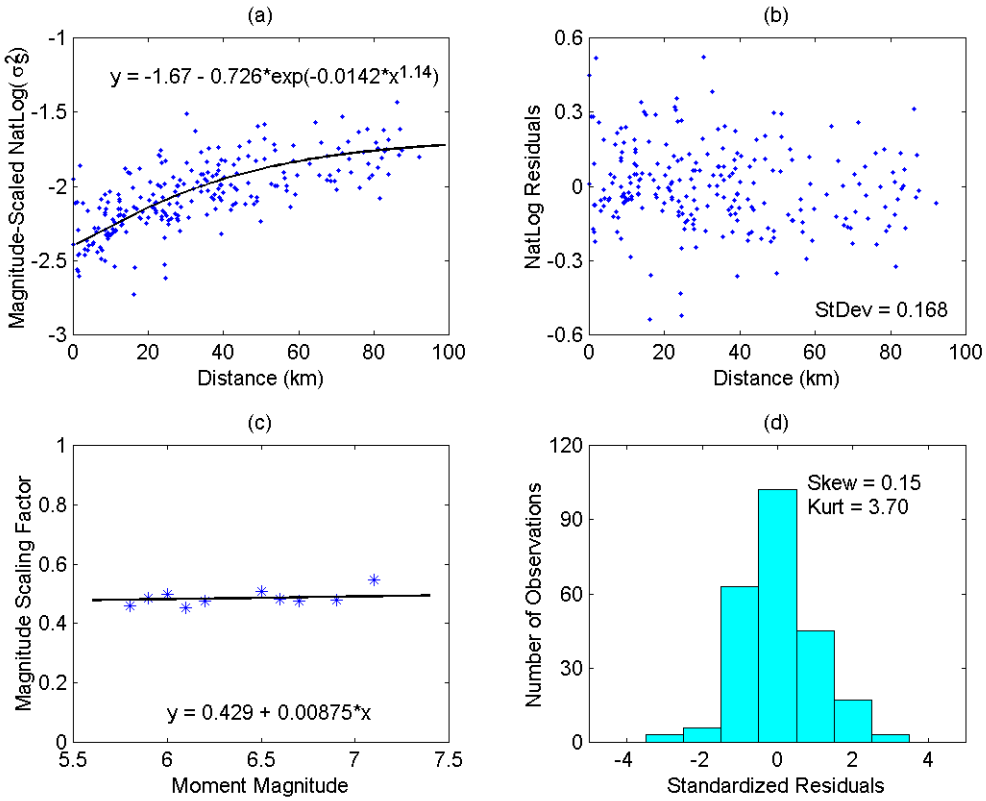

Figure 3.11: Results of a two step regression analysis for the natural logarithm of the variance of normalized phase difference for small Fourier amplitudes and all site classes. (a) The magnitude-scaled distance dependence; (b) the residuals from (a) as function of distance; (c) the magnitude dependent scaling factor; (d) histogram of the standardized residuals from (a).

The two-step regression was repeated for Site Class A&B, Site Class C, and Site Class D. The model parameters from these analyses are recorded in Table 3.2, along with the parameters that were obtained using recordings from the entire data set. The parameter σ represents the standard error of the regression.

The results of the regression analyses summarized in Table 3.2 are displayed graphically in Figure 3.12. In Figure 3.12(a), the magnitude-scaled variance is plotted as a function of distance for different site classes. The thick, solid line in Figure 3.12(a) is the same as the solid line in Figure 3.11(a). The variance for the rock sites (Site Class A&B) is considerably larger than the variance for the soil sites (Site Class C and Site Class D), while there is insignificant difference between Site Classes C and D. The apparent difference between Site Classes C and D for distances shorter than 10 km is

inconsequential, because there are very few data points to anchor the curves at very short distances.

The magnitude dependency of the variance is illustrated in Figure 3.12(b) for different site classes. The thick, solid line in Figure 3.12(b) is the same as the solid line in Figure 3.11(c). The variance does not seem to depend on the magnitude for the softer sites (Site Class C and Site Class D), and only mildly so for the rock sites.

To predict the value of the variance of normalized phase difference for small Fourier amplitudes, it is recommended to use Equations (3.11) and (3.12) with the parameters corresponding to Site Class A&B from Table 3.2 for rock sites, and the parameters corresponding to Site Class D from Table 3.2 for all non-rock sites.

Table 3.2: Regression results for σ_S^2.

Data Set	c_1	c_2	c_3	c_4	q_1	q_2	σ
All Sites	-1.67	-0.726	-0.0142	1.14	0.43	0.009	0.168
Site Class A&B	-1.46	-0.528	-0.0150	1.23	0.14	0.054	0.066
Site Class C	-2.10	-0.973	-0.0555	1.14	0.47	0.002	0.191
Site Class D	-2.04	-0.476	-0.0039	1.74	0.51	-0.003	0.176

Model: $$\ln\left(\sigma_S^2\right) = \frac{c_1 + c_2 \cdot \exp\left(c_3 \cdot D^{c_4}\right)}{q_1 + q_2 \cdot M_W}$$

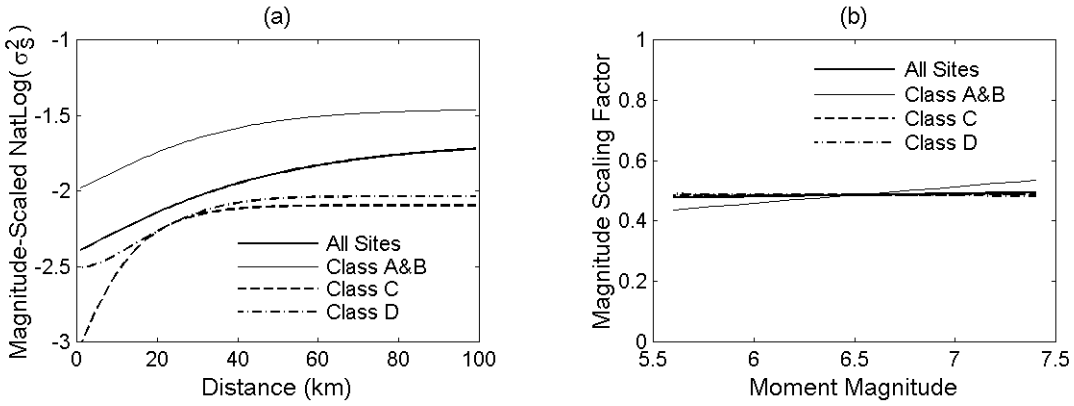

Figure 3.12: Results of a two step regression analysis for the variance of normalized phase difference for small Fourier amplitudes and different site classes. (a) The distance dependence of the magnitude-scaled variance; (b) the magnitude dependent scaling factor.

3.3.2 Secondary Parameters

Five more parameters, in addition to the fundamental parameters, are needed to fully define the Fourier phase difference distributions. These are:

1. The mean normalized phase difference for intermediate Fourier amplitudes,
2. the mean normalized phase difference for small Fourier amplitudes,
3. the variance of normalized phase difference for intermediate Fourier amplitudes,
4. the variance of normalized phase difference for large Fourier amplitudes, and,
5. the weight of the uniform distribution in the probability distribution of normalized phase difference for small Fourier amplitudes.

In this subsection, the first two parameters are regressed versus the mean normalized phase difference for large Fourier amplitudes, and the last three are regressed on the variance of normalized phase difference for small Fourier amplitudes.

The Mean Normalized Phase Difference for Intermediate and Small Amplitudes

The results of the regression analyses of the mean normalized phase difference for intermediate and small Fourier amplitudes versus the mean for large amplitudes are displayed in Figure 3.13. The results for the intermediate amplitudes are depicted in the left column and the results for the small amplitudes are in the right column. The plots at the top, (a) and (b), show the fitted lines, obtained through linear least squares regression, superimposed on the observed data points. The equation of the best line is also given in the upper right hand corner of each plot. The plots in the middle, (c) and (d), show how the residuals depend on the independent variable (the mean normalized phase difference for large Fourier amplitudes) and the standard deviation of the residuals is given in the lower right hand corner. In neither case is there an obvious trend in the residuals, which is as desired. At the bottom of Figure 3.13, (e) and (f), there are histograms of the standardized residuals; i.e. zero mean, unit standard deviation. The numbers reported on the graphs are the coefficients of skewness and kurtosis. In both cases, the residuals exhibit a positive skewness and kurtosis slightly larger than the kurtosis for a normal distribution of 3.0.

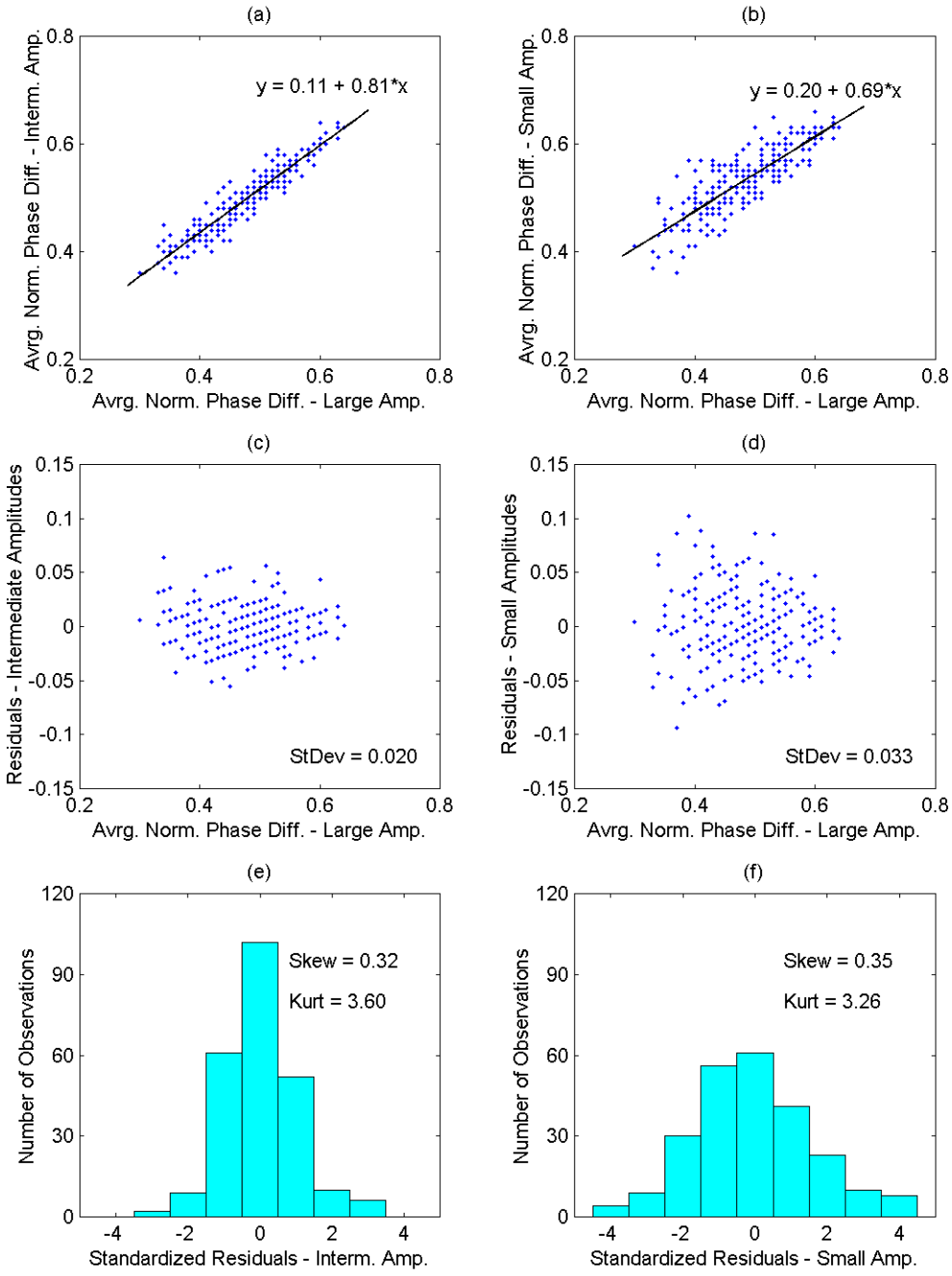

Figure 3.13: Regression results for mean phase differences. (a) Intermediate amplitudes vs. large amplitudes; (b) small amplitudes vs. large amplitudes; (c) residuals from the regression in (a); (d) residuals from the regression in (b); (e) histogram of standardized residuals from the regression in (a); (f) histogram of standardized residuals from the regression in (b).

The Variance of Normalized Phase Difference for Intermediate Amplitudes

Figure 3.14 displays the results from the regression analysis of the variance of normalized phase difference for intermediate Fourier amplitudes versus the variance for small amplitudes. In part (a), the best line is superimposed on the observed data points, in natural logarithm space. The equation of the best line is given in the lower right hand corner. The residuals from the linear regression are plotted in part (b), as function of the independent variable. The standard deviation is shown in the lower right hand corner. No trend is apparent from this plot. In part (c), the data points and the best line fit from (a) have been transformed into the original, linear space. A histogram of the standardized residuals from the linear regression is showed in part (d). The coefficient of skewness is –0.80, which implies a skewness to the left. The coefficient of kurtosis is 4.14, considerably higher than the value of 3 for a normal distribution.

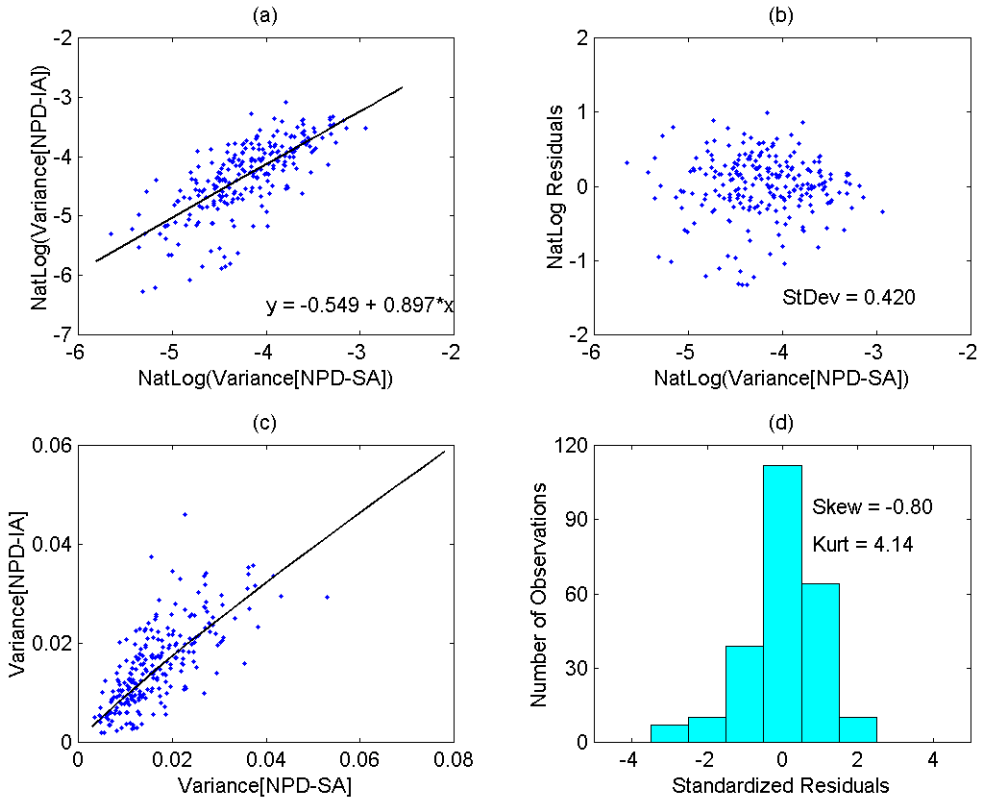

Figure 3.14: Results of regression analysis of variance of normalized phase difference for intermediate amplitudes vs. variance of normalized phase difference for small amplitudes. (a) Linear regression in natural logarithm space; (b) residuals of the regression in (a); (c) the regression in (a) transformed into linear space; (d) histogram of standardized residuals from (a).

The Variance of Normalized Phase Difference for Large Amplitudes

In Figure 3.15, the results from the regression analysis of the variance for large amplitudes versus the variance for small amplitudes are displayed. In part (a), the best line is superimposed on the observed data points, in natural logarithm space. The equation of the best line is given in the lower right hand corner. The residuals from the linear regression are plotted in part (b), as function of the independent variable. The standard deviation is shown in the lower right hand corner. It is approximately twice as large as in the previous figure. No trend is apparent from this plot. In part (c), the data points and the best line fit from (a) have been transformed into the original, linear space. A histogram of the standardized residuals from the linear regression is showed in part (d). The residuals exhibit a slight negative skewness. The coefficient of kurtosis is 2.37, considerably smaller than the kurtosis for the regression results in Figure 3.14.

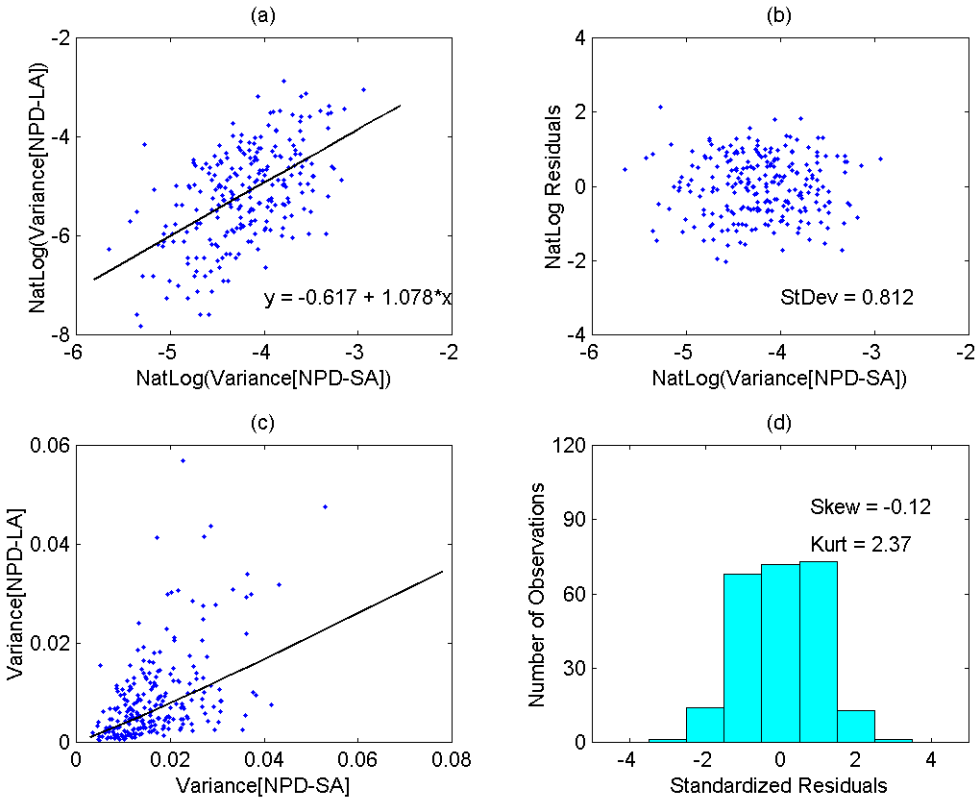

Figure 3.15: Results of regression analysis of variance of normalized phase difference for large amplitudes vs. variance of normalized phase difference for small amplitudes. (a) Linear regression in natural logarithm space; (b) residuals of the regression in (a); (c) the regression in (a) transformed into linear space; (d) histogram of standardized residuals from (a).

The Weight of the Uniform Distribution

The last beta parameter is the weight of the uniform distribution for small Fourier amplitudes. As suggested by the scatterplot in Figure 3.6, a linear regression is performed on the weight of the uniform distribution as function of the variance for small amplitudes. The results of such regression analyses are summarized in Figure 3.16. In Figure 3.16(a), the fitted line is superimposed on the observed data points. The equation of the regression line is displayed in the lower right hand corner of the figure. The residuals from the linear regression are plotted in Figure 3.16(b) as function of the independent variable, the variance of normalized phase difference for small Fourier amplitudes. For small values of the independent variable, the absolute value of the residuals tends to increase as the independent variable increases. This is due to the fact that up to a certain threshold value of the independent variable, there are observations of the dependent variable around its lower limit. The standardized residuals are plotted in Figure 3.16(c), and a histogram of the standardized residuals is displayed in Figure 3.16(d). The coefficients of skewness and kurtosis for the residuals are reported in Figure 3.16(d). The residuals display a considerable positive skewness, and the coefficient of kurtosis is 3.56.

The inhomogeneous distribution of the residuals with respect to the independent variable implies that it would be more desirable to select the weight of the uniform distribution as the independent variable and the variance of the normalized phase difference for small amplitudes as the dependent variable. However, the other secondary parameters, i.e. the variances of normalized phase difference for intermediate and large Fourier amplitudes, respectively, showed much better correlation with the variance than with the weight of the uniform distribution for small Fourier amplitudes. Therefore, it was decided to regress the weight of the uniform distribution on the variance, rather than vice versa.

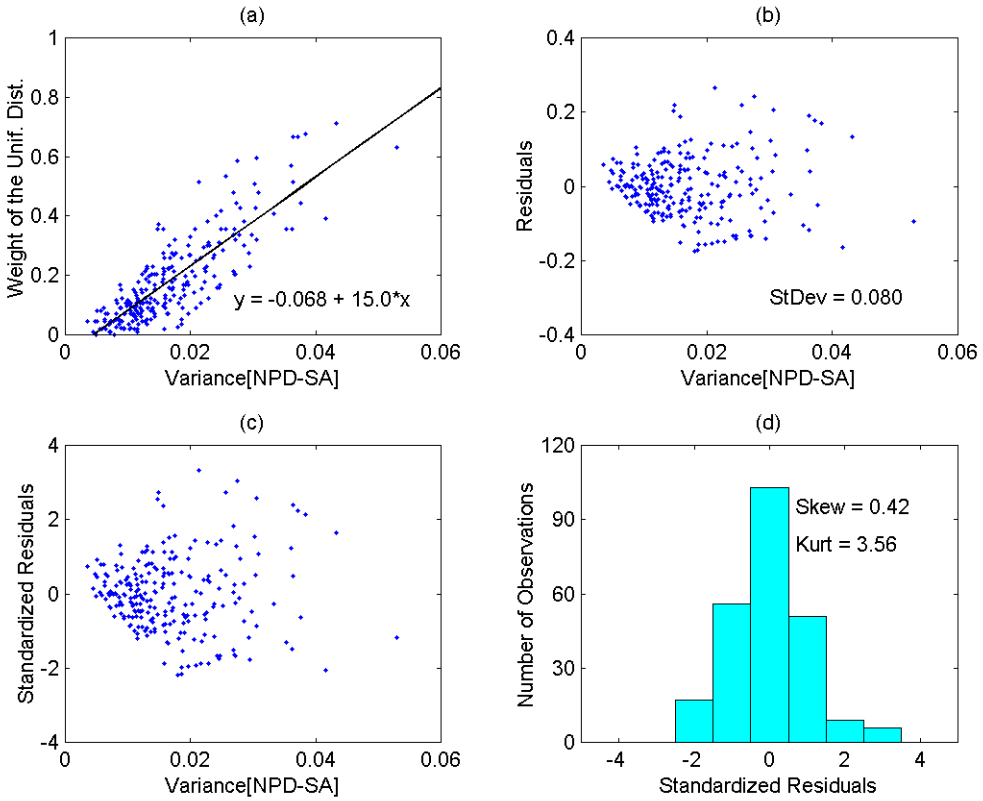

Figure 3.16: Results of regression analysis for the weight of the uniform distribution versus the variance of normalized phase difference for small Fourier amplitudes. (a) Linear regression; (b) residuals; (c) standardized residuals; (d) histogram of standardized residuals.

3.4 Model Validation

In Section 3.2 it was shown qualitatively that conditional beta distributions could be used to model the normalized Fourier phase differences – at least in that particular example. This single example does not, however, validate the beta model in general. For general validation, more exhaustive, systematic and quantitative tests of the method are needed.

In this section, several tests are performed to estimate how well the assumed model, i.e. the conditional beta distributions for normalized Fourier phase differences, fit real observations. Four different quality tests are performed: statistical goodness of fit tests for the distribution functions, and three different tests where the characteristics of simulated accelerograms are compared to the corresponding characteristics of recorded

accelerograms. These include comparisons of peak ground acceleration values, linear response spectra, and the temporal distribution of the energy content. All four tests are performed on the entire ground motion database that was used to develop the prediction formulas for the beta parameters.

3.4.1 Phase Difference Distributions

The Kolmogorov-Smirnov goodness of fit test is used to estimate the statistical goodness of fit of the conditional beta distributions. The statistic used to estimate how well an assumed probability distribution fits observed data is the maximum of the absolute difference between the assumed (or fitted) and observed (or empirical) cumulative distribution function:

$$S_n = \max_{\text{all } x} \left| F_n(x) - F_X(x) \right| \tag{3.13}$$

Here, S_n is the Kolmogorov-Smirnov statistic, $F_X(x)$ is the assumed cumulative distribution function, and $F_n(x)$ is the empirical cumulative distribution function. The empirical cumulative distribution is given by:

$$F_n(x_j) = \frac{j}{n}; \quad j = 1, 2, \ldots, n \tag{3.14}$$

where x_j is the j-th smallest sample and *n* is the number of observations; the sample size. The assumed probability distribution is rejected if the test statistic is larger than a certain critical value, i.e. if

$$S_n > S_{n,cr} \Rightarrow \text{reject} \tag{3.15}$$

For large samples (for example, n > 80), the critical value can be approximated by (Lindgren, 1976):

$$S_{n,cr} = \sqrt{\frac{-\ln(\alpha/2)}{2n}} \tag{3.16}$$

where α is the significance level of the test. The significance level is equal to the probability of rejecting the assumed distribution, when it is the true distribution. It is usually chosen to be a small number, very often of the order of 0.01 to 0.10.

A discrete 2048 points Fourier transform yields 1024 unique observations of phase difference (see Equation 3.5). As described in Section 3.2, fifty-five percent, or 563, belong to the small Fourier amplitudes, there are 358 observations in the intermediate category, and 103 belong to the large Fourier amplitudes category. The large-sample-approximation of Equation (3.16) can therefore be used for all three amplitude categories. The critical values for the Kolmogorov-Smirnov statistic, calculated according to Equation (3.16), are given in Table 3.3, for each Fourier amplitude category and three different significance levels.

Table 3.3: Critical values of the Kolmogorov-Smirnov statistic for normalized phase difference distributions.

	Small Amplitudes (n = 563)	**Intermediate Amplitudes (n = 358)**	**Large Amplitudes (n = 103)**
1% Significance	0.0686	0.0860	0.1604
5% Significance	0.0572	0.0718	0.1338
10% Significance	0.0516	0.0647	0.1206

Figure 3.17 shows examples of fitted (dashed lines) and recorded (solid lines) distributions for the normalized phase difference. The maximum difference between the two cumulative distribution functions for small Fourier amplitudes is 0.0659. Therefore, the fitted distribution is rejected at the 5% significance level, but not at the 1% significance level. For intermediate amplitudes, the maximum difference between the recorded and the fitted phase difference distributions is 0.1487, which means, that the fitted distribution is rejected at the 1% significance level. The maximum difference between the two phase difference distribution functions for large Fourier amplitudes is 0.0835. This value is smaller than all the values in the right most column of Table 3.3, so the fitted distribution is not rejected at any of the three significance levels.

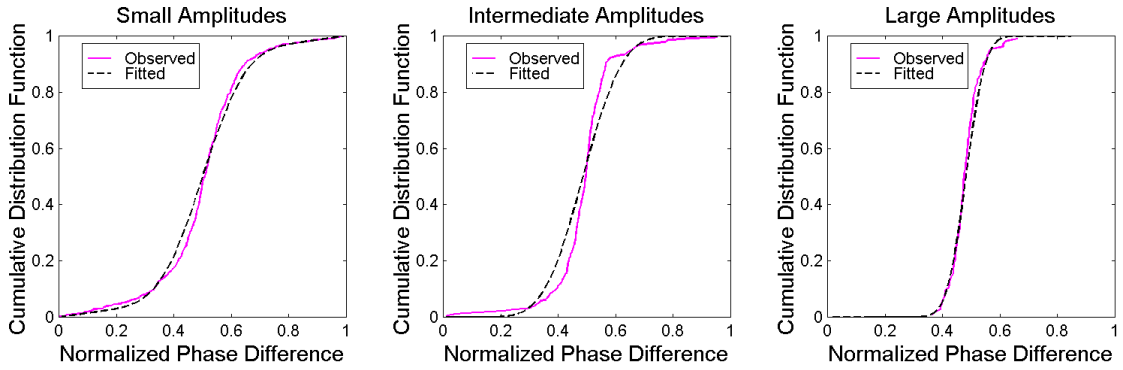

Figure 3.17: Comparison of observed phase difference distributions (solid lines) and fitted distributions (dashed lines) for small, intermediate and large Fourier amplitudes. The east-west component of the UC Santa Cruz record from the 1989 Loma Prieta, California earthquake.

The statistical goodness of fit results described above are representative for the earthquake ground motion database assembled in this study. In more than 80% of the cases, the fitted distributions cannot be rejected at the 10% significance level, and in half of the remaining cases, the fitted distribution is only rejected for one out of three Fourier amplitude categories. In fewer than 5% of the cases, a fitted distribution is rejected at the 5% significance level.

In general, the statistical goodness of fit of the beta distributions for normalized phase differences is satisfactory, as measured by the Kolmogorov-Smirnov test. It is of more interest, however, whether the accelerograms simulated using these beta distributions, adequately reproduce the relevant characteristics of recorded accelerograms. In the following subsection, the attributes of simulated accelerograms are compared to the corresponding attributes of recorded accelerograms.

3.4.2 Accelerograms

In the preceding subsection, the assumed and observed probability distributions for normalized phase difference were compared. In this subsection, the characteristics of simulated accelerograms, using the assumed phase difference distributions, are compared with the corresponding characteristics of recorded accelerograms. Three different characteristics are compared: peak values, elastic response spectra, and evolutionary behavior.

Peak Ground Acceleration

Figure 3.18 shows an example of a recorded accelerogram, followed by two examples of simulated accelerograms. The peak ground acceleration (PGA) of the recorded accelerogram is 0.41g. The mean PGA from ten simulations is 0.46g, and the standard deviation of the PGA is 0.05g.

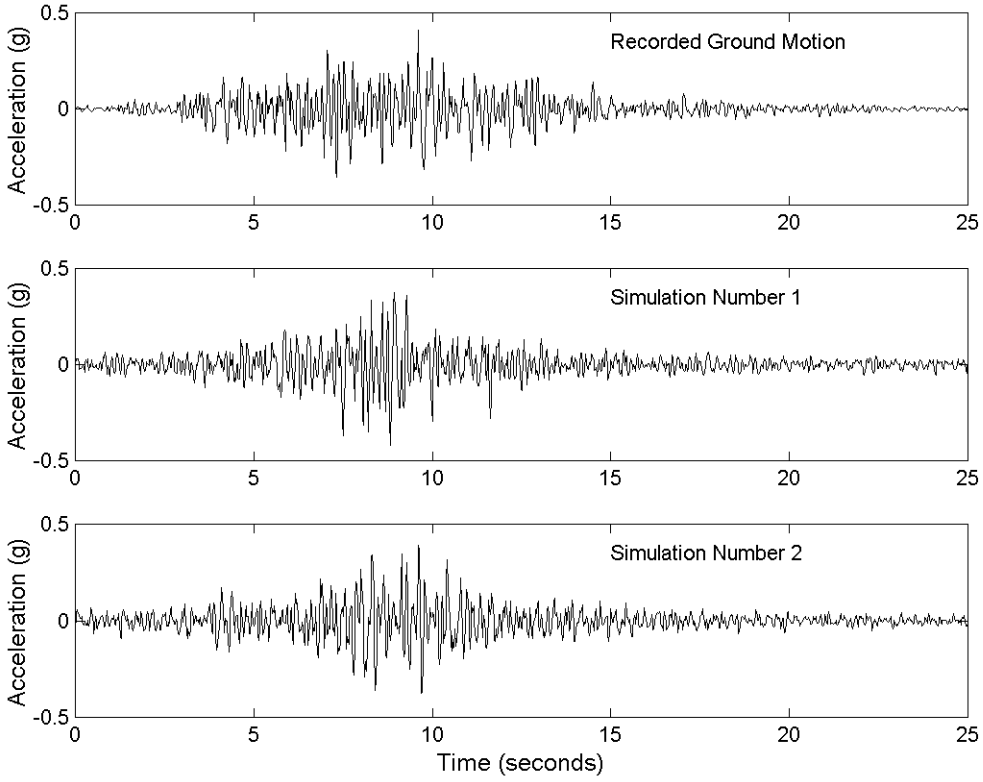

Figure 3.18: A recorded time history compared to two examples of simulated time histories using conditional beta distributions for Fourier phase differences. The east-west component of the UC Santa Cruz record from the 1989 Loma Prieta, California earthquake.

The results displayed in Figure 3.18 are very typical. In over 75% of the cases, the recorded PGA was within one standard deviation of the mean PGA from ten simulations, and in all the other cases, the recorded PGA was within two standard deviations of the mean.

Elastic Response Spectrum

The elastic response spectra are compared in Figure 3.19. The solid line represents the elastic pseudo acceleration response spectrum of the recorded ground motion, assuming a damping factor equal to 5% of critical damping. The dashed lines in Figure 3.19 represent the response spectra of ten simulated acceleration time histories. For all natural periods depicted in the figure (from 0.1 seconds to 2 seconds), the response spectra of the simulated time histories envelope the response spectrum of the recorded time history. The results in Figure 3.19 are representative of the entire ground motion data set.

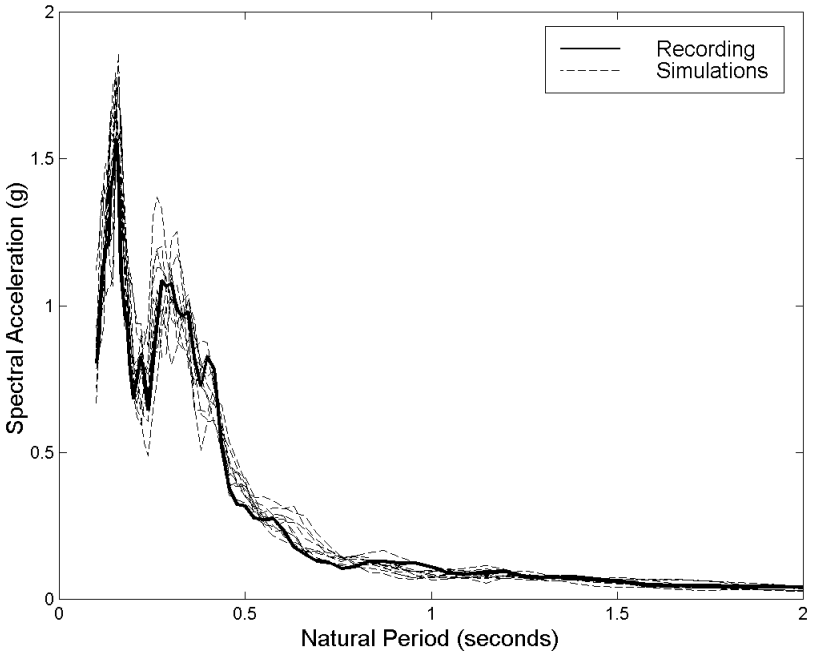

Figure 3.19: Elastic pseudo acceleration response spectra (5% damping). Solid line: the response spectrum of the east-west component of the UC Santa Cruz record from the 1989 Loma Prieta, California earthquake; dashed lines: ten simulations using conditional beta distributions for Fourier phase differences.

Cumulative Normalized Arias Intensity

Oftentimes, the temporal distribution of the energy content has a great effect on the response of a structure that is affected by earthquake ground motion. The last characteristic included in this comparison is the evolutionary behavior of the

accelerograms. In this study, the evolutionary behavior is quantified in terms of the cumulative normalized Arias intensity (Arias, 1970):

$$NI(t) = \frac{\int_0^t a^2(\tau)d\tau}{\int_0^{T_d} a^2(\tau)d\tau}; \quad 0 \le t \le T_d \tag{3.17}$$

where $NI(t)$ is the normalized Arias intensity at time t, $a(\tau)$ is the value of the acceleration time history at time τ, and T_d is the total duration of the accelerogram.

In Figure 3.20, the cumulative normalized Arias intensities from ten simulations are compared to the cumulative normalized Arias intensity of a recorded accelerogram. In general, the simulated accelerograms capture well the evolutionary characteristics of the recorded accelerogram. However, the energy release of the simulated accelerograms tends to be a bit smoother than the energy release of the recorded accelerograms. The cumulative normalized Arias intensity curves for the simulated time histories are not as flat towards the beginning as the curve for the recorded time history.

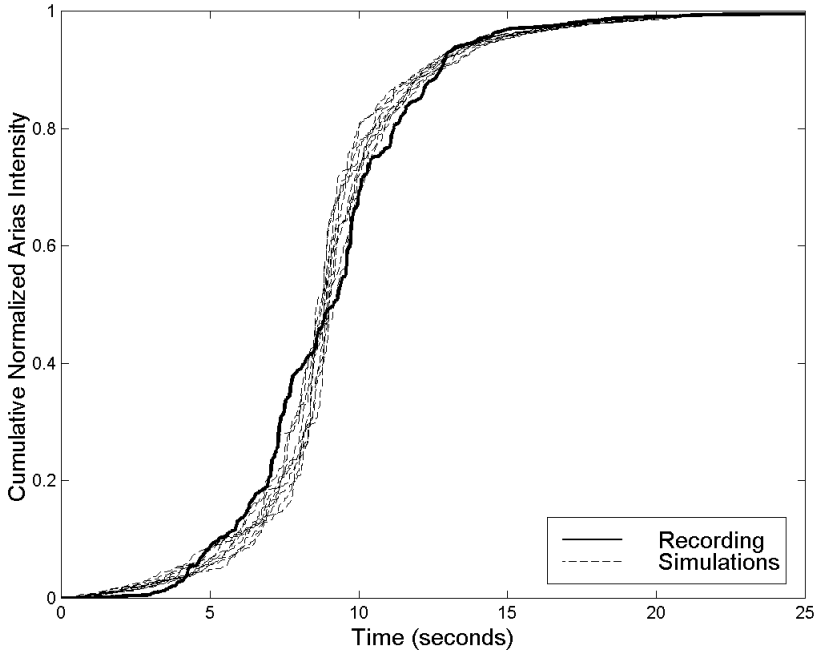

Figure 3.20: Cumulative normalized Arias intensity. Solid line: the cumulative Arias intensity of the east west component of the UC Santa Cruz record from the 1989 Loma Prieta, California earthquake; dashed lines: ten simulations using conditional beta distributions for Fourier phase differences.

3.5 Summary of Conditional Beta Distributions

In this chapter, it is shown that the Fourier phase angles of digital earthquake accelerograms are uniformly distributed, but not independent of each other. The dependency is captured through modeling of the phase differences, conditional on the Fourier amplitude. An empirical approach is developed, where the phase differences are modeled by a combination of beta and uniform distributions, for three different Fourier amplitude categories.

Using the empirical method developed in this chapter, seven parameters are necessary to completely define the phase difference distribution. These include the mean and variance of the normalized phase difference for small, intermediate and large Fourier amplitudes, respectively, and the relative weight of the uniform distribution for small Fourier amplitudes. These seven parameters are not independent of each other. Two of them, the mean corresponding to large Fourier amplitudes and the variance for small amplitudes, are shown to be fundamental, and the other five, secondary parameters can be derived from one of the two fundamental parameters.

The California ground motion database is used to develop prediction formulas for the beta parameters. The results of the regression analyses are summarized below. The parameter D is the shortest distance from the site to the surface projection of the seismogenic rupture in kilometers, and M_W is the moment magnitude of the earthquake.

Two of the seven model parameters are shown to be fundamental for the characterization of the Fourier phase differences: The mean normalized phase difference for large Fourier amplitudes, μ_L, and the variance of normalized phase difference for small Fourier amplitudes, σ_S^2. For an unknown site classification, the mean normalized phase difference for large Fourier amplitudes can be estimated using:

$$\mu_L = \frac{0.56 - 0.0023 \cdot D}{0.41 + 0.092 \cdot M_W}; \quad D \le 100\,\text{km}, 5.8 \le M_W \le 7.1$$

For Site Class A&B, the mean can be calculated according to:

$$\mu_L = \frac{0.60 - 0.0023 \cdot D}{-0.54 + 0.209 \cdot M_W}; \quad D \le 100\,\text{km}, 5.8 \le M_W \le 7.1$$

For Site Class C the mean is given by:

$$\mu_L = \frac{0.55 - 0.0021 \cdot D}{0.37 + 0.087 \cdot M_W}; \quad D \le 100\,\text{km}, 5.8 \le M_W \le 7.1$$

Finally, for Site Class D, the mean is:

$$\mu_L = \frac{0.55 - 0.0027 \cdot D}{0.51 + 0.077 \cdot M_W}; \quad D \le 100\,\text{km}, 5.8 \le M_W \le 7.1$$

The variance of the normalized phase difference for small Fourier amplitudes and an unknown site class can be estimated according to:

$$\ln\left(\sigma_S^2\right) = \frac{-1.67 - 0.726 \cdot \exp\left(-0.0142 \cdot D^{1.14}\right)}{0.43 + 0.009 \cdot M_W}; \quad D \le 100\,\text{km}, 5.8 \le M_W \le 7.1$$

For Site Class A&B the variance can be calculated using:

$$\ln\left(\sigma_S^2\right) = \frac{-1.46 - 0.528 \cdot \exp\left(-0.0150 \cdot D^{1.23}\right)}{0.14 + 0.054 \cdot M_W}; \quad D \le 100\,\text{km}, 5.8 \le M_W \le 7.1$$

For Site Classes C and D the variance can be computed using:

$$\ln\left(\sigma_S^2\right) = \frac{-2.04 - 0.476 \cdot \exp\left(-0.0039 \cdot D^{1.74}\right)}{0.51 - 0.003 \cdot M_W}; \quad D \le 100\,\text{km}, 5.8 \le M_W \le 7.1$$

Each of the five secondary parameters is inferred from one of the two fundamental parameters. The local site conditions are not accounted for explicitly, but they are considered implicitly, because the fundamental parameters depend on the site classification. The mean normalized phase difference for intermediate Fourier amplitudes is computed from the mean for large amplitudes:

$$\mu_I = 0.11 + 0.81 \cdot \mu_L$$

The mean normalized phase difference for small Fourier amplitudes is computed from the mean for large amplitudes according to:

$$\mu_S = 0.20 + 0.69 \cdot \mu_L$$

The variance of normalized phase difference for intermediate Fourier amplitudes is computed from the variance for small amplitudes:

$$\ln\left(\sigma_I^2\right) = 0.897 \cdot \ln\left(\sigma_S^2\right) - 0.549$$

The variance of normalized phase difference for large Fourier amplitudes is computed from the variance for small amplitudes:

$$\ln\left(\sigma_L^2\right) = 1.078 \cdot \ln\left(\sigma_S^2\right) - 0.617$$

The weight of the uniform distribution, *wu*, is determined from the variance of normalized phase difference for small Fourier amplitudes:

$$wu = \begin{cases} 0; & \sigma_S^2 \le 0.004533 \\ 15.0 \cdot \sigma_S^2 - 0.068; & \text{otherwise} \end{cases}$$

The Fourier phase difference model is validated through extensive statistical goodness of fit tests, as well as comparison of certain characteristics of the simulated and recorded accelerograms. These characteristics are: (i) the peak ground acceleration, (ii) the 5% damped elastic response spectrum, and (iii) the evolutionary behavior as quantified by the cumulative normalized Arias intensity.

CHAPTER 4
MODELING OF PHASE DIFFERENCES: METHOD OF ENVELOPES

An empirical method for the modeling of Fourier phase differences of earthquake accelerograms was presented in Chapter 3, where the Fourier amplitude domain was discretized into three categories and one model was fitted to the phase differences belonging to each amplitude category. In this chapter, a theoretical approach is presented, where a normal (Gaussian) distribution with amplitude-dependent parameters is used to model the phase difference distribution.

The conditional Fourier phase difference model presented in this chapter gives a theoretical basis for the empirical, parametric phase difference model presented in Chapter 3. A major virtue of this theoretical model is its reduced number of parameters, as compared to the parametric model, and their physical meaning. The conditional phase difference distribution requires only two parameters, a mean time $\bar{\tau}$ representing the time-centroid of the energy release, and a duration parameter Δ_T, which is a measure of how narrowly the energy release is focused in time.

The modeling approach presented in this chapter utilizes the method of envelopes for time-varying functions. The Hilbert transform and its properties are central to the method of envelopes. Therefore, the Hilbert transform is introduced in the first section of this chapter, followed by a section on the method of envelopes. Then, an analogy proposed by Nigam (1982) is built upon, yielding a method of envelopes for frequency-varying functions, and a model for the simulation of acceleration time histories is presented. Finally, prediction formulas are developed for the model parameters, based on the California ground motion database described in Chapter 2. The statistics on the phase difference distributions that are used in this chapter are tabulated in Appendix C.

4.1 The Hilbert Transform

The Hilbert transform of the function $f(t)$ is defined as:

$$Hi[f(t)] = \frac{1}{\pi} \int_{-\infty}^{\infty} \frac{f(\tau)}{t-\tau} d\tau \tag{4.1}$$

where $Hi[f(t)]$ is the Hilbert transform. Two important attributes of the Hilbert transform can be deducted from its definition: (i) the Hilbert transform of a real valued function is itself a real valued function, and (ii) the Hilbert transform and the original function are orthogonal to each other – i.e. they are $\pi/2$ out of phase. For example, the Hilbert transform of a cosine function is a sine function:

$$Hi[\cos(t)] = \sin(t) \tag{4.2}$$

Assume that the function $f(t)$ is a real valued function. Define a complex valued function, $g(t)$, such that $f(t)$ forms its real part and its Hilbert transform forms the imaginary part:

$$g(t) = f(t) + i \cdot Hi[f(t)] \tag{4.3}$$

The function $g(t)$, sometimes referred to as the analytic signal corresponding to $f(t)$, can be equivalently written as:

$$g(t) = C(t) \cdot \exp(i \cdot \Theta(t)) \tag{4.4}$$

where the magnitude of $C(t)$ is defined as the envelope function of $g(t)$, and $\Theta(t)$ is a time dependent phase angle. The time derivative of the phase angle is often referred to as the instantaneous frequency. These terms are helpful when dealing with the method of envelopes.

4.2 Envelopes of Time-Varying Functions

Consider the analytic signal $U(t)$, which can be represented as:

$$U(t) = X(t) + i \cdot \hat{X}(t) \tag{4.5}$$

where $\hat{X}(t)$ is the Hilbert transform of the Gaussian, stationary process $X(t)$:

$$X(t) = C(t) \cdot \cos[\Theta(t)] \tag{4.6}$$

$$\hat{X}(t) = C(t) \cdot \sin[\Theta(t)] \tag{4.7}$$

The amplitude at time t, $C(t)$, and the phase angle at time t, $\Theta(t)$, are uncorrelated random variables. The amplitudes, $C(t)$, follow a Rayleigh distribution, given by:

$$f_C(c) = \frac{c}{\sigma_X^2} \exp\left(-\frac{c^2}{2\sigma_X^2} \right); \quad c \geq 0 \tag{4.8}$$

where σ_X^2 is the variance of $X(t)$. The phase angles are uniformly distributed:

$$f_\Theta(\theta) = \frac{1}{2\pi}; \quad 0 \leq \theta \leq 2\pi \tag{4.9}$$

If the instantaneous frequency is defined as:

$$\Omega = \frac{d\Theta}{dt} = \dot{\Theta} \tag{4.10}$$

i.e. the instantaneous frequency is defined as the rate of change of the phase angle process $\Theta(t)$, the joint probability density of amplitude and frequency is given by (Sveshnikov, 1968; Winterstein, 1991):

$$f_{C\Omega}(c,\omega)=\frac{c^2}{\sigma_X^3\,\overline{\omega}\Delta\sqrt{2\pi}}\exp\left\{-\frac{c^2}{2\sigma_X^2}\left[1+\left(\frac{\omega-\overline{\omega}}{\overline{\omega}\Delta}\right)^2\right]\right\};\quad c\geq 0;\quad -\infty<\omega<\infty \tag{4.11}$$

where the mean frequency is given by:

$$\overline{\omega}=\frac{\lambda_1}{\lambda_0} \tag{4.12}$$

and λ_n is the n-th spectral moment about the origin:

$$\lambda_n=\int_0^\infty \omega^n S_X(\omega)d\omega;\quad n=0,1,2 \tag{4.13}$$

Here, $S_X(\omega)$ is the power spectral density of $X(t)$. The parameter Δ is a unitless parameter reflecting the spectral bandwidth. It is given by:

$$\Delta=\sqrt{\frac{\lambda_0\lambda_2}{\lambda_1^2}-1}=\sqrt{\frac{\lambda_2/\lambda_0}{(\lambda_1/\lambda_0)^2}-1} \tag{4.14}$$

The spectral bandwidth parameter Δ depends on the two spectral moment ratios, λ_1/λ_0 and λ_2/λ_0, and it approaches zero as the bandwidth of the power spectral density decreases.

The joint density of amplitude and frequency as defined in Equation (4.11), can be factored into the product of the conditional density of the frequency given the amplitude, and the amplitude density:

$$f_{C\Omega}(c,\omega)=f_{\Omega|C}(\omega|c)\cdot f_C(c) \tag{4.15}$$

Substituting Equation (4.8) for the amplitude density, one obtains:

$$f_{\Omega|C}(\omega|c)=\frac{1}{\sqrt{2\pi}\,\overline{\omega}\Delta\sigma_X/c}\exp\left\{-\frac{1}{2}\left(\frac{\omega-\overline{\omega}}{\overline{\omega}\Delta\sigma_X/c}\right)^2\right\};\quad -\infty<\omega<\infty \tag{4.16}$$

Hence, the conditional distribution of the instantaneous frequency given the amplitude is Gaussian, with mean

$$\mathrm{E}\left[\Omega|c\right] = \overline{\omega} = \frac{\lambda_1}{\lambda_0} \tag{4.17}$$

and variance

$$\mathrm{Var}\left[\Omega|c\right] = \left(\frac{\overline{\omega}\cdot\Delta}{c/\sigma_X}\right)^2 \tag{4.18}$$

The mean frequency in Equation (4.17) is independent of the amplitude, while the standard deviation in Equation (4.18) is inversely proportional to the normalized amplitude, c/σ_X . The dependency of the mean frequency and the mean +/- one standard deviation on amplitude are illustrated in Figure 4.1.

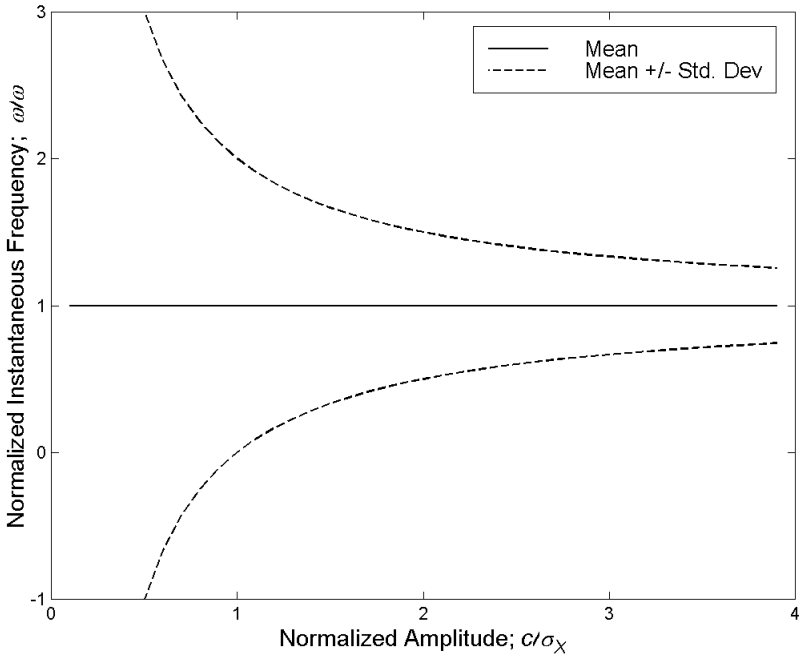

Figure 4.1: Conditional mean and mean +/- one standard deviation of normalized instantaneous frequency, $\omega/\overline{\omega}$, as function of normalized amplitude, c/σ_X . The spectral bandwidth parameter assumed here is $\Delta = 1$.

The method of envelopes, as presented above, is used to describe narrow band, stochastic processes in the time domain. In the following section, the method of envelopes is applied to a stochastic process in the frequency domain.

4.3 Envelopes of Frequency-Varying Functions

Nigam (1982) suggests applying the method of envelopes to a stochastic process where frequency is the indexing parameter, rather than time. A stationary process in the time domain is then analogous to a white process in the frequency domain, the power spectral density is replaced by the intensity function, and the spectral moments become intensity moments (see Table 4.1).

Assume that the process $Z(\omega)$ is an analytic signal in the frequency domain:

$$Z(\omega) = Y(\omega) + i \cdot \hat{Y}(\omega) \tag{4.19}$$

where $Y(\omega)$ is a zero-mean, stationary process in the frequency domain (a "white" process):

$$Y(\omega) = A(\omega) \cdot \sin[\Phi(\omega)] \tag{4.20}$$

Here, $A(\omega)$ is the Rayleigh distributed amplitude of $Z(\omega)$, and $\Phi(\omega)$ is the uniformly distributed phase angle. The process $Z(\omega)$ can be interpreted as the Fourier transform of an amplitude modulated stationary Gaussian noise process in the time domain:

$$Z(\omega) = \frac{1}{2\pi} \int_{-\infty}^{\infty} W(t) \cdot \exp(-i\omega t) dt \tag{4.21}$$

where

$$W(t) = \eta(t) \cdot X(t) \tag{4.22}$$

and $X(t)$ is a stationary, zero mean, real valued Gaussian noise process with power spectral density S_0. The function $\eta(t)$ is a deterministic amplitude modulation function, or

an envelope function. The envelope function is non-negative; positive inside the duration interval of the process $W(t)$, but zero outside of it:

$$\begin{aligned} &\eta(t) > 0; \quad t \in (0, T_d) \\ &\eta(t) = 0; \quad \text{otherwise} \end{aligned} \tag{4.23}$$

Figure 4.2 illustrates the processes $X(t)$ and $W(t)$, and the function $\eta(t)$.

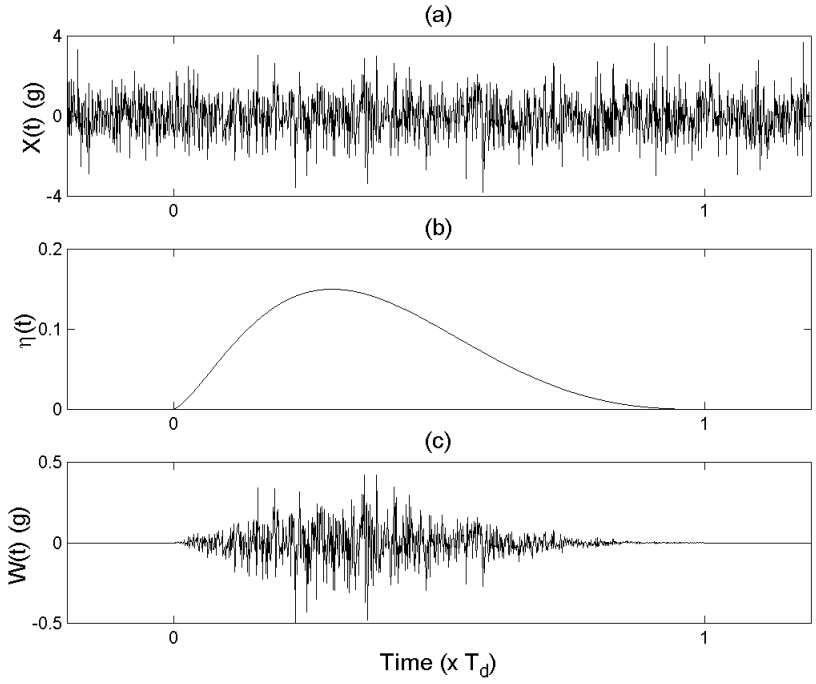

Figure 4.2: An example of an amplitude modulated process. (a) The stationary noise process, $X(t)$; (b) the amplitude modulation function, $\eta(t)$; (c) the modulated process, $W(t)$.

The process $W(t)$ is zero mean, Gaussian, real valued and causal, with the autocorrelation function:

$$R_W(t_1, t_2) = \mathrm{E}[W(t_1) \cdot W(t_2)] = \begin{cases} \eta(t_1) \cdot \eta(t_2) \cdot R_X(t_2 - t_1); & 0 \le t_1, t_2 \le T_d \\ 0; & \text{otherwise} \end{cases} \tag{4.24}$$

where $R_X(t_2 - t_1)$ is the autocorrelation function of $X(t)$. The autocorrelation function of the complex valued, zero mean, Gaussian process $Z(\omega)$ is given by:

$$R_Z(\omega_1,\omega_2) = \mathrm{E}[Z(\omega_1)\cdot Z^*(\omega_2)]$$
$$= \frac{1}{(2\pi)^2}\int_{-\infty}^{\infty}\int_{-\infty}^{\infty}\eta(t_1)\cdot\eta(t_2)\cdot R_X(t_2-t_1)\cdot\exp\{-i(\omega_2 t_2-\omega_1 t_1)\}dt_1 dt_2 \quad (4.25)$$

Since $X(t)$ is a Gaussian noise process, with the power spectral density S_0, its autocorrelation function is given by:

$$R_X(t_2-t_1) = 2\pi S_0\delta(t_2-t_1) \quad (4.26)$$

where $\delta(t_2-t_1)$ is the Dirac-delta function. Equation (4.25) then simplifies to:

$$R_Z(\omega_1,\omega_2) = R_Z(\omega_2-\omega_1) = \frac{S_0}{2\pi}\int_0^{T_d}\eta^2(t)\cdot\exp\{-i(\omega_2-\omega_1)t\}dt \quad (4.27)$$

The limits of integration could be changed because the envelope function is nonzero only within the interval (0, T_d).

The power spectral density of a stationary process and its autocorrelation function form a Fourier transform pair. Treating the frequency difference:

$$\varpi = \omega_2 - \omega_1 \quad (4.28)$$

as 'time lag', the 'power spectral density' of $Z(\omega)$ can be defined as:

$$S_Z(\tau) = \int_{-\infty}^{\infty} R_Z(\varpi)\cdot\exp(i\tau\varpi)d\varpi \quad (4.29)$$

where τ plays the role of frequency in conventional power spectral density functions, but has the units of time in this particular case. Substituting Equation (4.27) into Equation (4.29) and interchanging the order of integration yields:

$$S_Z(\tau) = S_0\int_0^{T_d}\eta^2(t)\cdot\left[\frac{1}{2\pi}\int_{-\infty}^{\infty}\exp\{-i\varpi(t-\tau)\}d\varpi\right]dt$$
$$= S_0\int_0^{T_d}\eta^2(t)\cdot\delta(t-\tau)dt$$

This gives:

$$S_Z(\tau)=\begin{cases} S_0\,\eta^2(\tau); & 0\le\tau\le T_d \\ 0; & \text{otherwise} \end{cases} \tag{4.30}$$

Now all the necessary components of the frequency-time domain analogy to the method of envelopes for narrow band processes have been introduced.

Table 4.1: The frequency domain analogy to the method of envelopes.

Envelopes of Time-Varying Functions	**Frequency-Domain Analogy**
The analytic signal $U(t)=X(t)+i\cdot\hat{X}(t)$	The frequency domain process $Z(\omega)=Y(\omega)+i\cdot\hat{Y}(\omega)$
Power spectral density function, $S_X(\omega)$	Intensity function, $\eta^2(t)$
Spectral moments, λ_n	Intensity moments, γ_n
Instantaneous frequency, the time derivative of phase: $\Omega=\frac{d\Theta}{dt}=\dot{\Theta}$	Frequency derivative of phase (units of time): $T=\frac{d\Phi}{d\omega}=\Phi'$

The real and imaginary parts of $Z(\omega)$, $Y(\omega)$ and $\hat{Y}(\omega)$, correspond to the Hilbert transform pair $X(t)$ and $\hat{X}(t)$ in Equations (4.6) and (4.7). The amplitude of $Z(\omega)$, $A(\omega)$, is a function of frequency and so is the phase, $\Phi(\omega)$. The marginal probability distributions of amplitude and phase are still Rayleigh and uniform, respectively, as in Equations (4.8) and (4.9). By defining the intensity moments as:

$$\gamma_n=\int_0^{T_d} t^n\eta^2(t)dt \tag{4.31}$$

the conditional distribution of the phase derivative with respect to frequency, τ, given the amplitude, a, can be obtained as:

$$f_{T|A}(\tau|a) = \frac{1}{\sqrt{2\pi}\,\bar{\tau}\Delta\sigma_Y/a}\exp\left\{-\frac{1}{2}\left(\frac{\tau-\bar{\tau}}{\bar{\tau}\Delta\sigma_Y/a}\right)^2\right\}; \quad -\infty < \tau < \infty \tag{4.32}$$

where the mean phase derivative

$$\mathrm{E}[\Phi'|a] = \bar{\tau} = \frac{\gamma_1}{\gamma_0} \tag{4.33}$$

represents the location (i.e. the time of occurrence) of the centroid of the intensity function, $\eta^2(t)$, and

$$\Delta_T = \sqrt{\frac{\gamma_0\gamma_2}{\gamma_1^2} - 1} = \sqrt{\frac{\gamma_2/\gamma_0}{(\gamma_1/\gamma_0)^2} - 1} \tag{4.34}$$

is a measure of how widely the intensity function is spread around its centroid. The parameter Δ_T is, therefore, a statistical measure of the effective duration of the process. Analogous to Equation (4.18), the conditional variance of the phase derivative is given by:

$$\mathrm{Var}[\Phi'|a] = \left(\frac{\bar{\tau}\cdot\Delta_T}{a/\sigma_Y}\right)^2 \tag{4.35}$$

where σ_Y^2 is the variance of $Y(\omega)$.

In the following section the application of the method of envelopes and its frequency domain analogy to the modeling of Fourier phase differences of earthquake accelerograms is demonstrated.

4.4 Parameter Estimation

In this section the application of the frequency domain analogy of the method of envelopes to the modeling of Fourier phase differences of digital earthquake accelerograms is illustrated. In particular, it is shown how the model parameters are estimated from a recorded (digitized) accelerogram. The east-west component of the UC Santa Cruz record from the 1989 Loma Prieta, California earthquake is taken as an example.

The parameter estimation involves whitening of the accelerogram in the frequency domain, and subsequent computations of the zeroth, first, and second moments of the whitened intensity function about the origin. The parameter estimation procedure is illustrated in Figure 4.3 and it is described step by step in the next paragraph. The left-hand column in Figure 4.3 (parts a, b, and c) pertains to the recorded accelerogram, while the column on the right (parts d, e, and f) relates to the whitened accelerogram.

The recorded acceleration time history is shown in Figure 4.3(a). It consists of 2000 points sampled at a sampling frequency of 50 Hz. Hence, the total duration of this accelerogram is 40 seconds, but only the first 25 seconds are shown here. The 2048-point discrete Fourier transform is evaluated, the real part of which is plotted as a function of frequency in Figure 4.3(b). Even though the Nyquist frequency is 25 Hz, the real part is not plotted here for frequencies higher than 15 Hz, because the energy content above 15 Hz is negligible as compared to the total energy of the accelerogram. It should be noted that the total duration and the entire frequency band are used in the calculations, not only the sections that are shown in Figure 4.3. The standard deviation envelope of the real part is plotted as a function of frequency in Figure 4.3(c). At discrete frequency number j, the value of this standard deviation envelope is defined by calculating the standard deviation of the real part of the discrete Fourier transform in a 25 sample wide window, centered at the j-th frequency component (this corresponds to approximately 0.6 Hz wide window in the frequency domain). The recorded real part is then divided by the standard deviation, frequency by frequency, resulting in the standardized real part that is plotted as a function of frequency in Figure 4.3(d). The imaginary part of the discrete Fourier transform is

standardized in a similar way. The standardized real and imaginary parts are stationary, zero mean, unit variance stochastic processes as a function of frequency.

The whitened, discrete Fourier transform now consists of the standardized real and imaginary parts. The whitened accelerogram, which is plotted as a function of time in Figure 4.3(e), is obtained by evaluating the inverse, discrete Fourier transform of the whitened Fourier transform. Note that this time history remains nonstationary in time, though with roughly constant frequency content. The whitened intensity function, which is shown in Figure 4.3(f), is simply the square of the whitened accelerogram. Now, the whitened intensity moments can be calculated according to:

$$\gamma_n = \sum_{k=1}^{N} t_k^n \cdot \eta^2(t_k); \quad n = 0,1,2 \tag{4.36}$$

where N is the order of the discrete Fourier transform (equal to 2048 in this study), and $\eta^2(t_k)$ is the value of the whitened intensity function for the k-th sampling point in the time domain. In this particular example, the whitened intensity moments are found to be:

$$\gamma_0 = 0.0377, \quad \gamma_1 = 0.316\,\text{sec}, \quad \gamma_2 = 3.13\,\text{sec}^2$$

which implies a centroid and a duration parameter equal to:

$$\bar{\tau} = \frac{\gamma_1}{\gamma_0} = 8.4\,\text{sec}, \quad \Delta_T = \sqrt{\frac{\gamma_0 \cdot \gamma_2}{\gamma_1^2} - 1} = 0.43$$

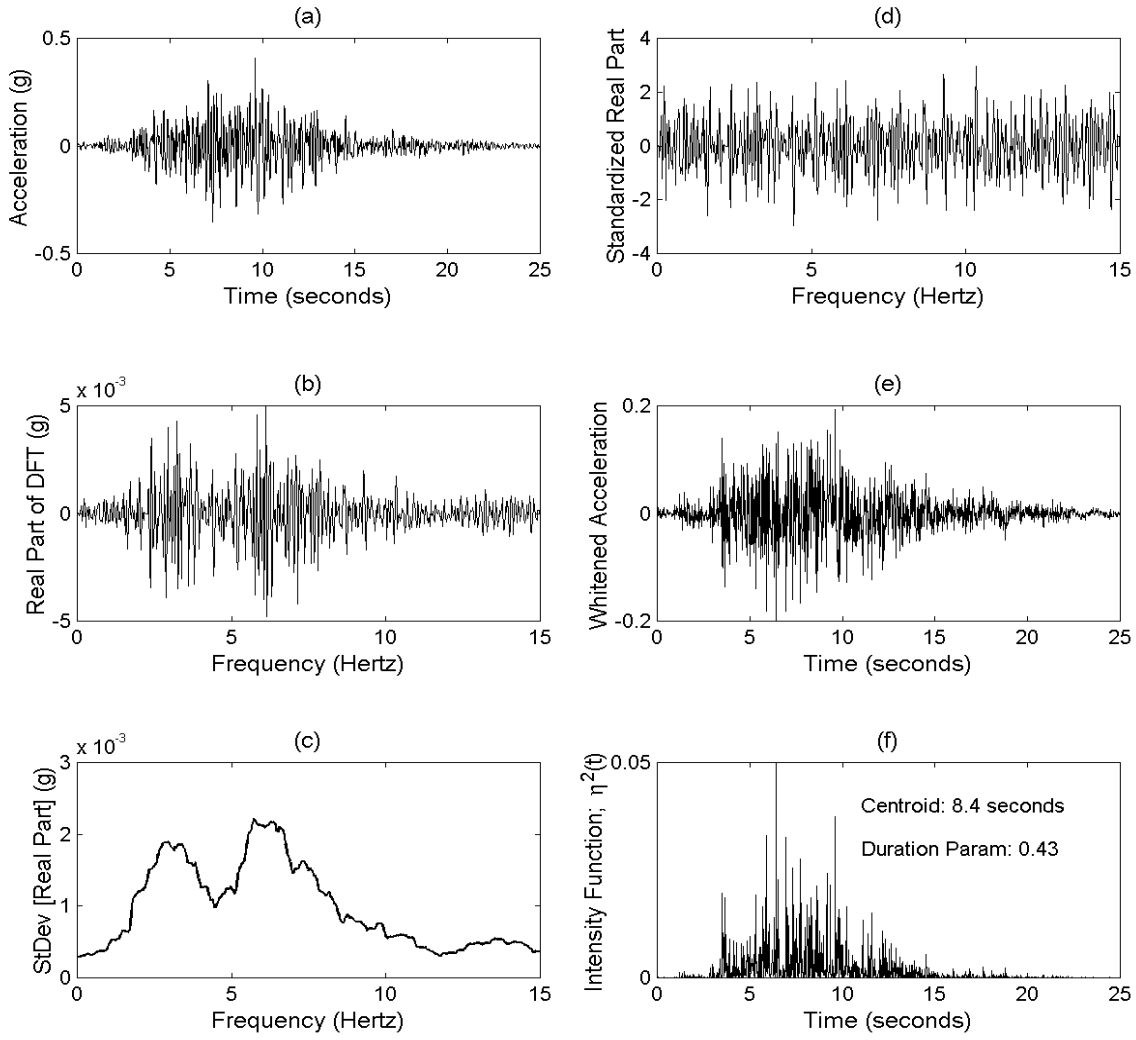

Figure 4.3: The whitening of an accelerogram. (a) The recorded east-west component of the UC Santa Cruz record from the 1989 Loma Prieta earthquake; (b) the real part of the discrete Fourier transform (DFT) of the recorded accelerogram; (c) the evolutionary standard deviation envelope of the real part of the discrete Fourier transform; (d) the standardized real part; (e) the whitened accelerogram; (f) the whitened intensity function.

The frequency domain analogy of the method of envelopes does not only require the standardized real and the imaginary parts to be stationary with respect to frequency, but they also have to be Gaussian and uncorrelated for any given frequency component. The Gaussianity of the standardized real and imaginary parts is investigated in Figure 4.4. A skewness coefficient of zero and a coefficient of kurtosis equal to three implies a Gaussian distribution. As can be seen from Figure 4.4, these criteria are met for all practical purposes.

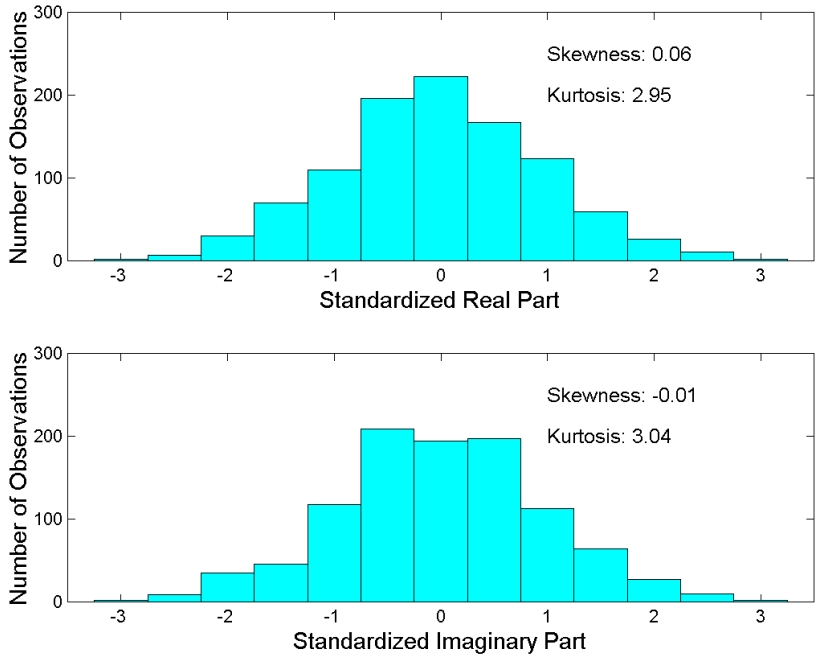

Figure 4.4: Histograms of the standardized real (top) and imaginary parts (bottom) for the east-west component of the UC Santa Cruz record from the 1989 Loma Prieta earthquake.

The correlation between the standardized real and imaginary parts is examined in Figure 4.5. The calculated correlation coefficient is exactly zero to the fourth decimal place, and the scatterplot exhibits no apparent pattern. It is, therefore, concluded that all the relevant requirements for the frequency domain analogy have been met.

In Figure 4.6, the phase differences from the east-west component of the UC Santa Cruz record from the 1989 Loma Prieta earthquake are plotted as a function of the whitened Fourier amplitude. Superimposed on the dots representing the observations in Figure 4.6 are the predicted mean phase difference (solid line) and the mean plus and minus one standard deviation (dashed lines). The predicted moments of the conditional phase difference distribution are obtained from Equations (4.33) and (4.35), multiplied by the sampling frequency, $\Delta\omega$. It should be noted that the observed phase differences are unwrapped to the finite interval $[-\pi, \pi]$, while the predicted mean and standard deviation are based on the assumption that the phase differences can take any real value. Therefore, the observed scatter might not agree well with the predicted standard deviation, especially for small amplitudes. Of course, this distinction between bounded and

unbounded phase definitions becomes immaterial once the inverse discrete Fourier transform is taken to recover the time history.

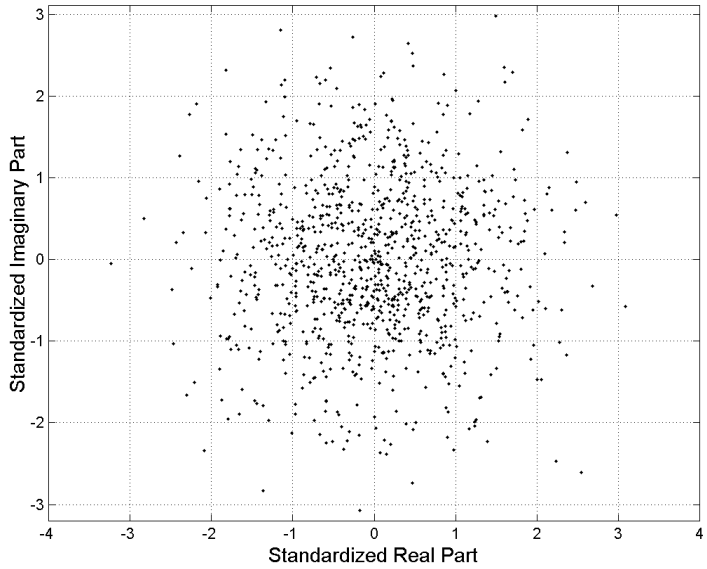

Figure 4.5: Scatterplot of the standardized imaginary versus the standardized real part for the east-west component of the UC Santa Cruz record from the 1989 Loma Prieta earthquake.

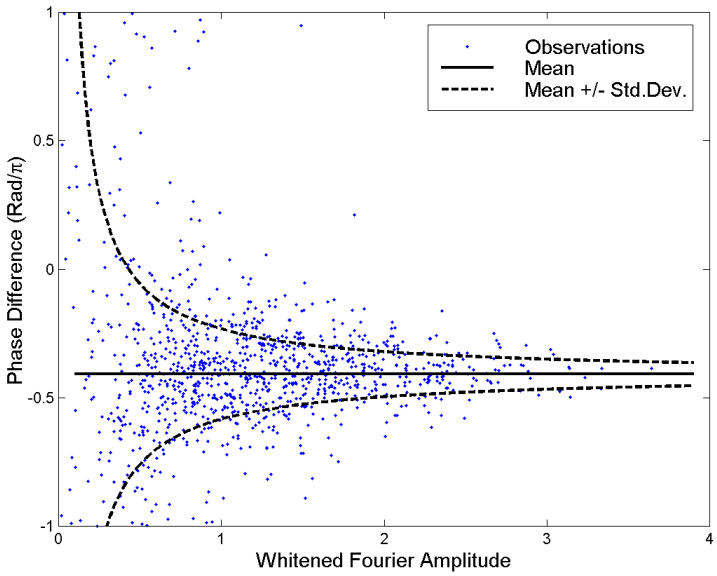

Figure 4.6: Observed unwrapped phase differences (dots) as function of the whitened Fourier amplitude (the amplitude is inferred from the standardized real and imaginary parts) for the east-west component of the UC Santa Cruz record from the 1989 Loma Prieta earthquake. Superimposed are the mean (solid line) and mean +/- one standard deviation (dashed lines) inferred from Equations (4.33) and (4.35).

Even though the results presented in Figures 4.3 through 4.6 are for a particular earthquake record, it should be noted that the analyses were performed on the entire California ground motion database and the results presented above are typical for the entire database. According to this, knowledge of the three whitened intensity moments is sufficient to simulate the Fourier phase differences of digital accelerograms. In the following section, the results of these analyses are used to develop prediction formulas for the parameters of the phase difference model.

4.5 Model Parameters

In Section 4.4 it was shown that three parameters are sufficient to describe the phase difference distribution of the whitened accelerogram: the zeroth, first, and second intensity moments. After whitening, the zeroth moment, which is equal to the area under the intensity function, is the same for all records. This leaves only two parameters to describe the shape of the whitened intensity function: the first and the second moments. In Figure 4.7, the second whitened intensity moment, γ_2 as defined in Equation (4.31), is plotted as function of the first whitened intensity moment, γ_1, for the database of California ground motion records described in Chapter 2. These two moments are obviously not independent of each other. The figure suggests a parabolic relationship between them.

A constant zeroth moment of the whitened intensity function and a parabolic relationship between the first and the second moments implies a constant duration parameter, Δ_T. This is corroborated in Figure 4.8, where the whitened duration parameter does not seem to depend significantly on the source to site distance. It should be noted that a constant duration parameter, Δ_T, does not imply a constant duration. It does imply, however, that the effective duration of the whitened accelerogram is proportional to the centroid of the whitened intensity function, $\bar{\tau}$.

Since the whitened duration parameter seems not to depend on the distance, the one remaining parameter, the centroid of the whitened intensity function, should be

sufficient to describe the distance dependence of the phase difference distribution. In Figure 4.9, the centroid is plotted as a function of distance for the California ground motion database. The centroid increases with distance. This behavior is expected, as the energy tends to arrive later and to be distributed over a longer time interval with increasing distance, due to the dispersion and scatter in the seismic wave train.

It is of interest to examine what effect the whitening of the accelerogram has on the parameters of the intensity function, i.e. the centroid and the unitless duration parameter. In Figure 4.10, the whitened intensity centroid is plotted as function of the recorded intensity centroid, along with the straight line $y = x$. There is a certain correlation apparent between the whitened and the recorded centroids. Therefore, the whitened centroid indicates where the centroid of the energy release of the recorded, unwhitened accelerogram is, i.e. it has a clear, physical meaning.

The relationship between the duration parameters of the whitened and recorded accelerograms is shown in Figure 4.11. In general, the whitening has the tendency to increase the duration of the.

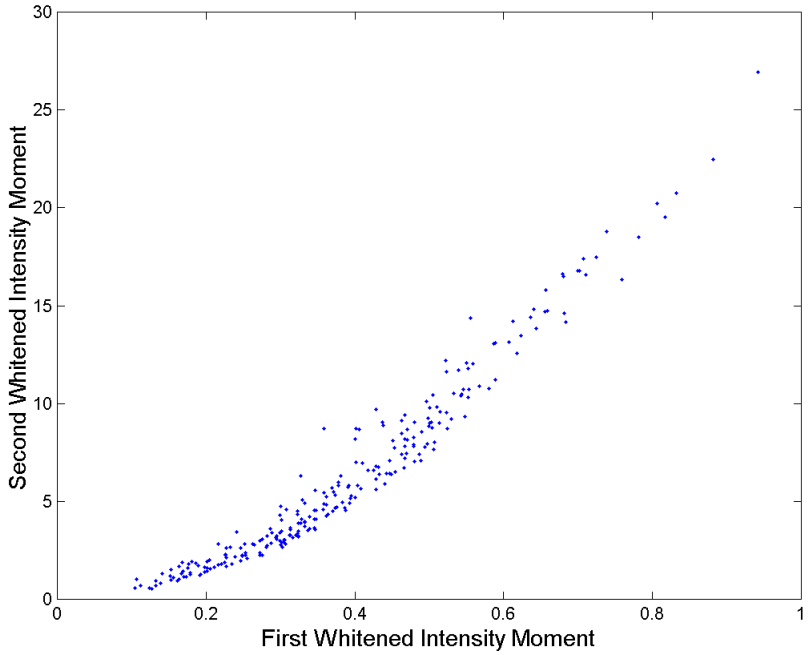

Figure 4.7: The second whitened intensity moment as function of the first whitened intensity moment for the California ground motion database.

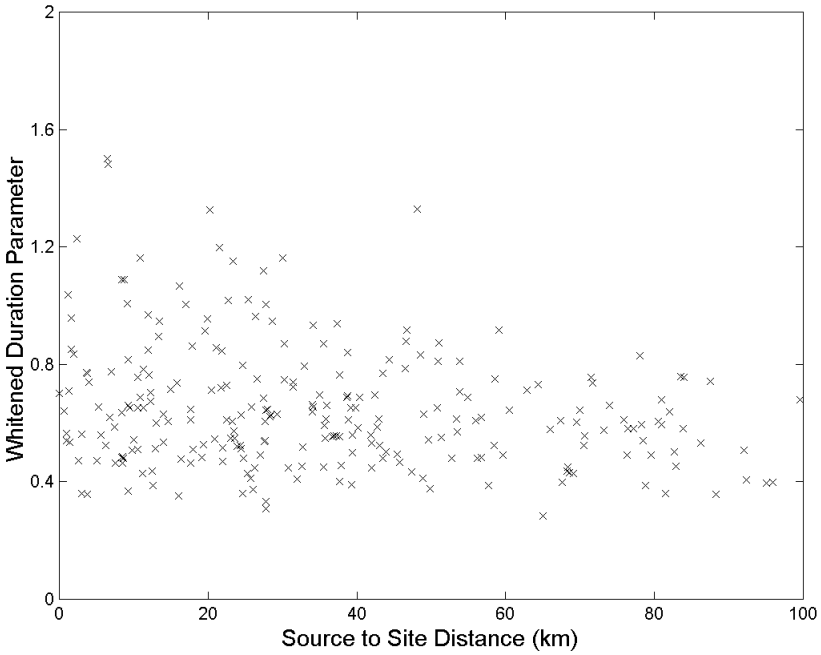

Figure 4.8: The whitened duration parameter, Δ_T, versus distance for the California ground motion database.

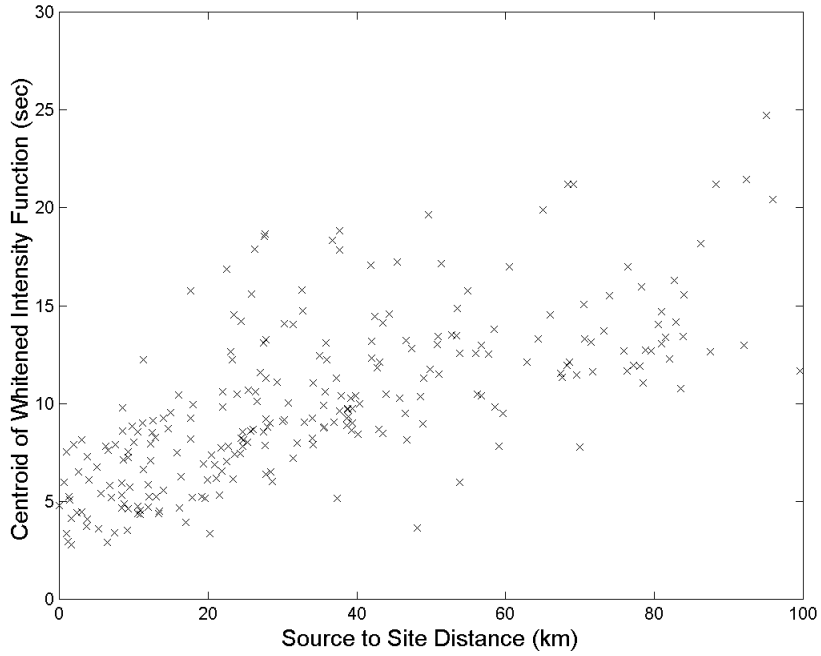

Figure 4.9: The centroid of the whitened intensity function, $\bar{\tau}$, versus distance for the California ground motion database.

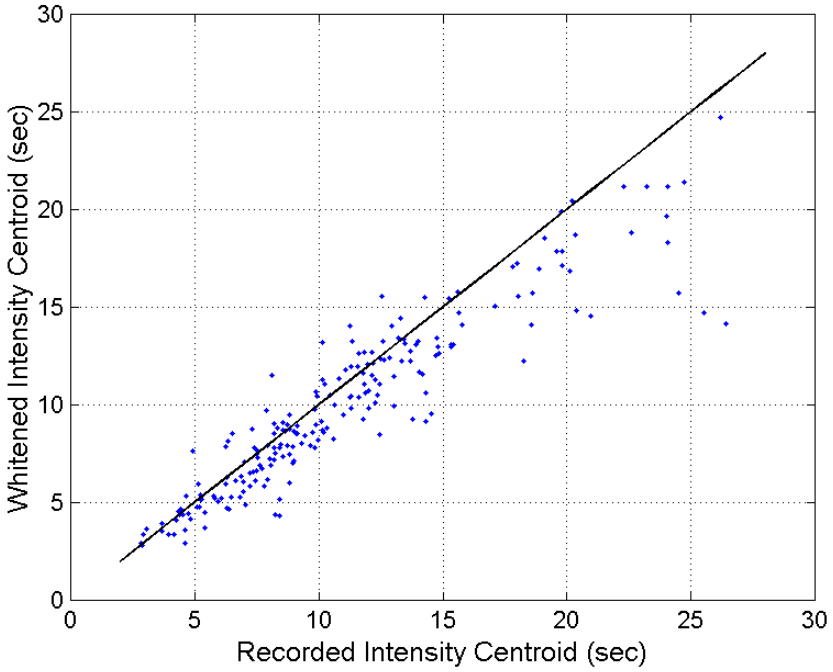

Figure 4.10: The centroid of the whitened intensity function versus the centroid of the recorded intensity function for the California ground motion database.

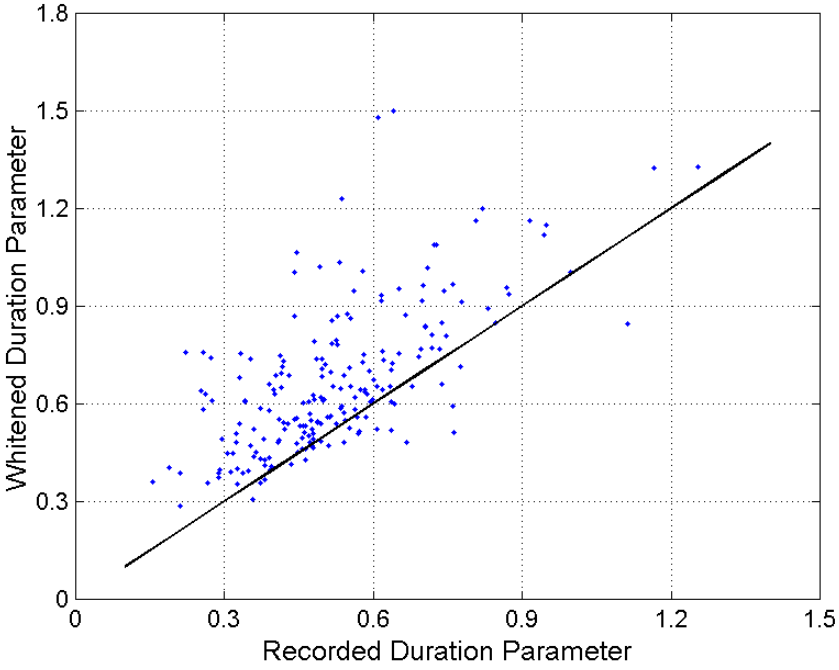

Figure 4.11: The whitened duration parameter versus the recorded duration parameter for the California ground motion database.

It has been shown in this chapter that the probability distribution of Fourier phase differences (Φ' given their amplitude *A*) for digital earthquake accelerograms can be described by a normal distribution, where the mean is constant and the standard deviation is inversely proportional to the Fourier amplitude. Knowledge of two parameters, $\bar{\tau}$ and Δ_T, is sufficient to determine the mean and the conditional standard deviation of the Fourier phase difference distribution; e.g. the centroid and the unitless width of the whitened intensity function, or alternatively, the first and second whitened intensity moments. In this section it was shown that the two parameters show strong statistical dependence, indicating that only one parameter is sufficient to completely define the phase difference distribution. In the following subsection, prediction formulas are developed for the parameters of the normal distribution for Fourier phase differences. The parameters chosen to describe the phase difference distribution are the first and second temporal moments of the whitened intensity function, γ_1 and γ_2, respectively. The first moment is chosen as a primary parameter, i.e. dependent on magnitude and distance, and the second moment is chosen as a secondary parameter, i.e. conditional on the first moment.

4.5.1 The First Whitened Intensity Moment

The two-step regression procedure described in Section 2.2 is applied to the first whitened intensity moment, γ_1. The functional form chosen for the regression analysis is

$$\gamma_1 = \frac{c_1 + c_2 \cdot \exp\left(c_3 \cdot D^{c_4}\right)}{c_M\left(M_W\right)} \tag{4.37}$$

where D is the distance, and c_1, c_2, c_3, c_4, and $c_M\left(M_W\right)$ are regression coefficients. This functional form is chosen because it conforms to the observed pattern of the data points. The coefficients $c_M\left(M_W\right)$ are magnitude-dependent scaling factors. In the second step of the regression procedure, a linear model is fitted to the magnitude scaling factors:

$$c_M = q_1 + q_2 \cdot M_W \tag{4.38}$$

Here, q_1 and q_2 are regression coefficients, and M_W is the moment magnitude of the earthquake.

The results of the regression analysis using the entire California ground motion data set are illustrated in Figure 4.12. In Figure 4.12(a), the magnitude-scaled first whitened intensity moment is plotted as a function of the source to site distance. The values of the regression parameters, obtained by non-linear least squares regression, are given at the top of the figure. In Figure 4.12(b), the residuals from the regression in Figure 4.12(a) are plotted as a function of distance. The standard deviation of the residuals is determined to be 0.0485. The residuals do not appear to depend on distance. A histogram of the standardized residuals is displayed in Figure 4.12(d). The coefficients of skewness and kurtosis, which can be used when modeling the dispersion of the residuals, if desired, are reported on the figure. The coefficient of skewness is 0.33, implying a positive skewness, and the coefficient of kurtosis is 3.2, implying a distribution that is slightly more peaked than the normal distribution. The results of the second step of the regression procedure are shown in Figure 4.12(c), where the magnitude scaling factor is regressed against moment magnitude. The scaling factor

decreases with magnitude, implying that the first whitened intensity moment – hence $\bar{\tau}$ and the effective duration – increases with the magnitude of the earthquake. This is not surprising, considering the longer source duration of the larger earthquakes.

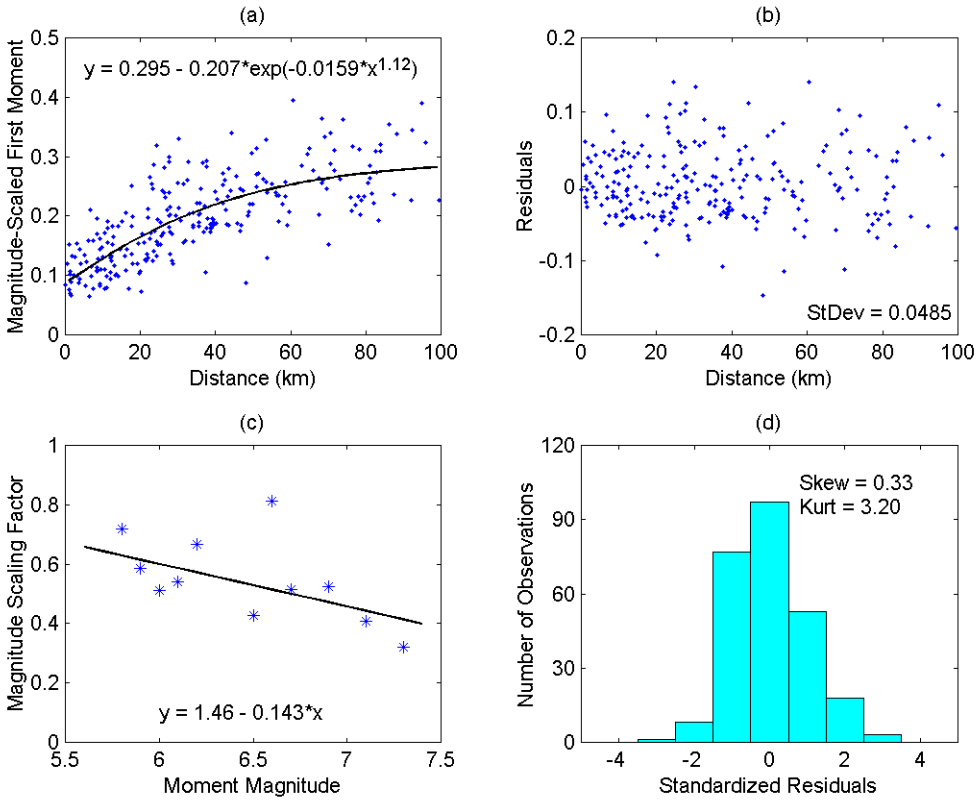

Figure 4.12: Results of a two step regression analysis for the first whitened intensity moment and all sites. (a) The distance dependence of the magnitude-scaled moment; (b) residuals from (a); (c) the magnitude dependent scaling factor; (d) histogram of the standardized residuals from (a).

The two-step regression was repeated for Site Class A&B, Site Class C, and Site Class D. The model parameters from these analyses are reported in Table 4.2, along with the parameters that were obtained using recordings from the entire data set. The parameter σ represents the standard deviation of the residuals from the regression.

The results of the regression analyses that are summarized in Table 4.2 are displayed graphically in Figure 4.13. In Figure 4.13(a), the predicted magnitude-scaled first moment is plotted as a function of distance for different site classes. The thick, solid

line in Figure 4.13(a) is the same as the solid line in Figure 4.12(a). The first moment is considerably lower for Site Class A&B than the softer site classes, indicating that the energy of accelerograms recorded at rock sites is concentrated closer to the beginning of the record, than the energy of accelerograms that are recorded at soil sites. There does not seem to be a significant difference between Site Class C, Site Class D, and All Sites, for the magnitude-scaled first moment.

The magnitude dependency of the first whitened intensity moment is illustrated in Figure 4.13(b) for different site classes. The thick, solid line in Figure 4.13(b) is the same as the solid line in Figure 4.12(c). The magnitude scaling factor is most sensitive to the magnitude for Site Class A&B, but it is practically identical for the other site classes.

Table 4.2: Regression results for γ_1 (sec).

Data Set	c_1	c_2	c_3	c_4	q_1	q_2	σ
All Sites	0.295	-0.207	-0.0159	1.12	1.46	-0.143	0.0485
Site Class A&B	0.165	-0.139	-0.0303	1.12	3.19	-0.410	0.0186
Site Class C	0.274	-0.223	-0.0528	0.86	1.68	-0.177	0.0411
Site Class D	0.259	-0.141	-0.0002	2.65	1.45	-0.143	0.0311

Model: $$\gamma_1 = \frac{c_1 + c_2 \cdot \exp\left(c_3 \cdot D^{c_4}\right)}{q_1 + q_2 \cdot M_W}$$

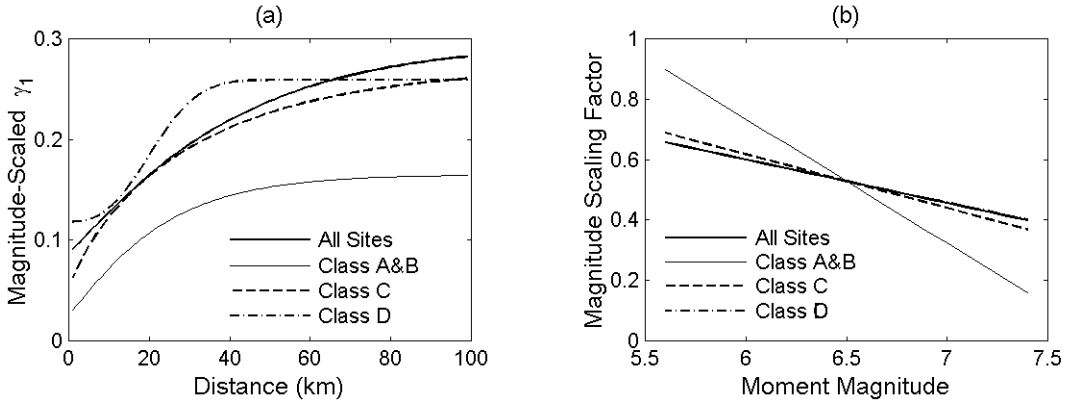

Figure 4.13: Results of a two-step regression analysis for the first whitened intensity moment and different site classes. (a) The distance dependence of the magnitude-scaled moment; (b) the magnitude dependent scaling factor.

For prediction purposes, it is recommended to use the regression results from Table 4.2 Site Class A&B, but to use the results pertaining to "All Sites" for all other site classes. This recommendation is made despite the fact that the shape of the regression curve for Site Class D in Figure 4.13(a) is different from the shape of all the other regression curves in the figure. If the regression parameters pertaining to "All Sites" are used, the standard prediction error – i.e. the standard deviation of the difference between the observed and predicted magnitude-scaled γ_1 – for Class D sites is 0.0402. While this standard prediction error is one-third higher than the standard deviation of the residuals obtained in the regression for Site Class D, it is still lower than the standard error obtained in the regression for either "All Sites" or Site Class C. Therefore, it is considered justifiable to use the regression results obtained from "All Sites" for Site Class D.

4.5.2 The Second Whitened Intensity Moment

In the discussion of Figure 4.7 it was suggested that the second whitened intensity moment would be a parabolic function of the first whitened intensity moment. The results of such a regression analysis are shown in Figure 4.14. In Figure 4.14(a), the data points are plotted as well as the best fit parabola, obtained by means of linear least squares regression. The residuals from that regression are plotted as function of the first whitened intensity moment in Figure 4.14(b). The histogram of the standardized residuals, which is displayed in Figure 4.14(d), reveals a rather strong positive skewness and a very high value of the coefficient of kurtosis. In Figure 4.14(c), the regression from 4.14(a) is transformed into natural logarithm space.

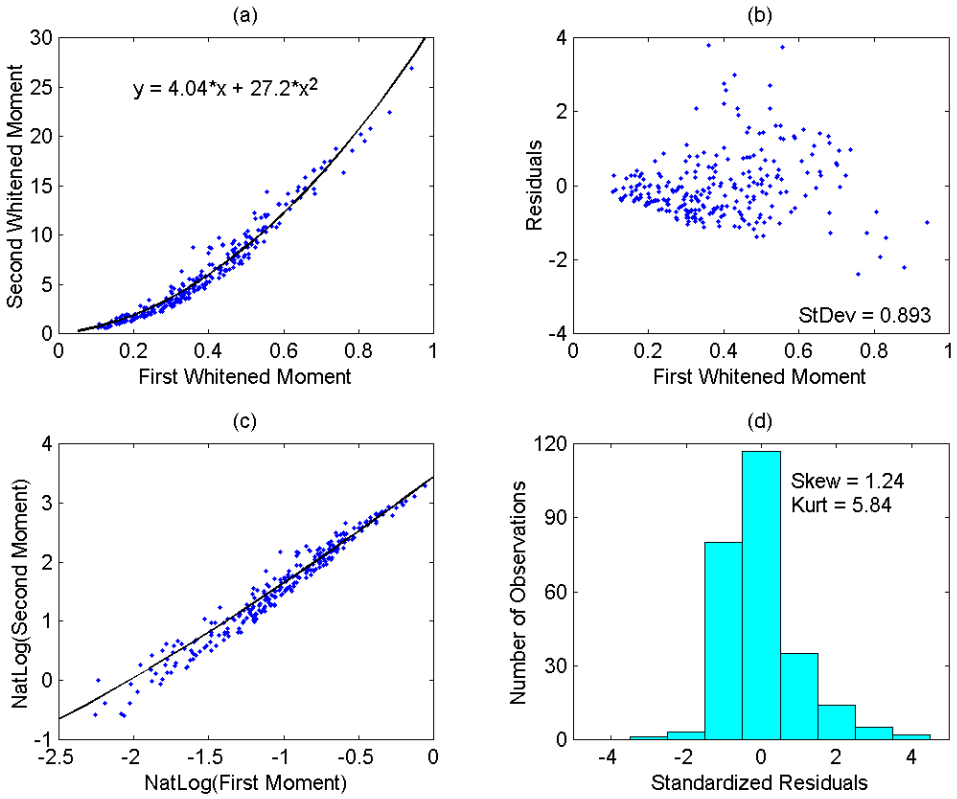

Figure 4.14: Results of a polynomial regression of the second whitened intensity moment as function of the first whitened intensity moment. (a) The polynomial regression; (b) the residuals from the regression in (a); (c) the regression in (a) transformed into natural logarithm space; (d) histogram of the standardized residuals from (a).

Figure 4.14(c) implies a linear relationship between the second and first whitened intensity moments in natural logarithm space. The results of such linear regression analysis are shown in Figure 4.15. In Figure 4.15(a), the best fit line, obtained by means of linear least squares regression, is superimposed on the data points. In Figure 4.15(b), the residuals from the linear regression are plotted as function of the independent parameter; the natural logarithm of the first whitened intensity moment. A histogram of the standardized residuals is displayed in Figure 4.15(d). The coefficients of skewness and kurtosis, which are reported on that figure, are rather high, but considerably smaller than those in Figure 4.14(d). The coefficient of skewness decreased from 1.24 to 0.83, and the coefficient of kurtosis dropped from 5.84 to 4.00. In Figure 4.15(c), the regression from 4.16(a) is transformed from natural logarithm space into linear space.

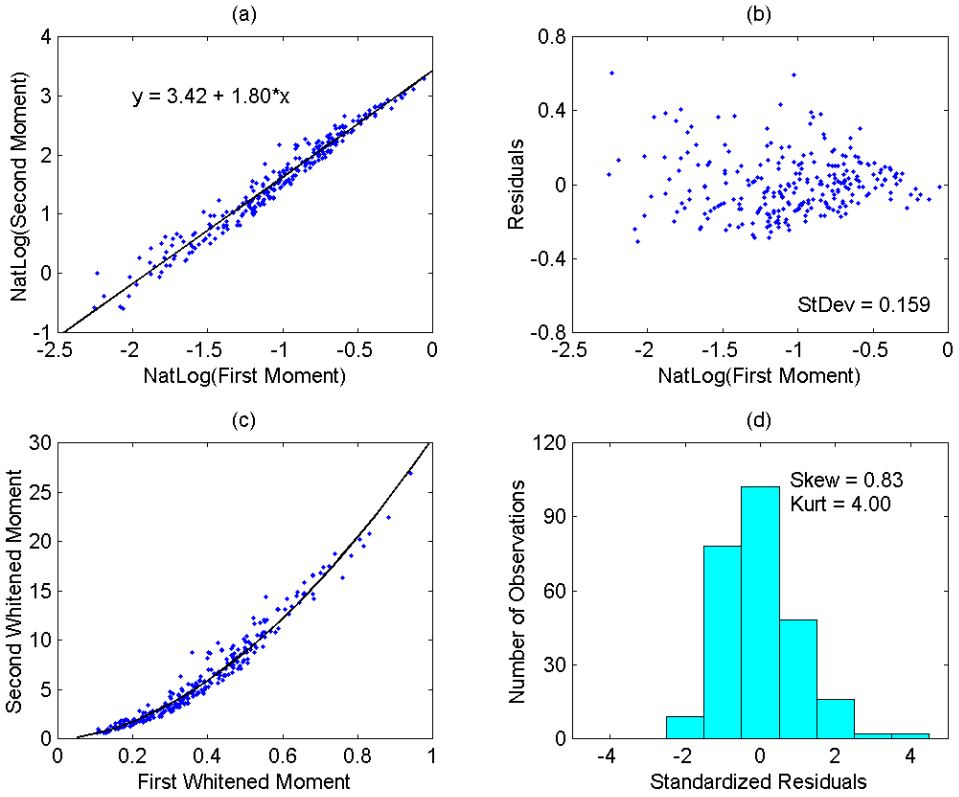

Figure 4.15: Results of a linear regression in natural logarithm space for the second whitened envelope moment as function of the first whitened envelope moment. (a) The linear regression in natural logarithm space; (b) the residuals from (a); (c) the regression in (a) transformed into linear space; (d) histogram of the standardized residuals from (a).

Based on the more desirable behavior of the residuals of the regression analyses presented in Figure 4.15 rather than the regression in Figure 4.14, the logarithmic regression model (in Figure 4.15) is preferred over the quadratic polynomial fit to the data (in Figure 4.14).

The linear regression was repeated for Site Class A&B, Site Class C, and Site Class D. The model parameters from these analyses are reported in Table 4.3, along with the parameters that were obtained using recordings from the entire data set. The parameter σ represents the standard deviation of the residuals from the regression.

The results of the regression analyses that are summarized in Table 4.3 are illustrated graphically in Figure 4.16. In Figure 4.16(a), the regression relationships are presented in logarithmic space, and in Figure 4.16(b), the relationships are transformed into linear space. There is negligible difference between the site classes. Therefore, it is recommended to use the results in Table 4.3 pertaining to "All Sites" for all site classes.

Table 4.3: Regression results for γ_2 (sec^2).

Data Set	c_1	c_2	σ
All Sites	3.42	1.80	0.159
Site Class A&B	3.34	1.70	0.117
Site Class C	3.39	1.73	0.171
Site Class D	3.43	1.82	0.174

Model: $\ln(\gamma_2) = c_1 + c_2 \cdot \ln(\gamma_1)$

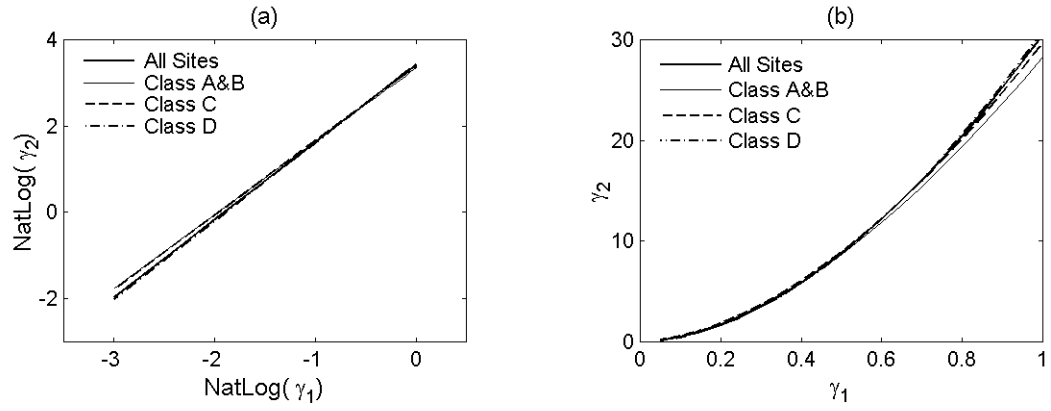

Figure 4.16: Results of a linear regression of the second whitened intensity moment versus the first whitened intensity moment for different site classes. (a) Logarithmic space; (b) linear space.

4.6 Model Validation

In Section 4.3 it was postulated that Fourier phase differences of digital earthquake accelerograms could be modeled by a normal distribution, where the mean is independent of the Fourier amplitude but the standard deviation is inversely proportional to the amplitude. In this section, several tests are performed to estimate how well the assumed model, i.e. the conditional normal distributions for Fourier phase differences, fit real observations. Four different quality tests are performed: statistical goodness of fit tests for the phase difference distributions, and three different tests where the characteristics of simulated accelerograms are compared to the corresponding characteristics of recorded accelerograms. These include comparisons of peak ground acceleration values, linear response spectra, and the temporal distribution of the energy content. All four tests are performed on the entire ground motion database that was used to develop the prediction formulas for the model parameters.

4.6.1 Phase Difference Distributions

Figure 4.17 shows a comparison of the Fourier phase angle and phase difference distributions between a recorded and a simulated accelerogram. The plots on the left hand side are for the recorded east-west component at the UC Santa Cruz station in the 1989, Loma Prieta earthquake. The plots on the right pertain to simulations, using conditional normal distributions for the Fourier phase differences. The parameters of the normal distribution are estimated according to the procedure described in Section 4.4, i.e., the centroid $\bar{\tau} = 8.4\,\text{sec}$ and the duration parameter $\Delta_T = 0.43$ are found from a whitened version of the recorded time history. The histograms of the phase angles, which are displayed in Figures 4.17(a) and 4.17(b), reveal a relatively uniform pattern. The histograms of phase differences, which are shown in Figures 4.17(c) and 4.17(d), are for all practical purposes identical; the difference is negligible. In Figures 4.17(e) the recorded phase differences are plotted as a function of the recorded Fourier amplitude, and the simulated phase differences are plotted as a function of the recorded Fourier amplitude in Figure 4.17(f). The gross characteristics of the scatterplot of the recorded phase differences are reproduced in the scatterplot of the simulated phase differences.

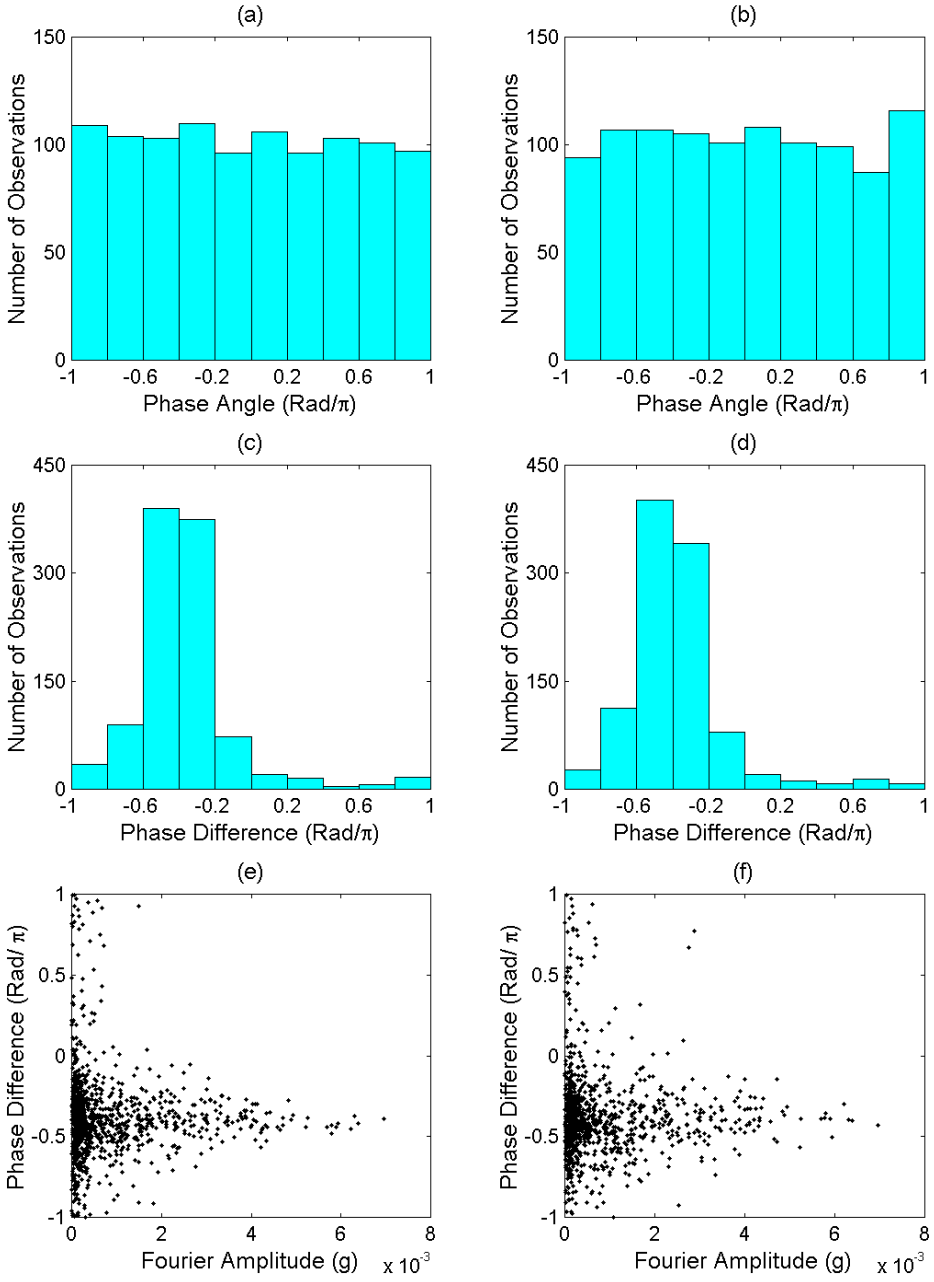

Figure 4.17: Comparison of recorded and simulated Fourier phase angles and phase differences for the east-west component of the UC Santa Cruz record from the 1989, Loma Prieta earthquake. (a) Histogram of recorded phase angles; (b) histogram of simulated phase angles; (c) histogram of recorded phase differences; (d) histogram of simulated phase differences; (e) recorded phase differences vs. recorded Fourier amplitudes; (f) simulated phase differences vs. recorded Fourier amplitudes.

Figure 4.17 provides a qualitative validation of the phase difference simulation model for this particular record, but a general and quantitative validation method is needed. Since the phase differences are simulated using a normal distribution, one might think that a Kolmogorov-Smirnov test, similar to the tests that were performed for the beta distributions in Subsection 3.4.1, might be useful. In the Kolmogorov-Smirnov goodness of fit test, an assumed cumulative distribution function is compared to an observed cumulative distribution function. Unfortunately, the Kolmogorov-Smirnov test is not applicable to the phase difference distributions, because the probability distribution of the recorded phase differences is not Gaussian as the assumed distribution is, due to the effects of phase wrapping and truncation. The recorded phase angles are limited to a 2π-wide interval, for example the interval $[-\pi, \pi]$. Hence, the recorded phase differences are limited to the interval $[-2\pi, 2\pi]$, and after unwrapping, the interval $[-\pi, \pi]$. Therefore, the recorded phase differences can never follow a normal distribution, not even a truncated normal distribution. However, a two-sample Kolmogorov-Smirnov test can be performed. In a two-sample Kolmogorov-Smirnov test, two empirical distributions are compared and it is determined whether there is a significant difference between them. The null-hypothesis is that the two observed distributions are different realizations of the probability distribution of the same underlying random variable. If the difference between the two observed distributions is not significant, the null-hypothesis is accepted. The true distribution, i.e. the probability distribution of the underlying random variable, is not necessarily known.

The simple choices for the two-sample Kolmogorov-Smirnov test are the marginal distributions of recorded and simulated Fourier phase differences, or the distributions of recorded and simulated Fourier phase angles. In Figure 4.18(a) the cumulative probability distribution functions of the Fourier phase angles are plotted. The solid line is the cumulative distribution for the accelerogram that was recorded at the UC Santa Cruz station in the 1989, Loma Prieta earthquake (the east-west component). This is the cumulative distribution that corresponds to the histogram in Figure 4.17(a). The dashed line in Figure 4.18(a) represents the cumulative distribution of the simulated phase angles; the cumulative distribution that corresponds to the histogram in Figure 4.17(b). The two phase angle distributions in Figure 4.18(a) are practically identical.

In Figure 4.18(b) the marginal cumulative phase difference distribution for the recorded accelerogram (solid line, corresponding to the histogram in Figure 4.17(c)) is plotted on top of the marginal distribution of the simulated phase differences (dashed line, corresponding to the histogram in Figure 4.17(d)). The term "marginal phase difference distribution" is used here because in this comparison, all the phase differences are grouped together, independent of their Fourier amplitudes. The two marginal phase difference distributions are nearly identical. It is hard to imagine a statistical goodness of fit test that would reject the hypothesis that these two realizations come from the same underlying distribution. However, the phase differences are simulated conditional on the amplitudes. Therefore, any statistical goodness of fit test used to estimate the quality of the simulation model should take this conditional characteristic into account. The marginal distributions in Figure 4.18(b) do not.

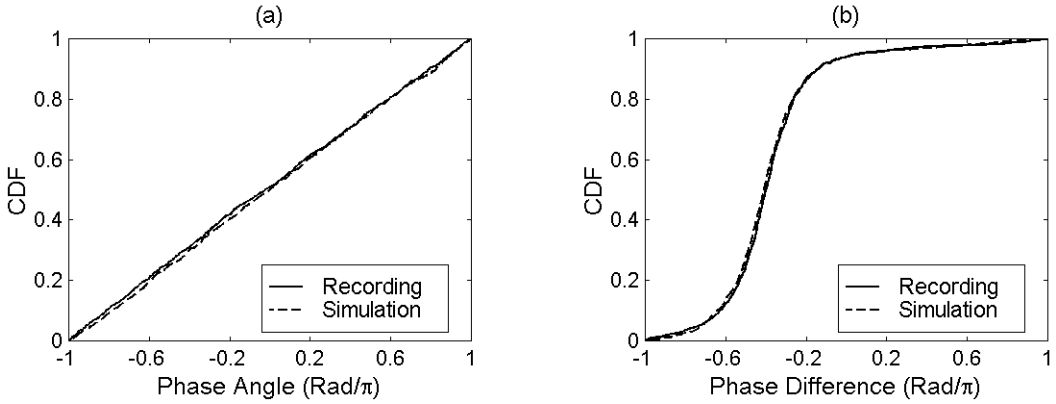

Figure 4.18: Cumulative probability distribution functions for recorded (solid lines) and simulated (dashed lines) phase angles (a) and phase differences (b). The east-west component of the UC Santa Cruz record from the 1989, Loma Prieta earthquake.

In Figure 4.19(a), the recorded Fourier phase differences are plotted as a function of the whitened Fourier amplitude – i.e. the amplitude after whitening of the accelerogram in the frequency domain. This is the same plot as in Figure 4.6, except that here the phase difference domain is $[-1.4\pi, 0.6\pi]$, rather than $[-\pi, \pi]$ as it is in Figure 4.6. This domain-shift was performed so that the mean phase difference, represented by the horizontal, solid line in the figure, would be in the center of the phase difference domain. The dashed lines in the figure represent the mean phase difference plus/minus one

standard deviation. Figure 4.19(b) is similar to Figure 4.19(a). The only difference is that in Figure 4.19(b) the simulated phase differences, rather than the recorded phase differences, are plotted as a function of the normalized Fourier amplitude. In Figures 4.19(c) and 4.19(d) the phase differences have been standardized, i.e. the mean phase difference has been subtracted from each value and then divided by the standard deviation corresponding to the particular normalized amplitude. Figure 4.19(c) shows results for the recorded accelerogram, and Figure 4.19(d) for the simulated phase differences. If the phase differences were not truncated, circular, or unwrapped, the dots in Figures 4.19(c) and 4.19(d) would represent realizations of a standardized random variable (zero mean, unit standard deviation), independent of the amplitude. This is clearly not the case, especially for the lowest normalized amplitudes. As the normalized amplitude approaches zero, the standard deviation, which is inversely proportional to the normalized amplitude, approaches infinity. Hence, as the phase differences only take finite values, the standardized phase difference approaches zero as the normalized amplitude approaches zero. However, because the recorded and simulated phase differences have been processed identically and their behavior conditional on the normalized Fourier amplitude has been taken into account, the two-sample Kolmogorov-Smirnov test can now be used to examine the validity of the phase difference modeling. It does not matter that the underlying distribution is not known. The cumulative distribution of the recorded standardized phase differences can be compared to the cumulative distribution of the standardized simulated phase differences. If the difference between the two cumulative distributions is insignificant, the phase difference simulation model is accepted.

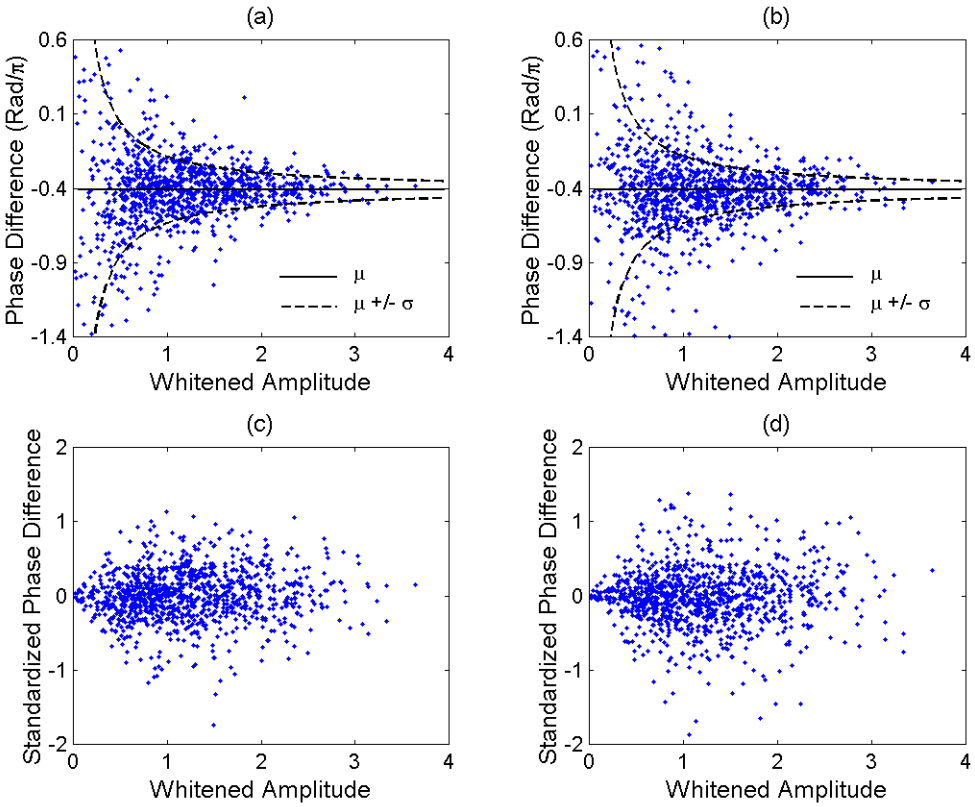

Figure 4.19: Standardization of phase differences for the east-west component of the UC Santa Cruz record from the 1989, Loma Prieta earthquake. (a) Recorded phase differences vs. whitened Fourier amplitudes; (b) simulated phase differences vs. whitened Fourier amplitudes; (c) standardized recorded phase differences vs. whitened Fourier amplitudes; (d) standardized simulated phase differences vs. whitened Fourier amplitudes.

The two-sample Kolmogorov-Smirnov goodness of fit test (sometimes also referred to as the Smirnov test) is used to determine whether two observed cumulative distribution functions are significantly different from each other. The statistic used to estimate whether the two distributions are significantly different is the maximum of their absolute difference:

$$S_{n_1 n_2} = \max_{\text{all } x} \left| F_{n_1}(x) - F_{n_2}(x) \right| \tag{4.39}$$

Here, $S_{n_1 n_2}$ is the Kolmogorov-Smirnov statistic, and $F_{n_1}(x)$ and $F_{n_2}(x)$ are the cumulative distribution functions for samples of size n_1 and n_2, respectively.

The cumulative distribution functions for the two samples are given by:

$$F_{n_i}(x_j) = \frac{j}{n_i}; \quad j = 1,2,\ldots,n_i; \quad i = 1,2 \tag{4.40}$$

where x_j is the j-th smallest observation. The assumption that the two samples are drawn from the same population is rejected if the test statistic is larger than a certain critical value, i.e. if

$$S_{n_1 n_2} > S_{n_1 n_2, cr} \Rightarrow \text{reject} \tag{4.41}$$

The critical value can be approximated by (Lindgren, 1976):

$$S_{n_1 n_2, cr} = \sqrt{\frac{-\ln(\alpha/2)}{2}\left(\frac{1}{n_1} + \frac{1}{n_2}\right)} \tag{4.42}$$

where α is the significance level of the test. The significance level is equal to the probability of rejecting the null-hypothesis; the assumption that the two samples are drawn from the same population, when the null-hypothesis true. The significance level is usually chosen to be a small number, very often of the order of 0.01 to 0.10.

A discrete 2048 point Fourier transform yields 1024 unique observations of phase difference (see Equation 3.7). The critical values for the two-sample Kolmogorov-Smirnov statistic, calculated according to Equation (4.42), are given in Table 4.4, for three different significance levels.

Table 4.4: Critical values of the two-sample Kolmogorov-Smirnov statistic for phase difference distributions ($n_1 = n_2 = 1024$).

Significance Level	**Critical Value**
0.01	0.0719
0.05	0.0600
0.10	0.0541

Figure 4.20 shows examples of simulated (dashed lines) and recorded (solid lines) probability distributions for the standardized phase difference. The maximum difference between the two cumulative distribution functions is 0.0429. This number is smaller than all the values in the right-hand column of Table 4.4, thus the basic assumption that the recorded and simulated distributions are two realizations of the same underlying random variable is not rejected at any of the three significance levels. The same holds true for the entire California ground motion database.

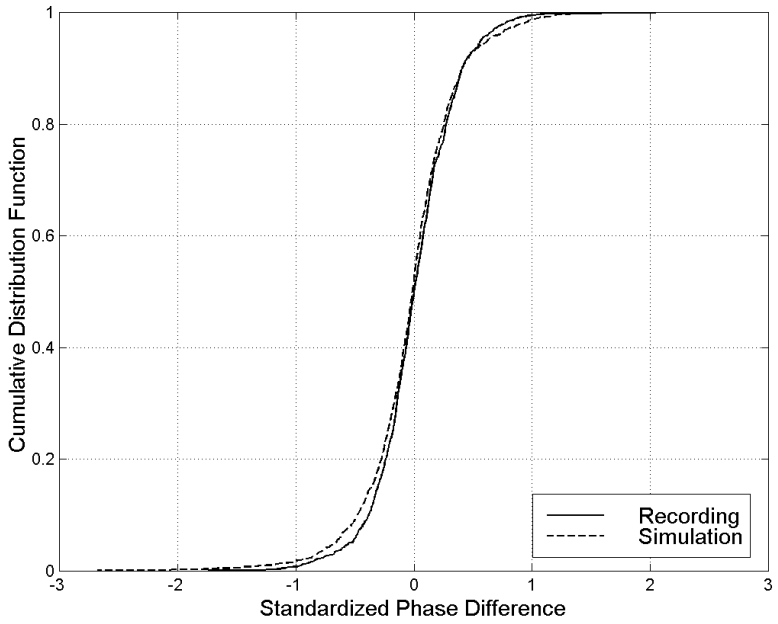

Figure 4.20: Cumulative probability distribution functions for the standardized phase differences (in Figure 4.19) corresponding to a recorded (solid line) and a simulated (dashed line) accelerogram. The east-west component of the UC Santa Cruz record from the 1989, Loma Prieta earthquake.

As described above, the statistical goodness of fit of the conditional normal distributions for phase differences is very good, as measured by the two-sample Kolmogorov-Smirnov test. It is of more interest, however, whether the accelerograms simulated using these probability distributions, adequately reproduce the relevant characteristics of recorded accelerograms. In the following subsection, the attributes of simulated accelerograms are compared to the corresponding attributes of recorded accelerograms.

4.6.2 Accelerograms

In this subsection, the characteristics of simulated accelerograms, using the conditional phase difference distributions, are compared with the corresponding characteristics of recorded accelerograms. Three different characteristics are compared: peak values, elastic response spectra, and evolutionary behavior.

Peak Ground Acceleration

In Figure 4.21, an example of a recorded accelerogram is displayed, along with two sample simulations. The gross characteristics of the recorded accelerogram are reproduced in the simulated accelerograms. The average peak ground acceleration from ten simulations is 0.46g and the standard deviation is 0.06g, while the recorded peak ground acceleration is 0.41g.

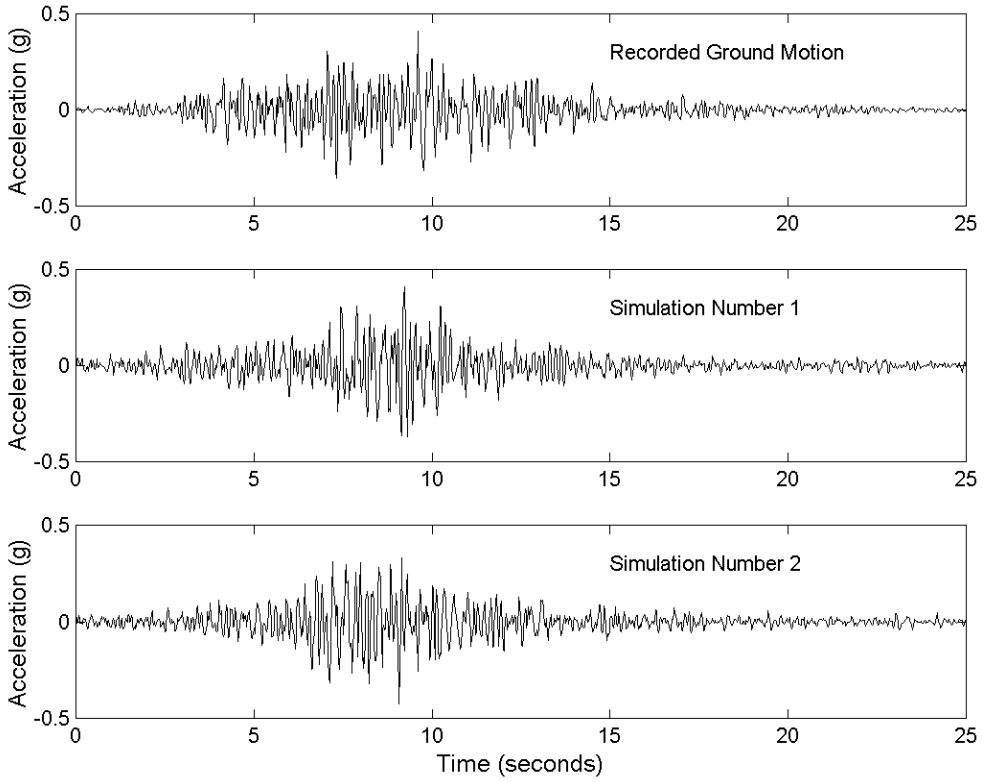

Figure 4.21: Examples of simulated accelerograms using a conditional normal distribution for the Fourier phase differences. The recorded east-west component of the UC Santa Cruz record from the 1989 Loma Prieta earthquake (top) and two example simulations (bottom two).

The results displayed in Figure 4.21 are typical for the entire ground motion data base. In the vast majority of cases, the recorded PGA is within one standard deviation of the mean of ten simulations, and in every case, the recorded PGA is within two standard deviations of the mean.

Elastic Response Spectrum

The elastic response spectra are compared in Figure 4.22. The solid line represents the elastic pseudo acceleration response spectrum of the recorded ground motion, assuming a damping ratio equal to 5% of critical damping. The dashed lines in Figure 4.20 represent the response spectra of ten simulated acceleration time histories. For all natural periods depicted in the figure (from 0.1 seconds to 2 seconds), the response spectra of the simulated time histories envelope the response spectrum of the recorded time history. The results in Figure 4.20 are representative of the entire ground motion data set.

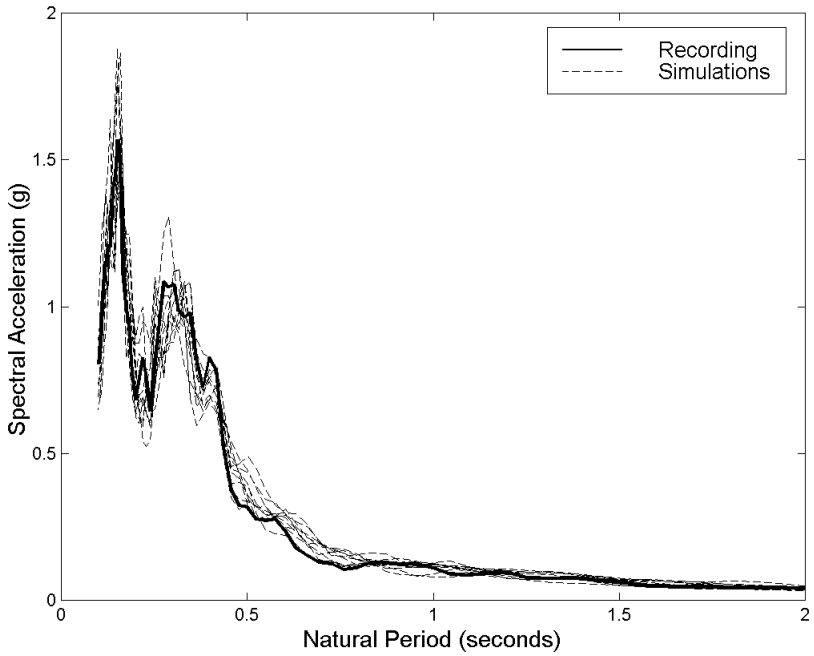

Figure 4.22: Elastic pseudo acceleration response spectra (5% damping). Dashed lines: ten simulations using a conditional normal distribution for the Fourier phase differences; solid line: the recorded response spectrum from the east-west component of the UC Santa Cruz record from the 1989 Loma Prieta earthquake.

Cumulative Normalized Arias Intensity

The evolutionary behavior of the simulated and recorded accelerograms is displayed in Figure 4.23. It is quantified in terms of the cumulative normalized Arias intensity, which is defined in Equation (3.17). The dashed lines in Figure 4.23 represent the cumulative normalized Arias intensity obtained from ten simulations, while the solid line represents the cumulative normalized Arias intensity of the recorded accelerogram. In general, the simulated accelerograms seem to capture well the evolutionary characteristics of the recorded accelerogram. The curves for the simulated accelerograms tend not to be as jagged as the curves for the recorded accelerograms, indicating a smoother evolutionary energy release.

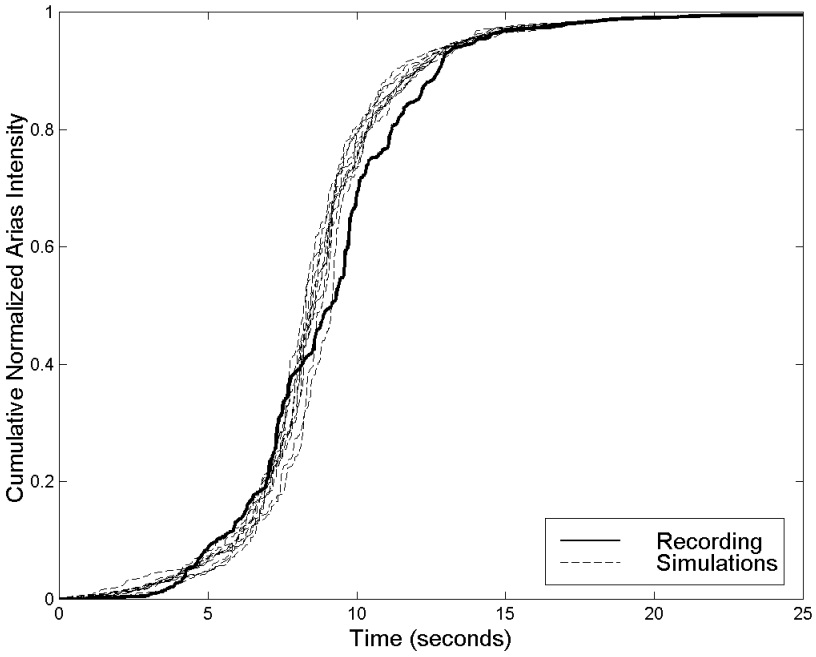

Figure 4.23: Cumulative normalized Arias intensity. Dashed lines: ten simulations using a conditional normal distribution for the Fourier phase differences; solid line: the cumulative normalized Arias intensity of the east-west component of the UC Santa Cruz record from the 1989 Loma Prieta earthquake.

This concludes the comparison of the characteristics of simulated accelerograms to those of recorded ones. In general, the comparison is found to be good.

4.7 Summary of Conditional Normal Distributions

Applying a frequency domain analogy initially proposed by Nigam (1982) to the method of envelopes for time-varying functions, it is shown that the Fourier phase differences of digital accelerograms can be modeled by a normal distribution with a constant mean and where the standard deviation is inversely proportional to the Fourier amplitude. The mean and the conditional standard deviation can be computed from the zeroth, first, and second intensity moments of the whitened accelerogram.

The California ground motion database is used to develop prediction formulas for the model parameters. The results of the regression analyses are summarized below. The parameter D is the shortest distance from the site to the surface projection of the seismogenic rupture in kilometers, and M_W is the moment magnitude of the earthquake.

The zeroth whitened intensity moment is a constant, given by:

$$\gamma_0 = 0.0380$$

The zeroth intensity moment is a unitless parameter.

For all non-rock sites, or an unknown site classification, the first whitened intensity moment is given by:

$$\gamma_1 = \frac{0.295 - 0.207 \cdot \exp\left(-0.0159 \cdot D^{1.12}\right)}{1.46 - 0.143 \cdot M_W}; \quad D \le 100 \text{ km}, \; 5.8 \le M_W \le 7.3$$

For Site Class A&B the first moment can be estimated according to:

$$\gamma_1 = \frac{0.165 - 0.139 \cdot \exp\left(-0.0303 \cdot D^{1.12}\right)}{3.19 - 0.410 \cdot M_W}; \quad D \le 100 \text{ km}, \; 5.8 \le M_W \le 7.3$$

The first whitened intensity moment has the unit of seconds.

The second whitened intensity moment can be derived from the first moment for all sites according to:

$$\ln(\gamma_2) = 3.42 + 1.80 \cdot \ln(\gamma_1)$$

The second whitened intensity moment has the unit of seconds squared.

An alternative to using the whitened intensity moments for the parameterization of the Fourier phase difference distributions would be to use the centroid, $\bar{\tau}$, and the unitless duration parameter, Δ_T, of the whitened intensity function. However, the intensity moments proved to be better suited for regression analyses.

The Fourier phase difference model is validated through extensive statistical goodness of fit tests, as well as comparison of certain characteristics of the simulated and recorded accelerograms. These characteristics are: (i) the peak ground acceleration, (ii) the 5% damped elastic response spectrum, and (iii) the evolutionary behavior as quantified by the cumulative normalized Arias intensity. In general, the comparison is found to be good.

CHAPTER 5
MODELING OF FOURIER AMPLITUDES

The modeling of Fourier amplitude spectra of earthquake accelerograms in a closed parametric form has received considerable attention in previous studies. The Fourier amplitude spectrum dictates how the total energy of the accelerogram is distributed in the frequency domain. The focus of this study is the nonstationary energy release in time, through modeling of the Fourier phase angle differences. However, for the purpose of completeness, two well-known Fourier amplitude models are reviewed in this chapter. In addition, a simple alternative approach is proposed, where the Fourier amplitude spectrum is represented by a scaled and truncated lognormal probability density function. The statistics on the Fourier amplitude spectra that are used in this chapter are tabulated in Appendix D. It should be emphasized that the Fourier phase difference models presented in the previous chapters do not depend on a particular Fourier amplitude model or any other specific spectral modeling.

5.1 Current Amplitude Models

Two popular Fourier amplitude models are reviewed in this section: the radiated source spectrum and the filtered Kanai-Tajimi spectrum. The radiated source spectrum was first introduced in seismology, but it is gaining popularity in engineering. The filtered Kanai-Tajimi spectrum has been one of the most commonly used amplitude models in the engineering community for the last decades. Given the necessary information, either of these Fourier amplitude models can be used with the models of the Fourier phase differences that were presented in the previous chapters.

5.1.1 Radiated Source Spectrum

The far-field Fourier amplitude spectrum of earthquake ground acceleration at a "hard rock" site is often described in terms of an attenuated source spectrum (e.g. Boore, 1983):

$$A(M_0, \omega_c, \theta, \varphi, R, \omega) = C \cdot E(M_0, \omega_c, \omega) \cdot G(\theta, \varphi, R) \cdot D(R, \omega) \cdot P(\omega) \qquad (5.1)$$

In Equation (5.1), C is a constant accounting for free-surface amplification and the partition of the radiated energy into two horizontal components, $A(\cdot)$ denotes the acceleration amplitude spectrum at the site, $E(\cdot)$ is the acceleration amplitude spectrum at the source, $G(\cdot)$ is a function that accounts for the radiation pattern of the seismic waves and geometric attenuation, $D(\cdot)$ is an anelastic attenuation function, and $P(\cdot)$ is a high-cut filter. The term M_0 denotes the seismic moment, ω_c is the corner frequency of the source spectrum, and the triple (θ, φ, R) describes the location of the site with respect to the source in spherical coordinates. The distance from the source to the site is denoted by R (R is used here as a generic distance parameter, because D is reserved for the shortest distance from a site to the surface projection of a seismogenic rupture), and ω represents circular frequency.

The constant C accounts for the free-surface amplification and the partition of the radiated energy into two horizontal components. The free-surface amplification factor is usually taken as equal to 2. If the energy in the ground motion is assumed to be equally divided into two horizontal components, the source spectrum has to be divided by a factor of $\sqrt{2}$ to get the amplitude spectrum for each component. Hence, in that case, the factor C becomes $2/\sqrt{2} = \sqrt{2}$ (Atkinson and Boore, 1995).

The source spectrum most often used is based on the omega-squared model, proposed by Brune (1970):

$$E(M_0, \omega_c, \omega) = \frac{\omega^2 \cdot M_0}{1 + (\omega/\omega_c)^2} \qquad (5.2)$$

This source spectrum is called the omega-squared model because for frequencies larger than the corner frequency, the Fourier amplitude spectrum for displacement goes down as the frequency squared. The corner frequency can be related to the seismic moment through the Brune stress drop parameter (Brune, 1970).

The $G(\cdot)$ function combines the effects of directivity and geometric attenuation. For propagating S waves, $G(\cdot)$ is given by (Kasahara, 1981):

$$G(\theta,\varphi,R)=\frac{\Psi(\theta,\varphi)}{4\pi\cdot\rho\cdot V_S^3\cdot R} \tag{5.3}$$

where $\Psi(\theta,\varphi)$ is the radiation pattern, ρ is the mass density of the medium, and V_S is the shear wave velocity.

The anelastic attenuation is due to frictional damping in the medium. It is usually modeled using the following exponential form (Aki and Richards, 1980):

$$D(R,\omega)=\exp\left(-\frac{\omega\cdot R}{2\cdot Q(\omega)\cdot V_S}\right) \tag{5.4}$$

where $Q(\omega)$ is the quality factor. The value of the quality factor depends on the medium and it has to be evaluated empirically. Sometimes, it is assumed to be independent of frequency.

The high-cut filter is intended to take into account the rapid decay of the amplitude spectrum at high frequencies, which is usually observed in recordings of earthquake ground acceleration. The filter is often characterized by the Kappa-filter (Atkinson, 1996):

$$P(\omega)=\exp\left(-\tfrac{1}{2}\kappa\omega\right) \tag{5.5}$$

where the parameter κ has to be evaluated empirically. As used here, κ is the zero distance intercept of the parameter $\kappa(R)$ as originally defined by Anderson and Hough (1984). In their definition of $\kappa(R)$, they combined the effects of anelastic attenuation and high frequency decay. Boore (1986) suggests an alternative high-cut filter:

$$P(\omega) = \frac{1}{\sqrt{1 + (\omega/\omega_{max})^8}} \tag{5.6}$$

Here, ω_{max} is the cut-off frequency proposed by Hanks (1982), who attributes this cut-off frequency to site effects, while Papageorgiou and Aki (1983) suggest that it is a source effect.

The radiated source spectrum is very comprehensive, but it requires too detailed knowledge of the source and the medium to be usable for all practical engineering situations. Furthermore, different source spectra and radiation patterns have to be used for each type of seismic waves. Therefore, a simpler Fourier amplitude model is sought for this study.

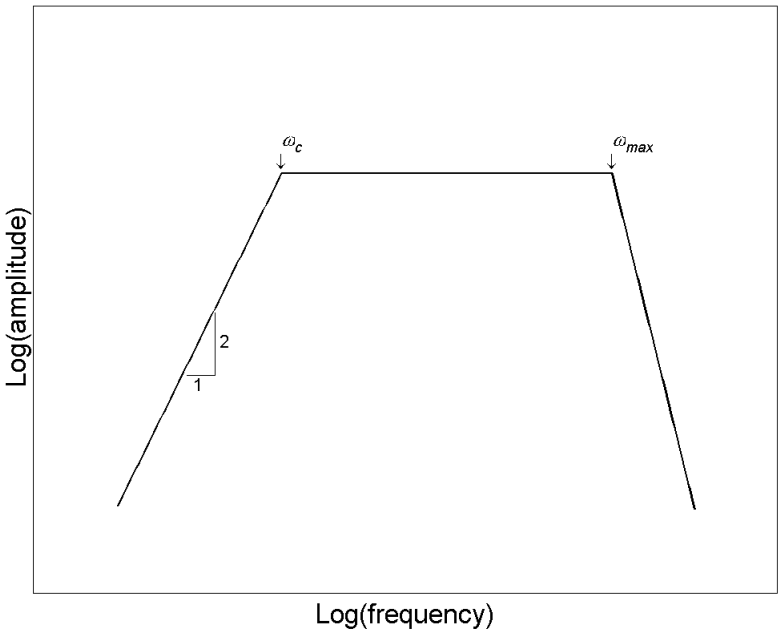

Figure 5.1: Schematic representation of the Fourier amplitude spectrum for earthquake ground acceleration (Equation 5.1) in logarithmic space.

5.1.2 Filtered Kanai-Tajimi Spectrum

An alternative model of the Fourier amplitude spectrum for earthquake ground acceleration, and one that is considerably simpler than the model presented previously, is based on the Kanai-Tajimi power spectral density (the relationship between power spectral density and Fourier amplitude is described in subsection 1.1.2). The Kanai-Tajimi power spectral density is obtained by filtering a stationary white noise process through a Kanai-Tajimi filter (Kanai, 1957; Tajimi, 1960):

$$S_{KT}(\omega) = \frac{1 + 4\xi_g^2 (\omega/\omega_g)^2}{\left[1 - (\omega/\omega_g)^2\right]^2 + 4\xi_g^2 (\omega/\omega_g)^2} S_0; \quad -\infty < \omega < \infty \tag{5.7}$$

where S_0 is the power spectral density of the underlying white noise process (see Fig. 5.2(a)), and the parameters ω_g and ξ_g can be interpreted as the characteristic frequency and damping ratio of the ground, respectively. The Kanai-Tajimi filter amplifies the frequencies around ω_g, attenuates higher frequencies, but does not change the amplitude of very low frequencies (Fig. 5.2(b)). The non-zero power spectral density for zero frequency poses a problem, because the power spectral densities for velocity and displacement are obtained by dividing ω^2 and ω^4, respectively, into the power spectral density for acceleration. Therefore, the Kanai-Tajimi power spectral density is often passed through a low-cut filter, resulting in a power spectral density function of the following form (Clough and Penzien, 1975):

$$S(\omega) = \frac{(\omega/\omega_{LC})^4}{\left[1 - (\omega/\omega_{LC})^2\right]^2 + 4\xi_{LC}^2 (\omega/\omega_{LC})^2} S_{KT}(\omega); \quad -\infty < \omega < \infty \tag{5.8}$$

The gain function for this low-cut filter is shown in Figure 5.2(c), and the resulting filtered Kanai-Tajimi power spectral density is illustrated in Figure 5.2(d).

The filtered Kanai-Tajimi power spectral density requires the estimation of five parameters: the intensity of the underlying white noise process, the characteristic frequency and the damping ratio at the site, and the two low-cut filter parameters, which can be site dependent. It is not straightforward to determine the site dependent

parameters. Therefore, a still simpler model for the Fourier amplitude spectrum is sought in this study.

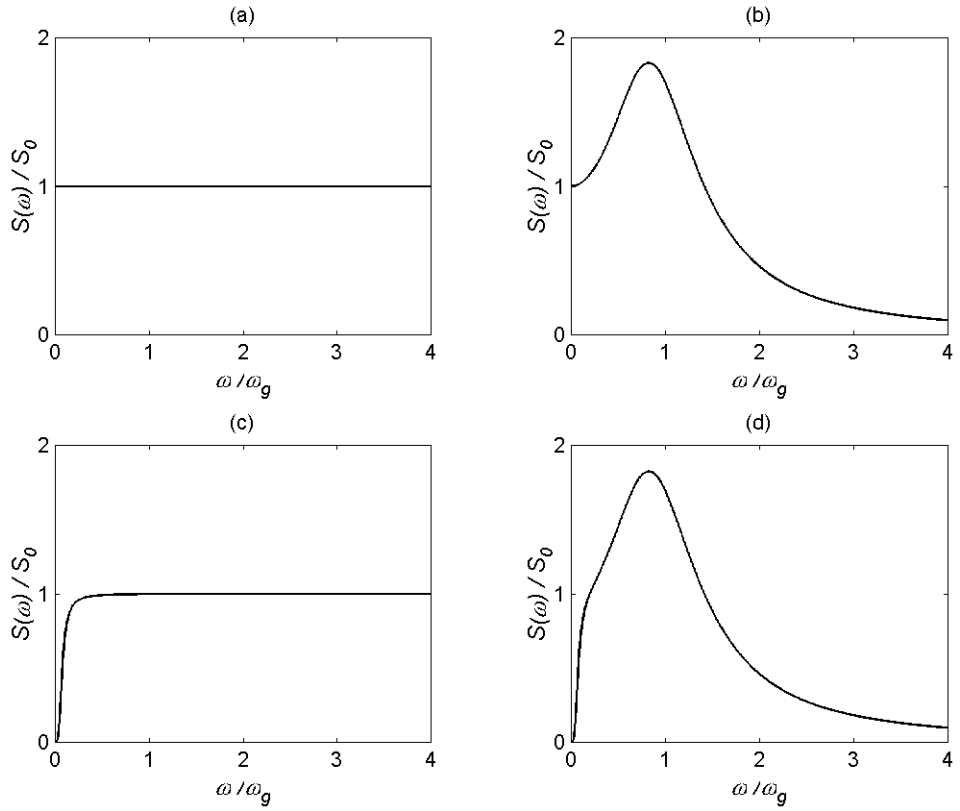

Figure 5.2: A low-cut filtered Kanai-Tajimi power spectral density as function of normalized frequency; ξ_g = 0.6, ξ_{LC} = 0.8 and $\omega_{LC} = \omega_g/15$. (a) The power spectral density of the noise process, (b) the Kanai-Tajimi power spectral density, (c) the low-cut filter, (d) the filtered Kanai-Tajimi spectrum.

5.2 Lognormal Density Function as Amplitude Spectrum

Several functional forms were investigated in this study for the modeling of Fourier amplitudes of earthquake ground acceleration. Among those were various probability density functions, such as the beta, chi-squared, gamma, lognormal, Weibull and Rayleigh distributions. It was found that, in general, a lognormal probability density

function fits the observed spectra reasonably well. The lognormal probability density function is given by:

$$f_X(x) = \frac{1}{x\sigma_{\ln X}\sqrt{2\pi}} \exp\left\{\frac{-[\ln(x) - \mu_{\ln X}]^2}{2\sigma_{\ln X}^2}\right\}; \quad x \geq 0 \tag{5.9}$$

where $\mu_{\ln X}$ is the logarithmic mean (the scale parameter) and $\sigma_{\ln X}$ is the logarithmic standard deviation (the shape parameter). This functional form was chosen because it is relatively simple, and yet it seems to be flexible enough to capture the gross characteristics of most observed amplitude spectra. Sabetta and Pugliese (1996) also use a lognormal density function to describe the Fourier amplitude spectrum.

In order to fit a lognormal density function to the amplitude spectrum, the frequency axis is first normalized such that the value of 1.0 corresponds to the Nyquist frequency. Then the amplitudes are scaled in such a way that the integral of the squared amplitudes with respect to normalized frequency equals one. This scaling is performed to facilitate the use of a probability density function. Finally, a lognormal probability density function is fitted to the scaled spectrum using the method of moments.

As an example, the Fourier amplitude spectrum for the east-west component of the UC Santa Cruz record from the 1989 Loma Prieta earthquake is shown in Figure 5.3(a) on a linear scale and in Figure 5.3(b) on a logarithmic scale. The recorded and scaled spectrum is denoted by the solid gray line, while the fitted lognormal density function is shown by the dashed black line. The lognormal density function achieves a reasonable fit with the recorded spectrum.

Three parameters are needed to completely define the smoothed Fourier amplitude spectrum. These parameters are: (1) the amplitude scaling factor, representing the total energy of the accelerogram, and (2) the scale and (3) the shape parameter of the lognormal probability density function, reflecting the central frequency and the spectral bandwidth of the accelerogram, respectively. In the following section, the California ground motion database is used to develop prediction formulas for the Fourier amplitude parameters.

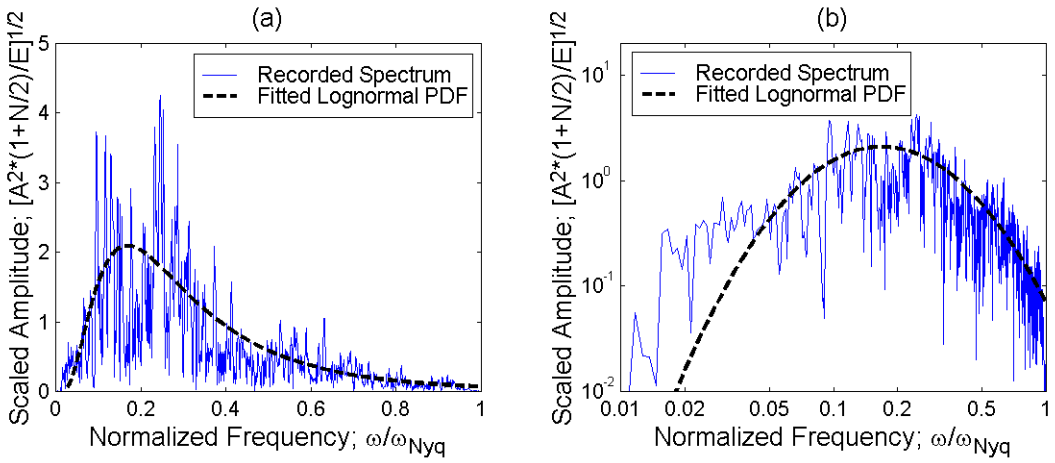

Figure 5.3: Scaled recorded Fourier amplitudes (solid gray line) versus normalized frequency and the fitted truncated lognormal probability density function (dashed black line) for the east-west component of the UC Santa Cruz record from the 1989 Loma Prieta, California earthquake in (a) linear space, and (b) logarithmic space.

5.3 Model Parameters

As described in the previous section, the scaled Fourier amplitude spectrum of an earthquake accelerogram can be modeled by a lognormal probability density function. There are three parameters necessary to completely define the spectrum: The total energy of the accelerogram, represented here by the sum of the squared Fourier amplitudes, and the two parameters needed to determine the scale parameter and the shape parameter of the lognormal probability density function. In this study, the parameters chosen to define the lognormal probability density function are (1) the first moment of the squared Fourier spectrum about the origin, and (2) the second central moment of the squared spectrum. These two moments, representing the central normalized frequency and the bandwidth of the Fourier amplitude spectrum, respectively, are computed from the digital Fourier amplitude spectrum according to

$$M_F = \frac{\sum_{n=0}^{N/2}\left(\frac{n}{N/2}\right)\cdot A_n^2}{\sum_{n=0}^{N/2} A_n^2} \tag{5.10}$$

$$V_F = \frac{\sum_{n=0}^{N/2}\left(\frac{n}{N/2}\right)^2 \cdot A_n^2}{\sum_{n=0}^{N/2} A_n^2} - \left(M_F\right)^2 \tag{5.11}$$

Here, M_F is the first spectral moment of the positive part of the two-sided amplitude spectrum about the origin, and V_F is the second, central spectral moment. A_n represents the Fourier amplitude of the n-th discrete frequency, and N is the order of the discrete Fourier transform. The ratio $n/(N/2)$ is equal to the normalized frequency of the n-th frequency component. The spectral moments defined in Equations (5.10) and (5.11) are related to the shape and scale parameters of the fitted lognormal probability density function in the following manner:

$$\sigma_{\ln X}^2 = \ln\left(1 + \frac{V_F}{M_F^2}\right) \tag{5.12}$$

$$\mu_{\ln X} = \ln\left(M_F\right) - \tfrac{1}{2}\sigma_{\ln X}^2 \tag{5.13}$$

The third Fourier amplitude parameter, the energy-like scaling factor, is the sum of the squared Fourier amplitudes:

$$E = \sum_{n=0}^{N/2} A_n^2 \tag{5.14}$$

These three parameters, the central frequency parameter M_F, the spectral bandwidth parameter V_F, and the energy parameter E, completely define the fitted, smooth amplitude spectrum. In this section, the California earthquake ground motion data is used to develop prediction formulas for the amplitude parameters.

The three Fourier amplitude parameters are not all independent of each other. In Figure 5.4, the bandwidth parameter is plotted as function of the central frequency parameter. In Figure 5.4(a), the parameters are plotted on a linear scale, while logarithmic scales are used in Figure 5.4(b). There is a clear positive correlation between the two

parameters. The linear plot indicates that the dispersion in the relationship increases with increasing central frequency. However, no such trend is apparent in the logarithmic plot. Therefore, it is preferable to perform linear regression in the logarithmic space.

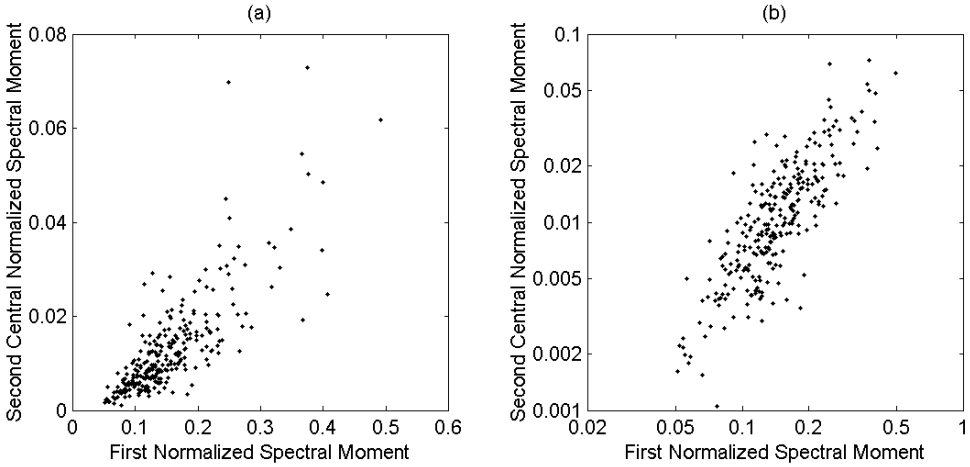

Figure 5.4: The relationship between the two spectral moments for the California ground motion database; the spectral bandwidth parameter, V_F, as function of the central frequency parameter, M_F, in (a) linear space, and (b) logarithmic space.

In Figure 5.5, the energy parameter, E, is plotted as function of the central frequency parameter, M_F. Note that the vertical scale is logarithmic, while the horizontal scale is linear. There is no apparent correlation, the two parameters seem to be independent of each other. Therefore, they are chosen as the independent parameters, and the second central moment is regressed on the first moment.

Two step regression analyses are performed on (1) the energy parameter, and (2) the central frequency parameter versus distance and magnitude. In addition, a regression relationship is developed between the bandwidth parameter and the central frequency parameter.

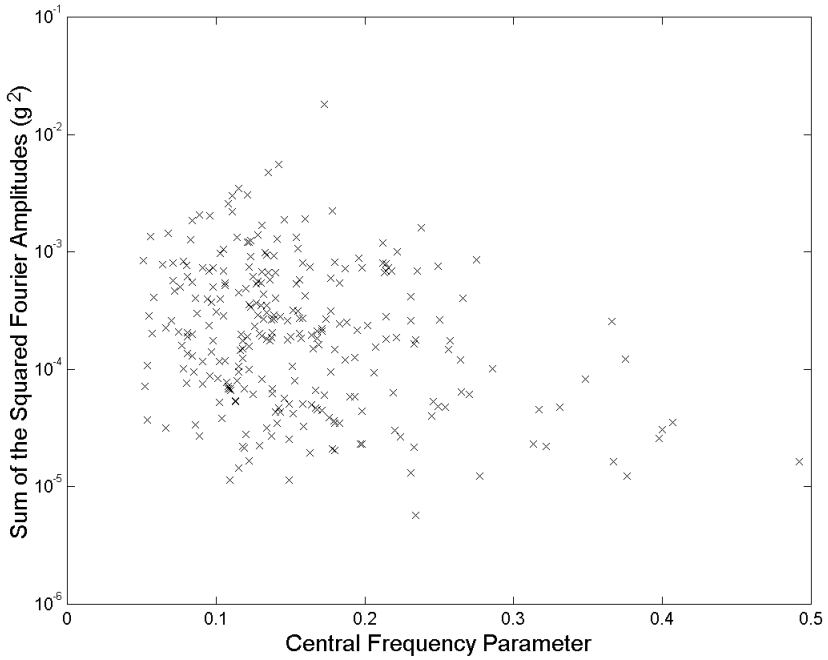

Figure 5.5: The energy parameter, E, as function of the central frequency parameter, M_F, for the California ground motion database.

5.3.1 The Energy Parameter

The results of a two step regression of the parameter E versus distance and magnitude using the entire California ground motion database are summarized in Figure 5.6. The model used in the first step is given by:

$$\ln(E) = \frac{c_1 + c_2 \cdot \exp\left(c_3 \cdot D^{c_4}\right)}{c_M(M_W)} \tag{5.15}$$

where D is the distance, and c_1, c_2, c_3, c_4, and $c_M(M_W)$ are regression coefficients. This functional form is chosen because it conforms to the observed pattern of the data points. The coefficients $c_M(M_W)$ are magnitude-dependent scaling factors. In the second step of the regression procedure, a linear model is fitted to the magnitude scaling factors:

$$c_M = q_1 + q_2 \cdot M_W \tag{5.16}$$

Here, q_1 and q_2 are regression coefficients, and M_W is the moment magnitude of the earthquake.

The distance dependence of the magnitude-scaled natural logarithm of the energy parameter is displayed in Figure 5.6(a). The equation of the regression curve is printed across the top of the figure. Due to energy dissipation and geometric spreading of the seismic waves, the energy content of the accelerograms decreases with distance. The rate of the energy attenuation decreases with increasing distance. The residuals from this regression are plotted in Figure 5.6(b) as function of distance. The residuals do not exhibit a distance dependence. The standard deviation of the residuals is reported in the lower right hand corner of Figure 5.6(b). A histogram of the standardized residuals is displayed in Figure 5.6(d). The coefficient of skewness, which is reported in Figure 5.6(d), is practically zero and the coefficient of kurtosis is close to 3. This implies that the residuals can be modeled by a normal distribution. The magnitude-dependent scaling factor is displayed in Figure 5.6(c). As can be seen, it increases with magnitude, confirming the general belief that the energy increases with earthquake magnitude.

The two-step regression was repeated for Site Class A&B, Site Class C, and Site Class D. The model parameters from these analyses are reported in Table 5.1, along with the parameters that were obtained using recordings from the entire data set. The parameter σ represents the standard error of the regression; it is the standard deviation of the residuals.

The results of the regression analyses that are summarized in Table 5.1 are displayed graphically in Figure 5.7. In Figure 5.7(a), the predicted magnitude-scaled natural logarithm of the energy parameter is plotted as a function of distance for different site classes. The thick, solid line in Figure 5.7(a) is the same as the solid line in Figure 5.6(a). For short distances, the energy parameter does not seem to depend on the site class, but the energy appears to attenuates faster with distance for the stiffer sites than the softer sites.

The magnitude dependency of the energy parameter is illustrated in Figure 5.7(b) for different site classes. The thick, solid line in Figure 5.7(b) is the same as the solid line in Figure 5.6(c). The scaling factor is most sensitive to the magnitude for Site Class A&B and it is least sensitive to the magnitude for Site Class D.

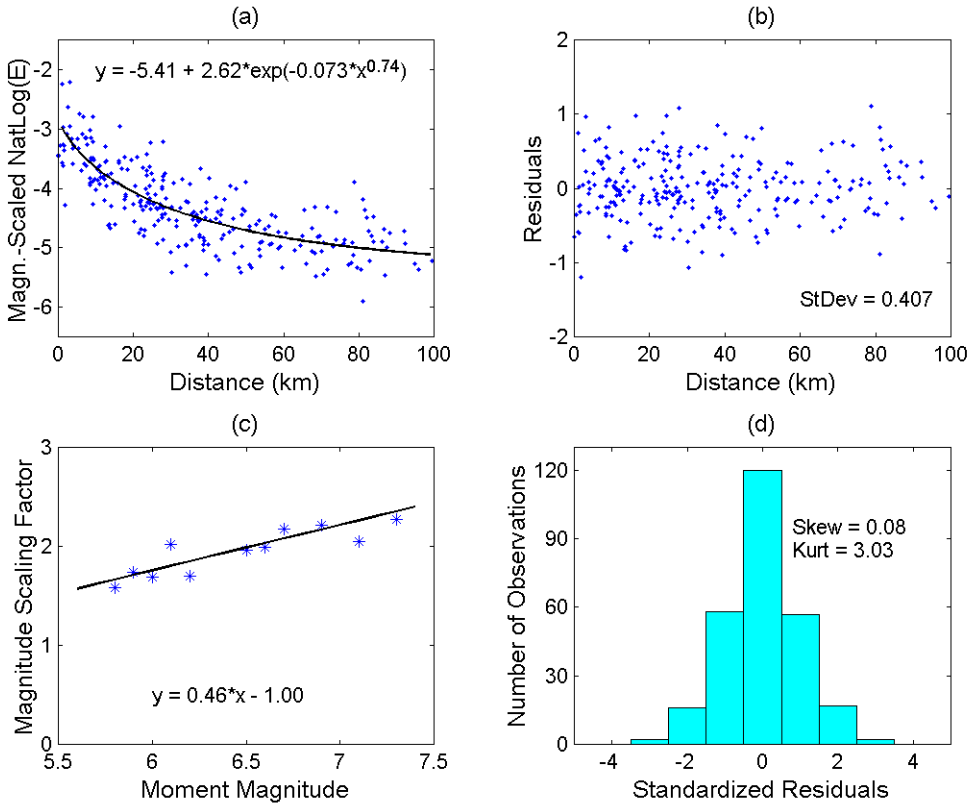

Figure 5.6: Results of a two step regression analysis for the energy parameter, *E*, for all sites. (a) The distance dependence of the magnitude-scaled natural logarithm of the energy parameter; (b) residuals from (a); (c) the magnitude dependent scaling factor; (d) histogram of the standardized residuals from (a).

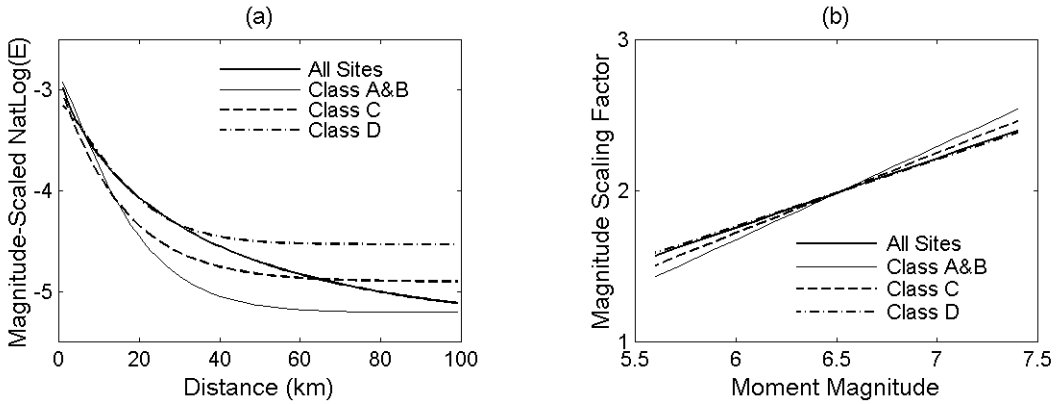

Figure 5.7: Results of a two-step regression analysis for the energy parameter, *E*, for different site classes. (a) The distance dependence of the magnitude-scaled natural logarithm; (b) the magnitude dependent scaling factor.

Table 5.1: Regression results for E (g^2).

Data Set	c_1	c_2	c_3	c_4	q_1	q_2	σ
All Sites	-5.41	2.62	-0.073	0.74	-1.00	0.460	0.407
Site Class A&B	-5.21	2.35	-0.028	1.24	-2.01	0.615	0.339
Site Class C	-4.90	1.97	-0.057	1.03	-1.47	0.532	0.436
Site Class D	-4.53	1.40	-0.019	1.36	-0.88	0.440	0.400

Model: $\ln(E) = \dfrac{c_1 + c_2 \cdot \exp\left(c_3 \cdot D^{c_4}\right)}{q_1 + q_2 \cdot M_W}$

5.3.2 The Central Frequency Parameter

The results of a two step regression analysis for the central frequency parameter, M_F, using the entire California ground motion data base, are displayed in Figure 5.8. It can be inferred from Figure 5.8(a) that the magnitude-scaled central frequency decreases very slightly with distance. High frequency ground motion tends to attenuate faster with distance than low frequency motion, causing the central frequency parameter to decrease with distance. The residuals from the regression in Figure 5.8(a) are plotted as function of distance in Figure 5.8(b). The residuals do not seem to depend on distance. A histogram of the standardized residuals is displayed in Figure 5.8(d). The residuals exhibit a positive skewness and the coefficient of kurtosis is 3.21. Therefore, the normal distribution might not be proper to model the residuals. The magnitude dependency of the central frequency parameter is indicated in Figure 5.8(c), where the magnitude dependent scaling factor is regressed versus moment magnitude. The central frequency tends to decrease with increasing magnitude. Larger earthquakes typically have larger rupture areas, implying longer source duration and, hence, lower frequency content. Therefore, the central frequency is expected to decrease with increasing magnitude.

The two-step regression was repeated for Site Class A&B, Site Class C, and Site Class D. The model parameters from these analyses are reported in Table 5.2, along with the parameters that were obtained using recordings from the entire data set. The parameter σ represents the standard deviation of the residuals from the regression.

The results of the regression analyses that are summarized in Table 5.2 are displayed graphically in Figure 5.9. In Figure 5.9(a), the magnitude-scaled natural logarithm of the central frequency parameter is plotted as a function of distance for different site classes. The thick, solid line in figure 5.9(a) is the same as the solid line in Figure 5.8(a). The central frequency parameter for Site Classes C and D are very similar, and considerably lower than the central frequency parameter for Site Class A&B. In addition, the central frequency parameter is consistently lower for Site Class D than for Site Class C. This is to be expected, because the natural frequency of softer soils is lower than the natural frequency of stiffer soils. It is also interesting to note that the central frequency parameter for Site Class A&B decreases more rapidly with distance than the central frequency parameter for either of the softer site classes, implying that the higher frequencies attenuate faster with distance than the lower frequencies.

The magnitude dependency of the natural logarithm of the central frequency parameter is illustrated in Figure 5.9(b) for different site classes. The thick, solid line in Figure 5.9(b) is the same as the solid line in Figure 5.8(c). The magnitude scaling factor for Site Class A&B is considerably more sensitive to the magnitude than the scaling factor for the other site classes.

Table 5.2: Regression results for M_F.

Data Set	c_1	c_2	q_1	q_2	σ
All Sites	-1.03	-0.0010	1.09	-0.082	0.227
Site Class A&B	-0.53	-0.0039	2.17	-0.248	0.297
Site Class C	-1.07	0.0002	1.10	-0.083	0.253
Site Class D	-1.12	-0.0019	0.80	-0.038	0.206

Model: $\ln(M_F) = \dfrac{c_1 + c_2 \cdot D}{q_1 + q_2 \cdot M_W}$

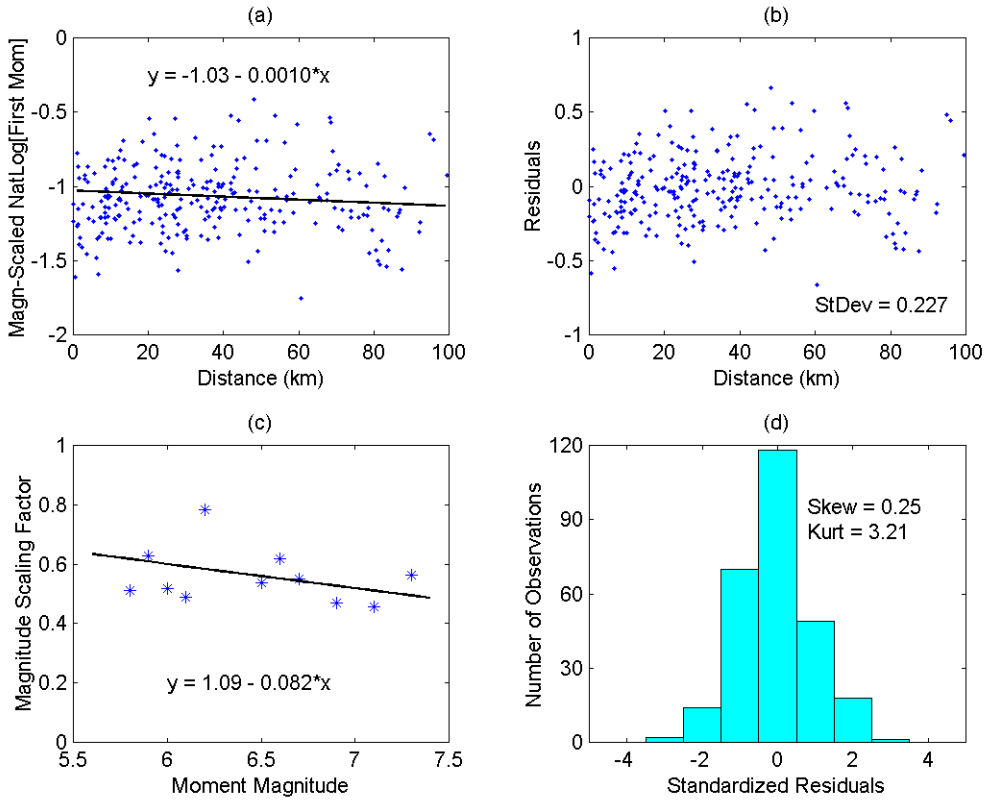

Figure 5.8: Results of a two step regression analysis for the central frequency parameter and all sites. (a) The distance dependence of the magnitude-scaled natural logarithm of the central frequency parameter; (b) residuals from (a); (c) the magnitude dependent scaling factor; (d) histogram of the standardized residuals from (a).

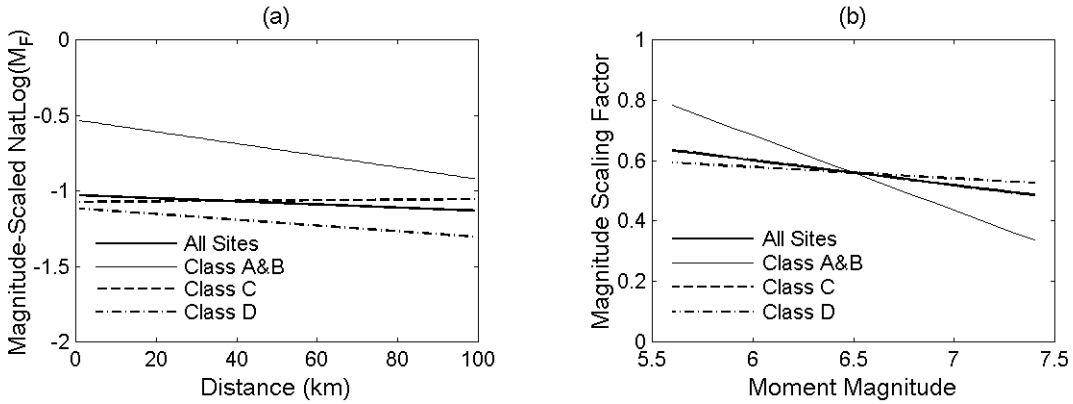

Figure 5.9: Results of a two-step regression analysis for the central frequency parameter for different site classes. (a) The distance dependence of the magnitude-scaled natural logarithm; (b) the magnitude dependent scaling factor.

5.3.3 The Spectral Bandwidth Parameter

A linear regression is performed on the spectral bandwidth parameter versus the central frequency parameter in natural logarithm space. The results of this regression, using the California ground motion data base, are summarized in Figure 5.10. In Figure 5.10(a), the regression line is superimposed on the observed data points. The results of the regression are transformed into linear space in Figure 5.10(c). The residuals of the linear regression in Figure 5.10(a) are plotted versus the independent parameter in Figure 5.10(b). No particular trend is observed. A histogram of the standardized residuals is shown in Figure 5.10(d). The residuals exhibit slight negative skewness. The coefficient of kurtosis for the residuals is 3.81, considerably larger than the value of 3 for a normally distributed random variable.

The linear regression was repeated for Site Class A&B, Site Class C, and Site Class D. The model parameters from these analyses are reported in Table 5.3, along with the parameters that were obtained using recordings from the entire data set. The parameter σ represents the standard deviation of the residuals from the regression.

The results of the regression analyses that are summarized in Table 5.3 are displayed graphically in Figure 5.11. In Figure 5.11(a), the relationships are presented in logarithmic space, and in Figure 5.11(b) they are in linear space. The thick, solid lines in Figure 5.11 are the same as the solid lines in Figure 5.10. It is apparent from Figure 5.11, that the relationship between the spectral bandwidth parameter, V_F, and the central frequency parameter, M_F, is practically the same for Site Class A&B as it is for Site Class C. These relationships are, in turn, very similar to the relationship between V_F and M_F that were obtained using the entire ground motion data set. Therefore, it is recommended to use the results from Table 5.3 pertaining to "All Sites" for all sites except for the softest sites, Site Class D. The relationship between V_F and M_F for Site Class D seems to be significantly different from all the other V_F - M_F relationships.

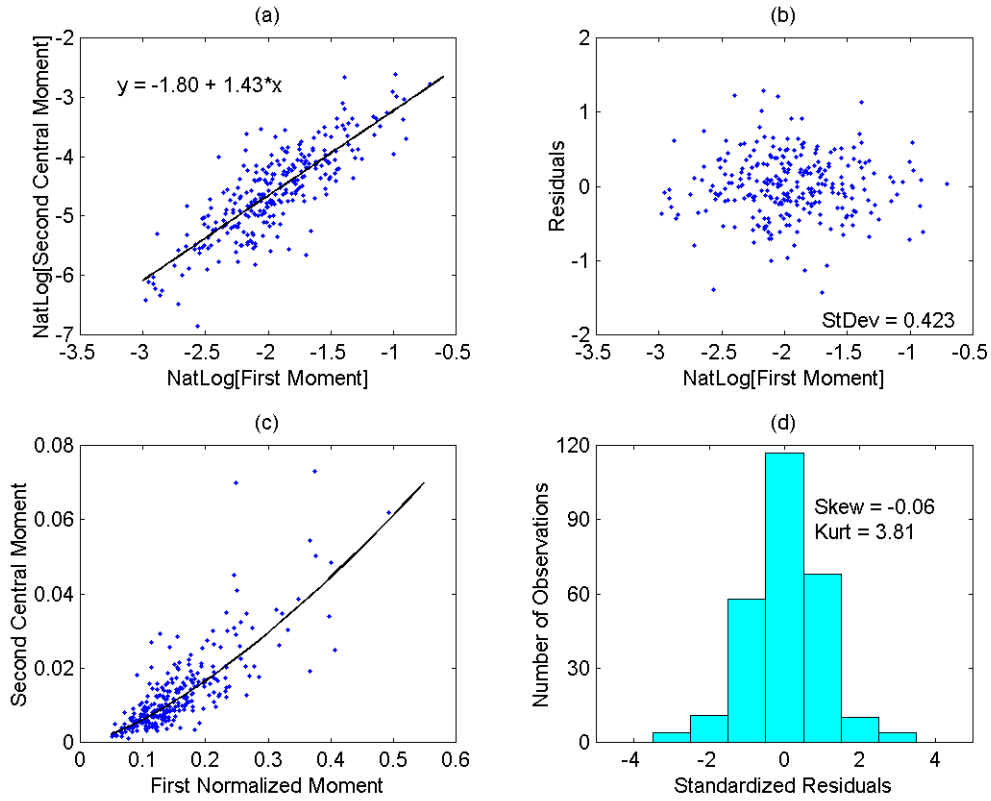

Figure 5.10: Results of a linear regression of the spectral bandwidth parameter versus the central frequency parameter for all sites. (a) The linear regression in natural logarithm space; (b) the residuals from the regression in (a); (c) the regression in (a) transformed into linear space; (d) histogram of the standardized residuals from (a).

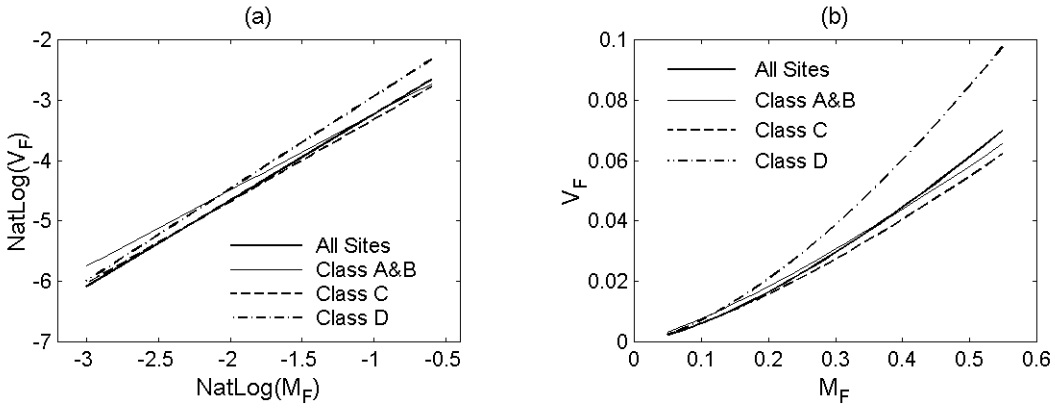

Figure 5.11: Results of a linear regression of the spectral bandwidth parameter versus the central frequency parameter for different site classes. (a) Logarithmic space; (b) linear space.

Table 5.3: Regression results for V_F.

Data Set	c_1	c_2	σ
All Sites	-1.80	1.43	0.423
Site Class A&B	-1.97	1.26	0.399
Site Class C	-1.96	1.36	0.350
Site Class D	-1.41	1.53	0.405

Model: $\ln(V_F) = c_1 + c_2 \cdot \ln(M_F)$

5.3.4 Examples of Predicted Fourier Amplitude Spectra

The effects of magnitude, distance, and site conditions on the Fourier amplitude spectra are illustrated in Figure 5.12. The spectra in Figure 5.12 are evaluated using the prediction formulas for the model parameters that are presented in the previous subsections.

The two spectra in Figure 5.12(a) are for a relatively close-by (source to site distance of 10 km) rock site (Site Class A&B), but two earthquakes of different moment magnitudes; 6 and 7. The area under the curve corresponding to the larger earthquake is larger than the area under the curve corresponding to the smaller event, indicating higher intensity of the ground motion. The larger event has considerably greater low-frequency content than the smaller event. The higher intensity and greater low-frequency content of the larger earthquake as compared to the smaller event can be attributed to a bigger rupture area.

The effects of distance on the predicted Fourier amplitude spectra can be inferred from a comparison of the two dashed curves in Figure 5.12. In Figures 5.12(a) and 5.12(b), the dashed line represents the spectrum at a rock site due to a magnitude 7 earthquake. In Figure 5.12(a), the source to site distance is 10 km, while the distance is 60 km in Figure 5.12(b). In addition to a lesser energy at the larger distance as compared to the shorter distance, the central frequency and the spectral bandwidth are also lower at the larger distance than at the smaller distance. This difference in the shape of the spectra is due to the faster attenuation with distance of the high-frequency ground motion than the low-frequency ground motion.

The effects of site conditions on the Fourier amplitude spectra are shown in Figure 5.12(b). The dashed line represents the spectrum at a site corresponding to Site Class A&B (rock site), while the dash-dot line is the Fourier amplitude spectrum at a site corresponding to Site Class D (sandy soils and stiff clays; Borcherdt, 1994). Both spectra in Figure 5.12(b) are due to a magnitude 7 earthquake and for a source to site distance equal to 60 km. The energy (and hence, the intensity) of the ground motion at the softer site (Site Class D) is larger than the energy at the stiffer site. In addition, the central frequency and the spectral bandwidth are lower at the softer site than at the stiffer site. The differences between the spectra in Figure 5.12(b) are consistent with observations made by other researchers (e.g., Seed et al., 1976; Borcherdt, 1994), that soft soils tend to filter out the high-frequency motion and sometimes to magnify the motion at a certain (relatively low) frequency.

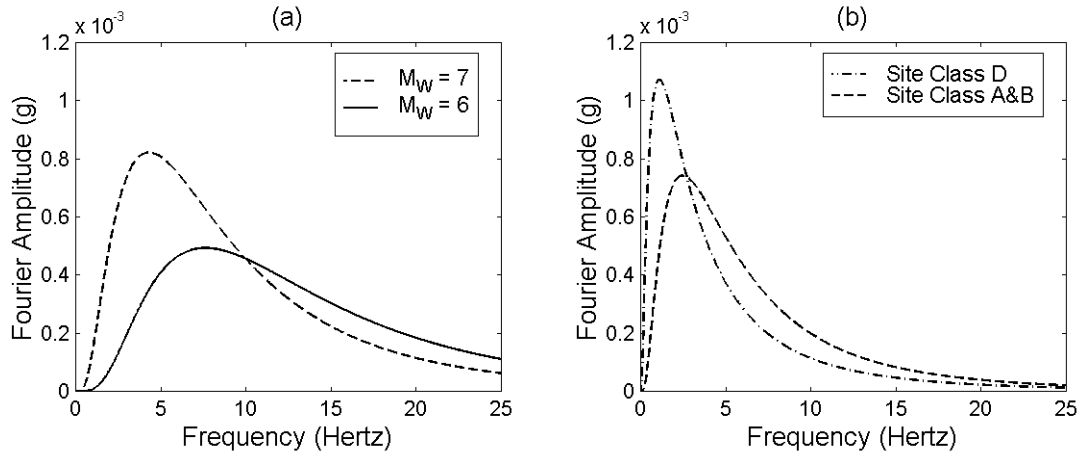

Figure 5.12: Examples of predicted Fourier amplitude spectra. (a) Spectra for earthquakes of moment magnitude 7 (dashed line) and 6 (solid line), for Site Class A&B and 10 km distance; (b) spectra for Site Class D (dash-dot line) and Site Class A&B, for an earthquake of moment magnitude 7 and a source to site distance of 60 km.

5.4 Summary of Amplitude Models

Two existing Fourier amplitude models, which can be used together with the Fourier phase difference models presented in the previous chapters, were reviewed in this chapter: the radiated source spectrum and the filtered Kanai-Tajimi power spectral density.

The radiated source spectrum model is very comprehensive. However, there are many parameters to be evaluated, and different source spectra and radiation patterns have to be used for each type of seismic waves. Furthermore, some of these parameters may be earthquake-specific. Therefore, the radiated source spectrum is not very well suited for predicting the earthquake ground motion from future events.

In order to use the filtered Kanai-Tajimi power spectral density, it is necessary to quantify five parameters. These include the intensity of the underlying white noise process, the characteristic frequency and damping ratio of the ground, and the two low-cut filter parameters. This model is significantly simpler to use than the radiated source spectrum. In this study, however, it was decided to propose a still simpler model for the Fourier amplitude spectrum; a model that easily lends itself to regression analyses for ground motion prediction purposes.

The alternative Fourier amplitude model proposed in this chapter is based on the lognormal probability density function. Only three parameters are needed to specify the Fourier amplitude spectrum: (1) the amplitude scaling factor, representing the total energy of the accelerogram, and (2) the scale and (3) the shape parameter of the lognormal probability density function, reflecting the central frequency and the bandwidth of the accelerogram, respectively.

The California ground motion database described in Chapter 2 is used to develop prediction formulas for the Fourier amplitude parameters E, M_F and V_F. The results of the regression analyses are summarized below. The parameter D is the shortest distance from the site to the surface projection of the seismogenic rupture in kilometers, and M_W is the moment magnitude of the earthquake.

The energy parameter is the sum of the squared Fourier amplitudes of an accelerogram that is digitized at a sampling frequency of 50 Hertz with a total duration of 40.98 seconds (2048 sample points). Its unit of measurement is g^2, where g is the acceleration of gravity at the surface of the Earth. The energy parameter is determined from the source to site distance and the moment magnitude of the earthquake. For an unknown site class, the energy parameter can be estimated according to:

$$\ln(E) = \frac{-5.41 + 2.62 \cdot \exp\left(-0.073 \cdot D^{0.74}\right)}{0.460 \cdot M_W - 1.00}; \quad D \le 100\,\text{km},\ 5.8 \le M_W \le 7.3$$

For Site Class A&B, the energy parameter can be calculated using:

$$\ln(E) = \frac{-5.21 + 2.35 \cdot \exp\left(-0.028 \cdot D^{1.24}\right)}{0.615 \cdot M_W - 2.01}; \quad D \le 100\,\text{km},\ 5.8 \le M_W \le 7.3$$

For Site Class C, the energy parameter is given by:

$$\ln(E) = \frac{-4.90 + 1.97 \cdot \exp\left(-0.057 \cdot D^{1.03}\right)}{0.532 \cdot M_W - 1.47}; \quad D \le 100\,\text{km},\ 5.8 \le M_W \le 7.3$$

For Site Class D, the energy parameter can be computed using:

$$\ln(E) = \frac{-4.53 + 1.40 \cdot \exp\left(-0.019 \cdot D^{1.36}\right)}{0.440 \cdot M_W - 0.88}; \quad D \le 100\,\text{km},\ 5.8 \le M_W \le 7.3$$

The central frequency parameter is determined from the source to site distance and the earthquake magnitude. For an unknown site class, it can be estimated according to:

$$\ln(M_F) = \frac{-1.03 - 0.0010 \cdot D}{1.09 - 0.082 \cdot M_W}; \quad D \le 100\,\text{km},\ 5.8 \le M_W \le 7.3$$

For Site Class A&B, the central frequency parameter can be calculated using:

$$\ln(M_F) = \frac{-0.53 - 0.0039 \cdot D}{2.17 - 0.248 \cdot M_W}; \quad D \le 100 \text{ km}, \ 5.8 \le M_W \le 7.3$$

For Site Class C, the central frequency parameter is given by:

$$\ln(M_F) = \frac{-1.07 + 0.0002 \cdot D}{1.10 - 0.083 \cdot M_W}; \quad D \le 100 \text{ km}, \ 5.8 \le M_W \le 7.3$$

For Site Class D, the central frequency parameter can be computed using:

$$\ln(M_F) = \frac{-1.12 - 0.0019 \cdot D}{0.80 - 0.038 \cdot M_W}; \quad D \le 100 \text{ km}, \ 5.8 \le M_W \le 7.3$$

The spectral bandwidth parameter is derived from the central frequency parameter. For Site Class D, the spectral bandwidth parameter can be estimated using:

$$\ln(V_F) = 1.53 \cdot \ln(M_F) - 1.41$$

For all other site classes than Site Class D (including unknown site classification), the spectral bandwidth parameter is given by:

$$\ln(V_F) = 1.43 \cdot \ln(M_F) - 1.80$$

CHAPTER 6
SPATIAL INTERPOLATION OF GROUND MOTION

Reliable information on earthquake ground motion at the location of a damaged structure is necessary in order to investigate the causes of damage, and to correlate ground motion to building damage. It is, however, very unlikely that a recording will be available for all sites of interest. Hence, there is a need to obtain estimates of earthquake ground motion through interpolation of earthquake accelerograms acquired from ground motion recording stations.

The previous chapters dealt with the generation of earthquake ground motion at individual sites. The time histories at different points were assumed to be independent of each other, which is sufficient for the design or analysis of ordinary structures that are small as compared to the wavelength of the propagating seismic waves. However, when dealing with large structures, such as long-span bridges, pipelines and dams, the spatial correlation of earthquake ground motion has to be taken into account. Whether the two suspension towers of the Golden Gate bridge move in phase or out of phase, for instance, has great effect on the response and the loading of the bridge.

In this chapter, a simple model for the spatial interpolation of earthquake ground motion is developed. Data from the SMART-1 accelerometer array in Taiwan are used to assess the accuracy of this model. The quantities being interpolated are the frequency characteristics of the digital earthquake accelerograms, i.e. the Fourier amplitudes and phase angles. This is motivated by the results of Chapters 3 and 4, which show the importance of preserving phase information (more precisely, phase differences) to simulate accelerograms at an individual site.

6.1 Problem Statement and Basic Assumptions

Imagine the following scenario: An estimate is sought of the acceleration time history at the site marked by the letter C in Figure 6.1. The distance between the epicenter and the site is δ_C. No recordings were obtained at the site. However, there are recordings available from adjacent recording stations; P_k. The epicentral distance of station P_k is δ_k. The distance between the site, C, and recording station P_k is d_k.

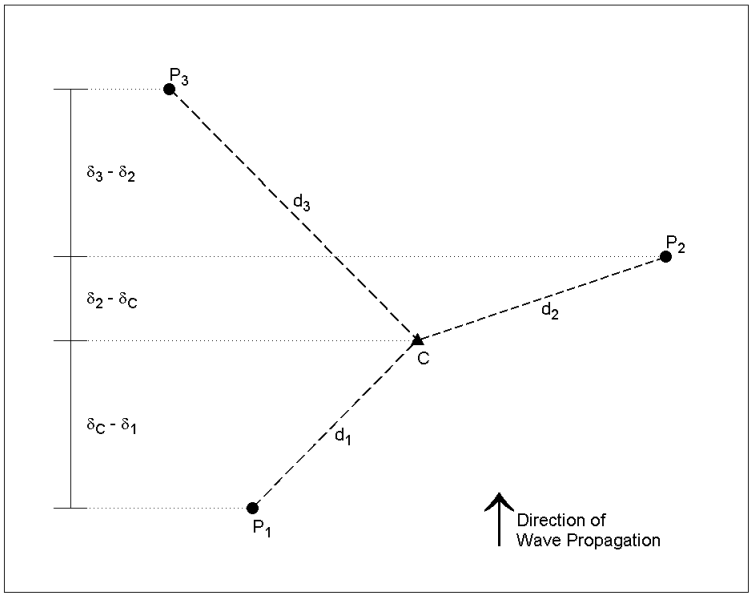

Figure 6.1: Schematic representation of the spatial interpolation problem. C marks the site where the time history is sought; P_k are recording stations.

The Fourier amplitude of the n-th discrete frequency component at recording station P_k is denoted by $A_k(\omega_n)$ and the Fourier phase angle of the same frequency component is denoted by $\Phi_k(\omega_n)$. When predicting the Fourier components $A_{C,k}(\omega_n)$ and $\Phi_{C,k}(\omega_n)$ at the site, C, from the corresponding components at recording station P_k, the following two basic assumptions are made.

- There is negligible energy attenuation or amplification, i.e. the Fourier amplitudes at the site are equal to the amplitudes at the recording station:

$$A_{C,k}(\omega_n) = A_k(\omega_n) \tag{6.1}$$

- Each frequency component propagates radially from the epicenter with a constant apparent phase velocity, $v(\omega_n)$. Hence, the Fourier phase angle can be predicted according to the simple dispersion relationship:

$$\Phi_{C,k}(\omega_n) = \Phi_k(\omega_n) - \frac{(\delta_C - \delta_k)\cdot \omega_n}{v(\omega_n)} \tag{6.2}$$

There are considerable difficulties in determining the apparent phase velocity a priori since it depends on many factors, such as the type of wave (P-wave, S-wave, Rayleigh, Love …), the properties of the medium, and the inclination of the wave ray with respect to horizontal. However, several methods exist to estimate the apparent phase velocity using available recordings; for example the Aligned Motion Method (Harichandran and Vanmarcke, 1984), the Cross Correlation Method (Loh, 1985; Oliviera, 1985), and the Frequency-Wave Number Method (Abrahamson and Bolt, 1987). In the analyses on the data from the SMART-1 array performed in this study, estimates of apparent wave velocity reported by Hao (1989) are used. These estimates were obtained using the Frequency-Wave Number Method.

Equations (6.1) and (6.2) do not generally yield the same predictions at the site for all recording stations. Therefore, the different predictions have to be combined in a "best estimate" of some sort, using spatial interpolation. The remainder of this chapter documents the search for that best estimate. Before going any further, however, the data used to assess the accuracy of the interpolation model are introduced.

6.2 Data and Data Processing

Recordings of earthquake accelerograms from closely spaced recording stations are rare. In this study, data from the SMART-1 array near Lotung in northeastern Taiwan are used to validate the ground motion interpolation model. In this section, the geometry of the array is described, as well as the data selection and data processing.

6.2.1 The SMART-1 Array

The deployment of the SMART-1 accelerograph array is described by Bolt et al. (1982), Abrahamson (1985), and Niazi (1990). The array consists of 39 tri-axial accelerographs (see Figure 6.2); one central station, C-00, three concentric circles each containing 12 equally spaced stations, and two external stations, E-01 and E-02. The three circles are named I (for Inner), M (for Middle), and O (for Outer). The stations in the circles are numbered consequently from 01 to 12, starting from north counting clockwise. The nominal radius of the inner circle is 200 meters, the radius of the middle circle is 1000 meters, and the radius of the outer circle is 2000 meters. The external stations are located approximately 3 and 5 kilometers south of the central station. The geometry of the array is illustrated in Figure 6.2 and a table with the coordinates and elevation of all the stations is in Appendix E. The topography is very flat. The elevation of all but three stations is between 2 and 10 meters. The lowest elevation is 2.4 m and the highest elevation is 18.1 meters.

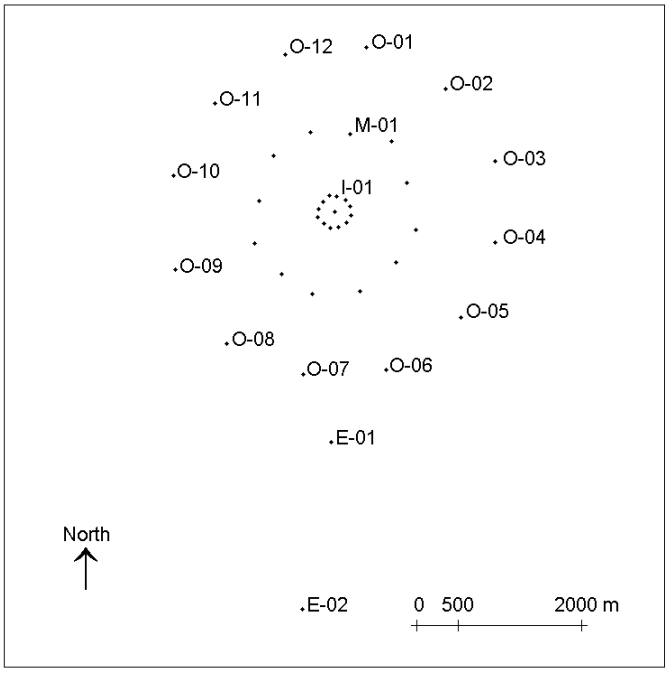

Figure 6.2: The geometry of the SMART-1 accelerometer array in Lotung, Taiwan.

The SMART-1 array is located in an alluvial plain, where the ground water table is at or near the ground surface. All stations except station E-02, which is located on a rock outcrop, are on soil. The depth of the soil column ranges from 170 meters in the southern end of the outer circle to 600 meters at the northern edge of the array. The estimated shear wave velocities in the uppermost 31 meters are given in Table 6.1.

Table 6.1: Shear wave velocity profile at the SMART-1 array site (Hao, 1989).

Depth (m)	0 – 5	5 – 8	8 – 13	13 – 31
V_S (m/s)	120	140	190	220

According to the shear wave velocity profile in Table 6.1, a shear wave would travel from a depth of 30 meters up to the surface in 0.167 seconds, which implies an average shear wave velocity of 180 m/s. According to the NEHRP site classification, the site of the SMART-1 array would be on the border between classes D and E (see Table 2.2), i.e. on the border between *Soil* and *Soft Soil*. A more detailed description of the geology can be found in Bolt et al. (1982) and Abrahamson (1985).

6.2.2 Data

Uncorrected digitized data from the SMART-1 array were obtained from the Earthquake Strong Motion CD-ROM collection published by the National Oceanic and Atmospheric Administration of the United States Department of Commerce (NOAA, 1996). The records were processed the same way as the California data, as described in Chapter 2.

The ground motion records were selected based on the following four criteria:

(1) Earthquake surface wave magnitude of at least 5.5.
(2) Uncorrected horizontal peak ground acceleration of at least 0.05 g.
(3) Epicentral distance between 10 and 100 kilometers.
(4) Focal depth less than 20 km.

The first two criteria are based on the assumption that smaller earthquakes and weaker ground motion do not pose a significant hazard to most structures. The third and fourth

criteria are meant to reduce the effects of vertically propagating seismic waves. The selection criteria enumerated above yielded records from four events, which are summarized in Table 6.2.

Table 6.2: Events recorded by the SMART-1 array that are used in this study.

Event No.	Date	M_S	Lat (°N)	Long (°E)	Depth (km)	Dist† (km)	Type*
5	29-Jan-1981	5.7	24.43	121.90	11.1	30	R
33	12-Jun-1985	5.8	24.57	122.19	3.3	45	O-N
39	16-Jan-1986	5.8	24.76	121.96	10.2	22	N
45	14-Nov-1986	7.8	23.99	121.83	13.9	77	R

† The distance is calculated between the center of the array and the epicenter of the earthquake.
* R represents reverse-slip, N is normal-slip, and O-N stands for oblique-normal-slip.

The information in Table 6.2 is taken from Niazi (1990), except for the surface wave magnitudes, which are from Abrahamson et al. (1987).

6.2.3 Geometric Interpolation Schemes

Based on the geometry of the SMART-1 array, three basic geometric interpolation schemes are defined: using station pairs, triangles, and circles to evaluate the quantity of interest (i.e. the Fourier transform of an acceleration time history) at the site of concern. The different geometric schemes are designed to examine the effect of the number of known points on the quality of the interpolation, as well as the effect of the layout and the spacing of stations on the quality. The quality of interpolation is measured in terms of the standard error, i.e. the standard deviation of the difference between the interpolated and the observed values.

The first geometric interpolation scheme involves using a pair of diametrically opposite stations to estimate the quantity of interest at the central station, C-00. All three stations are on a (nominally) straight line. The stations can be of equal distance from the central station, e.g. I-04 and I-10, or of different distance, e.g. I-04 and M-10. Two basic cases are examined: (i) the propagation-parallel case, where the line connecting the stations is parallel to the direction of seismic wave propagation, and (ii) the propagation-

perpendicular case, where the line connecting the stations is perpendicular to the direction of wave propagation.

Two different triangular interpolation schemes are defined from the geometry of the SMART-1 array. The first one is to define a nominally equilateral triangle from three stations in the same circle, and use the values at the corners to estimate the value of interest at the central station. An example of an inner circle equilateral triangle is shown in Figure 6.3. The distance from the known stations to the unknown one is 200 meters, and the sides of the triangle are 340 meters long. Stations from the Middle and Outer circles can also be used to form equilateral triangles, similar to the one shown in Figure 6.3.

Another triangulation possibility is to create an isosceles triangle, using the central station and two stations from the middle circle, as shown in Figure 6.4. The triangle in this figure can be used to estimate the value at station I-01 in the inner circle. The sides of this triangle are 1000 meters and 890 meters long, and the distance between the corner points and the interior point is 200 meters and 880 meters.

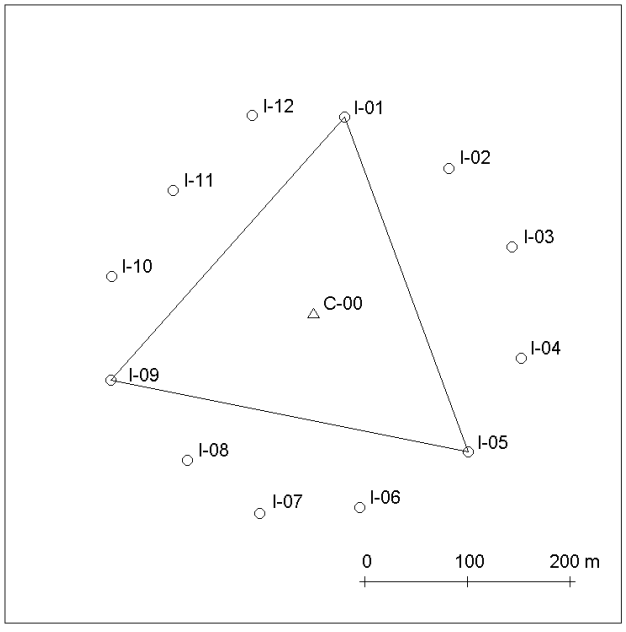

Figure 6.3: Equilateral inner circle triangle to predict values at the central station.

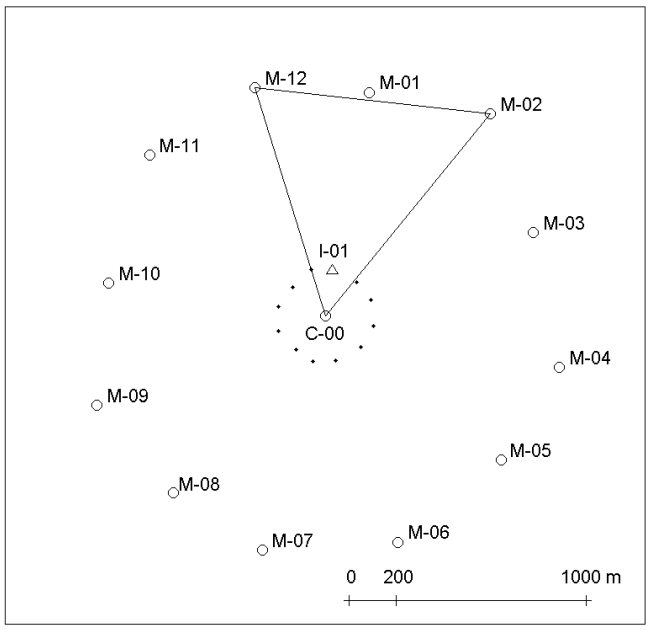

Figure 6.4: Isosceles triangle to predict values at the inner circle stations.

The third basic geometric interpolation scheme is to use all the stations in a given circle (inner, middle, or outer) to estimate the values at the central station.

In the following section, these geometric interpolation schemes are used to spatially interpolate the Fourier transform of digital accelerograms.

6.3 Interpolation of Discrete Fourier Transforms

Interpolation involves evaluating the weighted average of observed quantities. The discrete Fourier transform is a complex function, which can either be characterized by its real and imaginary parts, or its amplitude and phase angle. Hence, two questions arise: (i) how to assign the weights, and (ii) which quantities to interpolate.

It is common in spatial interpolation to define the weights to be inversely proportional to the distance between points, raised to a certain power. In this study, the weights are assigned inversely proportional to the squared distance between the station where the quantity is known and the site where the quantity is to be estimated. By taking

the weights to be inversely proportional to the distance squared rather than the distance itself, relatively more weight is given to close points.

The two methods most commonly used in averaging complex numbers are illustrated in Figure 6.5, where the average of the complex numbers $Z_1 = (-1+2i)$ and $Z_2 = (-1-4i)$ is sought. In Figure 6.5(a), the real and the imaginary parts are averaged separately, i.e.

$$\begin{aligned} \mathrm{Re}(CM) &= \frac{1}{N}\sum_{k=1}^{N}\mathrm{Re}(Z_k) \\ \mathrm{Im}(CM) &= \frac{1}{N}\sum_{k=1}^{N}\mathrm{Im}(Z_k) \end{aligned} \tag{6.3}$$

whereas the geometric mean is evaluated in Figure 6.5(b):

$$GM = \left[\prod_{k=1}^{N} Z_k\right]^{1/N} \tag{6.4}$$

Each averaging method has one obvious shortcoming. The amplitude of *CM* is much smaller than the amplitude of either Z_1 or Z_2, which can lead to a considerable underestimation of the total energy content of an interpolated accelerogram if this is the case for many frequency components. The amplitude of the geometric mean of N complex numbers is the N-th root of the product of the individual amplitudes. However, the phase angle of the geometric mean is not uniquely determined; there are N possible solutions (hence the two possible answers, GM_1 and GM_2, in Figure 6.5(b)). In this particular example, it could be argued that GM_2 should be chosen rather than GM_1, because the former has a negative real part, as do the numbers that are being averaged. However, this argument does not scale easily; it is not straightforward to design and implement a method to select the best candidate out of ten, for example, where the ten complex numbers being averaged are scattered over the complex plane.

In the following subsection, different methods for averaging complex numbers - as applied to the discrete Fourier transform of earthquake accelerograms - are discussed.

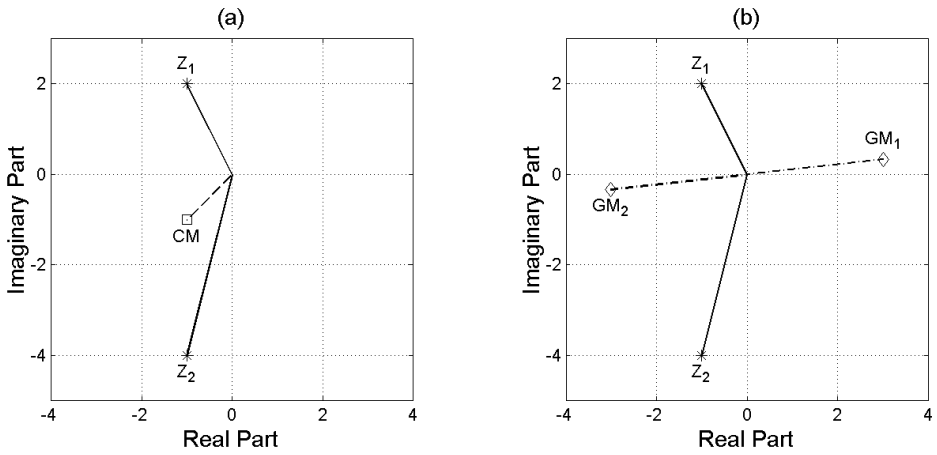

Figure 6.5: Averaging the complex numbers Z_1 and Z_2. (a) The real and the imaginary parts averaged separately; (b) the geometric mean.

6.3.1 Methods for Averaging Complex Numbers

As mentioned above, there are two basic methods for averaging complex numbers: (i) averaging the real and the imaginary parts separately, and (ii) evaluating the geometric mean. In this subsection, data from the SMART-1 array in Taiwan are used to estimate the quality of these methods, as well as to propose a third and improved method for the spatial interpolation of earthquake accelerograms in the frequency domain. The quality of the different averaging methods is assessed by comparing the results of interpolations, obtained using all the inner circle stations, to the accelerogram recorded at the central station, C-00. All the numerical results presented in this subsection are for the north-south component of Event 45 in Table 6.2.

In Figure 6.6, the recorded accelerogram is compared to an interpolated accelerogram obtained by averaging the real and the imaginary parts separately. The interpolated accelerogram looks like it has been passed through a low-pass filter, thus removing the high-frequency energy. The lesser high-frequency content of the interpolated time history as compared to the recorded one is obvious in Figure 6.7, where the Fourier amplitude spectra of the two time histories are shown. The energy of the interpolated accelerogram is lower, especially for the higher frequencies. Thus confirming the doubts expressed in the discussion of Figure 6.5 regarding the applicability of this method in averaging the discrete Fourier transforms of earthquake

accelerograms. However, as can be seen in Figure 6.8, averaging the real and imaginary parts separately yields good estimates of the Fourier phase angles (and hence phase differences). This agreement is particularly good at the relatively low frequencies (up to 10 Hz) where most of the accelerogram's energy is located.

It is clear from Figures 6.6 and 6.7 that averaging the real and imaginary parts separately can vastly underestimate the total energy in the earthquake accelerogram, especially the high-frequency content (i.e. above 1 Hertz). However, as can be seen from Figure 6.8, this averaging method gives very reasonable estimates of the Fourier phase angle spectrum. Therefore, it is decided to use this averaging method to infer the Fourier phase angles, while searching for another method to interpolate the Fourier amplitudes; a method that better preserves the energy content.

The interpolated accelerogram in Figure 6.9 is obtained by evaluating the geometric mean of the Fourier amplitudes of all the inner circle stations, while the Fourier phase angles are inferred from the averages of the real and imaginary parts, evaluated separately. The comparison with the recorded accelerogram is much better than observed in Figure 6.6. However, by comparing the Fourier amplitude spectra in Figure 6.10, some energy deficiency is apparent, which becomes evident in Figure 6.11 where the cumulative normalized Arias intensities are plotted as functions of time. It can be seen in Figure 6.11 that the total energy of the interpolated accelerogram is only approximately 70% of the total energy of the recorded accelerogram. Hence, evaluating the geometric mean Fourier amplitude does not preserve the energy sufficiently well.

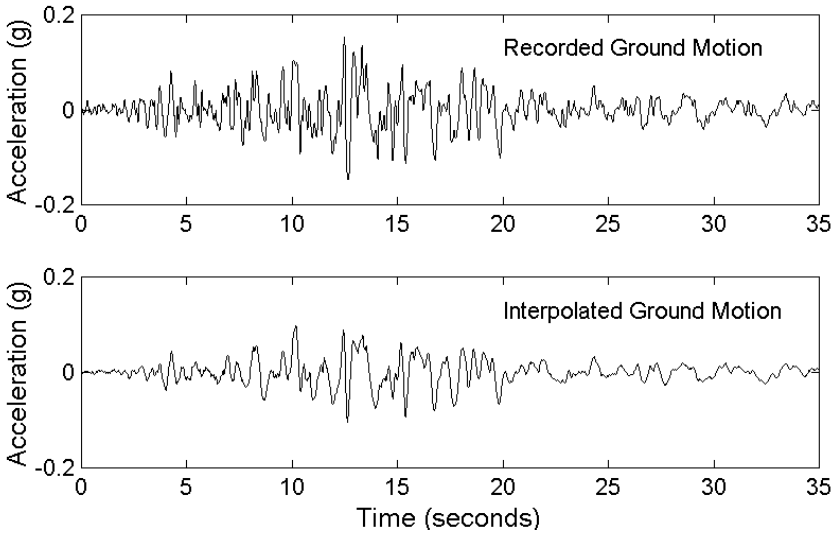

Figure 6.6: The recorded acceleration time history at station C-00 (top) and the interpolated time history (bottom) using all the recording stations of the inner circle, obtained by averaging the real and imaginary parts of the DFT's separately.

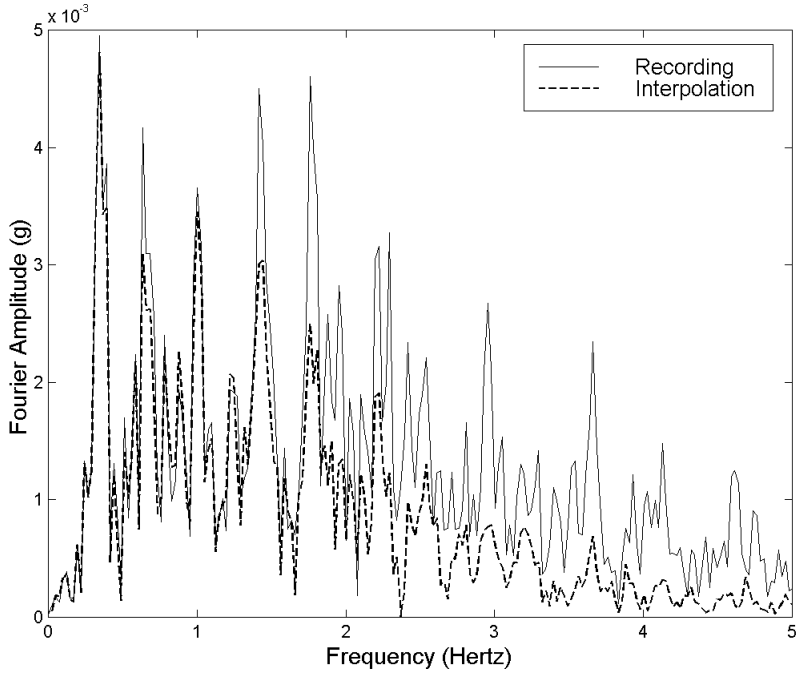

Figure 6.7: The recorded Fourier amplitude spectrum at C-00 (solid line) compared to the spectrum of the interpolated time history (dashed line) using all the recording stations of the inner circle, obtained by averaging the real and the imaginary parts of the DFT's separately.

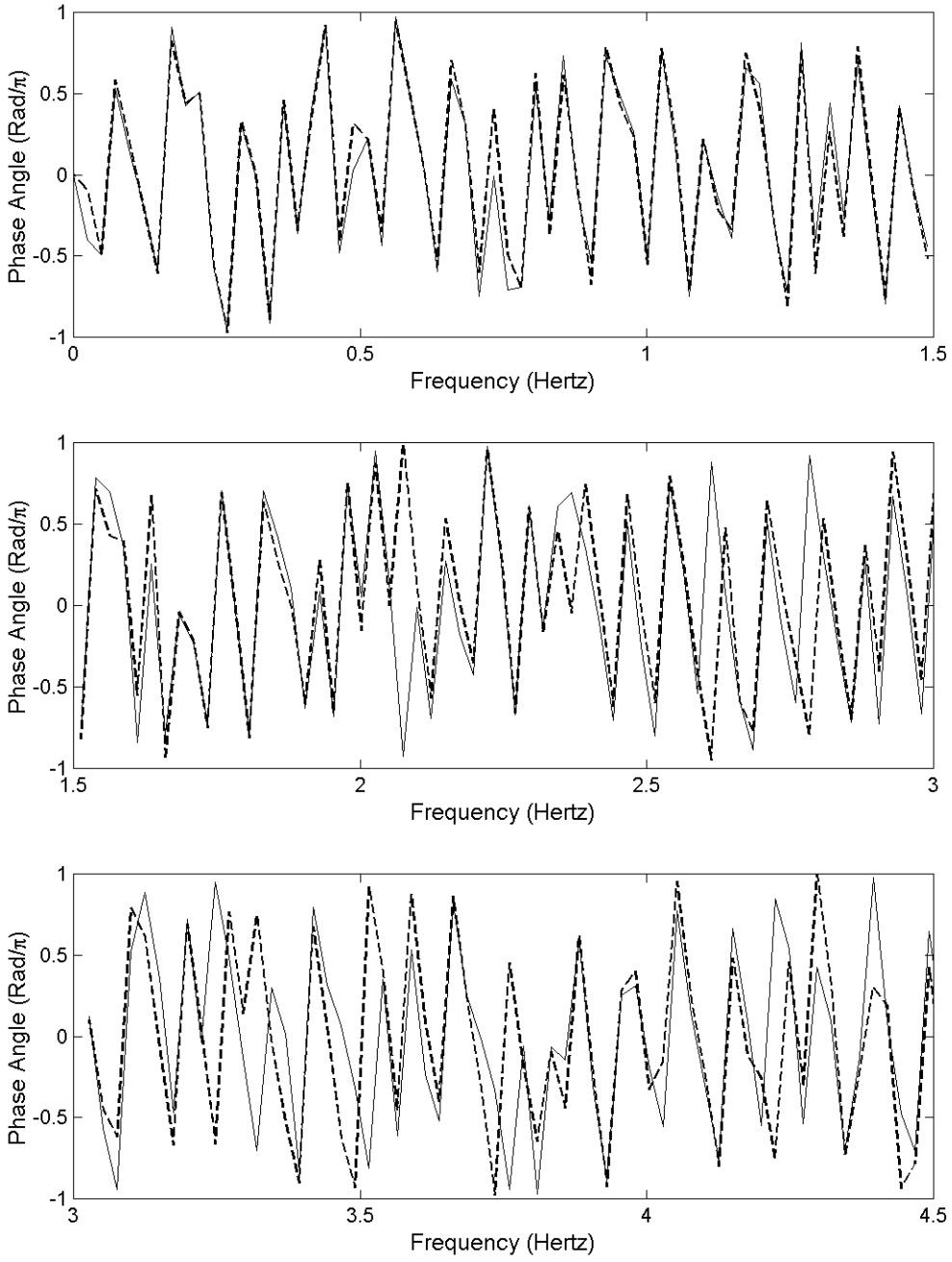

Figure 6.8: The recorded Fourier phase angle spectrum at C-00 (solid line) compared to the phase angle spectrum of the interpolated time history (dashed line) using all the recording stations of the inner circle, obtained by averaging the real and the imaginary parts of the DFT's separately.

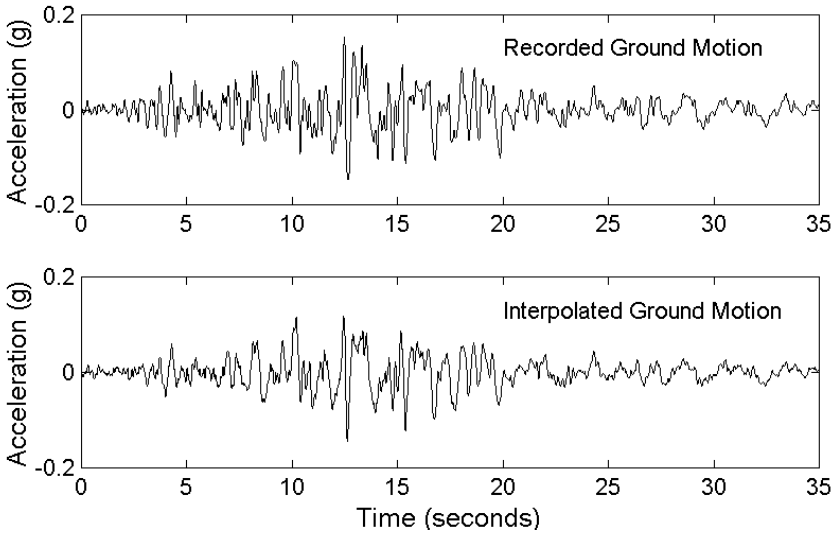

Figure 6.9: The recorded acceleration time history at station C-00 (top) and the interpolated time history (bottom) using all the recording stations of the inner circle, obtained by evaluating the geometric mean of the Fourier amplitudes, but inferring the Fourier phase angles from averaging the real and imaginary parts separately.

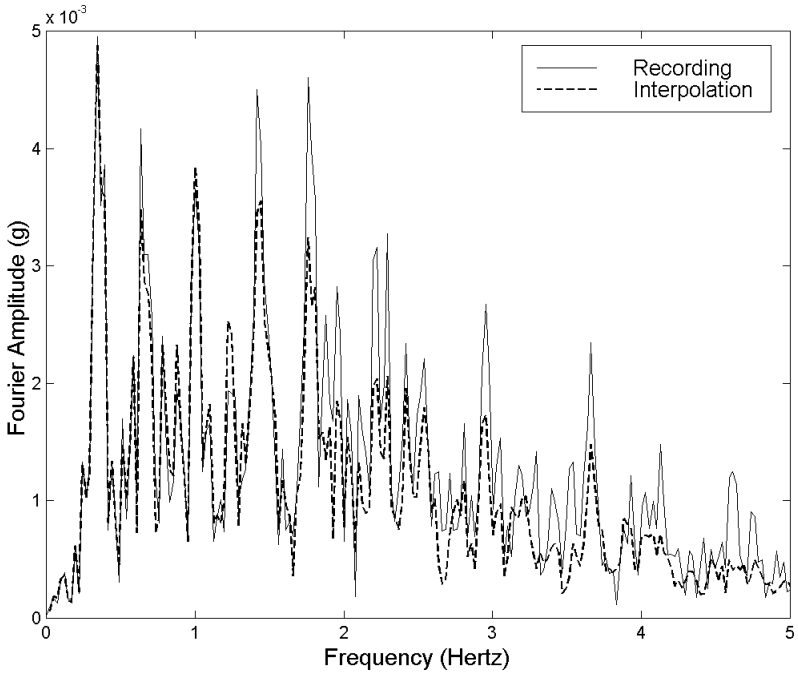

Figure 6.10: The recorded Fourier amplitude spectrum at C-00 (solid line) compared to the interpolated spectrum (dashed line) using all the recording stations of the inner circle, obtained by evaluating the geometric mean.

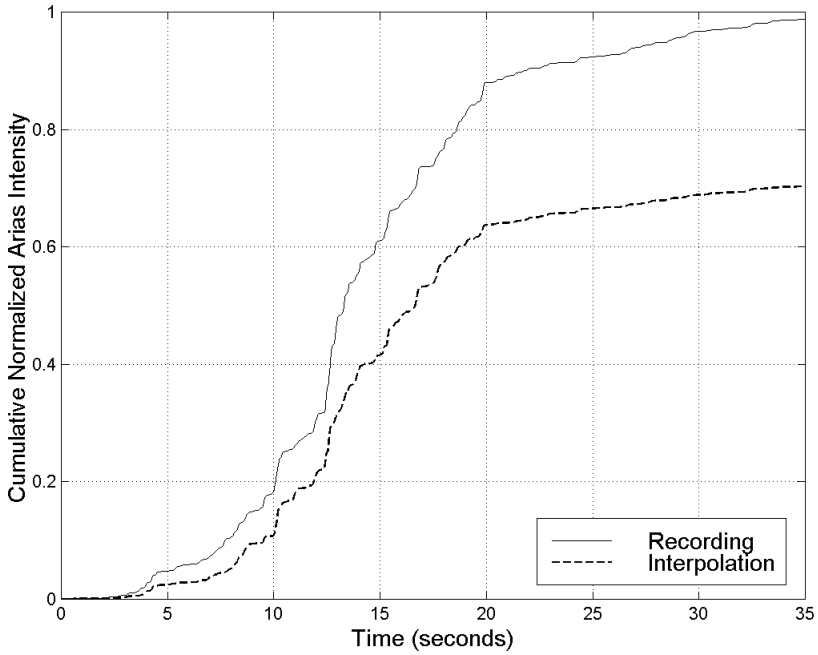

Figure 6.11: The cumulative normalized Arias intensity of the recording at C-00 (solid line) compared to the cumulative normalized Arias intensity of the interpolated time history (dashed line) in Figure 6.9. The cumulative intensities are normalized w.r.t. the Arias intensity of the recorded accelerogram.

If the goal is to preserve the average energy of the recorded accelerograms in the spatial interpolation, the squared Fourier amplitudes should be averaged. It is, therefore, proposed here to average the squared Fourier amplitudes. The geometric average of the Fourier amplitudes is never larger than the arithmetic average, which, in turn, is never larger than the square root of the average of the squared amplitudes.

In Figure 6.12, the interpolated accelerogram is compared to the recorded accelerogram. The interpolation is obtained by evaluating the average of the squared Fourier amplitudes of all the recording stations in the inner circle, while the phase angles are inferred from the averages of the real and imaginary parts, evaluated separately. The comparison of the time histories seems good. The Fourier amplitude spectra and the cumulative normalized Arias intensities of the two time histories are shown in Figures 6.13 and 6.14, respectively. There is still some energy deficiency apparent in the interpolation. The Arias intensity of the interpolated time history is only approximately 85% of the Arias intensity of the recorded time history. However, this deficiency is due

to the fact that the Arias intensity of the recordings made at the inner circle stations is on the average 15% lower than the intensity of the recording made at the center.

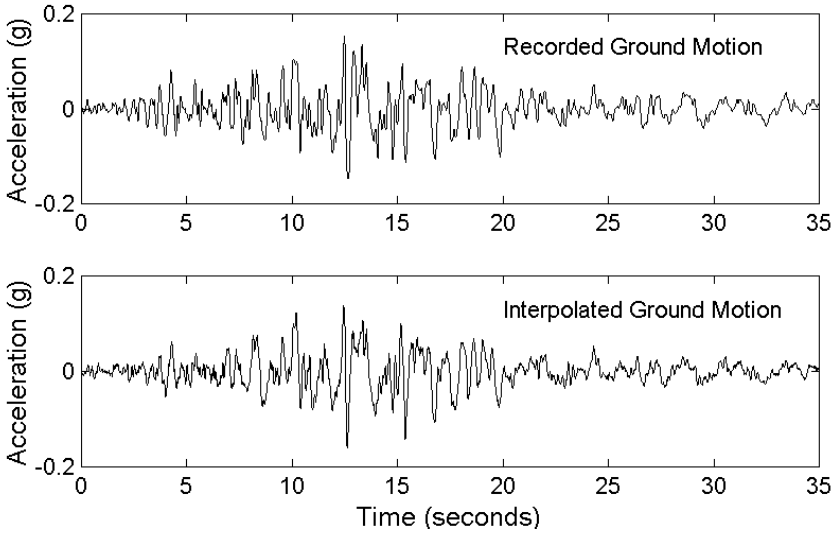

Figure 6.12: The recorded acceleration time history at station C-00 (top) and the interpolated time history (bottom) using all the recording stations of the inner circle, obtained by averaging the squared Fourier amplitudes, but inferring the Fourier phase angles from averaging the real and imaginary parts separately.

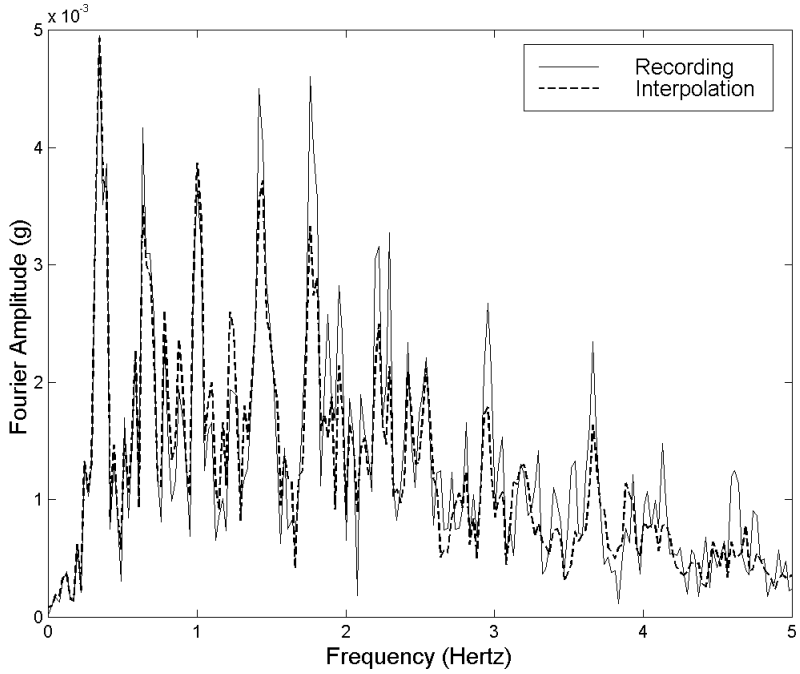

Figure 6.13: The recorded Fourier amplitude spectrum at C-00 (solid line) compared to the interpolated spectrum (dashed line) using all the recording stations of the inner circle, obtained by averaging the squared Fourier amplitudes.

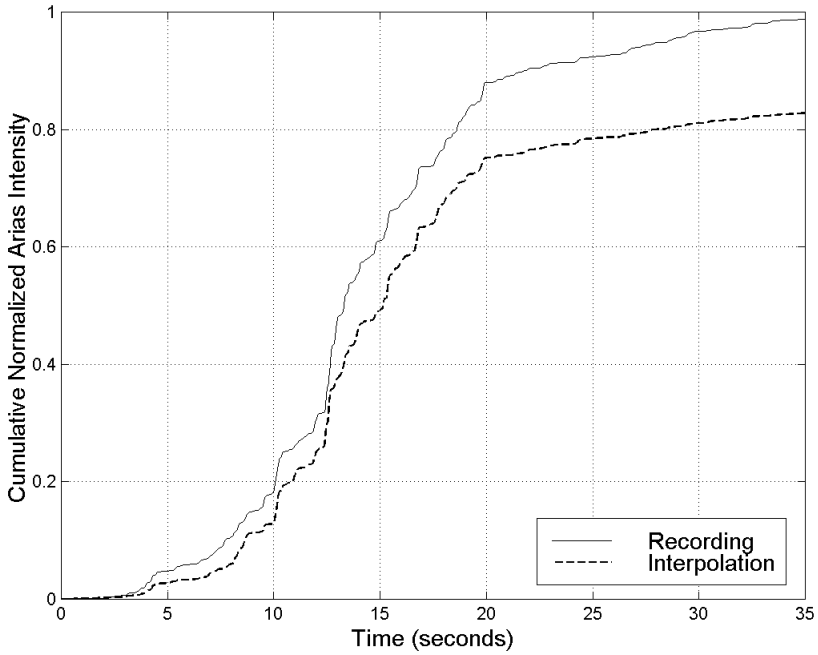

Figure 6.14: The cumulative normalized Arias intensity of the recording at C-00 (solid line) compared to the cumulative normalized Arias intensity of the interpolated time history (dashed line) in Figure 6.12. The cumulative intensities are normalized w.r.t. the Arias intensity of the recorded accelerogram.

In summary, the following recommendations are made regarding the averaging of the complex discrete Fourier transform of earthquake acceleration time histories:

- In order to preserve the average energy of the recorded accelerograms, the squared Fourier amplitudes should be averaged.
- The Fourier phase angles should be inferred from the average real part and the average imaginary part.

The results from these recommendations are compared, schematically, to the two conventional complex number averaging methods in Figure 6.15.

Examples of the interpolation of Fourier amplitudes and phase angles for recorded ground motions are given in the following subsections, where the proposed averaging method is used for the geometric interpolation schemes introduced in subsection 6.2.3.

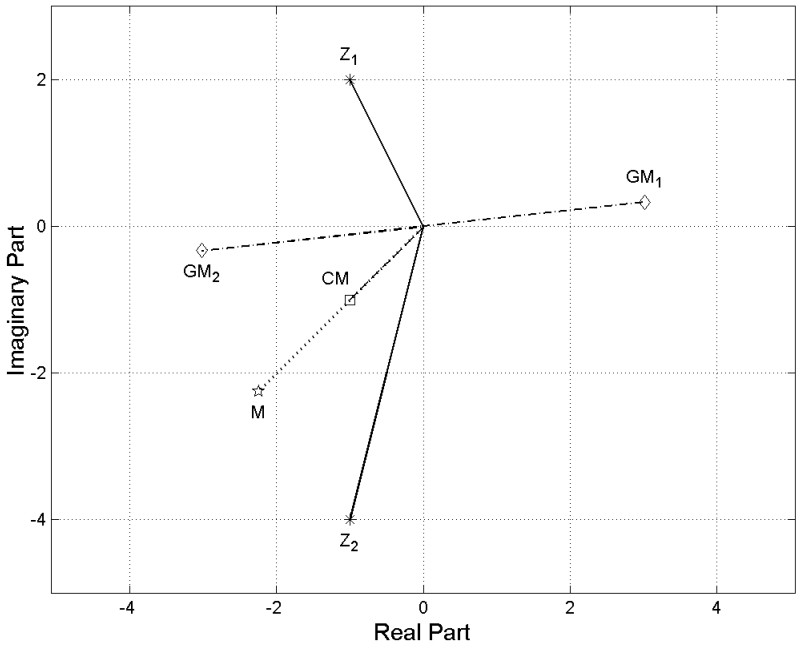

Figure 6.15: Averaging the complex numbers Z_1 and Z_2. The results of the proposed method, *M*, compared to results obtained by averaging the real and the imaginary parts separately, *CM*, and by evaluating the geometric mean, GM_1 or GM_2.

6.3.2 Interpolation of Fourier Amplitudes

For a given discrete frequency component, the interpolated Fourier amplitude at the site, C, is evaluated as the square root of the weighted average of the squared amplitudes at the recording stations. The relative weight for each station is inversely proportional to the squared distance between the station and the site.

$$\hat{A}_C(\omega_n) = \sqrt{\frac{1}{\sum_k w_k} \sum_k w_k \cdot A_{C,k}^2(\omega_n)} = \sqrt{\frac{1}{\sum_k w_k} \sum_k w_k \cdot A_k^2(\omega_n)} \qquad (6.5)$$

$$w_k = \frac{1}{d_k^2}$$

In Equation (6.5), $\hat{A}_C(\omega_n)$ is the interpolated Fourier amplitude corresponding to the n-th discrete frequency, ω_n, at the site; $A_{C,k}(\omega_n)$ is the Fourier amplitude at C as predicted

from recording station *k*, which is equal to the recorded Fourier amplitude at station *k*, $A_k(\omega_n)$, according to the assumption in Equation (6.1); w_k is the weight assigned to recording station *k* for prediction at the site; and d_k is the distance between the site and station *k*. In the simplest case of equally distant recording stations, the weights are all equal and Equation (6.5) yields simply the square root of the average of the squared amplitudes, as discussed previously.

In Figures 6.16 through 6.24, results from the amplitude interpolation model in Equation (6.5) are compared to recordings made at the central station of the SMART-1 array. First, results from two-point interpolations are presented, followed by interpolations using triangles and circles. The results presented here are all from Event 45, the largest event ever recorded by the SMART-1 array, but similar results were obtained for all the other events listed in Table 6.2.

Two-Point Interpolation

In Figures 6.16 through 6.18, the recorded Fourier amplitude spectrum at station C-00 is compared to the estimated spectrum at C-00, using two-point interpolation. The interpolation in Figure 6.16 is obtained using a pair of inner circle stations, while the interpolations in Figures 6.17 and 6.18 are obtained using a pair of middle circle stations and outer circle stations, respectively. The interpolated Fourier amplitude spectrum obtained using a pair of inner circle stations, where the station spacing is 200 meters, compares well with the recorded amplitude spectrum; the standard error of the interpolated amplitudes is $1.45 \cdot 10^{-4}$ g. As may be expected, the frequency-by-frequency comparison is not as good for the middle and outer circle interpolations as for the inner circle interpolation. The standard error of the interpolated amplitudes is $2.44 \cdot 10^{-4}$ g for the middle circle interpolation, and the standard error is $2.84 \cdot 10^{-4}$ g for the outer circle interpolation. In general, there is not much difference in quality between middle and outer circle interpolations, while the quality of the inner circle interpolations is approximately twice as good as the quality of either the middle or the outer circle interpolations. However, even though the interpolated spectra in Figures 6.17 and 6.18 do not compare exactly to the recorded spectrum on a frequency by frequency basis, their gross characteristics (i.e. the total energy, central frequency and bandwidth) are similar.

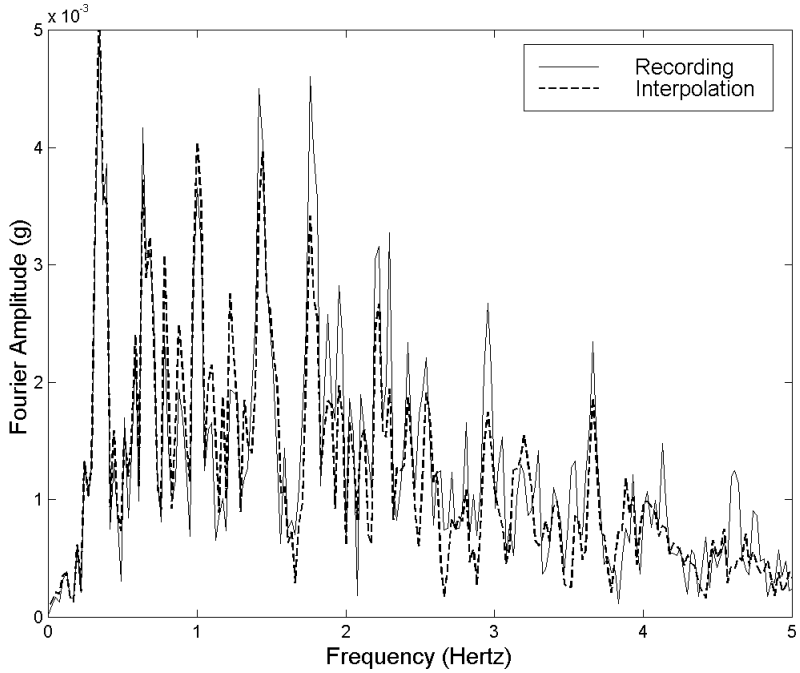

Figure 6.16: The recorded Fourier amplitude spectrum at station C-00 (solid line) compared to the interpolated spectrum (dashed line) using the station pair (I-03,I-09).

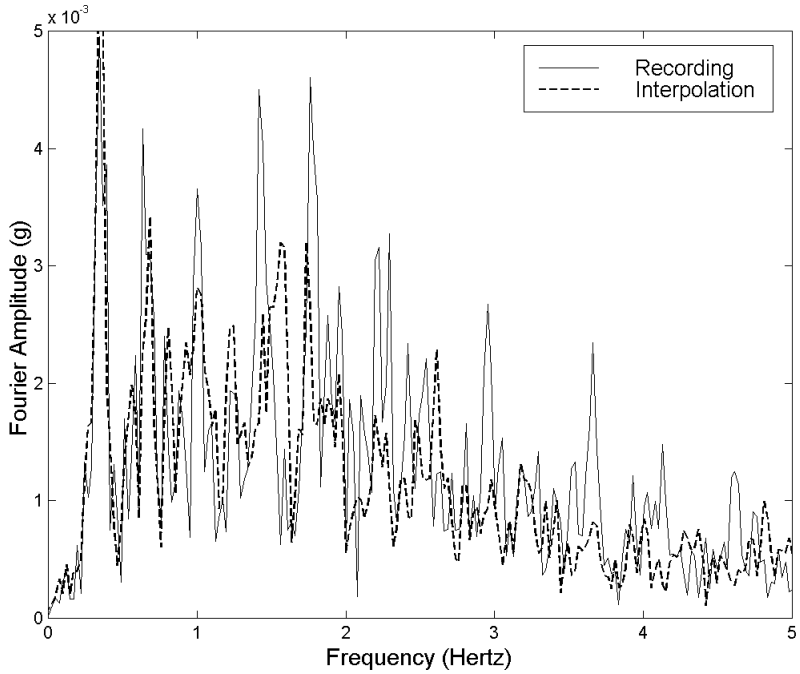

Figure 6.17: The recorded Fourier amplitude spectrum at station C-00 (solid line) compared to the interpolated spectrum (dashed line) using the station pair (M-03,M-09).

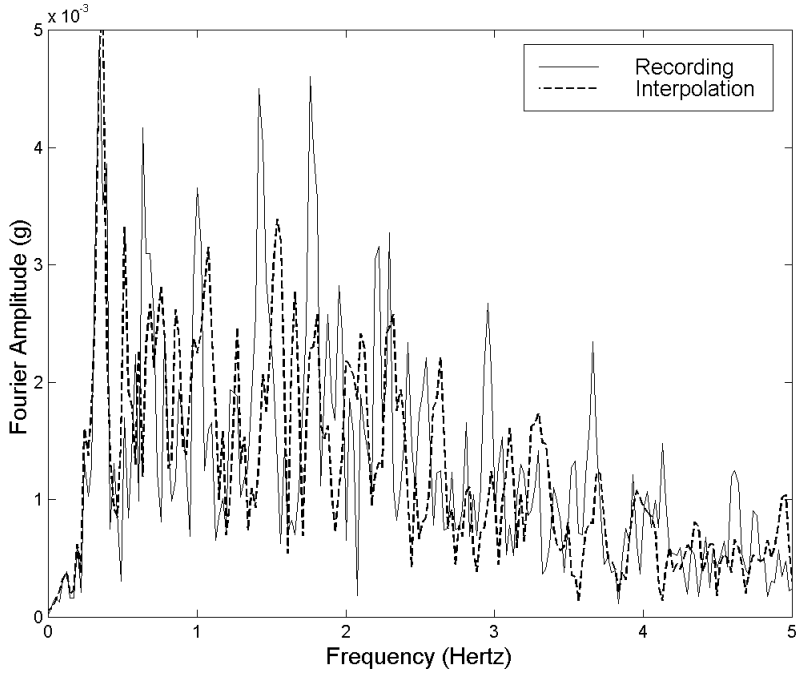

Figure 6.18: The recorded Fourier amplitude spectrum at station C-00 (solid line) compared to the interpolated spectrum (dashed line) using the station pair (O-03,O-09).

Three-Point Interpolation

In Figures 6.19 through 6.21, the recorded Fourier amplitude spectrum at station C-00 is compared to the estimated spectrum at C-00, using triangular interpolation. The interpolation results shown in Figure 6.19 are for an equilateral, inner circle triangle, the example in Figure 6.20 is for an equilateral middle circle triangle, and in Figure 6.21, the interpolation results using an equilateral outer circle triangle are presented. The standard error of the interpolated amplitudes is $1.39 \cdot 10^{-4}$ g for the inner circle triangle, $2.66 \cdot 10^{-4}$ g for the middle circle triangle, and $2.67 \cdot 10^{-4}$ g for the outer circle triangle. In general, the quality of the triangular interpolation is slightly, but not significantly, better than the quality of the two-point interpolations. Note in fact that in this particular case, the quality of the three-point interpolation for the middle circle stations is a little worse than the quality of the two-point interpolation. As in the two-point case, the gross characteristics are reproduced by a coarse triangular interpolation (from middle or outer circle stations), while the inner circle stations produce approximately twice the quality, on a frequency by frequency basis.

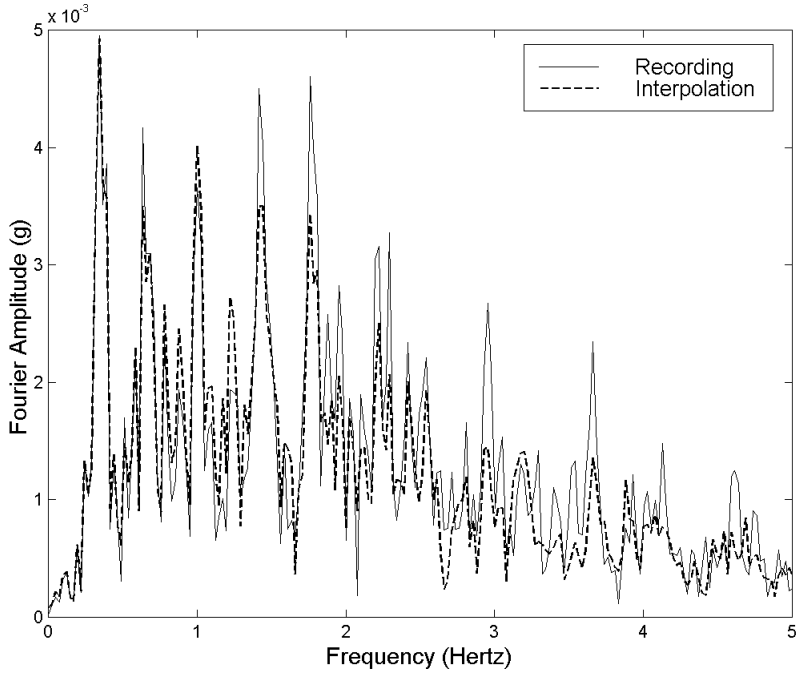

Figure 6.19: The recorded Fourier amplitude spectrum at station C-00 (solid line) compared to the interpolated spectrum (dashed line) using the triangle (I-03,I-07,I-11).

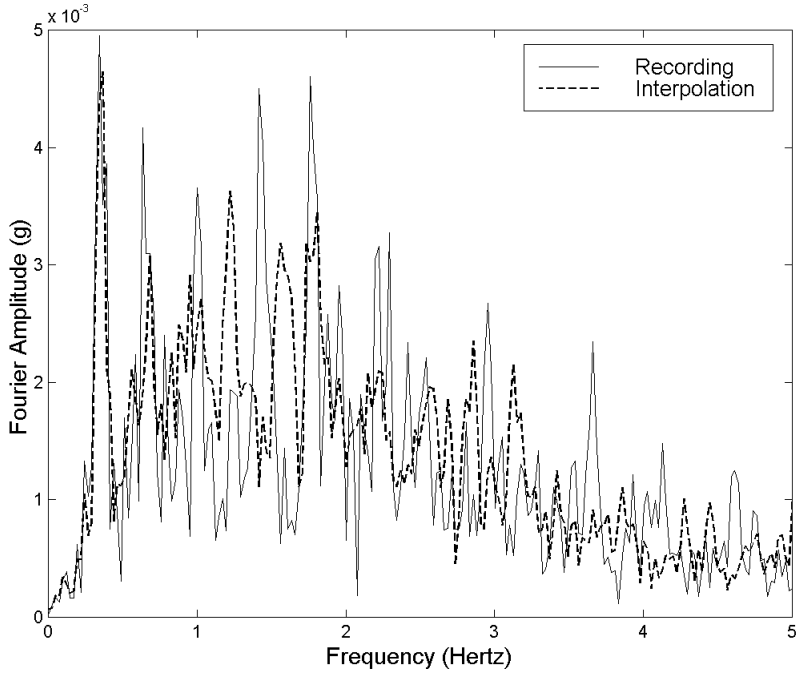

Figure 6.20: The recorded Fourier amplitude spectrum at station C-00 (solid line) compared to the interpolated spectrum (dashed line) using the triangle (M-03,M-07,M-11).

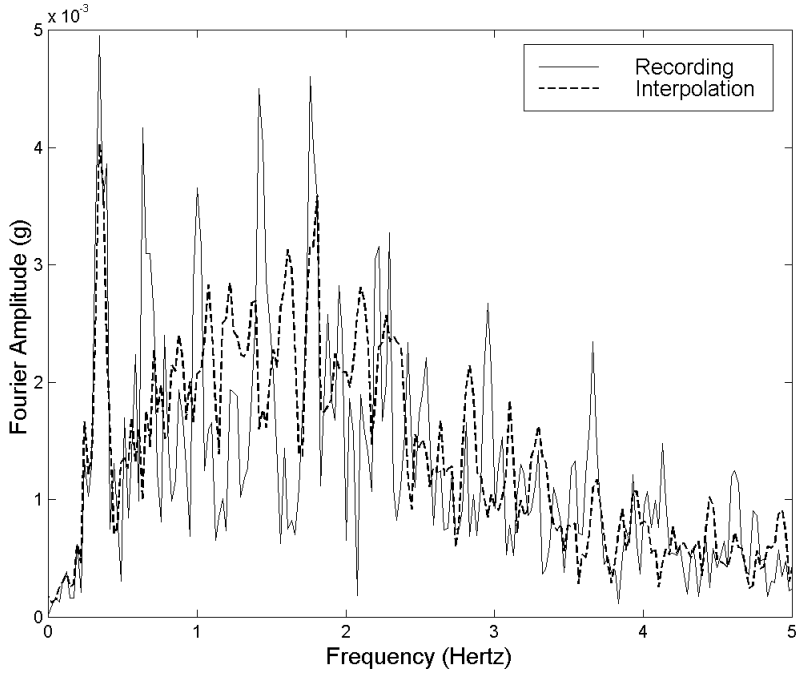

Figure 6.21: The recorded Fourier amplitude spectrum at station C-00 (solid line) compared to the interpolated spectrum (dashed line) using the triangle (O-03,O-07,O-11).

Interpolation using all the Stations in a given Circle

In Figures 6.22 through 6.24, the recorded Fourier amplitude spectrum at station C-00 is compared to the interpolated spectrum at C-00, using recordings from all twelve stations in a given circle. The interpolation results shown in Figure 6.22 are from the inner circle, the example in Figure 6.23 is from the middle circle, and in Figure 6.24, the interpolation results using all the stations of the outer circle are presented. The standard error of the interpolated amplitudes is $1.27 \cdot 10^{-4}$ g for the inner circle, $2.25 \cdot 10^{-4}$ g for the middle circle, and $2.44 \cdot 10^{-4}$ g for the outer circle. In general, the quality of the twelve-point interpolation is slightly better than the quality of the two-point and three-point interpolations. As observed in the two- and three-point interpolations, the quality of the inner circle interpolation is almost twice as good as the quality of the middle and outer circle interpolations.

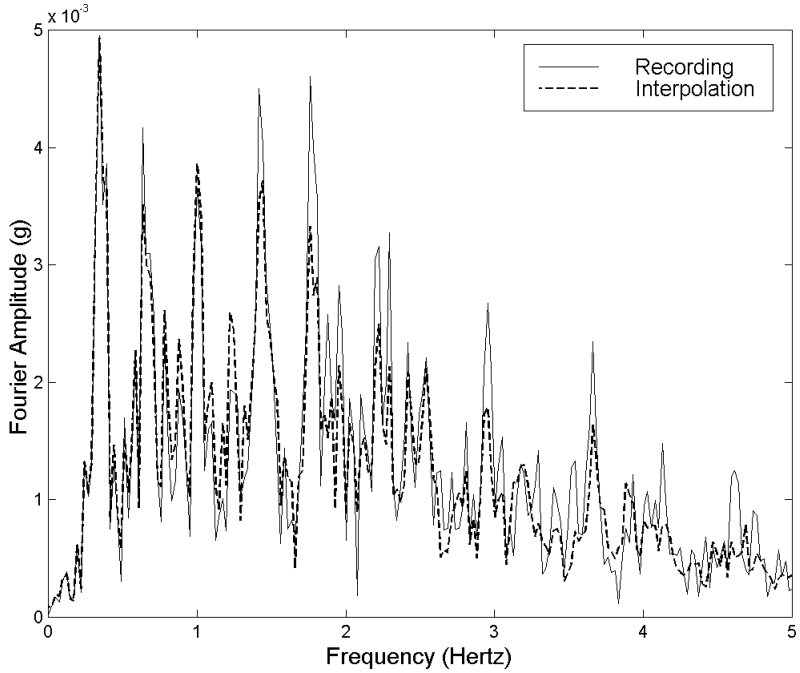

Figure 6.22: The recorded Fourier amplitude spectrum at station C-00 (solid line) compared to the interpolated spectrum (dashed line) using all inner circle stations. (Same as Figure 6.13).

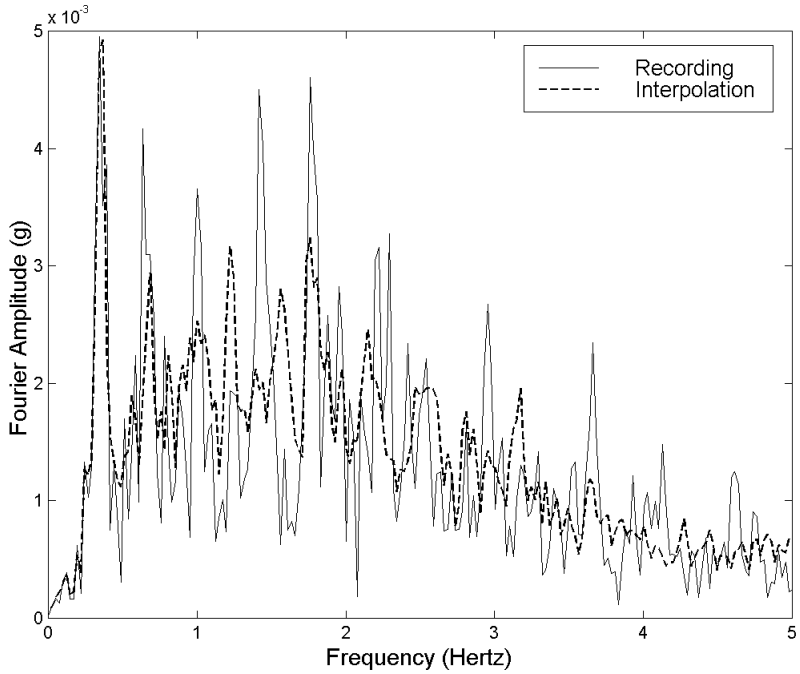

Figure 6.23: The recorded Fourier amplitude spectrum at station C-00 (solid line) compared to the interpolated spectrum (dashed line) using all middle circle stations.

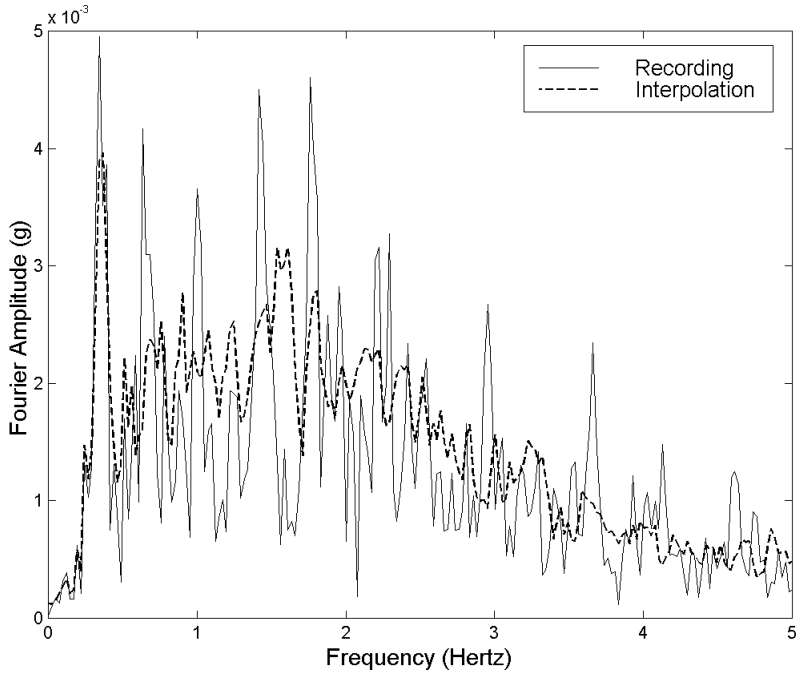

Figure 6.24: The recorded Fourier amplitude spectrum at station C-00 (solid line) compared to the interpolated spectrum (dashed line) using all outer circle stations.

Summary of Amplitude Interpolation

The Fourier amplitude interpolation model presented in Equation (6.5) yields quite satisfactory results, at least with respect to the gross characteristics of the amplitude spectra (the total energy, central frequency, and bandwidth). If the inter-station spacing is less than 200 meters, the standard error of the interpolated Fourier amplitudes, frequency by frequency, is on the average 40% to 50% less than if the spacing is larger than 1000 meters. Whether the spacing is 1 or 2 kilometers does not have much effect on the quality of the interpolation, as measured by the standard error. Using twelve surrounding points rather than two to interpolate the amplitude, and keeping the distance between the site and the recording stations the same, lowers the standard error of the interpolation only by 10% to 15%, on the average. The interpolated Fourier amplitude spectrum becomes smoother as more points are used in the interpolation and as the inter-station spacing increases.

6.3.3 Interpolation of Fourier Phase Angles

The interpolated Fourier phase angle of the n-th discrete frequency component at the site, C, is inferred from the weighted averages of the real and imaginary parts of the predicted discrete Fourier transforms:

$$\hat{\Phi}_C(\omega_n) = \arctan\left(\frac{\sum_k w_k \cdot \mathrm{Im}\left[A_{C,k}(\omega_n)\cdot \exp\left(j\cdot \Phi_{C,k}(\omega_n)\right)\right]}{\sum_k w_k \cdot \mathrm{Re}\left[A_{C,k}(\omega_n)\cdot \exp\left(j\cdot \Phi_{C,k}(\omega_n)\right)\right]}\right) \qquad (6.6)$$

$$w_k = \frac{1}{d_k^2}$$

In Equation (6.6) $\hat{\Phi}_C(\omega_n)$ is the interpolated Fourier phase angle corresponding to discrete frequency ω_n at the site, C; $A_{C,k}(\omega_n)$is the Fourier amplitude at the site as predicted by the recording at station number *k*; $\Phi_{C,k}(\omega_n)$ is the Fourier phase angle at the site as predicted by the recording at station *k*; w_k is the weight assigned to station number *k* for prediction at the site; and d_k is the distance between the site and station number *k*. Recall from Section 6.1 that the Fourier amplitudes are assumed to stay the same, i.e.

$$A_{C,k}(\omega_n) = A_k(\omega_n) \qquad (6.1)$$

where $A_k(\omega_n)$ is the Fourier amplitude of the n-th discrete frequency component of the recording at station number *k*. Recall furthermore, that each frequency component is assumed to propagate radially from the epicenter with a constant apparent phase velocity, $v(\omega_n)$. Hence, the Fourier phase angle at the site can be predicted according to the simple dispersion relationship:

$$\Phi_{C,k}(\omega_n) = \Phi_k(\omega_n) - \frac{(\delta_C - \delta_k)\cdot \omega_n}{v(\omega_n)} \qquad (6.2)$$

where $\Phi_k(\omega_n)$ is the Fourier phase angle of the n-th discrete frequency component of the recording at station number *k*, δ_C is the epicentral distance of the site, and δ_k is the epicentral distance of station number *k*.

In Figures 6.25 through 6.35, results from the phase angle interpolation model given in Equation (6.6) are compared to recordings for the geometric interpolation schemes described in subsection 6.2.3. First, results from two-point interpolations are presented, followed by results from triangular interpolations and interpolations using all the recording stations of a given circle. The results presented here are all from Event 45, the largest event ever recorded by the SMART-1 array, but similar results were obtained for all the other events listed in Table 6.2.

Two-Point Interpolation

In Figures 6.25, 6.27 and 6.29, the recorded Fourier phase angle spectrum at station C-00 is compared to the estimated spectrum at C-00, using two-point interpolation. The interpolation error (the observed phase angle minus the interpolated phase angle) is plotted as function of frequency in Figures 6.26, and 6.28. The standard deviation of the interpolation error for each 1.5 Hz wide frequency band is also reported in the figures. The interpolation results presented in Figures 6.25 and 6.26 are for a propagation-perpendicular pair of inner circle stations, while the results in Figures 6.27 and 6.28 are from interpolation of a propagation-parallel inner circle pair. Due to lesser dispersion effects, one would expect the interpolation from the propagation-perpendicular pair to yield better results than the interpolation from the propagation-parallel pair. This expectation can be confirmed, both by visual inspection and by comparing the standard deviations of the interpolation errors reported in Figures 6.26 and 6.28. The comparison between the recorded and interpolated phase angles is poorer for higher frequencies.

The interpolation results for a pair of propagation-perpendicular middle circle stations are presented in Figure 6.29. The comparison between the recorded and the interpolated phase angles is much poorer for the middle circle stations than the inner circle stations. Since the comparison in Figure 6.29 is so poor, it is not thought necessary to show the interpolation error as a function of frequency. The comparison is even worse for a pair of propagation-parallel stations. Therefore, no example results of such interpolation are shown.

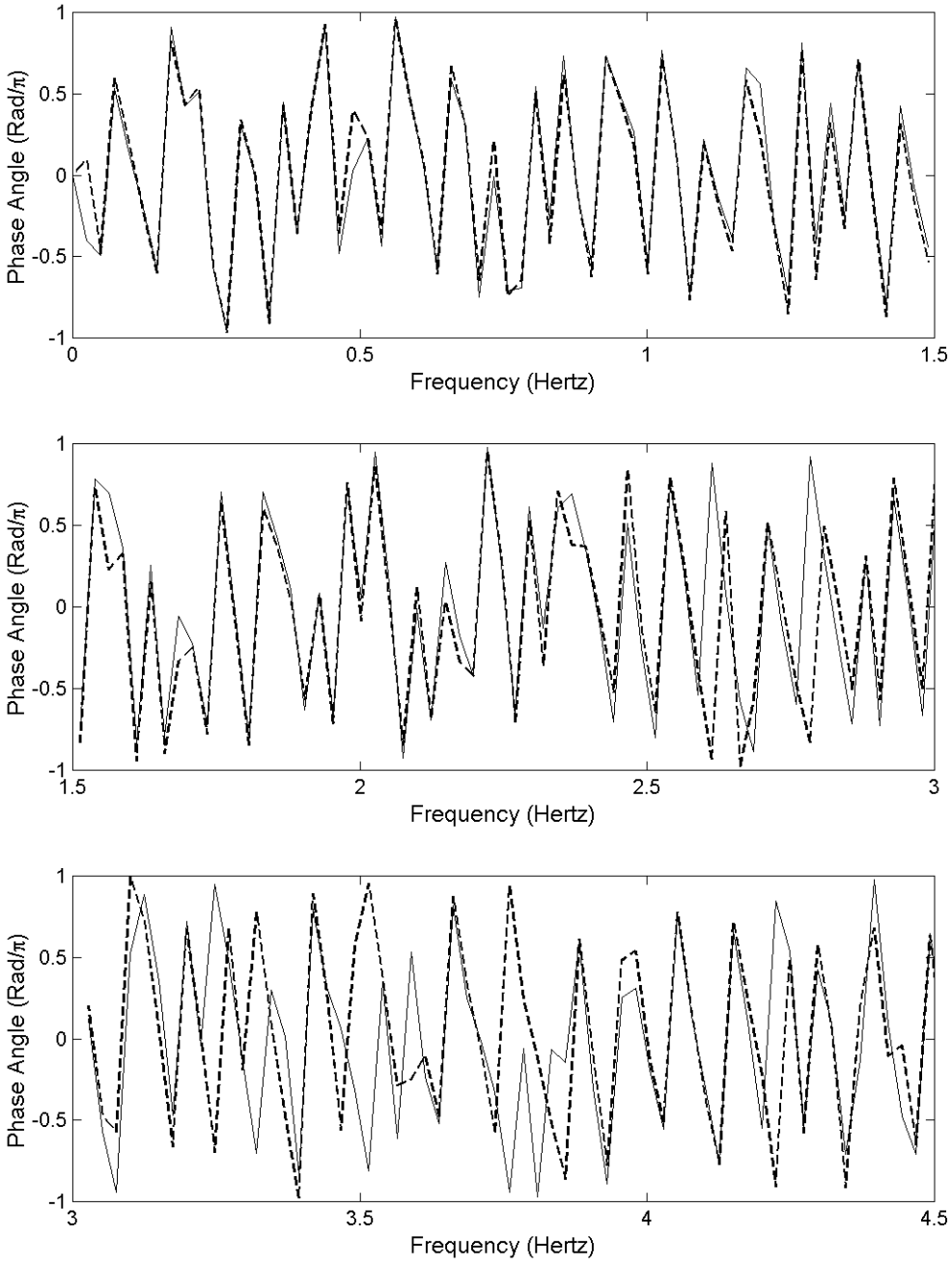

Figure 6.25: The recorded Fourier phase angle spectrum at station C-00 (solid line) compared to the interpolated phase spectrum (dashed line) using the propagation-perpendicular inner circle station pair (I-03,I-09).

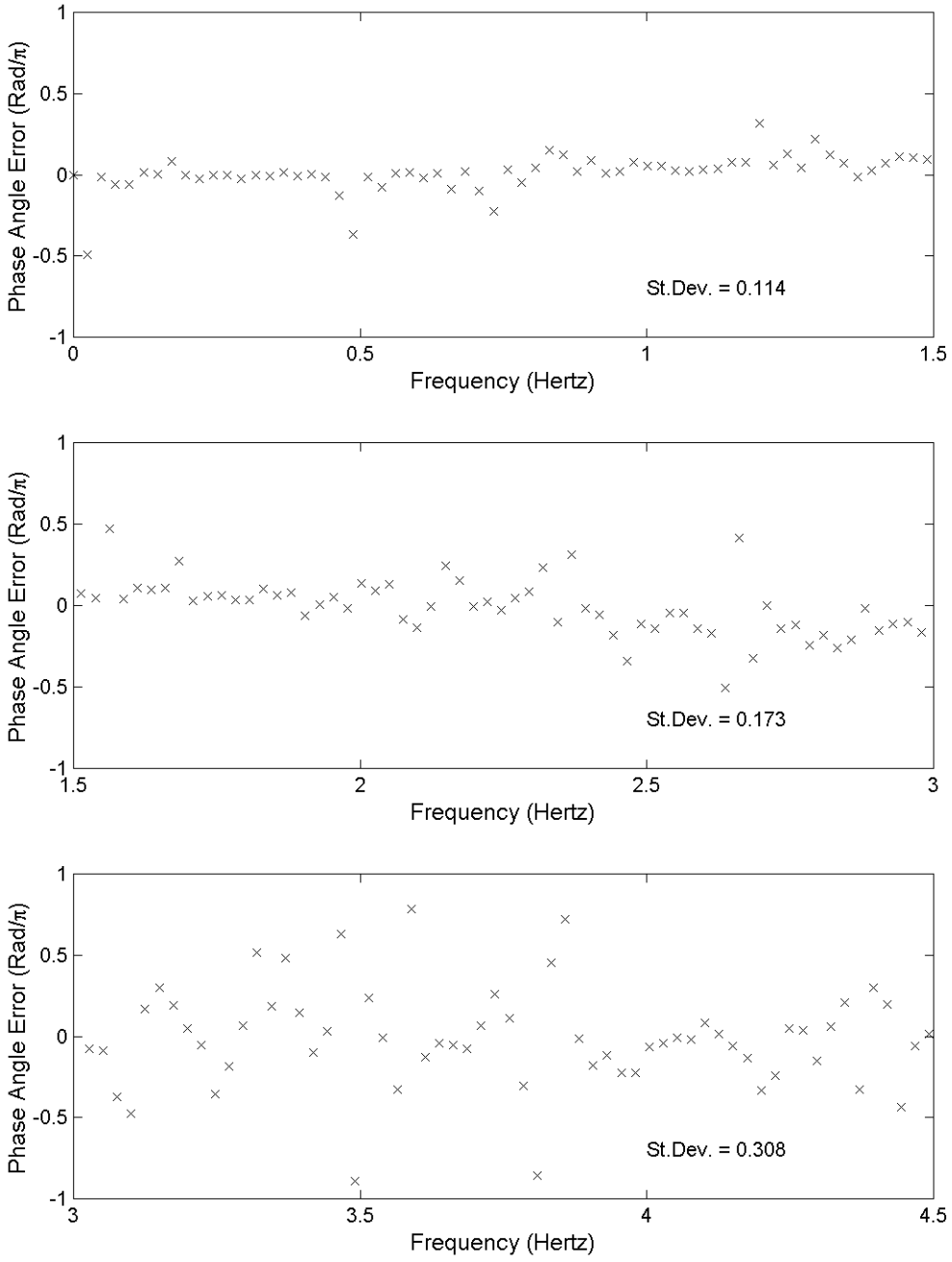

Figure 6.26: The Fourier phase angle interpolation error at station C-00 for the propagation-perpendicular inner circle station pair (I-03,I-09).

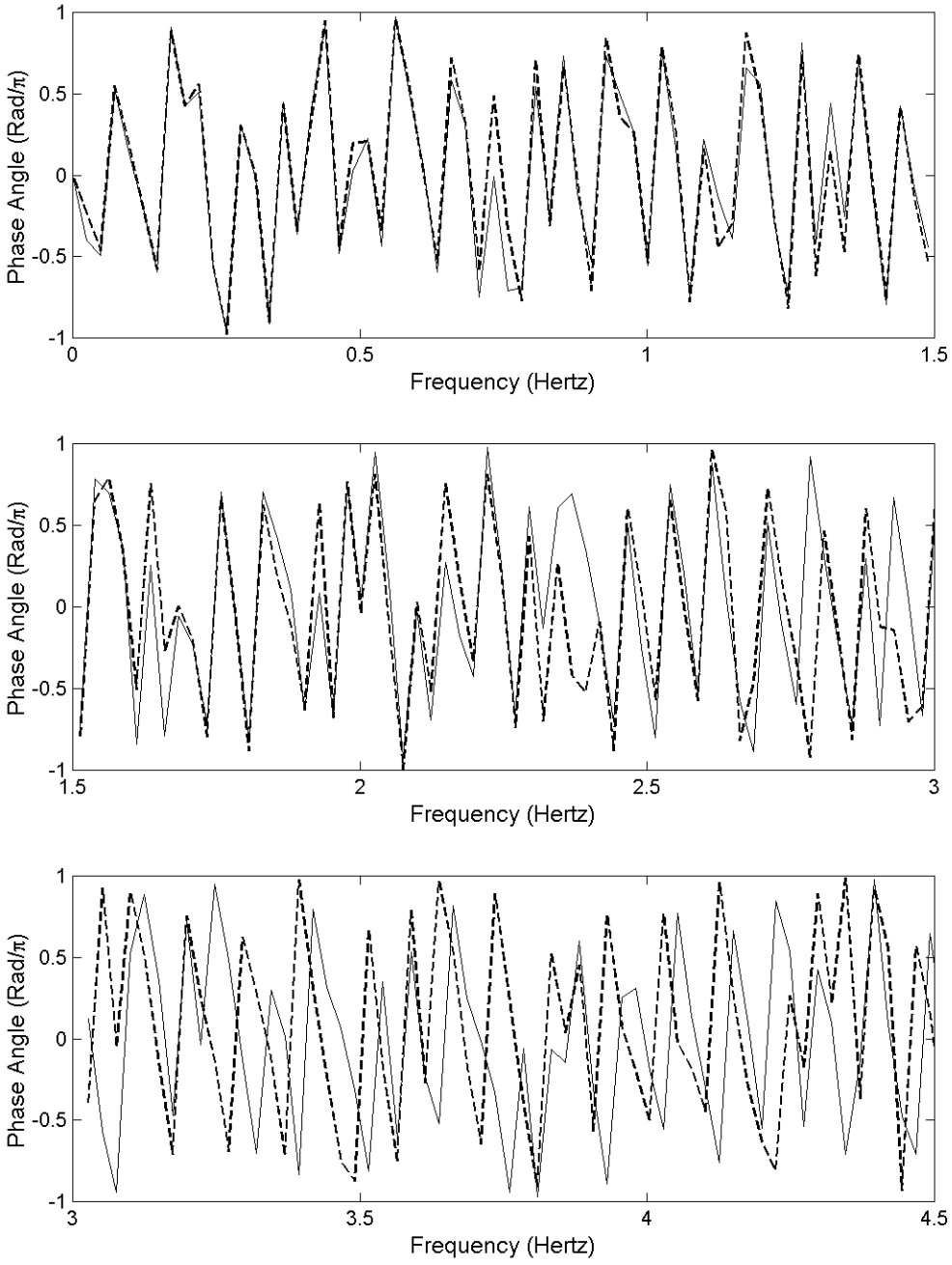

Figure 6.27: The recorded Fourier phase angle spectrum at station C-00 (solid line) compared to the interpolated phase spectrum (dashed line) using the propagation-parallel inner circle station pair (I-06,I-12).

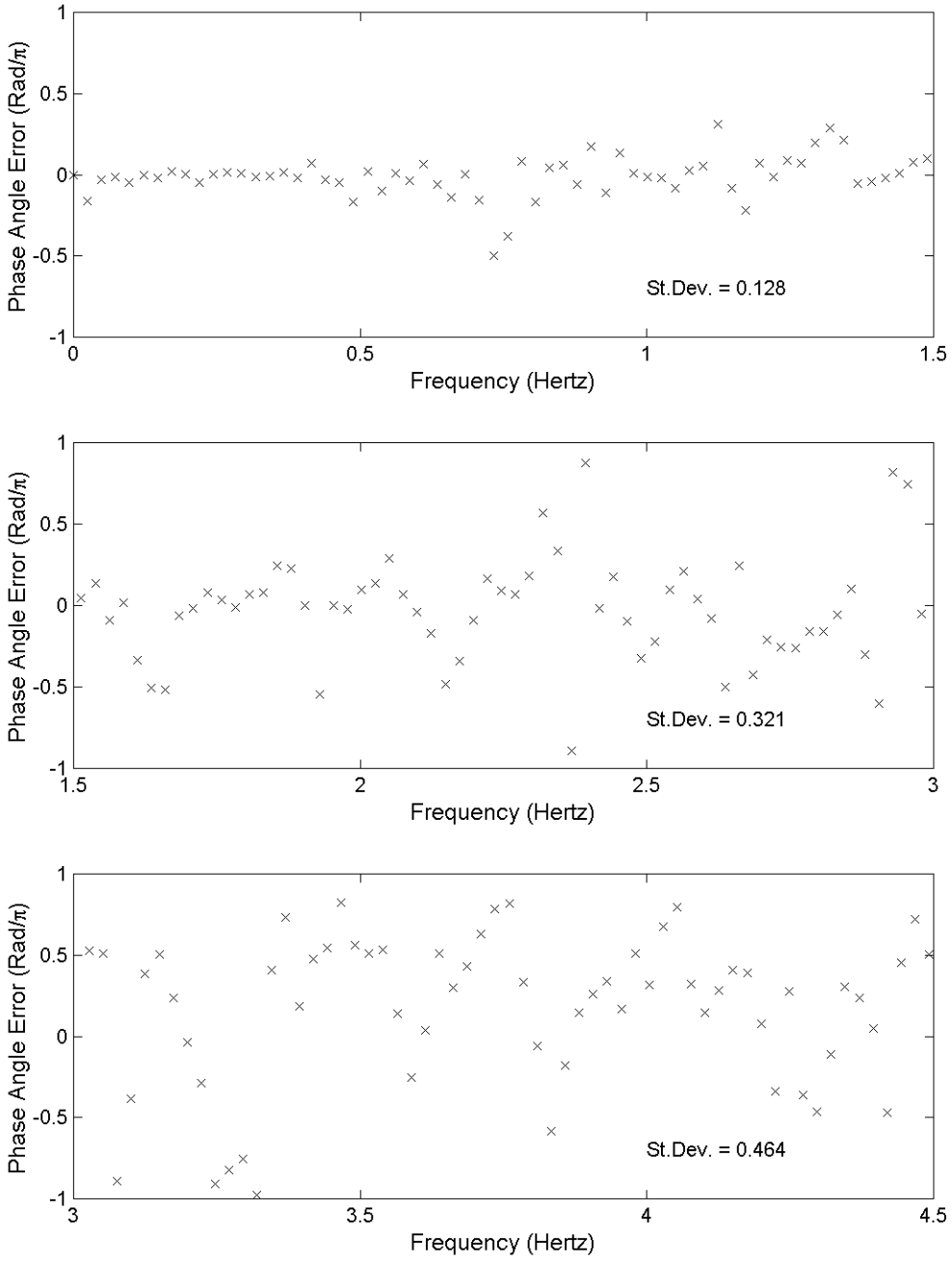

Figure 6.28: The Fourier phase angle interpolation error at station C-00 for the propagation-parallel inner circle station pair (I-06,I-12).

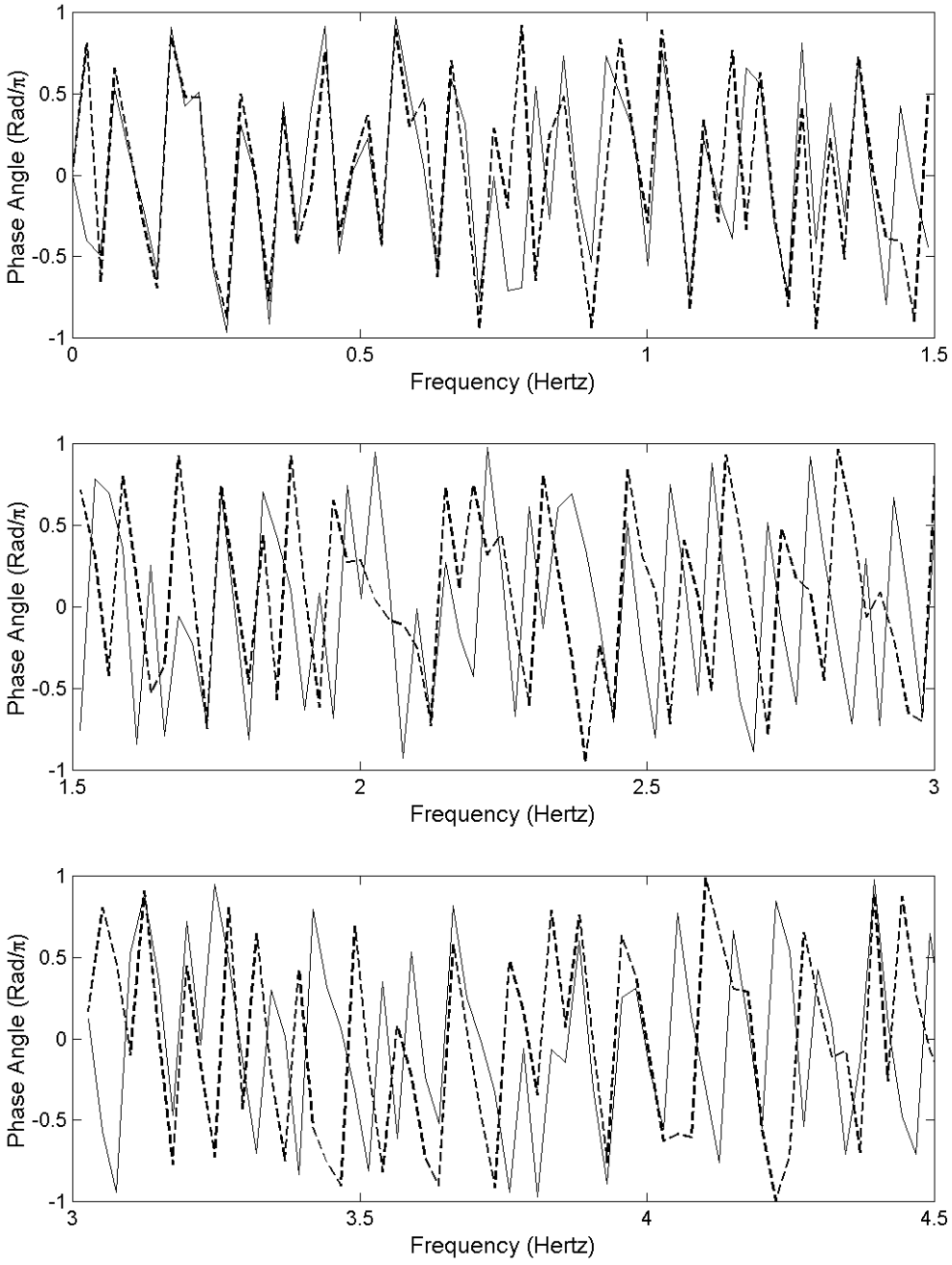

Figure 6.29: The recorded Fourier phase angle spectrum at station C-00 (solid line) compared to the interpolated phase spectrum (dashed line) using the propagation-perpendicular middle circle station pair (M-03,M-09).

Three-Point Interpolation

In Figures 6.30 and 6.32, the recorded Fourier phase angle spectrum at station C-00 is compared to the estimated spectrum at C-00, using triangular interpolation. The interpolation error (the difference between the observed and the interpolated phase angle) obtained using an equilateral inner circle triangle is plotted as function of frequency in Figure 6.31. The standard deviation of the interpolation error for each 1.5 Hz wide frequency band is also reported in Figure 6.31.

The phase angle interpolation results presented in Figures 6.30 and 6.31 are for an equilateral, inner circle triangle. The comparison between the recorded and interpolated phase spectra is quite good, especially for frequencies lower than 3 Hz. It is interesting to compare the results of this triangular interpolation to the results of the two-point interpolation presented in Figures 6.25 through 6.28. Tthe quality of the triangular interpolation is not significantly different from the quality of the interpolation using the propagation-perpendicular pair (Figures 6.25 and 6.26), while the triangular interpolation yields better results than the interpolation that uses the propagation-parallel station pair (Figures 6.27 and 6.28).

The phase angle interpolation results presented in Figure 6.32 are from an equilateral, middle circle triangle. This interpolation yields significantly worse results than the interpolation from the inner circle triangle. The quality of the interpolation from the middle circle triangle is similar to that from the wave-perpendicular, middle circle pair, as shown in Figure 6.29.

The quality of the phase angle interpolation from an outer circle triangle is found to be even poorer than the quality of interpolation from the middle circle triangle described above. Therefore, the phase angle interpolation results from an outer circle triangle are not shown here.

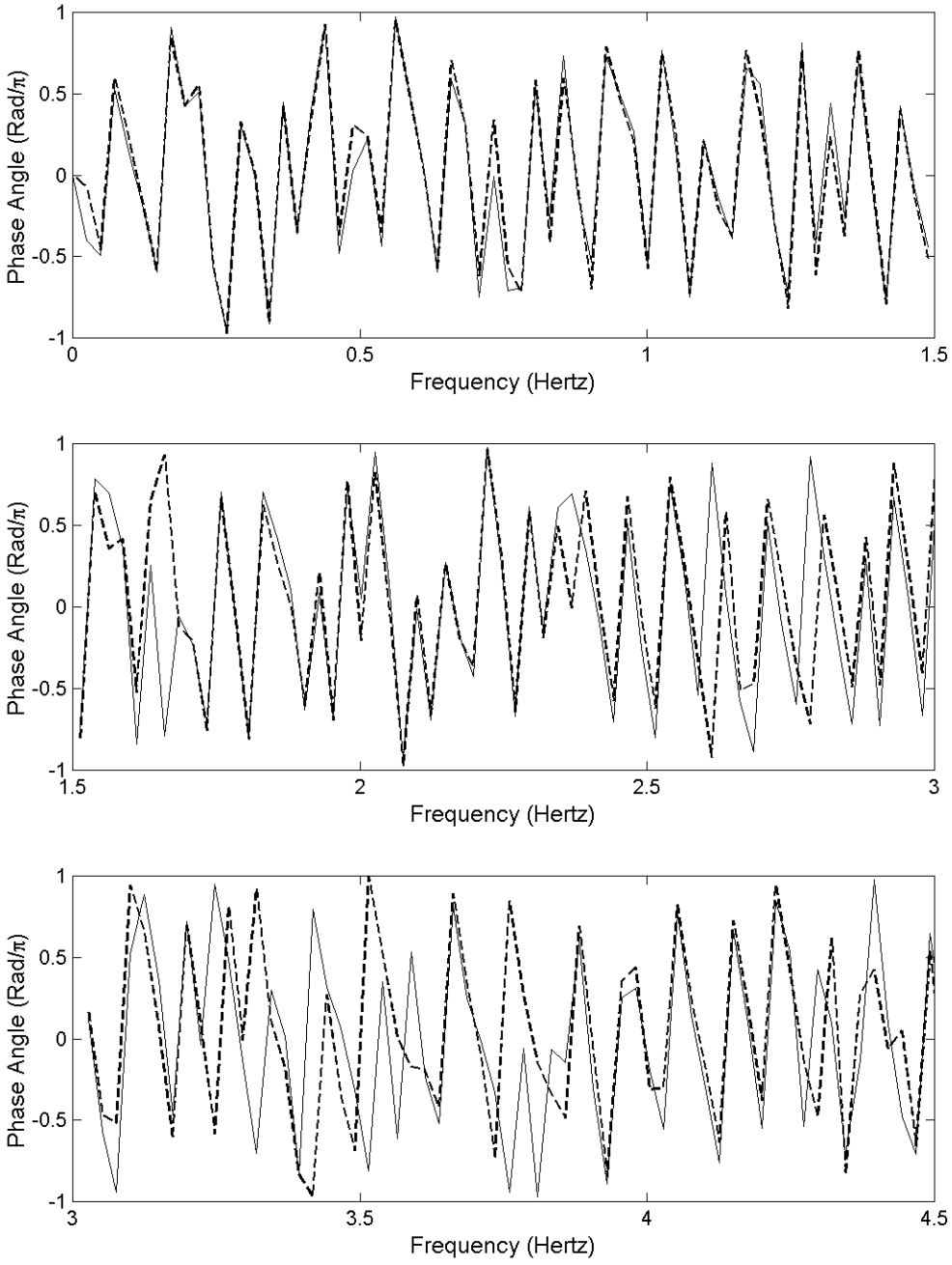

Figure 6.30: The recorded Fourier phase angle spectrum at station C-00 (solid line) compared to the interpolated phase spectrum (dashed line) using the inner circle triangle (I-03,I-07,I-11).

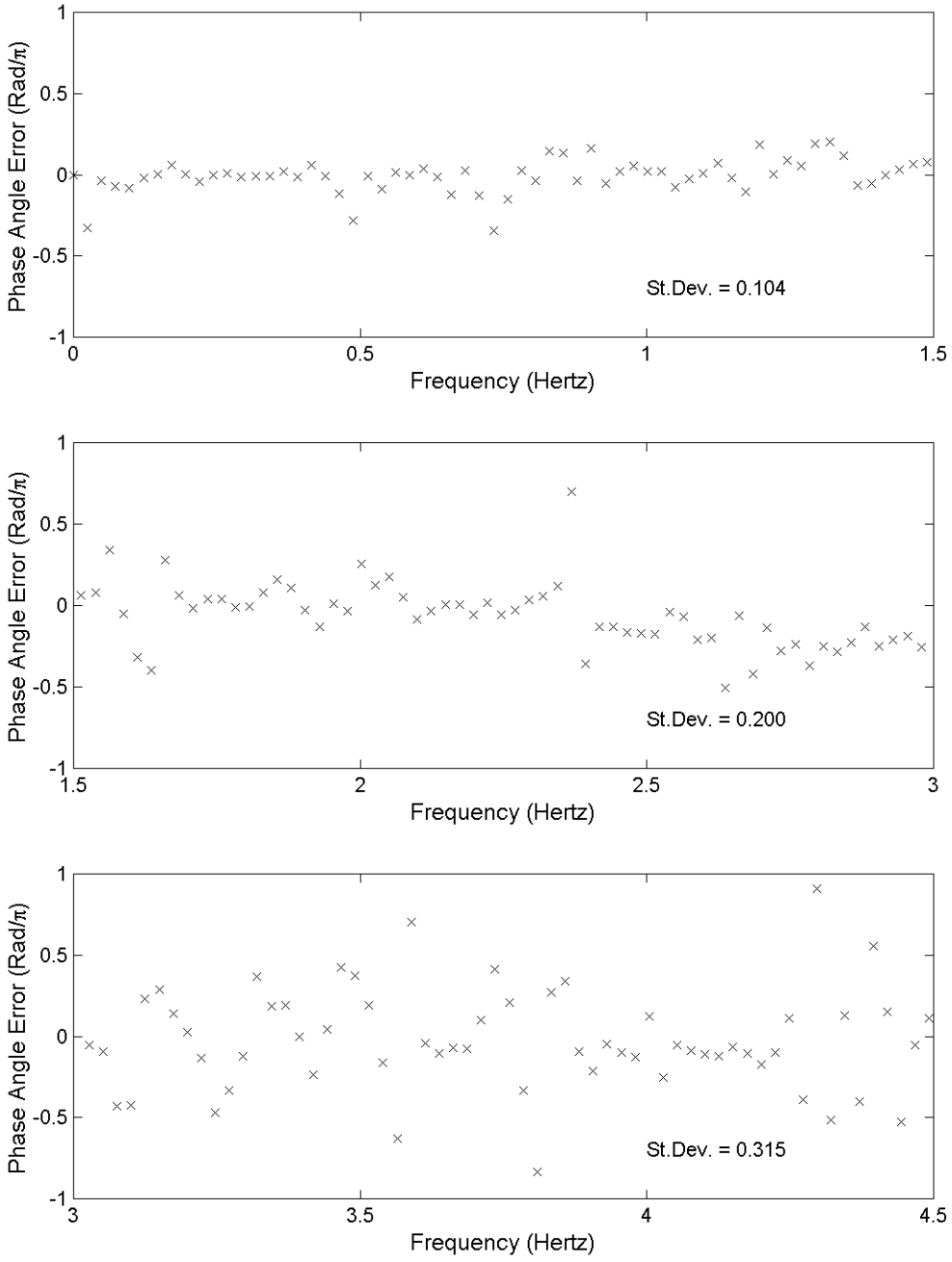

Figure 6.31: The Fourier phase angle interpolation error at station C-00 for the inner circle triangle (I-03,I-07,I-11).

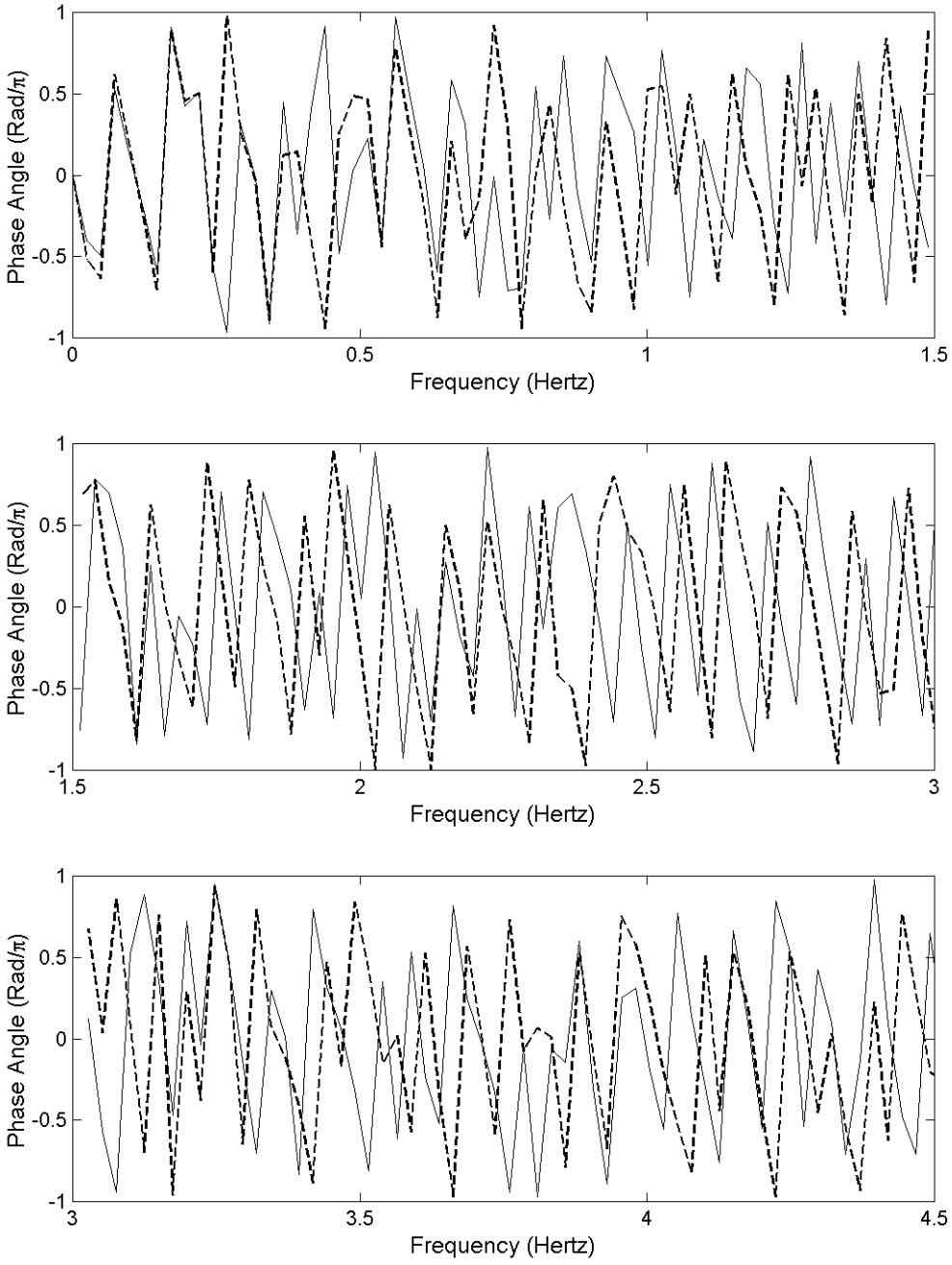

Figure 6.32: The recorded Fourier phase angle spectrum at station C-00 (solid line) compared to the interpolated phase spectrum (dashed line) using the middle circle triangle (M-03,M-07,M-11).

Interpolation using all the Stations in a given Circle

In Figures 6.33 and 6.35, the recorded Fourier phase angle spectrum at station C-00 is compared to the interpolated spectrum at C-00, using all the recording stations in a given circle. The interpolation error (the observed phase angle minus the interpolated phase angle) for the inner circle interpolation is plotted as function of frequency in Figure 6.34. The standard deviation of the interpolation error for each 1.5 Hz wide frequency band is also reported in Figure 6.34.

The phase angle interpolation results presented in Figures 6.33 and 6.34 are from all the stations in the inner circle. The comparison between the recorded and interpolated phase spectra is good for frequencies lower than 3 Hz. It is interesting to compare the results of this interpolation to the results of the triangular interpolation, presented in Figures 6.30 and 6.31, and the results of the propagation-perpendicular pair interpolation, presented in Figures 6.25 and 6.26. It is seen that it does not make much difference whether two propagation-perpendicular, three, or all twelve inner circle stations are used to evaluate the Fourier phase angle at the central station through spatial interpolation.

The phase angle interpolation results presented in Figure 6.35 are from all the stations in the middle circle. This interpolation yields significantly poorer results than the interpolation from the inner circle. Furthermore, the quality of the phase interpolation from all the middle circle stations is similar to that from the propagation-perpendicular middle circle pair, as shown in Figure 6.29, and to the quality of the interpolation from the middle circle triangle, as shown in Figure 6.32.

The quality of the phase angle interpolation using all the available recordings from the outer circle is found to be even poorer than the quality of interpolation using the middle circle stations, described above. Therefore, the phase angle interpolation results from the outer circle are not shown here.

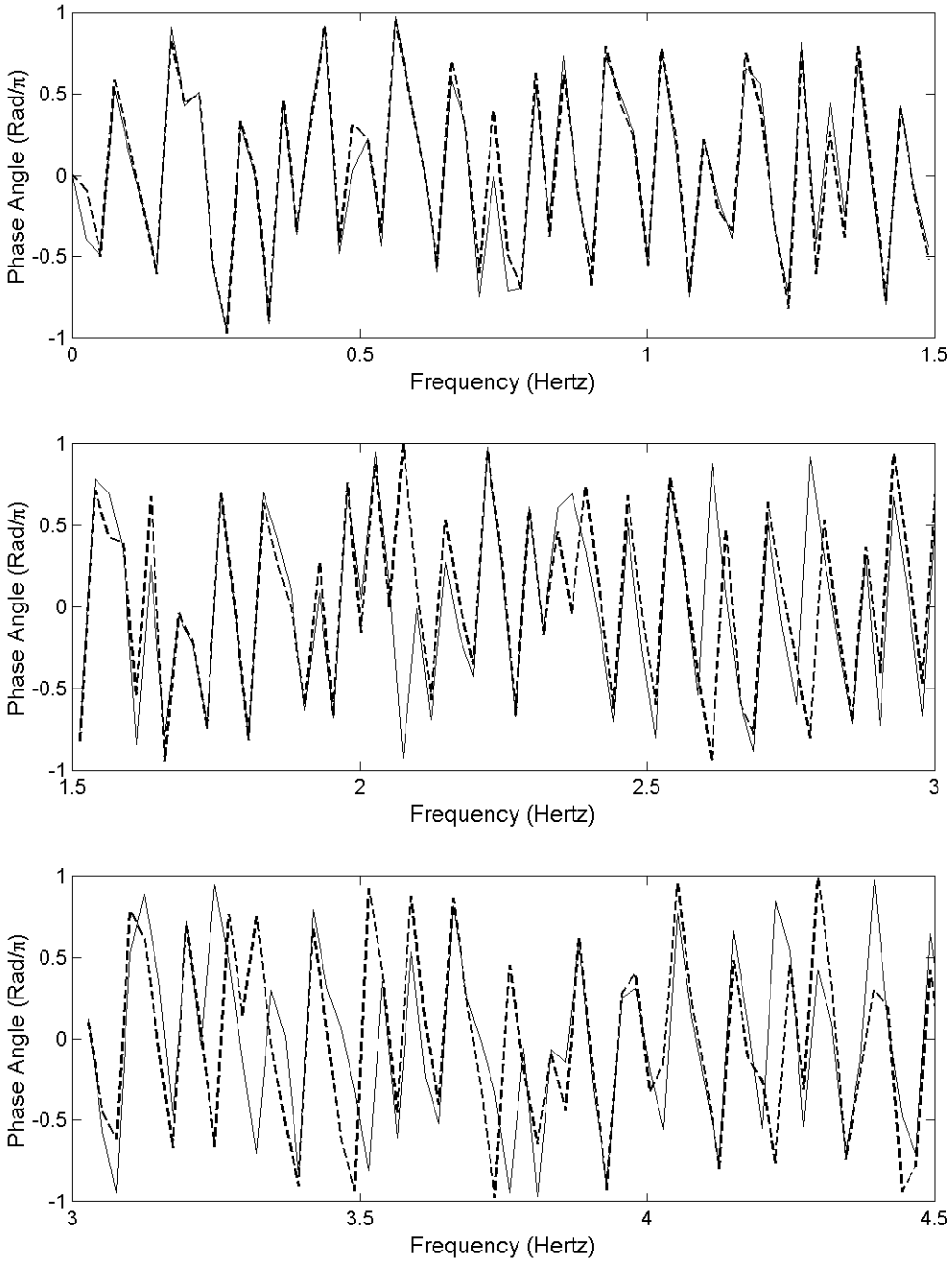

Figure 6.33: The recorded Fourier phase angle spectrum at station C-00 (solid line) compared to the interpolated phase spectrum (dashed line) using all stations in the inner circle.

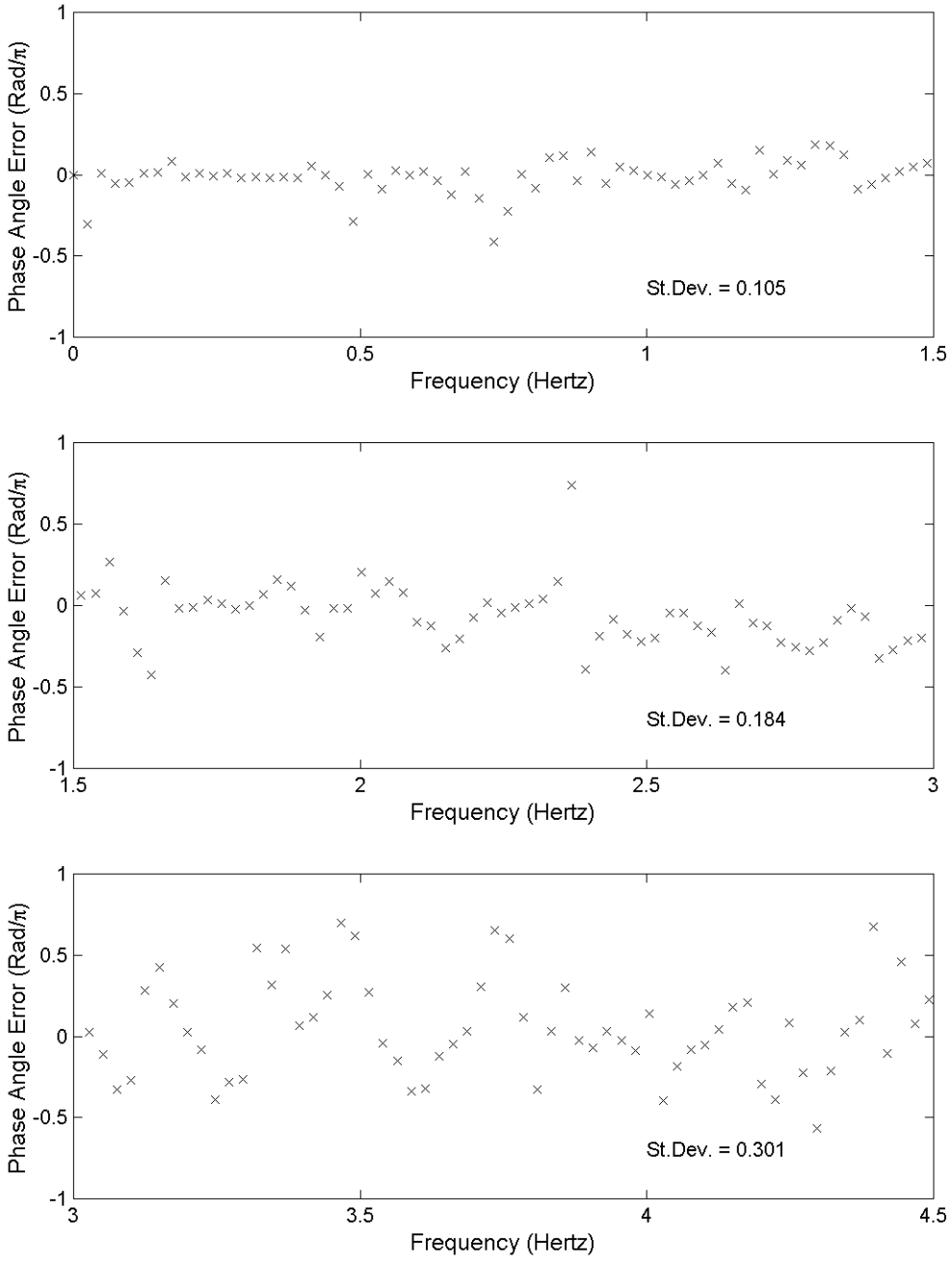

Figure 6.34: The Fourier phase angle interpolation error at station C-00 using all stations in the inner circle.

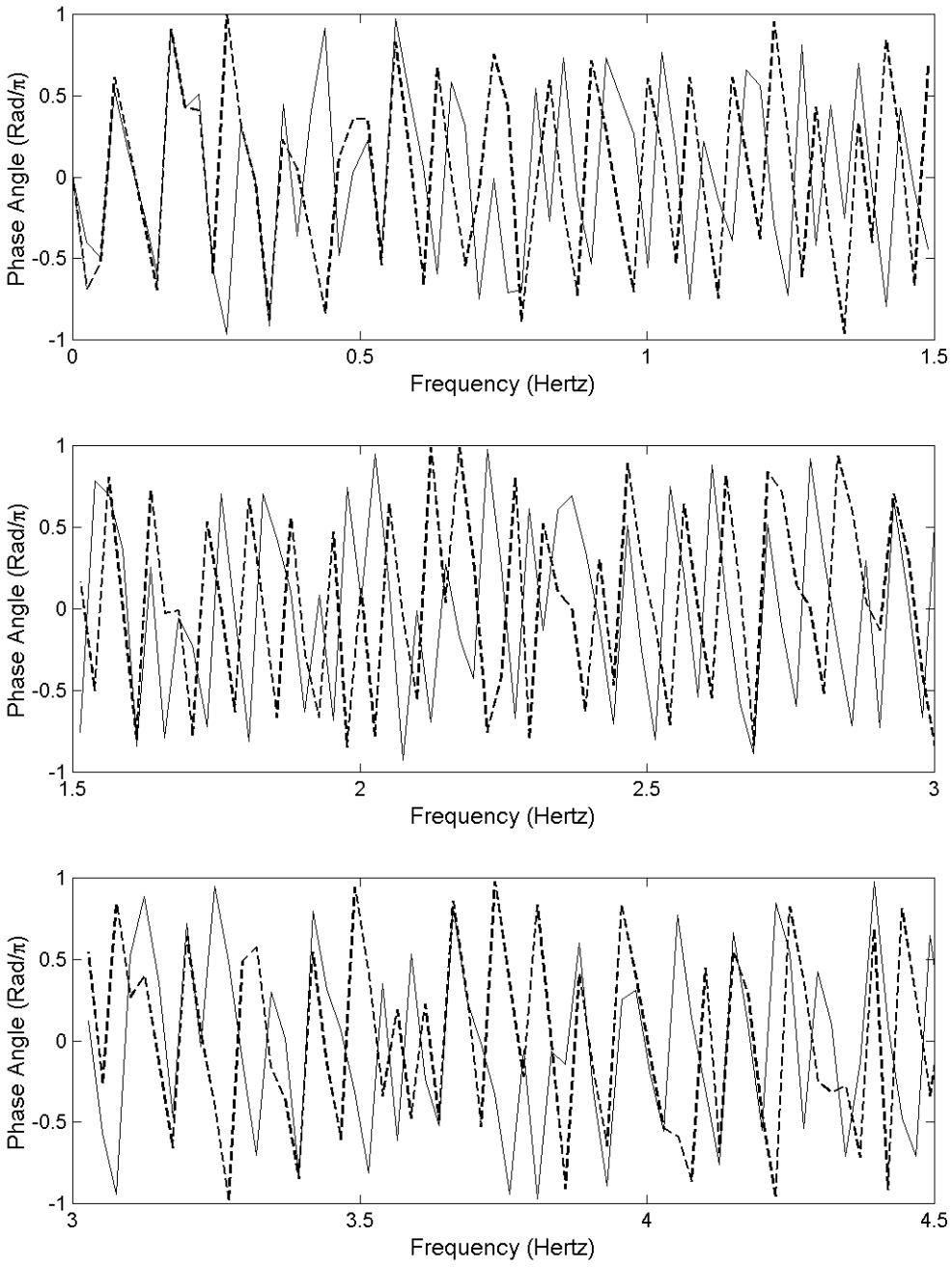

Figure 6.35: The recorded Fourier phase angle spectrum at station C-00 (solid line) compared to the interpolated phase spectrum (dashed line) using all stations in the middle circle.

Summary of Phase Angle Interpolation

The Fourier phase angle interpolation model presented in Equation (6.6) yields satisfactory results for inter-station spacing up to 200 meters and frequencies up to 3 Hertz. The model could possibly be extended up to a frequency of 4 Hertz and a spacing of 500 meters, but not to frequencies or distances beyond these. When using only two points to interpolate the phase angles, the line connecting the two points and the point for which the phase angles are to be determined, should be perpendicular to the direction of wave propagation. This increases the quality of the interpolation. The quality of the phase angle interpolation is not significantly affected whether twelve or three points are used in the interpolation. In either case, the quality of the interpolation is similar to the quality of the interpolation from the propagation-perpendicular station pair.

6.4 Interpolated Time Histories

In the previous section, the quality of the spatial interpolation was evaluated in the frequency domain. It is ultimately of considerable interest, of course, to study whether the interpolated accelerograms, obtained by inverting the interpolated discrete Fourier transform, closely resemble the recorded time histories in the time domain. In this section, interpolated time histories are compared to the recorded time history at the central station, C-00. The time histories themselves are compared, as well as their nonstationary characteristics, as indicated by the cumulative normalized Arias intensity. In view of the results of Chapters 3 and 4, it is anticipated that the cases in which the Fourier phase differences (and hence the phase angles) are well predicted also show good agreement in their nonstationary time domain characteristics.

In Figures 6.36 through 6.39 the results of two-point interpolations are compared to the recorded ground motion at the central station, C-00. The two interpolated time histories in Figure 6.36 are obtained using recordings from pairs of diagonally opposite inner circle stations. The line connecting the pair I-03 and I-09 is perpendicular to the direction of wave propagation, while the line connecting the pair I-06 and I-12 is parallel to the direction of wave propagation. The interpolated time history obtained from the propagation-perpendicular pair (the time history in the middle) resembles the recorded

time history better than the interpolation obtained using the propagation-parallel pair (the time history at the bottom). Note, for example, the build-up during the first 5 seconds, and the strong shaking segment between the 10th and 20th seconds. The improvement in results using the propagation-perpendicular interpolation rather than the propagation-parallel interpolation is not surprising, because it was shown in the previous section that the quality of the phase interpolation is better for a propagation-perpendicular pair than a propagation-parallel pair.

The nonstationary characteristics of the two interpolated time histories in Figure 6.36 are compared to the nonstationary characteristics of the recorded time history in Figure 6.37, where the cumulative normalized Arias intensities are shown as functions of time. The cumulative intensity of each time history is normalized with respect to its own Arias intensity. Hence, the curves are bounded between zero and one. The nonstationary characteristics of the recorded time history and the two interpolated time histories are very similar, as can be seen in Figure 6.37, where the three curves are nearly on top of each other.

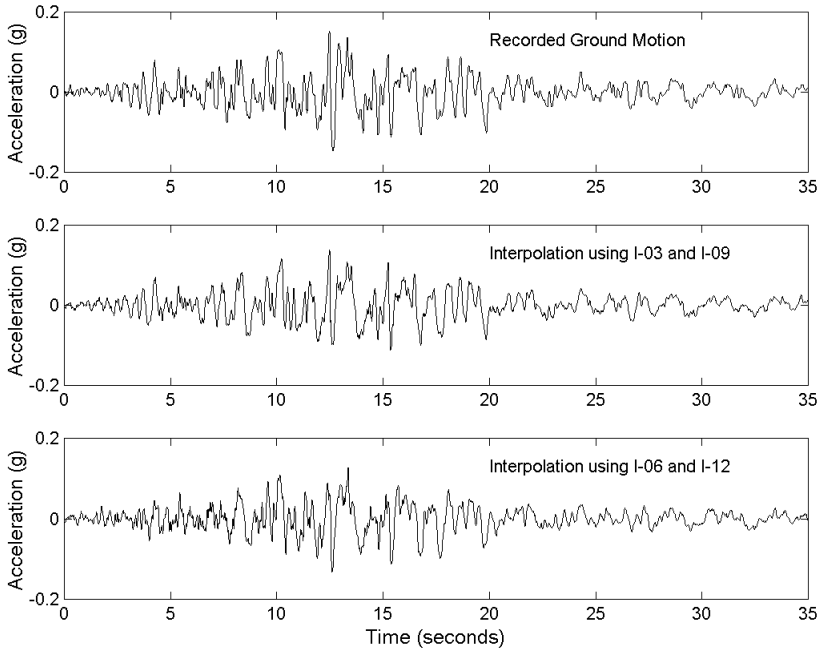

Figure 6.36: The recorded acceleration time history at station C-00 (top) and interpolated time histories (bottom two) using two diagonally opposite inner circle stations. The line connecting the pair (I-03,I-09) is perpendicular to the direction of wave propagation, while the line connecting I-06 and I-12 is parallel to the direction of wave propagation.

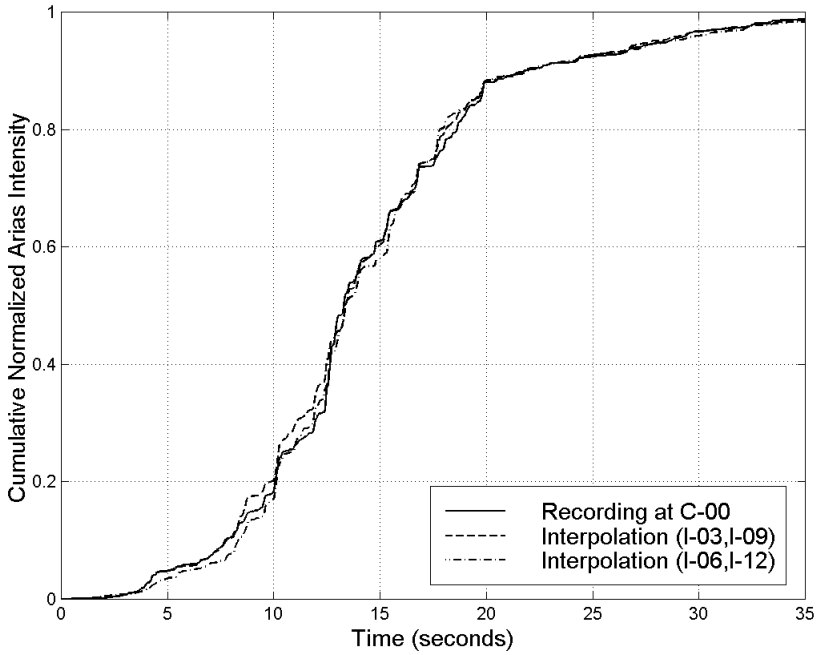

Figure 6.37: The cumulative normalized Arias intensities of the recording at station C-00 (solid line) and the two interpolated time histories from Figure 6.36.

In Figure 6.38, the recorded time history at the central station is shown together with three interpolated time histories. The interpolated time histories are all obtained using recordings from a pair of propagation-perpendicular recording stations. The time history at the bottom is from a pair of outer circle stations, the second from the bottom is from a pair of middle circle stations, and the third from the bottom is from a pair of inner circle stations. The inner circle interpolation, where the inter-station spacing is 200 meters, bears the closest resemblance to the recorded time history.

The cumulative normalized Arias intensities of the four time histories in Figure 6.38 are shown in Figure 6.39. The cumulative intensity of each time history is normalized with respect to its own Arias intensity. The cumulative intensity curve for the inner circle interpolation (the dashed line) is practically on top of the recorded cumulative intensity curve (the solid line), while the cumulative intensity curves for the middle and outer circle interpolations are somewhat different from the other two.

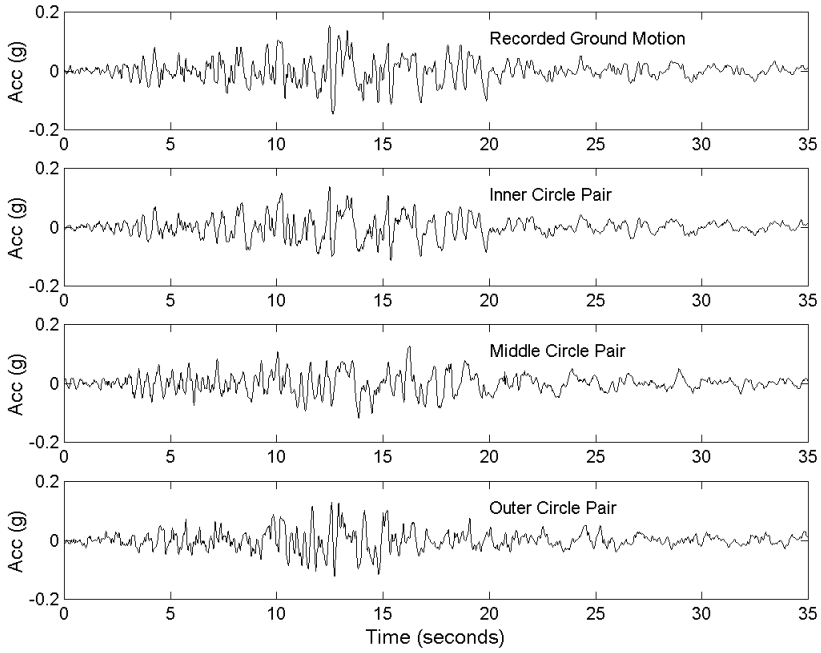

Figure 6.38: The recorded acceleration time history at station C-00 (top) and interpolated time histories (bottom three) using a pair of propagation-perpendicular stations.

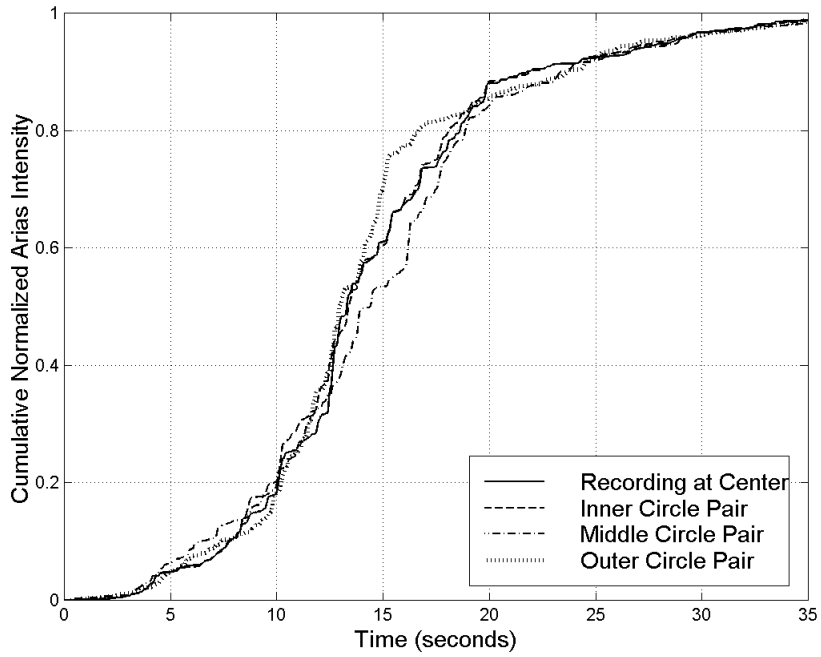

Figure 6.39: The cumulative normalized Arias intensities of the recording at station C-00 (solid line) and the two interpolated time histories from Figure 6.38.

It has been shown that the characteristics of the two-point interpolations from the middle and outer circle are not the same as the characteristics of the recorded time history at the center, both in the time domain (in this section) and the frequency domain (in the previous section). Nevertheless, it is interesting to note that these interpolations do yield acceleration time histories whose characteristics are similar to those of recorded earthquake accelerograms.

In Figure 6.40, the recorded acceleration time history at the central station, C-00, is compared to three interpolated time histories, each obtained using recordings from three inner circle stations that form an equilateral triangle. The three interpolations are similar to each other and they are very similar to the recorded time history. The nonstationary characteristics of all four time histories are shown in Figure 6.41, where the cumulative normalized Arias intensities are plotted as functions of time. The cumulative intensity of each time history is normalized with respect to its own Arias intensity. The four cumulative intensity curves are practically on top of each other.

The quality of the three-point inner circle interpolations is comparable to, or only slightly better than the quality of the interpolation using a pair of inner circle propagation-perpendicular stations. Therefore, it could be argued that there is no need for the third point in the interpolation. However, the quality of the three-point interpolations is considerably better than the quality of the interpolation obtained from the propagation-parallel pair. Since the quality of the three-point interpolations does not seem to depend on the orientation of the triangle with respect to the direction of seismic wave propagation, a three-point interpolation is, in general, preferred over a two-point interpolation.

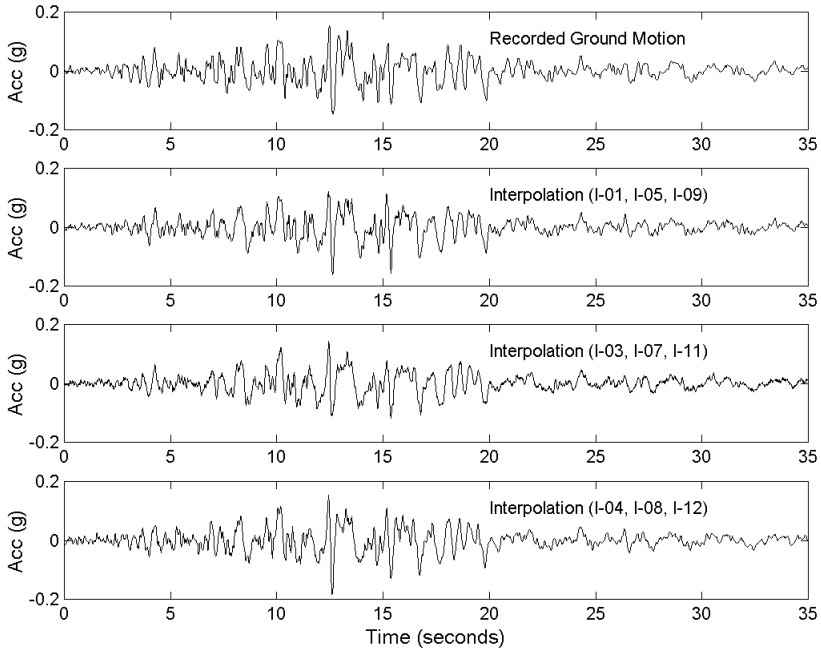

Figure 6.40: The recorded acceleration time history at station C-00 (top) and interpolated time histories (bottom three) using inner circle triangles.

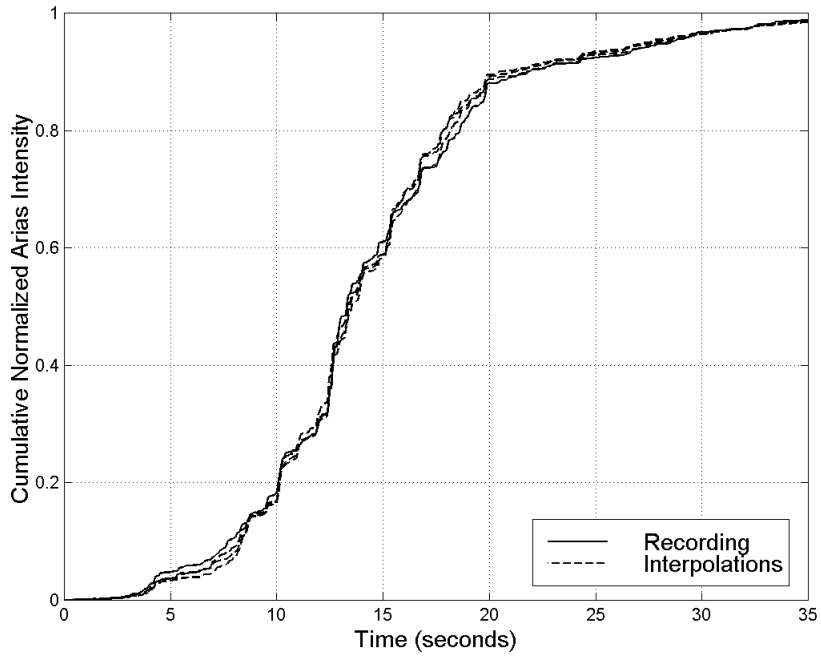

Figure 6.41: The cumulative normalized Arias intensities of the recording at station C-00 (solid line) and the three interpolated time histories from Figure 6.40.

In Figure 6.42, the recorded acceleration time history at the central station, C-00, is compared to three interpolated time histories, each obtained using recordings from three stations that form an equilateral triangle. The time history at the bottom is from an outer circle triangle, the time history second from the bottom is from a middle circle triangle, and the time history second from the top is from an inner circle triangle. The inner circle interpolation resembles best the recorded time history, while the outer circle interpolation bears the worst resemblance to the recorded time history.

The cumulative normalized Arias intensities for all four time histories in Figure 6.42 are plotted as functions of time in Figure 6.43. The cumulative intensity of each time history is normalized with respect to its own Arias intensity. Hence, the curves are bounded between zero and one. The nonstationary characteristics of the three-point inner circle interpolation (dashed line) and the recorded time history (solid line) are very similar to each other, while the nonstationary characteristics of the three-point interpolations for both the middle and outer circle stations are somewhat different from the other two.

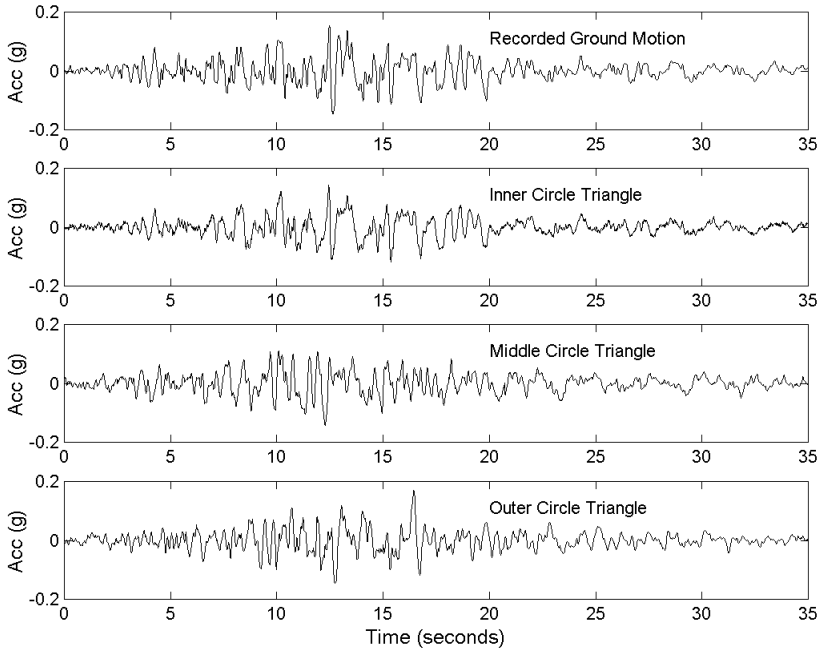

Figure 6.42: The recorded acceleration time history at station C-00 (top) and interpolated time histories (bottom three) using equilateral triangles (stations 03, 07, and 11).

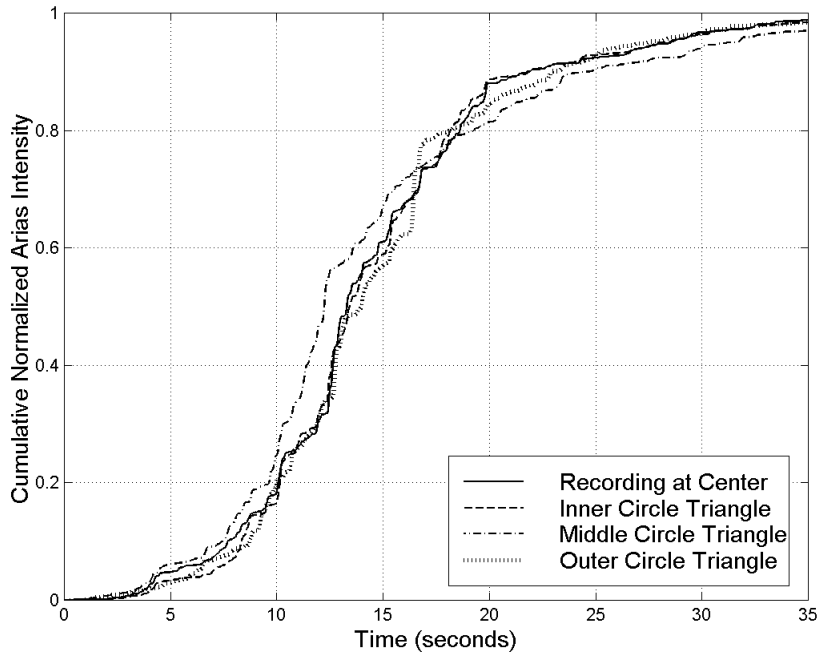

Figure 6.43: The cumulative normalized Arias intensities of the recording at station C-00 (solid line) and the three interpolated time histories from Figure 6.42.

It has been shown in this section that going from a pair of propagation-perpendicular stations up to using three recording stations does only marginally increase the quality of the interpolation in the time domain (the quality in the frequency domain was dealt with in the previous section). The main advantage of using a three-point interpolation rather than a two-point interpolation is the independence of the former regarding the orientation with respect to the direction of seismic wave propagation. The obvious question to ask next is whether using more than three recording stations does significantly affect the quality of the interpolation in the time domain.

In Figure 6.44, the recorded acceleration time history at the central station, C-00, is compared to three interpolated time histories, each obtained using recordings from all available stations in a given circle. The time history at the bottom is from the outer circle, the time history second from the bottom is from the middle circle, and the time history second from the top is from the inner circle. The inner circle interpolation resembles best the recorded time history, while the outer circle interpolation bears the worst resemblance to the recorded time history.

The cumulative normalized Arias intensities of all four time histories in Figure 6.44 are plotted as functions of time in Figure 6.45. The cumulative intensity of each time history is normalized with respect to its own Arias intensity. The cumulative intensity curve for the inner circle interpolation (dashed line) is almost on top of the cumulative intensity curve for the recorded time history (solid line). The cumulative intensity curve for the middle circle interpolation (dash-dot line) more closely resembles the cumulative intensity curve for the recorded time history, than the cumulative intensity curve for the outer circle interpolation does.

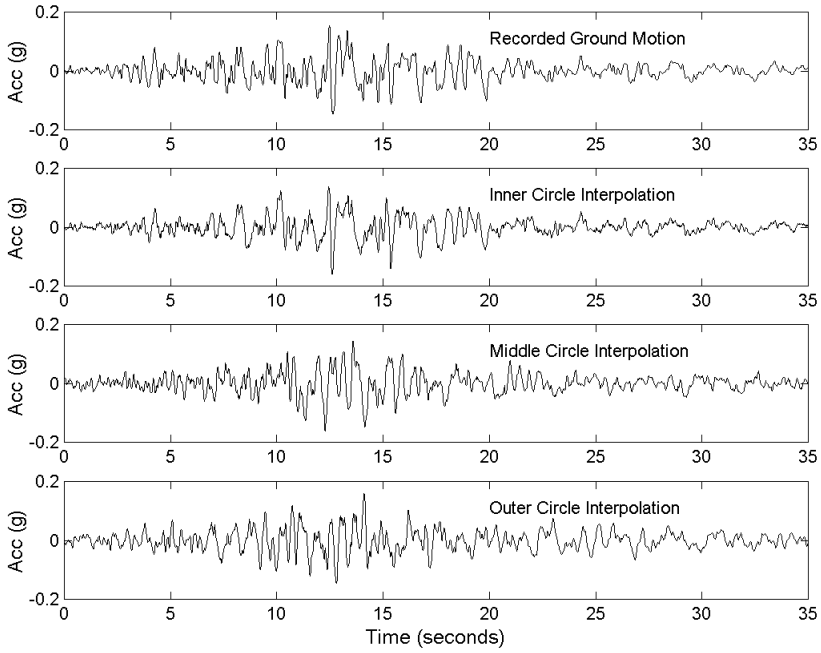

Figure 6.44: The recorded acceleration time history at station C-00 (top) and interpolated time histories (bottom three) using all the recording stations in a given circle.

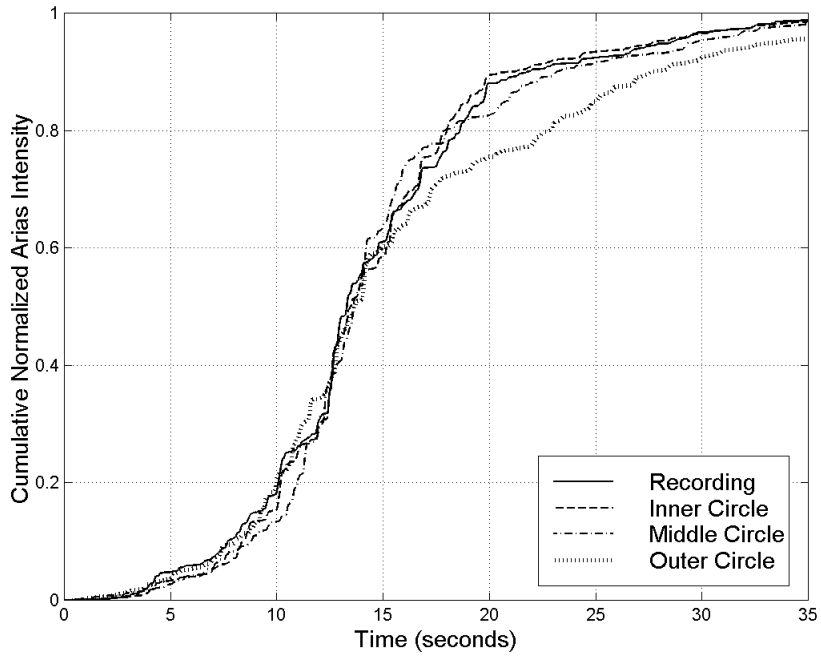

Figure 6.45: The cumulative normalized Arias intensities of the recording at station C-00 (solid line) and the three interpolated time histories from Figure 6.44.

The question whether “more is better”, i.e. whether using twelve rather than three recording stations in the spatial interpolation yields considerably better results has not yet been answered. In Figure 6.46, the recorded acceleration time history at the central station, C-00, is compared to three interpolated time histories, each obtained using recordings from stations in the outer circle. The time history second from the top is obtained using a pair of propagation-perpendicular stations (O-03 and O-09), the time history second from the bottom is from an equilateral triangle (O-03, O-07, O-11), and the time history at the bottom is obtained using all available recordings from the outer circle.

The cumulative normalized Arias intensities of all four time histories in Figure 6.46 are plotted as functions of time in Figure 6.47. The cumulative intensity of each time history is normalized with respect to its own Arias intensity. Hence, the curves are bounded between zero and one.

The lesson learned from Figures 6.46 and 6.47 is that using more stations (i.e. the entire circle, as opposed to either two or three stations) does not necessarily increase the quality of the interpolation in the time domain. The time history at the bottom in Figure 6.46 bears the least resemblance to the recorded time history, and in Figure 6.47, the nonstationary characteristics of the time history using the entire circle is most different from the evolutionary characteristics of the recorded time history.

In subsections 6.3.2 and 6.3.3 it was shown that the interpolation quality in the frequency domain increases only marginally when all the stations in a given circle are used, as compared to using only two (propagation-perpendicular) or three stations. In the time domain, the quality of the interpolation increases also marginally for the inner and middle circle stations (radii of 200 meters and 1000 meters, respectively), but the quality is slightly worse for the outer circle stations (nominal radius of 2000 meters). However, the quality of the three-point interpolations is not orientation-dependent, but the quality of the two-point interpolations is. It is therefore concluded that a three-point interpolation scheme is effective for the spatial interpolation of earthquake ground motion.

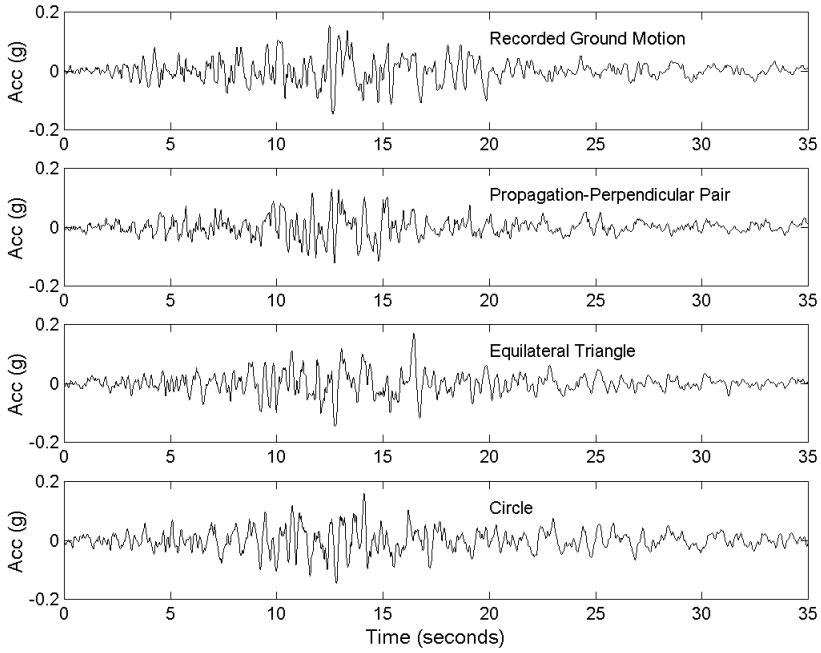

Figure 6.46: The recorded acceleration time history at station C-00 (top) and interpolated time histories (bottom three) using recordings from stations in the middle circle.

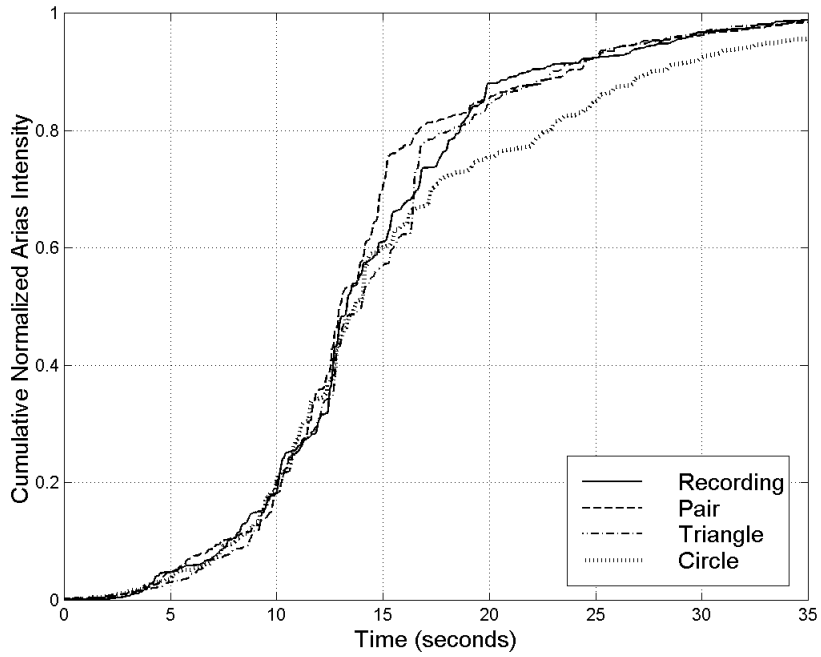

Figure 6.47: The cumulative normalized Arias intensities of the recording at station C-00 (solid line) and the three interpolated time histories from Figure 6.46.

6.5 Delaunay Triangulation

Consider the situation of having obtained a set of ground motion recordings (or simulations) at fixed stations, but it is desired to estimate the ground motion at sites in between the stations. In order to use the spatial interpolation model developed in this chapter, it is necessary to define a geometric interpolation scheme.

In the analyses described in previous sections, the regular geometry of the SMART-1 array was taken advantage of in the definition of the geometric interpolation schemes. In real world situations, however, one is most likely faced with a mesh of irregularly located recording stations. The problem then becomes how to define an effective geometric interpolation scheme from a general mesh of points. This section provides a simple and effective strategy to solve that problem.

It was shown in the previous sections, that triangular interpolation schemes yield effective and accurate interpolation results. After defining a mesh of triangles, the discrete Fourier transform interpolation model given in Equations (6.5), and (6.6), which includes the basic assumptions put forward in Equations (6.1) and (6.2), can be used to estimate the Fourier transform at any interior point.

There are many ways to define a set of triangles from a given mesh of points. One of the most effective triangulation strategies is the Delaunay Triangulation. In Delaunay Triangulation, a set of triangles is defined using a mesh of points, such that no points are contained in any triangle's circumscribed circle. The concept of Delaunay Triangulation is explained in Figure 6.48(a). The figure contains a mesh of four points: P1, P2, P3, and P4. The circle circumscribing the triangle (P1,P2,P3) does not include the point P4, and the circle circumscribing the triangle (P1,P3,P4) does not include the point P2. Conversely, the triangulation in Figure 6.48(b) is not Delaunay Triangulation, because the circle circumscribing the triangle (P1,P2,P4) does include the point P3. The Delaunay Triangulation is desirable, because it yields the most regular mesh of triangles possible. The closer the triangles are to being equilateral, the better they are suited for interpolation. Note that the two triangles in Figure 6.48(a) are closer to being equilateral than the triangles in Figure 6.48(b).

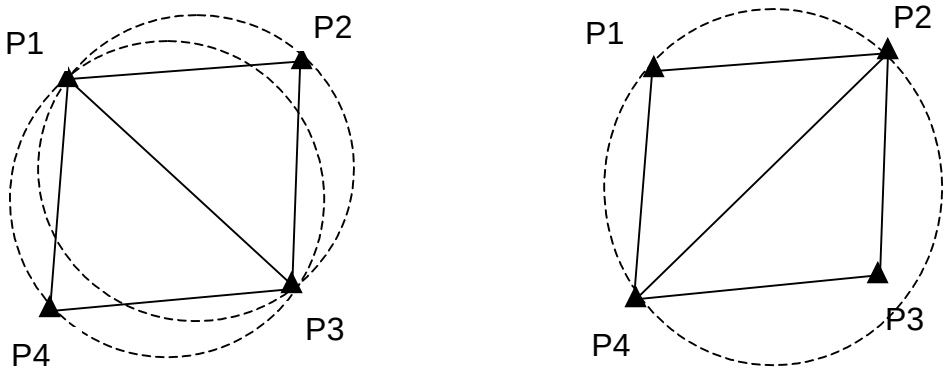

Figure 6.48: Delaunay Triangulation. (a) is an example of Delaunay Triangulation, but (b) is not.

Given a set of recordings (or simulations) at fixed sites, it is therefore proposed to use Delaunay triangulation to define the geometric interpolation scheme, when possible.

6.6 Summary of Spatial Interpolation

A simple method for the spatial interpolation of earthquake accelerograms in the frequency domain is developed in this chapter. The basic assumptions are that (i) the Fourier amplitude at the site is the same as the recorded amplitude at the station, and (ii) each frequency component propagates radially from the epicenter with a constant apparent phase velocity:

$$A_{C,k}(\omega_n) = A_k(\omega_n)$$

$$\Phi_{C,k}(\omega_n) = \Phi_k(\omega_n) - \frac{(\delta_C - \delta_k)\cdot \omega_n}{v(\omega_n)}$$

Here, $A_k(\omega_n)$ denotes the Fourier amplitude of the n-th discrete frequency component at recording station P_k, $\Phi_k(\omega_n)$ is the Fourier phase angle of the same frequency component, $A_{C,k}(\omega_n)$ and $\Phi_{C,k}(\omega_n)$ are the Fourier components at the site C as inferred

from station P_k, δ_C is the epicentral distance of the site, δ_k is the epicentral distance of recording station P_k, and $v(\omega_n)$ is the apparent propagation velocity of the n-th frequency component.

The Fourier amplitudes are interpolated according to:

$$\hat{A}_C(\omega_n) = \sqrt{\frac{1}{\sum_k w_k} \sum_k w_k \cdot A_{C,k}^2(\omega_n)}$$

$$w_k = \frac{1}{d_k^2}$$

where d_k is the distance between the site and the recording station P_k. The phase angles are interpolated using:

$$\hat{\Phi}_C(\omega_n) = \arctan\left(\frac{\sum_k w_k \cdot \mathrm{Im}\left[A_{C,k}(\omega_n) \cdot \exp\left(j \cdot \Phi_{C,k}(\omega_n)\right)\right]}{\sum_k w_k \cdot \mathrm{Re}\left[A_{C,k}(\omega_n) \cdot \exp\left(j \cdot \Phi_{C,k}(\omega_n)\right)\right]} \right)$$

$$w_k = \frac{1}{d_k^2}$$

Data from the SMART-1 array in Taiwan are used to validate the Fourier transform interpolation method, where interpolations are compared to recordings. The Fourier amplitude interpolation model yields good results for inter-station spacing up to 2 kilometers. The quality of the phase angle interpolation is more dependent on spacing and frequency than the amplitude interpolation. In general, the interpolated phase angles compare well with the recorded ones for inter-station spacing up to 200 meters and frequencies less than 3 Hz. The interpolated phase angles do not compare well with recorded phase angles for frequencies over 5 Hz or inter-station spacing larger than 1 kilometer.

Even though the interpolated phase angles do not compare well with the recorded ones for large inter-station spacings or high frequencies, the resulting time histories do look realistic. Therefore, the spatial interpolation method developed in this chapter can be

used to predict time histories for inter-station spacing larger than 1 kilometer, if it is not desired to estimate the differential motion between the two sites.

It is shown that a triangular interpolation scheme is an effective way to yield accurate results. A two-point interpolation can yield as good results as the triangular interpolation, provided that the two interpolation points and the site at which the ground motion is to be estimated are on a straight line that is perpendicular to the direction of the seismic wave propagation. Using twelve points rather than three points does not produce significantly better interpolation results.

CHAPTER 7
CASE STUDY: THE NORTHRIDGE EARTHQUAKE

In the preceding chapters, new models for the simulation and spatial interpolation of earthquake ground motion were presented and validated. In this chapter, these models are applied to the 1994 Northridge, California, earthquake. The intent is to demonstrate the applicability of the models.

The Northridge earthquake occurred at 4:31 a.m. Pacific Standard Time on January 17, 1994. The epicenter was at 118.54° West and 34.21° North (Hauksson and Jones, 1995) in the San Fernando Valley, approximately 30 km west-northwest of downtown Los Angeles. The moment magnitude of the earthquake was M_w = 6.7. Analyses of seismograms imply an almost pure thrust motion on a plane striking north-northwest and dipping down to the south-southwest. The earthquake originated at the down-dip, southeastern corner of this plane (at a depth of 19 km) and ruptured upwards and about 15 km to the northwest. Wald and Heaton (1994) found no evidence of slip above 7 km depth.

Strong motion accelerograms from the Northridge earthquake were obtained from more than two-hundred ground response stations throughout southern California. These stations are operated by many different agencies, most of them by the California Division of Mines and Geology, the U.S. Geological Survey, or the University of Southern California. The study presented in this chapter only utilizes recordings from 45 stations operated by the California Division of Mines and Geology. There are several reasons for using data from only these 45 stations:

- By using sparse records from a single agency, the situation immediately following a catastrophic event is better reproduced.
- Only records from stations within a certain distance interval are of interest; no near-field records or weak-motion far-field records are included.
- Only uncorrected records from stations whose sensor properties (for signal processing purposes) are readily available are used in this study.

A map showing the location of the recording stations with respect to the epicenter is displayed in Figure 7.1. The stations that are used in this case study are tabulated in Appendix F.

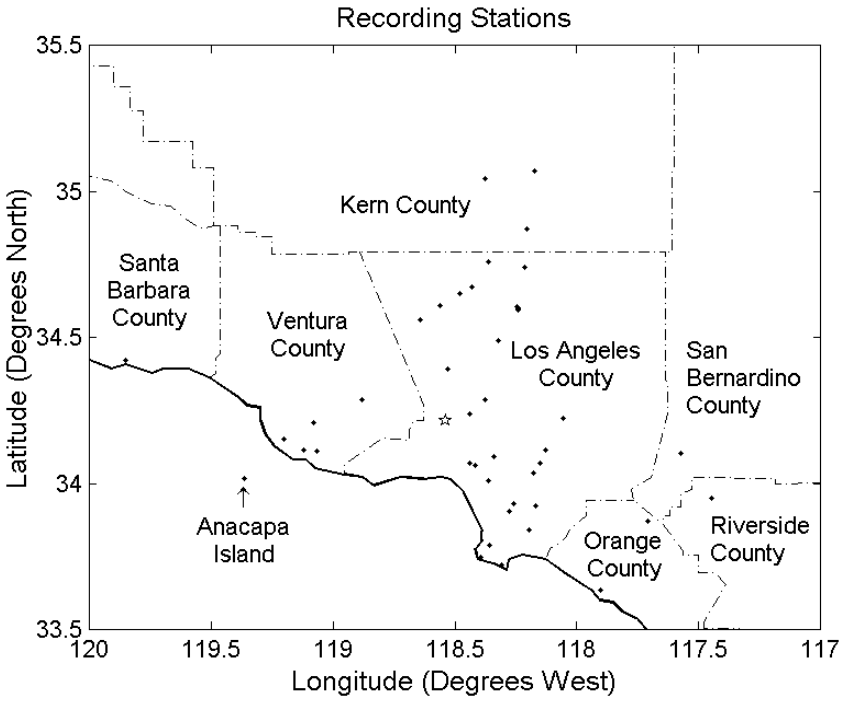

Figure 7.1: A map showing the location of the recording stations (dots) used in this chapter. The star marks the epicenter of the Northridge earthquake.

In the following section, ground motion intensity maps (showing peak ground acceleration as well as spectral acceleration at selected natural periods) from simulated time histories are compared to maps obtained from recordings in the Northridge earthquake. In Section 7.2, the spatial interpolation method presented in Chapter 6 is used to estimate the acceleration time history that a certain highway bridge, which collapsed in the earthquake, is likely to have experienced.

7.1 Ground Motion Intensity Maps

In this section, the results from the ground motion simulation model presented in Chapters 4 and 5 are compared to recordings made in the Northridge earthquake. The focus is on the east-west component of surface ground acceleration. The recordings at the 45 stations shown in Figure 7.1 are used to estimate the model parameters as function of distance from the surface projection of the seismogenic rupture.

In Figures 7.2 through 7.5, the results of the simulations are compared to the recordings, station by station. Ten simulations are performed at each location and the mean and the mean plus or minus one standard deviation of various ground motion intensity parameters are compared to those of the recorded ground motion. The ground motion intensity parameters that are compared are the peak ground acceleration, and the elastic, 5% damped pseudo spectral accelerations corresponding to natural periods of 0.3, 1.0 and 2.0 seconds. These natural periods are chosen because they are often taken as representative of the fundamental periods for low-rise, mid-rise and high-rise steel frame structures, respectively. The recorded ground motion intensity parameters and summary statistics of the simulated ground motion intensity parameters are tabulated in Appendix F.

The simulated peak ground accelerations are compared to the recorded peak ground accelerations in Figure 7.2. In Figure 7.2(a) the relationship between the simulated and recorded peak ground accelerations is plotted on a linear scale and in Figure 7.2(b) the relationship is plotted on a logarithmic scale. The mean peak ground accelerations from ten simulations are plotted, along with the mean +/- one standard deviation, as functions of the recorded peak ground acceleration. The solid line represents the line $y = x$. For 26 stations out of 45, the recorded peak ground acceleration is within one standard deviation from the mean of the simulated peak ground accelerations. This scatter is consistent with common statistical models. For example, 68% of all outcomes will lie within one standard deviation of the mean for a Gaussian distribution.

The simulated spectral accelerations corresponding to natural periods of 0.3, 1.0 and 2.0 seconds are compared to the recorded spectral accelerations in Figures 7.3, 7.4 and 7.5, respectively. In general, the agreement of the spectral acceleration is better than

the agreement of the peak ground acceleration. For a natural period of 0.3 seconds, the recorded spectral acceleration is within one standard deviation of the mean for 37 stations of 45. For natural periods of 1.0 and 2.0 seconds, the recorded spectral acceleration is within one standard deviation of the mean for 34 stations of 45.

The recorded quantity (peak ground acceleration or spectral acceleration corresponding to a natural period of 0.3, 1.0 and 2.0 seconds) is never more than two standard deviations away from the corresponding mean from ten simulations. In general, it is concluded from Figures 7.2 through 7.5 that the simulated ground motions are statistically consistent with the recorded time histories across the various stations.

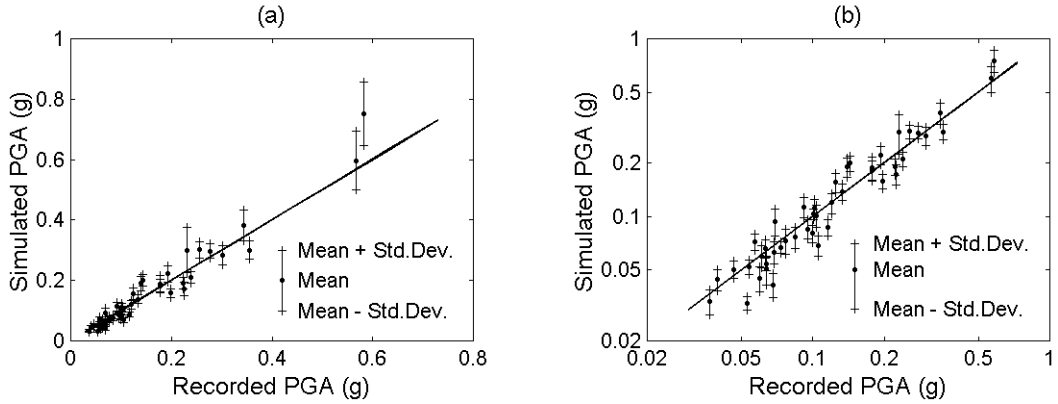

Figure 7.2: Statistics (from ten simulations) of peak ground acceleration as functions of the recorded peak ground acceleration for the east-west component at 45 stations in the 1994 Northridge earthquake. (a) Linear space; (b) logarithmic space.

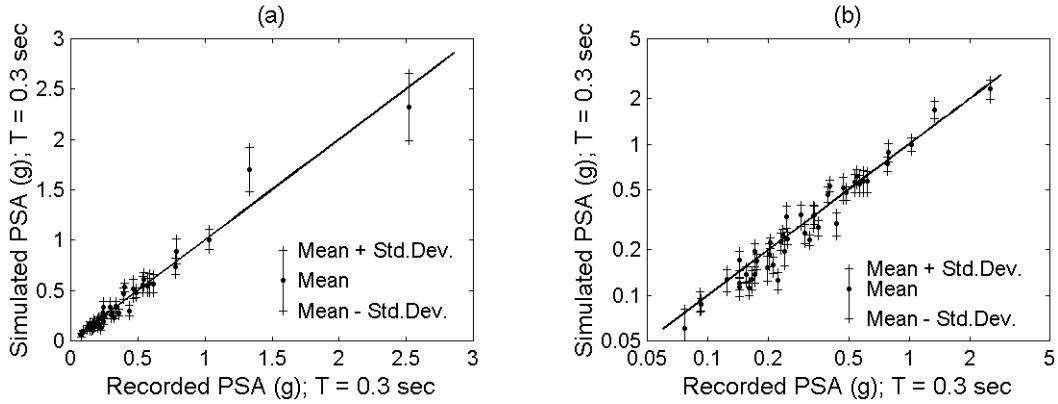

Figure 7.3: Statistics (from ten simulations) of spectral acceleration, corresponding to a natural period of 0.3 sec, as functions of the recorded spectral acceleration for the east-west component at 45 stations in the 1994 Northridge earthquake. (a) Linear space; (b) logarithmic space.

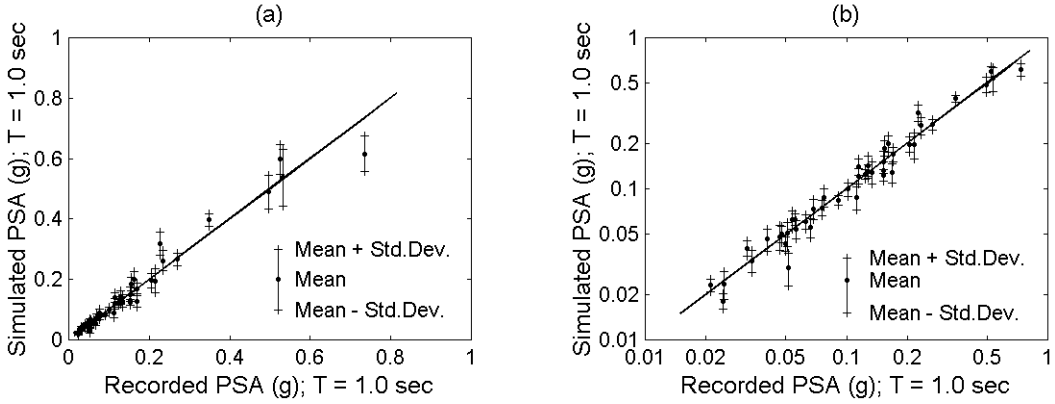

Figure 7.4: Statistics (from ten simulations) of spectral acceleration, corresponding to a natural period of 1.0 sec, as functions of the recorded spectral acceleration for the east-west component at 45 stations in the 1994 Northridge earthquake. (a) Linear space; (b) logarithmic space.

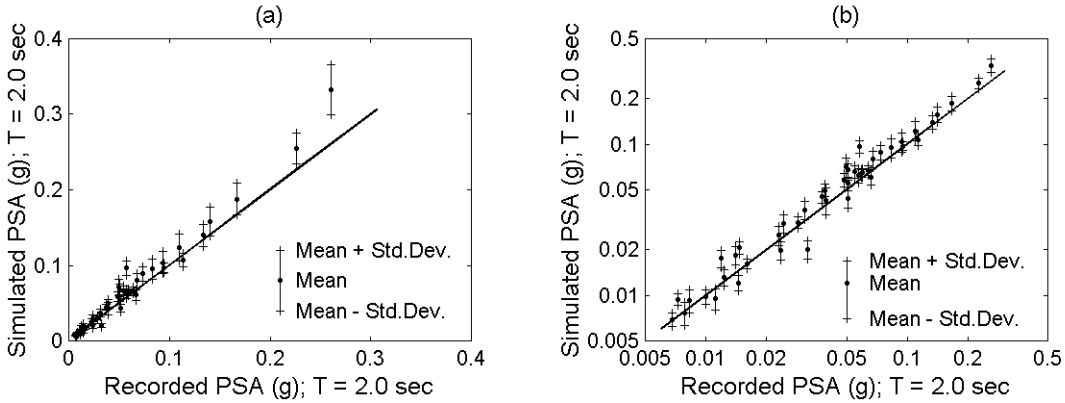

Figure 7.5: Statistics (from ten simulations) of spectral acceleration, corresponding to a natural period of 2.0 sec, as functions of the recorded spectral acceleration for the east-west component at 45 stations in the 1994 Northridge earthquake. (a) Linear space; (b) logarithmic space.

Having compared characteristics of the simulated time histories to the recorded ones station by station, it is of interest to compare ground motion intensity maps created from simulated time histories to intensity maps obtained from recorded time histories. This comparison is performed in terms of contour maps, which are presented in Figures 7.6 through 7.9. The solid contour lines are derived from the recorded ground motions at

the 45 recording stations shown in Figure 7.1. The dashed contour lines in Figures 7.6 through 7.9 are derived from simulated accelerograms. Ten simulations are performed at each point of a rectangular grid and the quantity that is contoured is the average result from the ten simulations. The grid is defined between 117.0 and 120.0 degrees west, and between 33.5 and 35.5 degrees north. It has a constant spacing of 0.1 degrees, both in latitude and longitude, which corresponds to approximately 9 km spacing in the east-west direction and 11 km spacing in the north-south direction.

A contour map of the peak ground acceleration of the east-west component in the Northridge earthquake is displayed in Figure 7.6. Contour maps for the spectral acceleration corresponding to a natural period of 0.3, 1.0 and 2.0 seconds are shown in Figures 7.7, 7.8 and 7.9, respectively. In general, the comparison between the simulated and the recorded ground motion intensity maps is good. However, several observations regarding their systematic differences can be made:

- The simulated contours for the 0.3 second spectral acceleration tend to be more elongated towards the northwest than the recorded contours – especially those representing spectral acceleration of 1.0 g and 1.5 g. This difference could be due to a directivity effect, which is not captured by the simulation model.
- The simulated contours for the 2.0 second spectral acceleration tend to be outside the corresponding recorded contours. This may imply a slight underestimation of the attenuation in the simulation model for this long-period motion.

The relatively small differences that are observed between the recorded and simulated contour maps are not necessarily due to shortcomings in the simulation model or in the estimation of the model parameters. These differences could also be caused by the different spatial distribution of the grid points as compared to the recording stations.

In this section, the applicability of the earthquake ground motion simulation model for the generation of ground motion intensity maps over an entire region has been shown. In the following section, the interpolation of ground motion time histories is demonstrated.

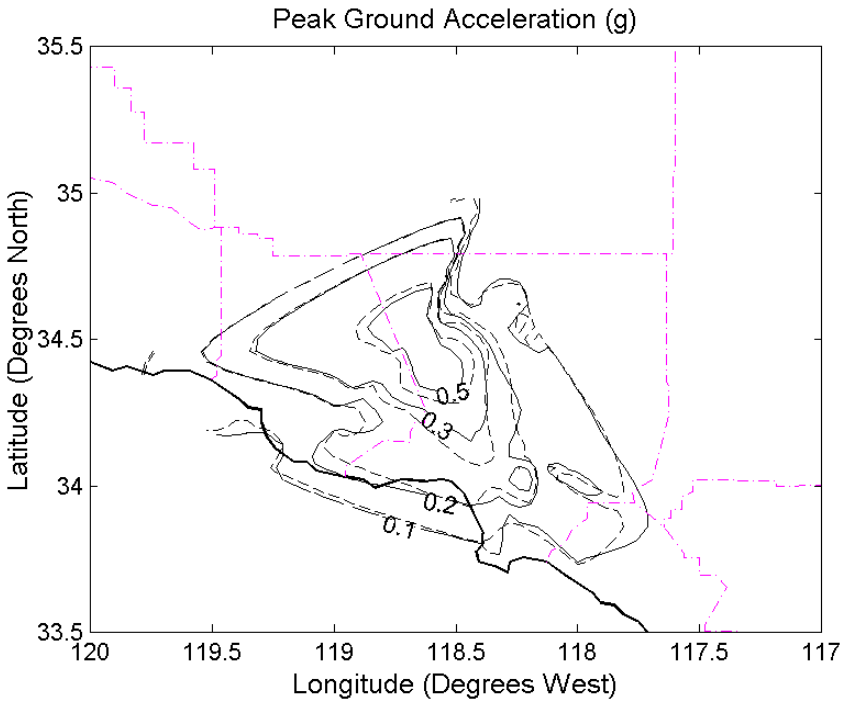

Figure 7.6: A contour map showing recorded (solid lines) and simulated (dashed lines) peak ground acceleration for the east-west component in the 1994 Northridge earthquake.

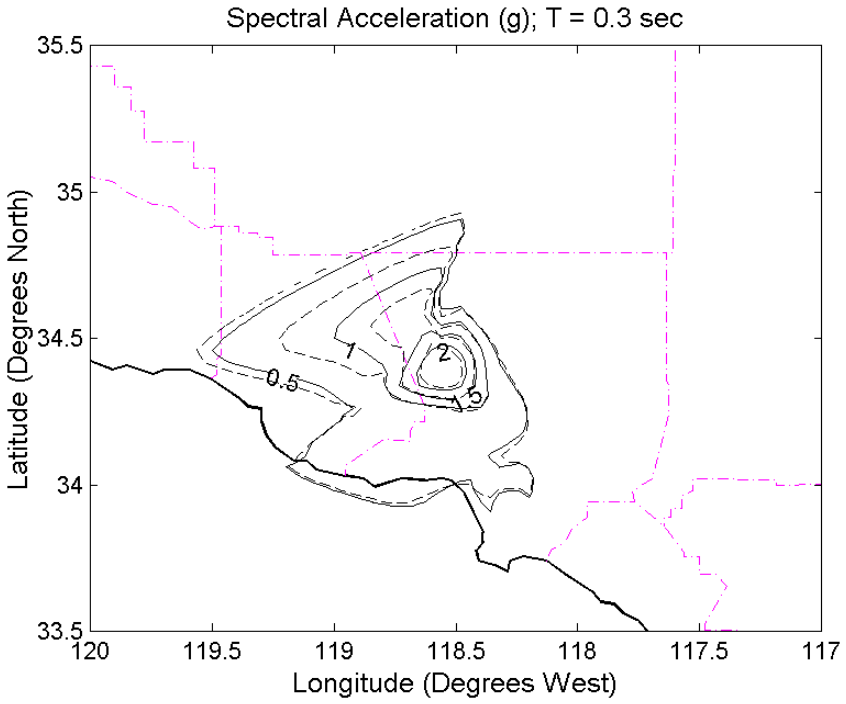

Figure 7.7: A contour map showing recorded (solid lines) and simulated (dashed lines) spectral acceleration, corresponding to a natural period of 0.3 sec, for the east-west component in the 1994 Northridge earthquake.

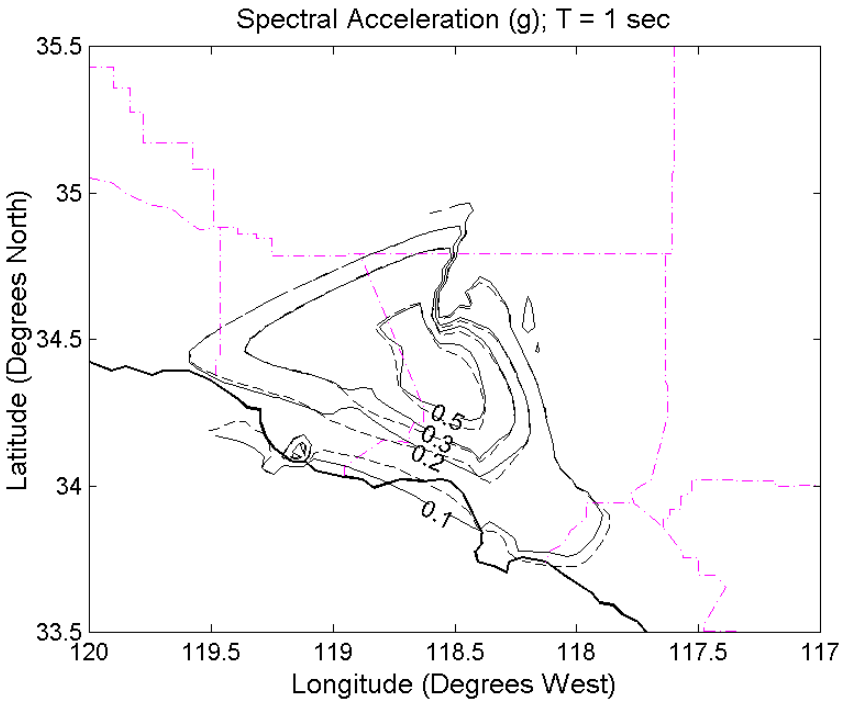

Figure 7.8: A contour map showing recorded (solid lines) and simulated (dashed lines) spectral acceleration, corresponding to a natural period of 1.0 sec, for the east-west component in the 1994 Northridge earthquake.

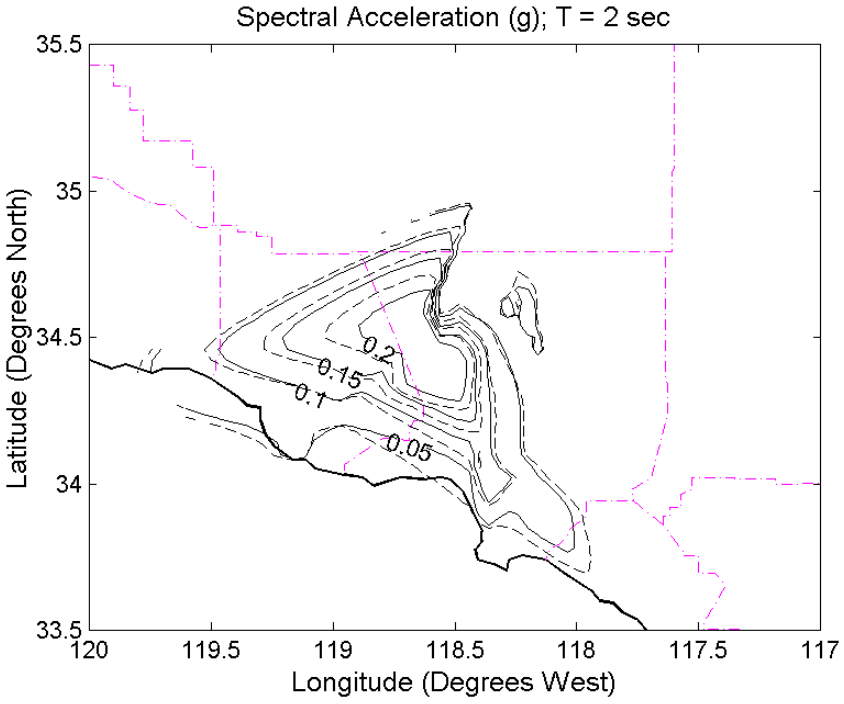

Figure 7.9: A contour map showing recorded (solid lines) and simulated (dashed lines) spectral acceleration, corresponding to a natural period of 2.0 sec, for the east-west component in the 1994 Northridge earthquake.

7.2 Interpolation of Time Histories

In order to correlate ground motion to building damage, it is necessary to have a recording of a ground motion at the location of the damaged facility. This is very rarely the case. Instead, one is faced with inferring the ground motion from near by, or in many cases not so near by, recording stations. In Chapter 6, a method for the interpolation of earthquake ground motion in the frequency domain was proposed. In this section, its application is demonstrated by taking an example from the Northridge earthquake.

One of the highway bridges that collapsed in the Northridge earthquake was the La Cienega and Venice undercrossing on the I-10 Santa Monica Freeway (bridge number 53-1609). It is located approximately 25 km southeast of the epicenter. The collapse of this bridge was attributed to brittle shear failure of the concrete columns, due to insufficient transverse reinforcement (Moehle et al., 1995). The bridge was designed and constructed in the 1960's.

To learn exactly what went wrong, however, it is not sufficient to only identify the deficiencies in the design and construction of the bridge. To complete the picture, it is necessary to obtain information on the ground motion at the site. No recordings were obtained at the site. The three ground response stations closest to the site are Baldwin Hills (BHA; epicentral distance of 28.1 km), the Hollywood Storage Building parking lot (HSL; epicentral distance of 23.0 km) and the Century City Country Club (LCN; epicentral distance of 20.2 km). These are shown on the map in Figure 7.10. The Baldwin Hills station is located approximately 3.2 km south-southeast of the site, the Century City station is about 5.2 km to the northwest, and the Hollywood Storage Building is roughly 6.6 km to the north-northeast of the bridge site. The site and the three recording stations are all located in the Los Angeles Basin, with comparable local soil conditions.

In this section, the recorded time histories at Baldwin Hills, Century City, and the Hollywood Storage Building are used to estimate the ground motion that the La Cienega and Venice undercrossing on I-10 is likely to have experienced. First, a three-point interpolation is used to estimate the ground motion at the site, using the triangular interpolation scheme introduced and recommended in Chapter 6. Then, the effects of

different apparent phase velocities are examined. Finally, results from a two-point interpolation are compared to the results from the three-point interpolation.

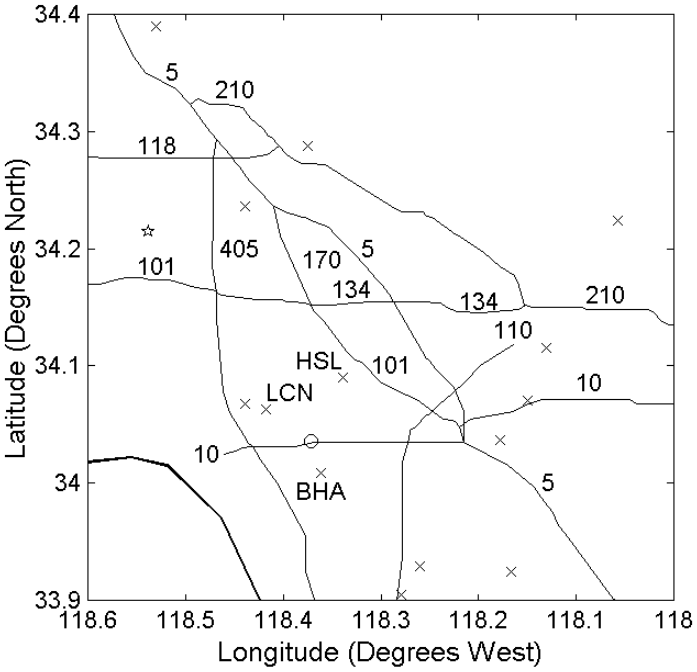

Figure 7.10: A map showing the major highways in the Los Angeles region. The star marks the epicenter of the Northridge earthquake. The crosses denote recording stations. The circle shows the location of the La Cienega - I 10 undercrossing.

7.2.1 Three-Point Interpolation

The Fourier amplitude and Fourier phase spectra of the ground motion at the bridge site are estimated as the weighted averages of the corresponding quantities inferred from the surrounding recording stations. The weights are inversely proportional to the squared distance between the site and the stations (see Equations 6.1, 6.2, 6.5 and 6.6). The apparent phase velocity used in this interpolation is 4 km/s for all frequency components. A quick and approximate frequency-wave number analysis yielded estimates of the apparent phase velocity ranging between 3.5 km/s and 5 km/s. The value of 4 km/s was chosen as a representative value, but a sensitivity study with respect to this parameter is included in the following subsection.

The results of the interpolation of the east-west component of the acceleration are shown in Figures 7.11 through 7.13, while the results for the north-south component are displayed in Figures 7.14 through 7.16. Figures 7.11 and 7.14 show the recorded and interpolated time histories. The time axis in all the graphs in this chapter starts at 2.8 seconds after 4:31 a.m. PST. All time histories are 41 seconds long (2048 points at 50 Hz sampling frequency), but only the first 25 seconds are shown here. Figures 7.12 and 7.15 show the elastic, 5% damped pseudo acceleration response spectra, and Figures 7.13 and 7.16 show the cumulative, normalized Arias intensities. The Arias intensity of each time history is normalized with respect to the Arias intensity (i.e., the total energy) of the interpolated time history. Hence, the nonstationary characteristics as well as the total energy of the recorded time histories can easily be compared to the corresponding attributes of the interpolated time history on a single plot.

The recorded east-west components and the interpolated time history are shown in Figure 7.11. The recorded peak ground accelerations are 0.26 g, 0.23 g and 0.24 g, at stations LCN, HSL and BHA, respectively. The peak ground acceleration of the interpolated time history is 0.24 g. The response spectrum of the interpolated time history is similar to the response spectra of the recorded time histories, as shown in Figure 7.12. The nonstationary characteristics and the total energy of the time histories are compared in Figure 7.13. Everything is as expected. The total energy at the stations closer to the epicenter than the site (LCN and HSL) is larger than the total energy of the interpolated time history, and the total energy at the station that is farther away from the epicenter (BHA), is smaller than the energy of the interpolated time history. Furthermore, the cumulative intensity curves in Figure 7.13 never cross each other. The cumulative energy at the site is always larger than the cumulative energy at BHA, while it is always smaller than the cumulative energy at HSL. The cumulative energy at LCN, the recording station that is closest to the epicenter, is always larger than the cumulative energy at any of the other three locations.

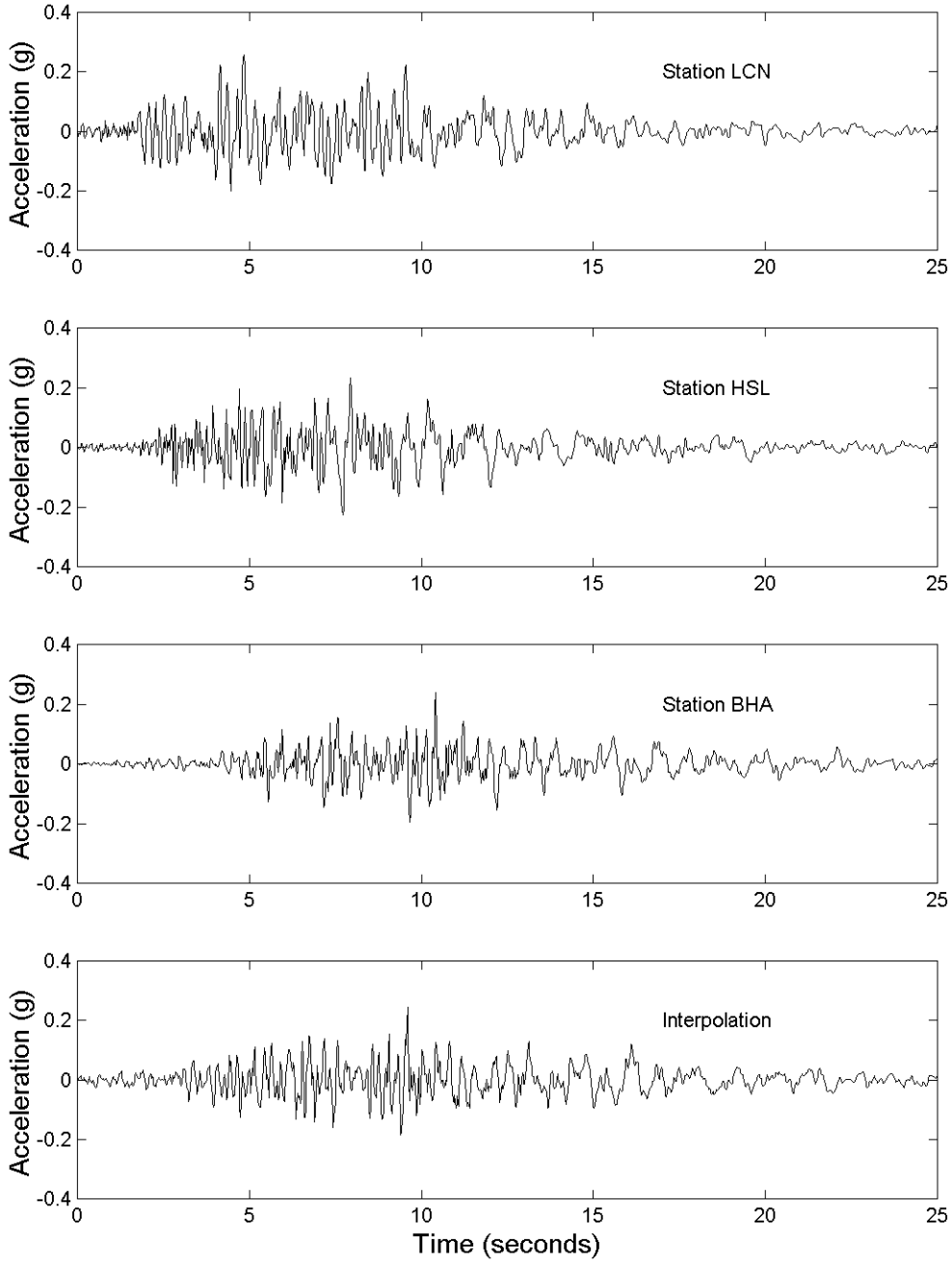

Figure 7.11: The east-west component of the recorded acceleration time histories at stations LCN, HSL and BHA, and the interpolated time history.

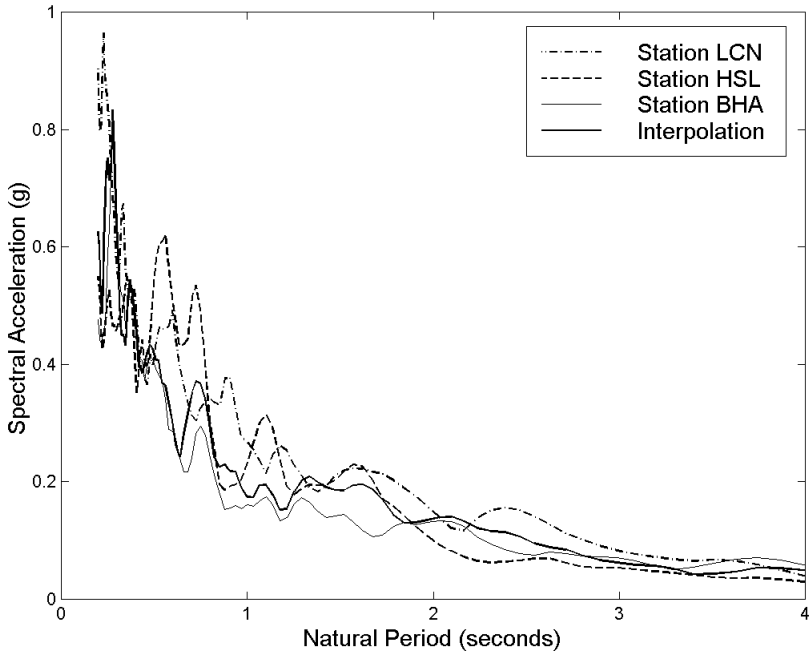

Figure 7.12: The elastic, 5% damped, pseudo acceleration response spectra for the east-west component of the recorded acceleration time histories at stations LCN, HSL and BHA, and for the interpolated time history.

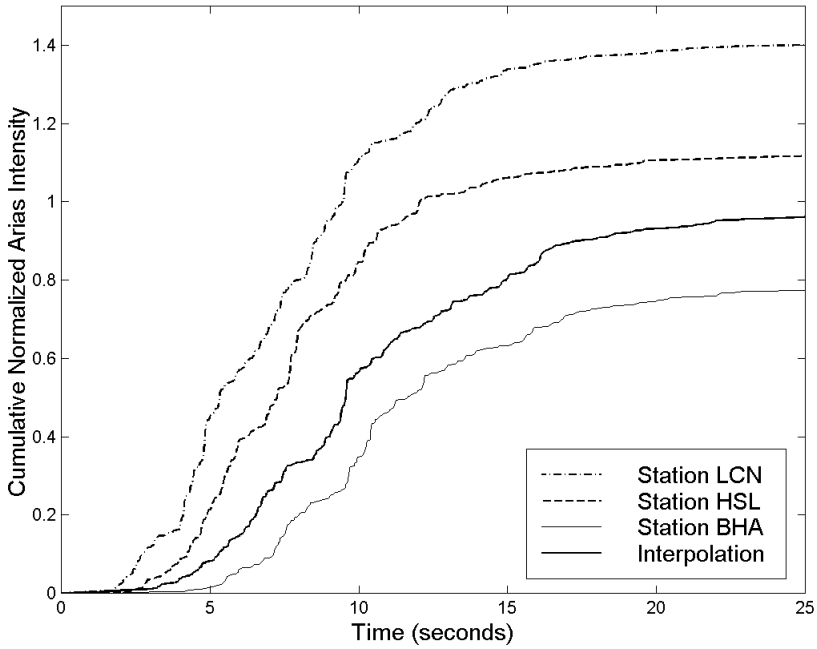

Figure 7.13: Cumulative normalized Arias intensity for the east-west component of the recorded acceleration time histories at stations LCN, HSL and BHA, and for the interpolated time history. The Arias intensities are normalized w.r.t. the intensity of the interpolated time history.

The results of the interpolation of the north-south component of the ground surface acceleration are displayed in Figures 7.14, 7.15 and 7.16. The time history recorded at the Hollywood Storage Building (HSL) is very different from the other two recordings (see Fig. 7.14). The recorded peak ground accelerations are 0.22 g, 0.39 g and 0.17 g, at stations LCN, HSL and BHA, respectively. The peak ground acceleration of the interpolated time history is 0.23 g. It is evident from the response spectra in Figure 7.15 that the HSL record has larger high-frequency content (natural periods lower than 1 second, or frequencies higher than 1 Hertz) than the other records. Furthermore, the total energy of the HSL record is obviously larger than the total energy of the other two records, as can be seen in the cumulative normalized Arias intensity plot in Figure 7.16.

Clearly, the Hollywood Storage Building record has very different characteristics than the records obtained at Baldwin Hills or the Century City Country Club, which affects the interpolated time history. It would be interesting to know why the characteristics of the north-south component of the HSL record are so different from the characteristics of the north-south components of the other two records (LCN and BHA), while the characteristics of the east-west components of all three records are relatively similar to each other. The reason could be that the Hollywood Storage Building station is on the northern edge of the Los Angeles Basin, close to the Santa Monica Mountains and considerably closer to the mountains than the other two stations. It is possible that the proximity of the HSL station to the Santa Monica Mountains affects the north-south component of the ground motion, while not having significant effect on the east-west component.

In view of the above, perhaps station HSL should be excluded from the interpolation when the ground motion at the site of the La Cienega and Venice undercrossing on the Santa Monica Freeway is estimated. The effects of that exclusion are investigated in subsection 7.2.3, but first, the sensitivity of the interpolation with respect to different estimates of apparent phase velocity is examined.

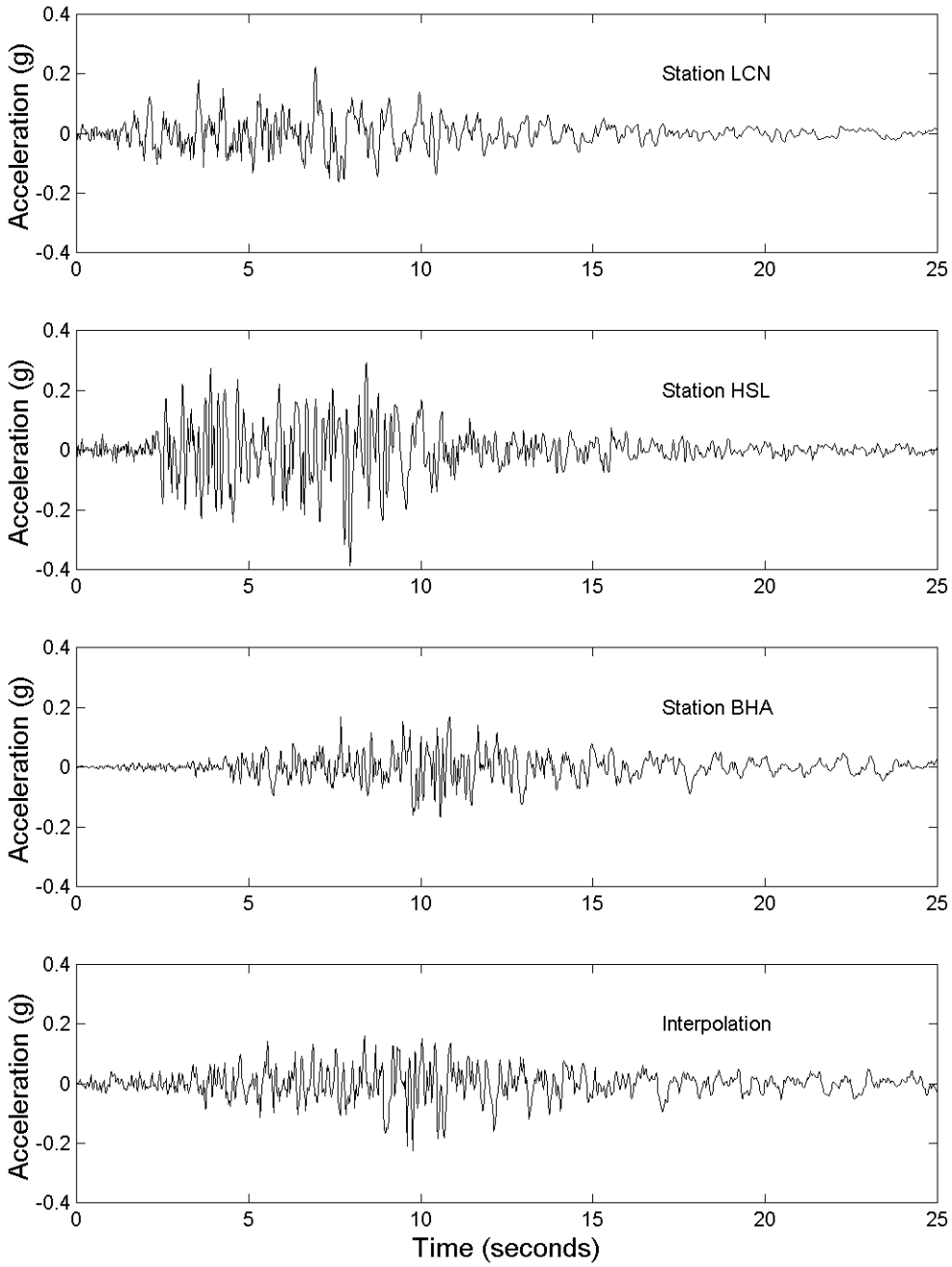

Figure 7.14: The north-south component of the recorded acceleration time histories at stations LCN, HSL and BHA, and the interpolated time history.

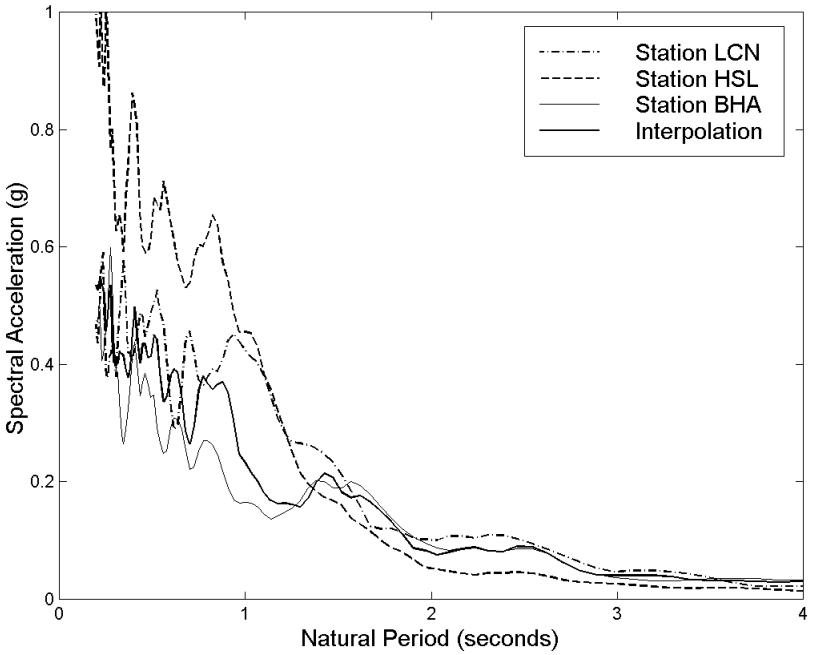

Figure 7.15: The elastic, 5% damped, pseudo acceleration response spectra for the north-south component of the recorded acceleration time histories at stations LCN, HSL and BHA, and for the interpolated time history.

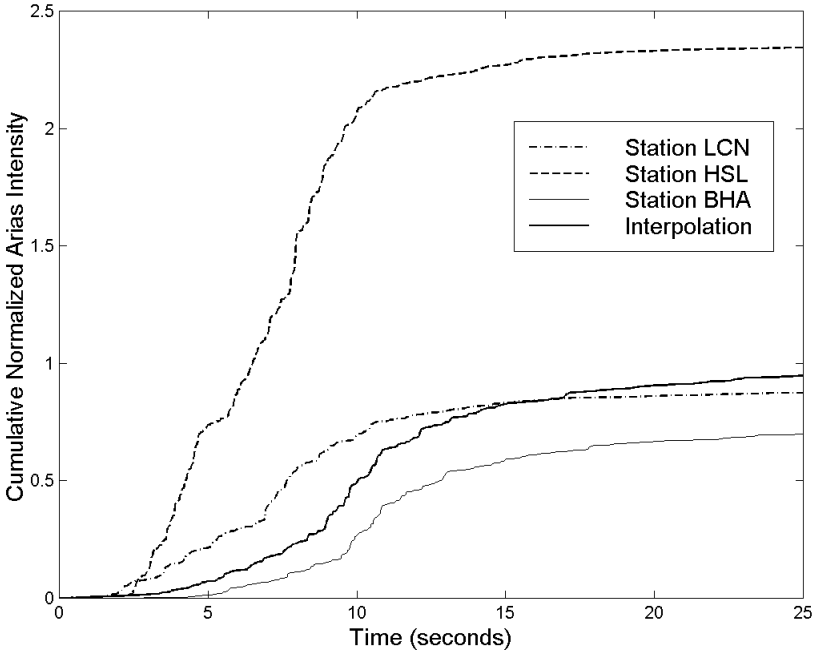

Figure 7.16: Cumulative normalized Arias intensity for the north-south component of the recorded acceleration time histories and for the interpolated time history. The intensities are normalized w.r.t. the intensity of the interpolated time history.

7.2.2 Effects of the Apparent Phase Velocity

As mentioned at the beginning of the last subsection, estimates of the apparent phase velocity in the propagation of the seismic wave train in the region ranged from 3.5 km/s to 5 km/s. Clearly, it is important to estimate this parameter correctly, if reliable estimates of the differential movement between two points are to be obtained. However, it is not as clear whether the particular value of this parameter has significant effect on the results of an interpolation as described in the preceding subsection. Therefore, the results of basic sensitivity analyses are presented in this subsection.

The east-west component of the three recordings obtained at the Century City Country Club (LCN), the Hollywood Storage Building parking lot (HSL) and the Baldwin Hills station (BHA) are again used here to estimate the east-west component of the acceleration time history at the site of the La Cienega and Venice undercrossing on the Santa Monica Freeway (see the map in Figure 7.10). The interpolation model presented in Equations (6.5) and (6.6) is used, including the basic assumptions put forward in Equations (6.1) and (6.2). In each interpolation, the apparent phase velocity is assumed to be the same for all frequency components. However, the three-point interpolation is performed using three different values for the apparent phase velocity: 3 km/s, 4 km/s and 5 km/s.

In Figure 7.17 the three interpolated time histories are displayed, assuming an apparent phase velocity of 3, 4 and 5 km/s, respectively. All time histories are qualitatively, even though the peak values are slightly different; 0.22 g, 0.24 g and 0.25 g, for an apparent velocity of 3, 4 and 5 km/s, respectively. The response spectra and the cumulative Arias intensity plots in Figures 7.18 and 7.19, respectively, are also very close to each other. It is, therefore, concluded that whether the apparent phase velocity is 3, 4, or 5 km/s, does not significantly affect the results of the three-point interpolation.

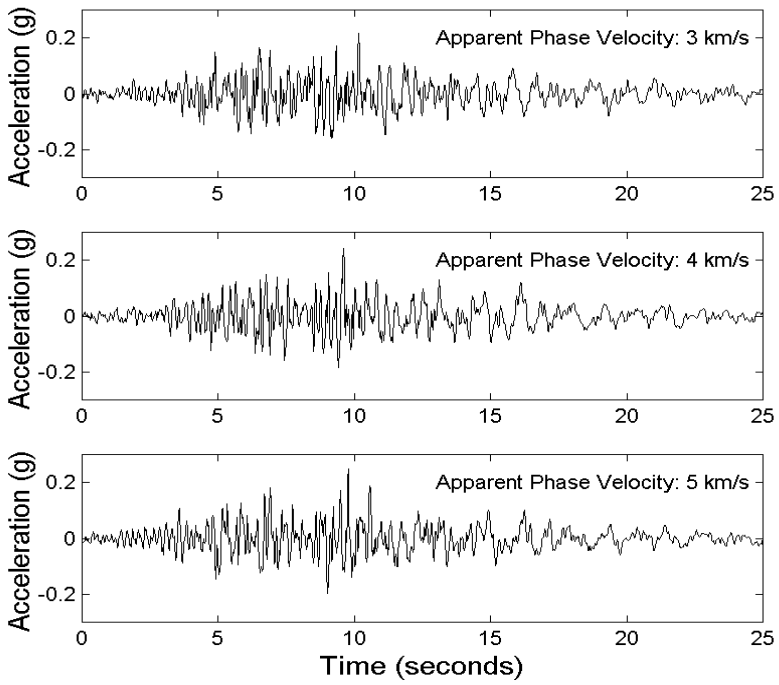

Figure 7.17: Interpolated acceleration time histories, using the east-west component of recordings at stations LCN, HSL and BHA, but three different apparent phase velocities.

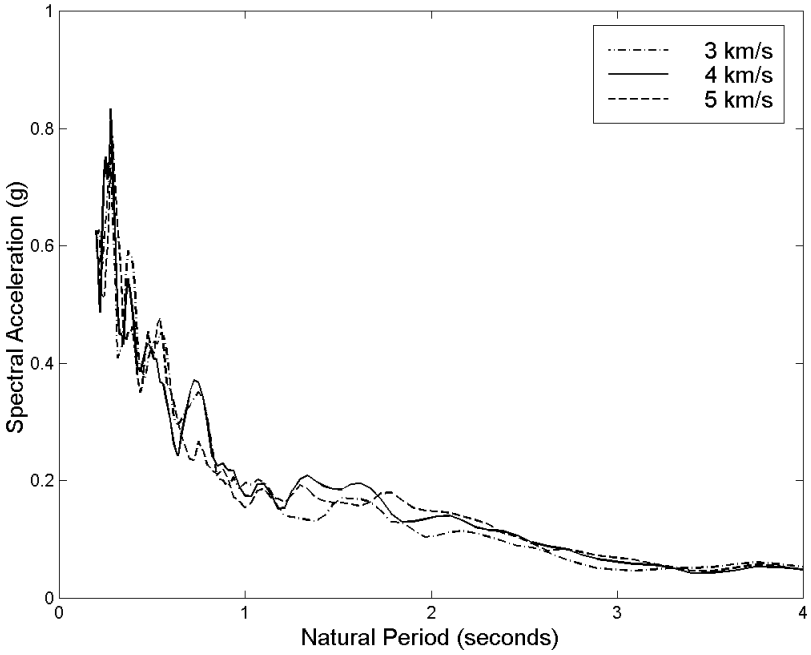

Figure 7.18: The elastic, 5% damped, pseudo acceleration response spectra for the time histories in Figure 7.17.

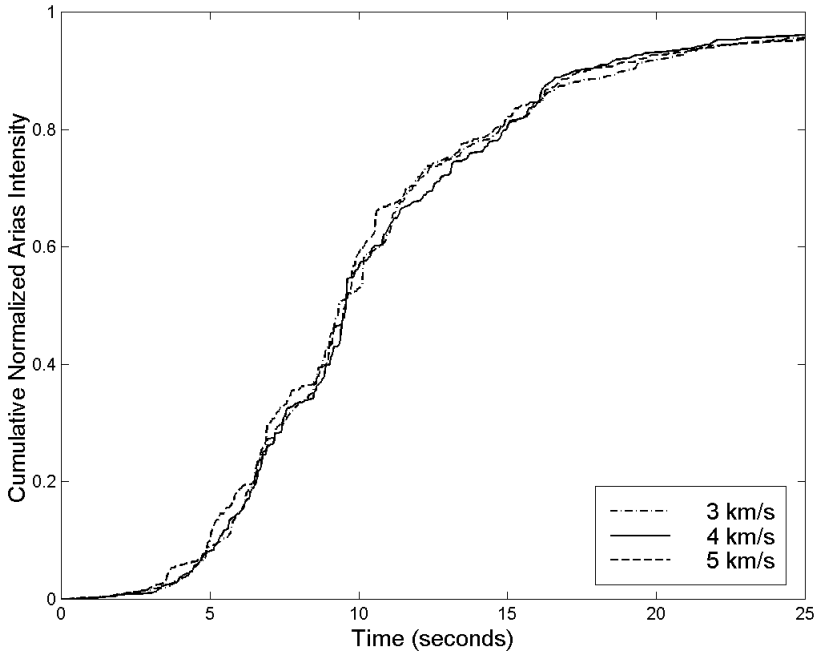

Figure 7.19: The cumulative normalized Arias intensities for the time histories in Figure 7.17.

7.2.3 Two-Point Interpolation

It was pointed out in subsection 7.2.1 that the characteristics of the north-south component of the recorded accelerogram in the Hollywood Storage Building parking lot (HSL) are considerably different from the characteristics of the north-south components recorded at the Baldwin Hills station (BHA) or the Century City Country Club (LCN). This difference could be due to the proximity of the HSL station to the Santa Monica Mountains. It is interesting to see what effect the exclusion of the HSL record from the interpolation has on the results. This subsection presents the results of the two-point interpolation, using recordings obtained at stations LCN and BHA to estimate the ground motion at the site of the La Cienega and Venice undercrossing on the Santa Monica Freeway, and compares those results with the results of the three-point interpolation, which were presented in subsection 7.2.1.

In Figure 7.20, the east-west component of the time histories recorded at stations LCN and BHA are plotted, as well as the interpolated time history. The recorded peak ground accelerations are 0.26 g and 0.24 g at stations LCN and BHA, respectively, and

the peak ground acceleration of the interpolated time history is 0.22 g. The elastic, 5% damped response spectra are shown in Figure 7.21. The response spectrum of the interpolated time history is, in general, between the recorded response spectra. Nothing surprising is revealed by the cumulative Arias intensity plot in Figure 7.22. The total energy of the interpolated time history is less than the energy of the recording made closer to the epicenter, but larger than the energy of the recording made farther away from the epicenter. Furthermore, the energy build-up with time is as expected, the energy arrives first at the point closest to the epicenter (station LCN), and last at the point farthest away from the epicenter (station BHA). Note, that the shape of the curve representing the interpolated time history matches more closely to the shape of the curve corresponding to the recording made at station BHA than the recording made at station LCN. This is because in the interpolation procedure, the weighted average of the components of the recordings, where the weights are inversely proportional to the squared distance between the recording station and the site in question. Hence, the relative weight of station BHA is 72%, while the relative weight of station LCN is only 28%.

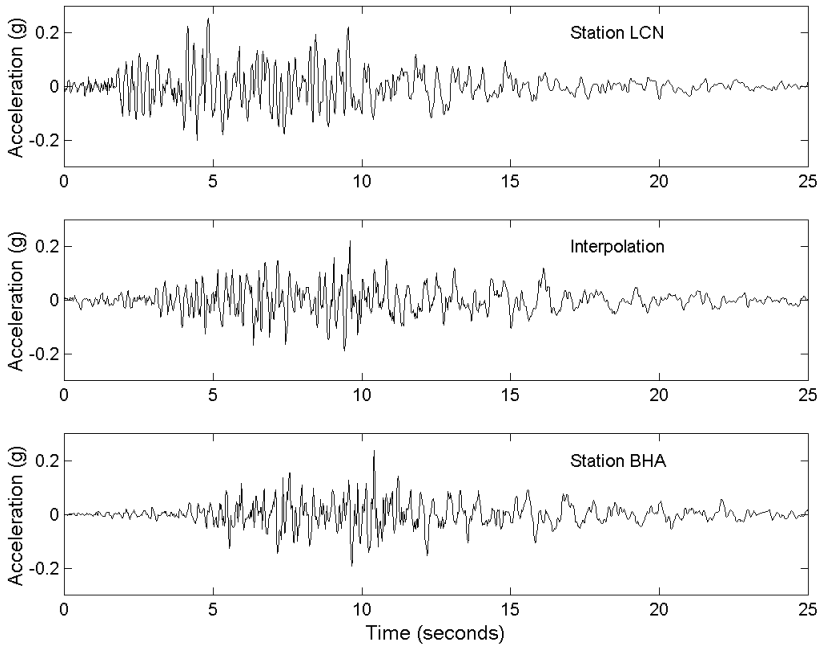

Figure 7.20: The east-west component of the recorded acceleration time histories at stations LCN and BHA, and the interpolated time history.

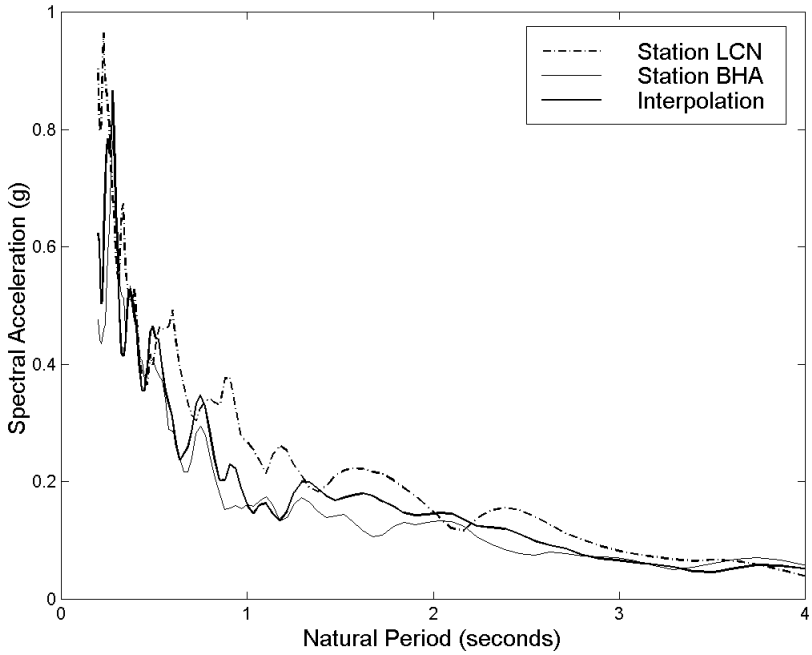

Figure 7.21: The elastic, 5% damped pseudo acceleration response spectra for the east-west component of the recorded time histories at stations LCN and BHA, and for the interpolated time history.

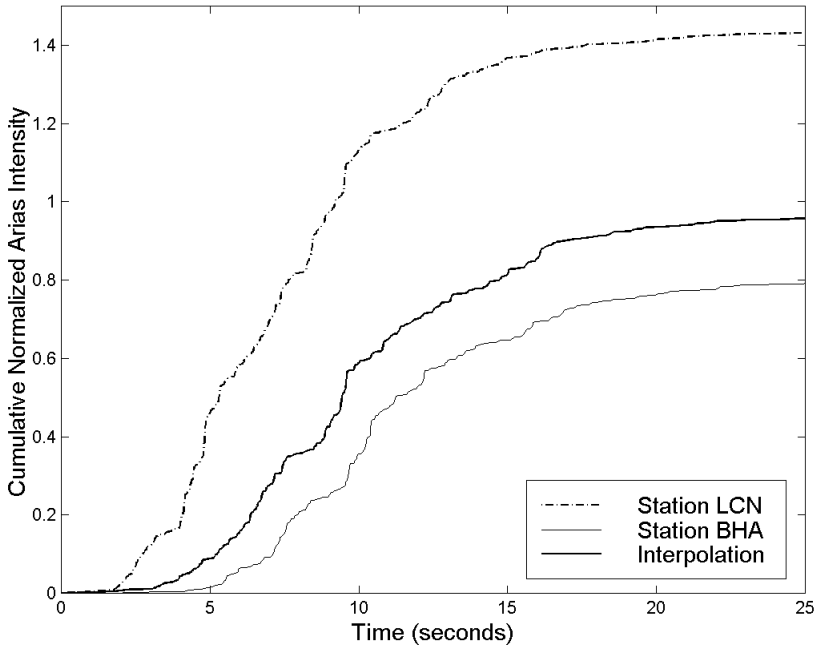

Figure 7.22: The cumulative, normalized Arias intensities for the east-west component of the recorded acceleration time histories at stations LCN and BHA, and for the interpolated time history. The Arias intensities are normalized w.r.t. the intensity of the interpolated time history.

The results of the two-point interpolation of the north-south component are illustrated in Figures 7.23 through 7.25. The recorded time histories are shown along with the interpolated time history in Figure 7.23. The recorded peak ground accelerations are 0.22 g and 0.17 g for stations LCN and BHA, respectively. The peak ground acceleration of the interpolated time history is 0.21 g. The elastic response spectra are shown in Figure 7.24 and the cumulative normalized Arias intensities are plotted in Figure 7.25. In both cases, the curve corresponding to the interpolated time history is between the curves representing the two recordings. As expected, the shape of the interpolation-curves more closely resembles the shape of the curve corresponding to station BHA than to that of station LCN.

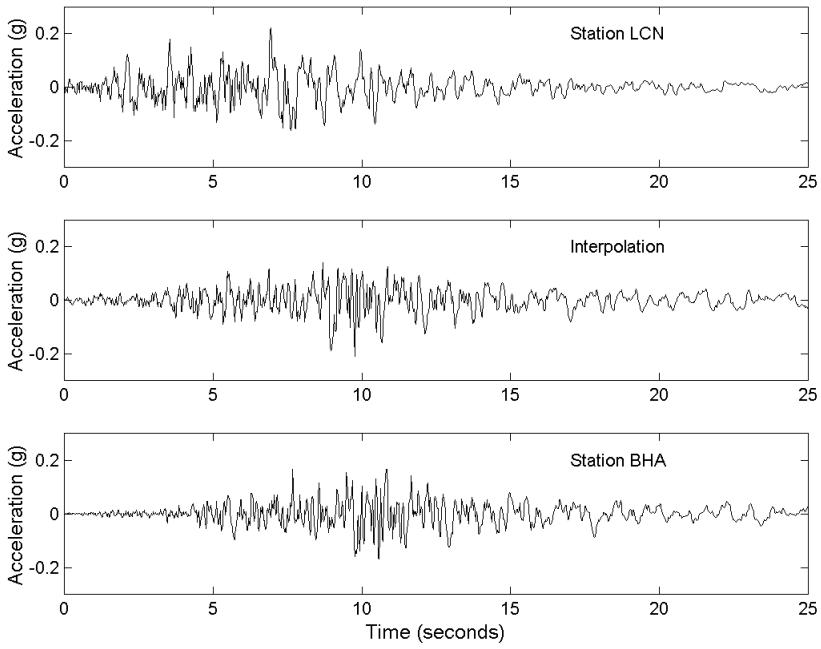

Figure 7.23: The north-south component of the recorded acceleration time histories at stations LCN and BHA, and the interpolated time history.

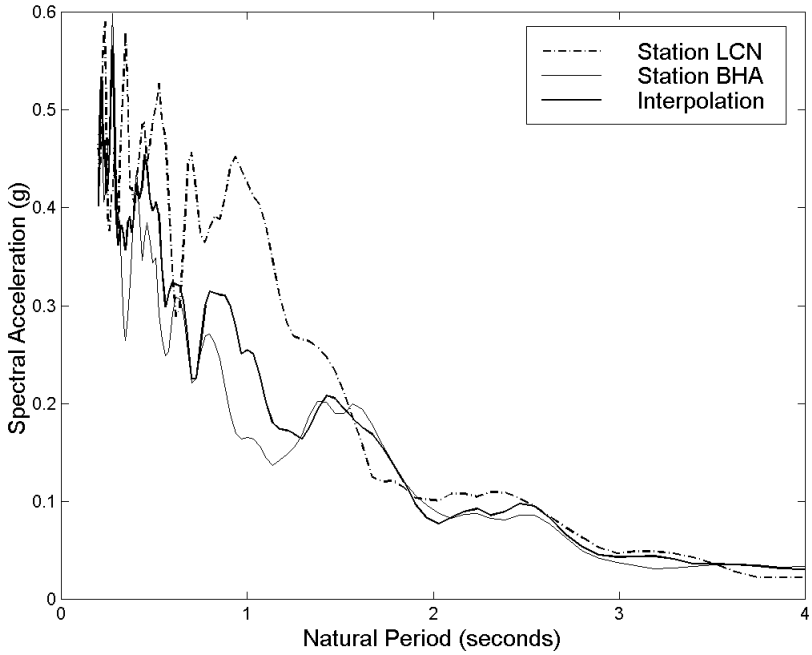

Figure 7.24: Elastic, 5% damped pseudo acceleration response spectra for the north-south component of the recorded acceleration time histories at stations LCN and BHA, and for the interpolated time history.

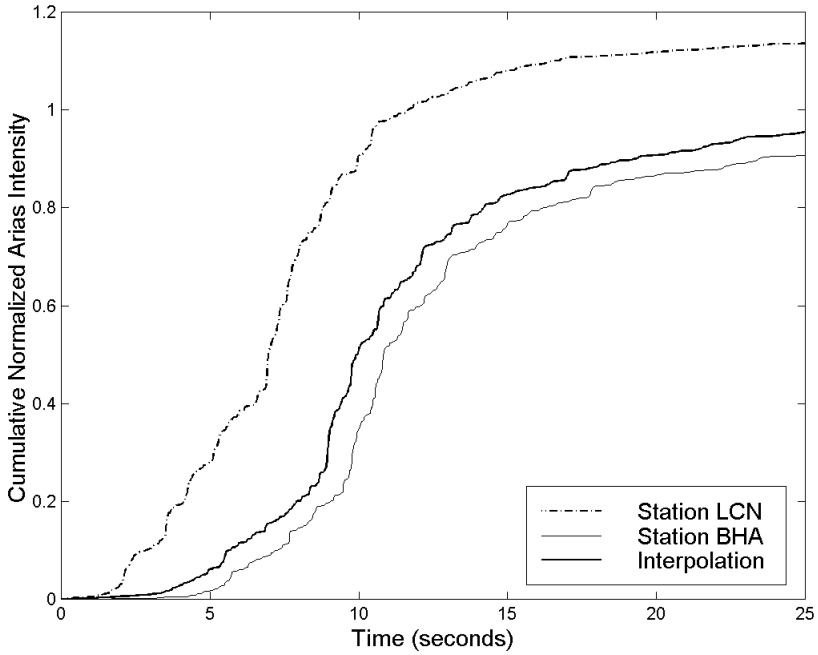

Figure 7.25: Cumulative, normalized Arias intensities for the north-south component of the recorded acceleration time histories at stations LCN and BHA, and for the interpolated time history. The Arias intensity is normalized w.r.t. the intensity of the interpolated time history.

In Figure 7.26, the two time histories obtained using three-point and two-point interpolation of the north-south component are compared. The peak ground accelerations are 0.23 g and 0.21 g for the three-point and two-point interpolation, respectively. It is evident, just by looking at these time histories, that the three-point interpolation has larger high-frequency content. That is confirmed in Figure 7.27, where the response spectra are compared. The response spectrum of the three-point interpolation is consistently higher than the response spectrum for the two-point interpolation, for periods under 1 second (frequencies higher than 1 Hertz). The cumulative normalized Arias intensities are compared in Figure 7.28. The most important feature there is that the total energy of the three-point interpolation is approximately 30% larger than the total energy of the two-point interpolation. The energy build-up of the three-point interpolation is also slightly faster than the build-up of the two-point interpolation, before the ratio stabilizes at 1.3 around the 10 seconds mark.

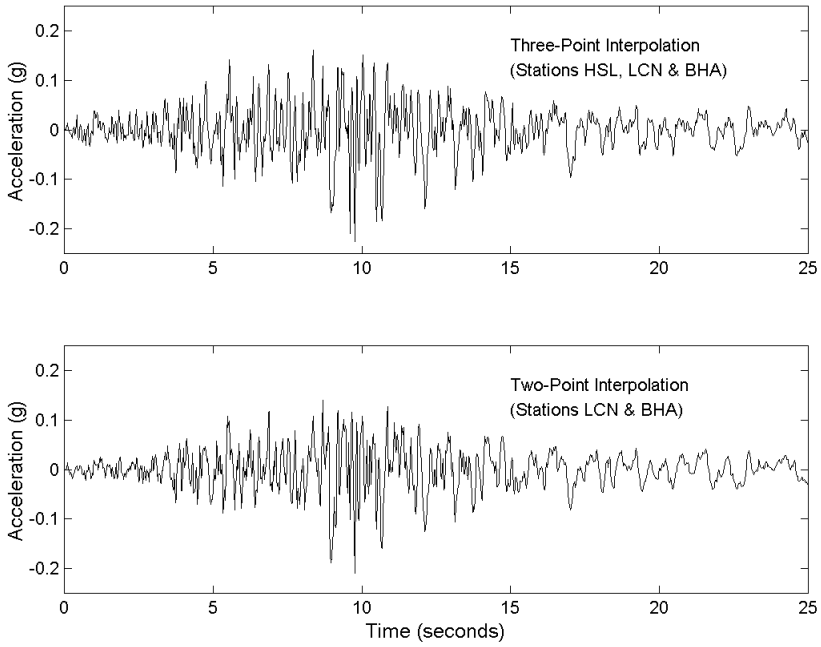

Figure 7.26: The north-south component of the interpolated acceleration time history at the La Cienega–I10 undercrossing, using three- and two-point interpolation, respectively.

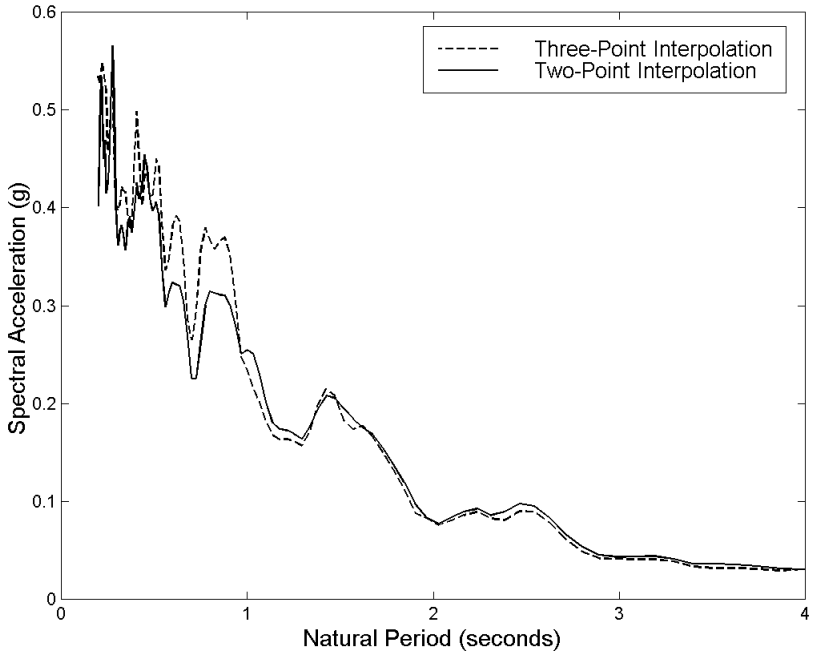

Figure 7.27: The elastic, 5% damped pseudo acceleration response spectra for the north-south component of the interpolated acceleration time history at the La Cienega–I10 undercrossing, using three- and two-point interpolation.

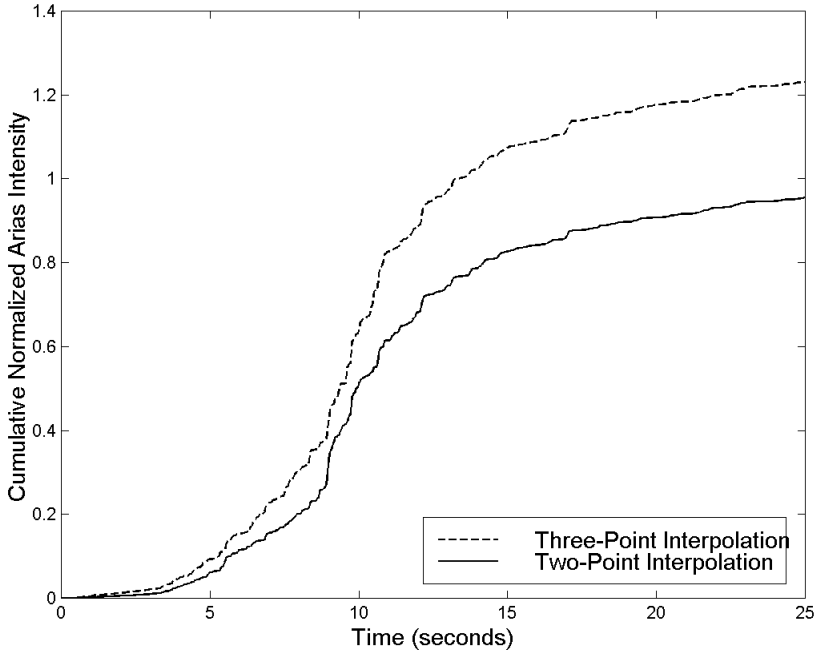

Figure 7.28: The cumulative, normalized Arias intensities for the north-south component of the interpolated acceleration time history at the La Cienega–I10 undercrossing. The Arias intensity is normalized w.r.t. the intensity of the two-point interpolation.

Considering the results presented in this section, it is tempting not to include the record from the Hollywood Storage Building parking lot in the interpolation of the north-south component at the bridge site. As mentioned earlier, it is possible that the proximity of the Hollywood Storage Building to the northern boundary of the Los Angeles Basin, i.e., its proximity to Santa Monica Mountains, had an adverse effect on the north-south component of the ground motion, while not affecting the east-west component. In order to choose between the two-point and three-point interpolations of the north-south component, it is possible to evaluate the response of the bridge using the results of both interpolations, and see whether either, or both, could have caused the damage that was observed. This is, however, beyond the scope of this study.

As pointed out in Chapter 6, it is in general preferable to use three-point interpolation rather than two-point interpolation. The three-point interpolation is preferred because its results are found to be not as sensitive to the orientation with respect to the direction of seismic wave propagation as the results of a two-point interpolation – given that the local conditions at the recording stations and the interpolation site are alike. Ultimately, decisions on how many and which stations to use when interpolating earthquake ground motion have to be made on a case by case basis, using substantial engineering judgement.

CHAPTER 8
SUMMARY AND CONCLUSIONS

The research described in this report concerns the modeling of horizontal earthquake ground motion. The ground motion is characterized by a digital acceleration time history. The modeling is performed in the frequency domain and the accelerograms are obtained by evaluating the inverse, discrete Fourier transform. This research includes two main topics: (1) the simulation of earthquake ground motion at a given site, and (2) the spatial interpolation of earthquake ground motion.

8.1 Summary

Simulation

The ground motion simulation models developed in this research are calibrated and validated using 277 uniformly processed horizontal ground motion records from 11 recent California earthquakes. The moment magnitude of the earthquakes ranges from 5.8 to 7.3. The source to site distance for all the records, which is taken as the shortest distance from the site to the vertical projection of the seismogenic rupture on the surface of the Earth, is less than 100 km.

By properly modeling the probability distribution of the Fourier phase differences conditional on the Fourier amplitude, the Fourier transform of an accelerogram can be described. The acceleration time history is then obtained by evaluating the inverse transform. The sampling frequency and the total duration of the accelerograms are fixed at 50 Hertz and 40.98 seconds (2048 points), respectively. Two methods are developed for the simulation of phase differences.

The first method is referred to as the parametric approach, where the Fourier amplitudes are classified into three categories: small, intermediate and large. For each amplitude category, a beta distribution or a combination of a beta distribution and a uniform distribution are defined for the phase differences. Seven parameters are needed

to completely define the phase difference distributions. Of these, however, only two are fundamental as the other five parameters are found to be dependent of these two and functional relationships are formulated to capture this dependency. A California ground motion database, which is processed for uniformity with respect to baseline correction, sampling frequency, total duration and filtering, is then used to develop prediction formulas for the model parameters. The fundamental phase difference parameters are estimated from the moment magnitude of the earthquake, the distance from the site to the surface projection of the seismogenic rupture, and the NEHRP site classification, while the secondary parameters are derived from one of the fundamental parameters.

The second approach for the modeling of Fourier phase differences is based on the method of envelopes for narrow band stochastic processes, where frequency, rather than time, is treated as the indexing parameter of the process. In the case of the frequency domain analogy, the term "narrow band" refers to the shape of the intensity function (or, alternatively, the amplitude modulation function) in the time domain. This leads to a Gaussian distribution for the Fourier phase differences, where the mean phase difference is independent of the Fourier amplitude, but the standard deviation is a continuous, decreasing function of the amplitude. Two parameters are necessary to fully define the phase difference distribution, but they are not independent of each other. The California ground motion database is used to develop prediction formulas for the model parameters.

The Fourier amplitude spectrum is modeled as a scaled, lognormal probability density function. Three parameters are necessary to define the Fourier amplitude spectrum; representing the total energy of the accelerogram, the central frequency, and the spectral bandwidth. The California ground motion database is used to develop prediction formulas for these parameters. The first two parameters are estimated from the magnitude, distance, and site classification, while the third parameter is inferred from the central frequency.

Interpolation

Data from four earthquakes recorded at the SMART-1 accelerograph array in Lotung, Taiwan are used to assess the accuracy of the interpolation model. The earthquakes are all shallow (focal depth less than 15 km), and their surface wave magnitude is between

5.7 and 7.8. The distance from the center of the array to the epicenters of the earthquakes ranges from 22 km to 77 km. Different approaches are used to interpolate the amplitude and the phase angle of the discrete Fourier transform.

The interpolated Fourier amplitude is taken as the square root of the weighted average of the observed squared amplitudes, where the weights are inversely proportional to the squared inter-station spacing.

Interpolation of Fourier phase angles is more complicated than the interpolation of the amplitudes, due to wave dispersion and phase wrapping. First, a dispersion relationship is used to predict the phase angles at the site for which the ground motion is to be estimated, using the observed phase angles and the apparent propagation velocity of the seismic waves. Then, the interpolated phase angle is derived from the weighted, complex average of the predicted Fourier transforms. The weights are the same as for the amplitude interpolation, i.e. they are inversely proportional to the squared inter-station distance.

8.2 Conclusions

The objective of this study – to develop a simple and efficient method for rapid evaluation of horizontal earthquake ground motion at any site for a given region, based on readily available source, path and site characteristics, or (sparse) recordings – was accomplished.

Simulation

The earthquake ground motion simulation methods developed in this research present a unified approach for the evaluation of the discrete Fourier transform (both the amplitude and the phase spectrum) of earthquake accelorgrams, based on the magnitude of the earthquake, the source to site distance, and the local site conditions.

The parametric method for the simulation of Fourier phase differences is purely empirical and simple to use. The parametric method does not work well for ground motion records where the temporal energy release is nearly evenly distributed over the total duration. Extensive statistical goodness of fit tests were performed on the simulated

phase difference distributions, using the Kolmogorov-Smirnov test and the California ground motion database. In general, the comparison between the simulated and recorded phase difference distributions is found to be good.

The frequency domain analogy of the method of envelopes for narrow band processes provides a theoretical basis for the empirical parametric method. The simulation method based on the analogy of the method of envelopes is more robust than the parametric method, especially for long source to site distances. The analogy hinges on the assumption that the shape of the intensity function in the time domain resembles the shape of the power spectral density of a narrow band process. If this assumption is not valid, the analogy does not hold. Therefore, the simulation methods developed in this research cannot be used to simulate low-intensity and long-duration accelerograms, or accelerograms with bi-modal intensity functions, for example. Extensive statistical goodness of fit tests were performed on the simulated standardized phase difference distributions, using the two-sample Kolmogorov-Smirnov test and the California ground motion database. In general, the comparison between the simulated standardized phase differences and the recorded standardized phase differences is found to be good.

The simulated ground motion time histories capture the pertinent characteristics of the recorded time histories in the California database through proper modeling of the Fourier phase differences, conditional on the Fourier amplitude. This is accomplished without an explicit use of an amplitude modulation function or a strong ground motion duration. The "pertinent characteristics" include peak ground acceleration, elastic response spectra, and the temporal distribution of energy release (evolutionary behavior). It is interesting to note that the nonstationary characteristics of earthquake accelerograms can be fully described by only two independent parameters. In the parametric method, these two parameters are the mean normalized phase difference for large Fourier amplitudes, μ_L, and the variance of normalized phase difference for small Fourier amplitudes, σ_S^2. The two sufficient parameters in the frequency domain analogy of the method of envelopes are the centroid, $\bar{\tau}$, and the unitless duration parameter, Δ_T, of the whitened intensity function. In most cases, even one parameter is sufficient; i.e. γ_1, the first whitened intensity moment.

Because of its robustness and its theoretical basis, the frequency domain analogy of the method of envelopes is, in general, recommended over the parametric method when simulating the Fourier phase differences of earthquake accelerograms. However, the parametric method has its appeal because it is faster and easier to implement.

The Fourier phase difference models presented in this study do not depend on a particular Fourier amplitude model. The user can employ any amplitude model. In addition, the phase difference models can be used to generate a number of "equivalent" accelerograms from a target accelerogram – recorded or simulated – using the Fourier amplitude spectrum of the target accelerogram. Alternatively, the user can specify a power spectral density or a response spectrum, from which a Fourier amplitude spectrum can be derived, in association with a target accelerogram or a triplet of earthquake magnitude, distance, and site classification. The target accelerogram (or the triplet of magnitude, distance, and site classification) has to be specified in order to infer the parameters of the phase difference distributions.

The simulation methods developed in this research are not intended to replace more robust geophysical models. Instead, they provide for a rapid simulation of acceleration time histories for engineering purposes over a wide range of magnitudes and distances.

Interpolation

The spatial interpolation model developed in this research can be used for both simulated and recorded acceleration time histories. The model does not depend on any simplifying assumptions regarding Gaussianity or stationarity.

The accuracy of the interpolation model is assessed using data from the SMART-1 array in Taiwan, where the characteristics of interpolated accelerograms are compared to the characteristics of recorded accelerograms. The Fourier amplitude interpolation yields good results for inter-station spacing up to 2 kilometers.

The interpolated phase angles compare well with the recorded phase angles for inter-station spacings up to 200 meters and frequencies less than 3 Hertz. Therefore, it is concluded that this interpolation method yields good estimates of the differential motion between two stations if the distance between them is less than 200 meters and most of the

energy in the ground motion is contained within the frequency band between 0 and 3 Hertz. It is possible that the quality of the phase angle interpolation can be improved by more accurate (frequency dependent) estimates of the apparent phase velocity.

The triangular interpolation scheme appears to be effective and sufficient. Using all twelve stations in a given circle of the array does not improve the quality of the interpolation significantly, as compared to using a triplet of stations (a triangle). If only a pair of stations is used, the quality of the interpolation is very sensitive to the direction of the seismic wave propagation, relative to the direction of the line connecting the two stations. It yields the best interpolation results if the connecting line is perpendicular to the direction of wave propagation.

It is important to note that the conditions at the site at which the acceleration time history is sought ought to be similar to the conditions at the stations that are used in the interpolation. These conditions include, but are not limited to, the local soil conditions, nearby geologic features, and the surrounding topography.

The quality of the phase angle interpolation restricts the reliable estimates of differential ground motion to relatively limited ranges of spacings and frequencies. However, the spatial interpolation model developed in this research provides an effective method to estimate the ground motion at a site, using recordings from stations located up to several kilometers away.

8.3 Future Work

The ground motion simulation models developed in this study do not include directivity or near-source effects. The directivity can be taken into account by introducing a new path parameter in addition to the source to site distance: the azimuth angle of the site with respect to the direction of rupture propagation. Abrahamson and Singh (1986), for example, specifically address the issue of directivity and phase angles. Somerville (1997) and Somerville et al. (1997) discuss directivity and near-source effects on spectral acceleration levels and strong motion duration. The pulse-like characteristic, which is often observed in recordings that are made at near-source sites, can be included by the duration parameter, Δ_T , in the frequency domain analogy of the method of envelopes. In

the context of this research, directivity and near-source effects would require a parametric study of the duration parameter, Δ_T, or a specific model of the second intensity moment, γ_2, as a function of the first intensity moment, γ_1.

Many researchers suggest that the level and characteristics of earthquake ground motion depend on the type of faulting. There are three different types of pure faulting mechanisms: strike-slip, reverse-slip, and normal-slip. The strong motion data set used in this study does not include any recordings from normal-slip events. A preliminary attempt was made to distinguish between strike-slip and reverse-slip events in the development of prediction formulas for the parameters of the phase difference models. An earthquake is considered strike-slip in this study if the rake angle is within 45 degrees of horizontal. This is the same definition as used by Sadigh et al. (1997). Analysis of the data at hand did not reveal a systematic difference between strike-slip and reverse-slip earthquakes. The local site conditions had much more effect on the model parameters than the type of faulting. However, a more thorough study of the effects of different faulting mechanism on the parameters of the phase difference models is in order.

In Chapters Three, Four, and Five, prediction formulas were developed for the parameters of the ground motion simulation models, using the California ground motion database that is described in Chapter Two. In the seventh chapter, recordings from the Northridge earthquake were used to develop formulas for the model parameters as functions of distance specifically for that earthquake. In order to combine previously developed predictive relationships (i.e. the relationships developed in Chapters 3, 4, and 5) and newly recorded accelerograms (from any future earthquake), it would be helpful to develop a Bayesian formulation for the updating of the model parameters.

The Fourier amplitude model that was proposed in Chapter 5 is smooth. On the other hand, typical amplitude spectra for recorded accelerograms are jagged, or irregular. The effect of this smoothing was not investigated systematically. If the spectral smoothing is believed to affect the structural response (or demand) significantly, the spectral amplitudes could be simulated where the mean amplitude for a given frequency is inferred from the smooth spectrum.

The ground motion models developed in this study were validated by comparing the peak values, the elastic response spectra, and the cumulative normalized Arias

intensities of the simulated or interpolated accelerograms to the corresponding characteristics of recorded accelerograms. To earn a widespread acceptance in the structural engineering community for these ground motion models, a systematic validation has to be performed using nonlinear characteristics, such as nonlinear response spectra or dissipated hysteretic energy, for example. A systematic validation of that kind was not performed in this research. However, the few examples that were studied did indicate a better correlation of the nonlinear characteristics of accelerograms simulated using the models developed in this study with the corresponding characteristics of recorded accelerograms, than the traditional simulation models which assume the Fourier phase angles to be uniformly distributed and mutually independent.

APPENDIX A
CALIFORNIA RECORDING STATIONS

Most of the recording stations that are listed in Table A.1 are operated by the California Division of Mines and Geology under the California Strong Motion Instrumentation Program, or the United States Geological Survey as part of the National Strong Motion Program.

The data on the recording stations are compiled from the following sources:

- http://docinet3.consrv.ca.gov/csmip/
- http://nsmp.wr.usgs.gov/data.html
- http://smdb.crustal.ucsb.edu/
- Boore et al. (1993, 1994, 1997).

Site classifications are according to the NEHRP classification scheme (BSSC, 1994). Classification of individual recording sites is inferred from:

- Boore et al. (1993, 1994, 1997)
- Borcherdt (1994)
- http://smdb.crustal.ucsb.edu/ows-bin/owa/summary5.main
- Park and Elrick (1998)
- Tinsley and Fumal (1985).

Table A.1: California recording stations that are used in this study.

Station Code	Site Class	Latitude (°N)	Longitude (°W)	Owner *	Name / Location
A01	E	37.545	122.231	CDMG	APEEL Array #1, Foster City
A02	E	37.520	122.250	USGS	APEEL Array #2, Redwood City
A07	C	37.484	122.313	USGS	APEEL Array #7, Pulgas Water Temple
A10	C	37.465	122.343	USGS	APEEL Array #10, Skyline Blvd.
A1E	E	37.623	122.130	CDMG	APEEL Array #1E, Pt. Eden Way, Hayward
A2E	D	37.657	122.082	USGS	APEEL Array #2E, Muir School, Hayward
A3E	C	37.657	122.061	CDMG	APEEL Array #3E, CSUH, Stadium Grounds
AEP	D	32.651	115.332	IDEI	Aeropuerto Mexicali
AGR	D	32.621	115.301	IDEI	Agrarias
AGW	D	37.398	121.952	CDMG	Agnew, State Hospital
ALF	C	34.070	118.150	CDMG	Alhambra, Fremont School
AMB	A&B	34.560	115.743	CDMG	Amboy
ANB	C	34.758	118.361	CDMG	Antelope Buttes, Lake Hughes Array
ANI	C	34.016	119.362	CDMG	Anacapa Island, Ranger Residence
ANV	D	34.580	118.199	CDMG	Anaverde Valley, City Ranch
BAD	C	33.889	117.926	ACOE	Brea Dam, Downstream
BCR	D	32.693	115.338	USGS	Bonds Corner, Highways 115 & 98
BHA	D	34.009	118.361	CDMG	Baldwin Hills, Los Angeles
BKR	C	35.272	116.066	CDMG	Baker, Fire Station
BRA	D	32.991	115.512	USGS	Brawley Airport, Hangar
BRN	C	35.002	117.650	CDMG	Boron
BRS	C	34.887	117.047	CDMG	Barstow
C02	D	35.733	120.288	CDMG	Cholame Shandon Array #2, Parkfield
C05	D	35.697	120.328	CDMG	Cholame Shandon Array # 5W, Parkfield
C08	D	35.671	120.359	CDMG	Cholame Shandon Array # 8W, Parkfield
C12	C	35.639	120.404	CDMG	Cholame Shandon Array #12W, Parkfield
CAL	D	33.130	115.520	USGS	Calipatria, Fire Station
CAP	D	36.974	121.952	CDMG	Capitola, 405 Capitola Ave.
CC4	D	33.360	115.590	USGS	Coachella Canal Station #4, Siphon 15
CFH	A&B	37.778	122.513	CDMG	Cliff House, 1090 Pt. Lobos, San Francisco
CHC	C	34.459	118.650	CDMG	Castaic, Hasley Canyon, Lake Hughes Array
CHU	D	32.484	115.240	IDEI	Chihuahua
CLS	C	37.046	121.803	CDMG	Corralitos, 1473 Eureka Canyon Rd.
CMO	D	34.208	119.079	CDMG	Camarillo, Lake Hughes Array
CMP	D	32.572	115.083	IDEI	Compuertas
CPR	C	32.421	115.301	IDEI	Cerro Prieto
CUC	D	32.545	115.235	IDEI	Cucapah
CXO	D	32.669	115.492	USGS	Calexico, Fire Station
CYC	C	37.124	121.551	CDMG	Coyote Lake Dam, Downstream
DLT	D	32.356	115.195	IDEI	Delta
DMH	C	37.740	122.433	CDMG	Diamond Heights, 80 Digby St., San Francisco
DOW	D	33.924	118.167	CDMG	Downey, County Maintenance Bldg.
DSP	C	33.962	116.509	CDMG	Desert Hot Springs, Fire Station, Pierson Blvd.
E01	D	32.960	115.319	USGS	El Centro Array #1, Borchard Ranch
E02	D	32.916	115.366	USGS	El Centro Array #2, Keystone Rd.
E03	E	32.894	115.380	USGS	El Centro Array #3, Pine Union School
E04	D	32.864	115.432	USGS	El Centro Array #4, 2905 Anderson Rd.
E05	D	32.855	115.466	USGS	El Centro Array #5, James Road

Station Code	Site Class	Latitude (°N)	Longitude (°W)	Owner *	Name / Location
E06	D	32.839	115.487	USGS	El Centro Array #6, 551 Huston Rd.
E07	D	32.829	115.504	USGS	El Centro Array #7, Imperial Valley College
E08	D	32.811	115.530	USGS	El Centro Array #8, 95 E Cruickshank Rd.
E10	D	32.780	115.567	USGS	El Centro Array #10, EC Community Hospital
E11	D	32.752	115.594	USGS	El Centro Array #11, McCabe Union School
E12	D	32.718	115.637	USGS	El Centro Array #12, 907 Brockman
E13	D	32.709	115.683	USGS	El Centro Array #13, Strobel Residence
ECP	C	34.177	118.096	CDMG	Eaton Canyon Park, Altadena
EDA	D	32.796	115.535	USGS	El Centro Differential Array
ELC	D	32.794	115.549	USGS	El Centro Array #9, Imp. Vall. Irrigation District
ELZ	D	34.662	118.387	CDMG	Elizabeth Lake
EMV	D	37.844	122.295	USGS	6363 Christie Ave., Emeryville, Ground Station
ERB	A&B	40.498	124.294	USGS	Eel River Valley Array, Bunker Hill
ERC	C	40.563	124.348	USGS	Eel River Valley Array, Centerville Beach
ERF	C	40.599	124.154	USGS	Eel River Valley Array, Fortuna Fire Station
ERL	C	40.644	124.219	USGS	Eel River Valley Array, Loleta Fire Station
ERR	C	40.699	124.200	USGS	Eel River Valley Array, Coll. of the Redwoods
ERU	D	40.735	124.207	USGS	Eel River Valley Array, South Bay Union School
EUR	D	40.801	124.148	CDMG	Eureka, Apartment Building, Free Field
FER	D	40.576	124.262	USGS	Eel River Valley Array, Ferndale Fire Station
FFP	C	34.088	116.919	USGS	Forest Falls Post Office, Mill Creek Canyon
FMS	D	37.535	121.929	USGS	Fremont, Calaveras Array
FRT	C	40.584	124.145	CDMG	Fortuna, Supermarket (Safeway)
FTI	C	35.268	116.684	CDMG	Fort Irwin
FVR	C	33.925	116.389	USGS	Fun Valley, Reservoir 361
FYP	D	33.869	117.709	CDMG	Featherly Park, Park Maintenance Building
G01	A&B	36.973	121.572	CDMG	Gilroy Array #1, Gavilan College Water Tank
G02	D	36.982	121.556	CDMG	Gilroy Array #2, Mission Trails Motel
G03	D	36.987	121.536	CDMG	Gilroy Array #3, Sewage Plant
G04	D	37.005	121.522	CDMG	Gilroy Array #4, San Ysidro School
G06	C	37.026	121.484	CDMG	Gilroy Array #6, San Ysidro
G07	D	37.033	121.434	CDMG	Gilroy Array #7, Mantelli Ranch
GIL	C	36.973	121.568	CDMG	Gilroy, Gavilan College Geology Building
GOF	C	37.009	121.569	CDMG	Gilroy, Old Firehouse
GPK	A&B	34.118	118.299	USGS	Griffith Park Observatory, Los Angeles
H01	A&B	33.599	117.132	CDMG	Murrieta Hot Springs, Collins Ranch
H02	A&B	33.640	117.094	CDMG	Winchester, Bergman Ranch
H03	A&B	33.681	117.056	CDMG	Winchester, Hidden Valley Farms
H04	D	33.718	117.022	CDMG	Winchester, Page Bros Ranch
H05	D	33.729	116.979	CDMG	Hemet Fire Station, 895 Stetson
H06	D	33.760	116.960	CDMG	San Jacinto, Valley Cemetery
H08	C	33.797	116.880	CDMG	San Jacinto, SOBODA
H10	A&B	33.851	116.852	CDMG	Silent Valley, Poppet Flat
HAD	D	36.888	121.413	USGS	Hollister Airport, Differential Array
HBL	D	33.662	117.997	CDMG	Huntington Beach, Lake St. Fire Station
HCH	D	36.851	121.402	USGS	Hollister City Hall Annex
HES	C	34.405	117.311	CDMG	Hesperia
HSL	D	34.090	118.339	CDMG	Hollywood Storage Bldg., Parking Lot
HSP	D	36.848	121.397	CDMG	Hollister, South & Pine

Station Code	Site Class	Latitude (°N)	Longitude (°W)	Owner *	Name / Location
HUV	D	33.697	118.023	USGS	Huntington Beach, 18401 Springdale
HVP	D	32.812	115.377	USGS	Holtville, Post Office
HVR	D	37.338	121.714	CDMG	Halls Valley, Grant Ranch
HWB	C	37.670	122.086	CDMG	Hayward, BART Station Parking Lot
IGU	D	33.905	118.279	CDMG	Inglewood, Union Oil Yard
INI	D	33.717	116.156	CDMG	Indio, Coachella Canal
INO	D	33.747	116.214	USGS	Indio, Jackson Road, Southern Calif. Gas Co.
JST	C	34.131	116.314	CDMG	Joshua Tree, 6715 Park Blvd.
L01	C	34.674	118.430	CDMG	Lake Hughes Array #1, Lk. Hughes Fire Station
L04	C	34.650	118.478	CDMG	Lake Hughes Array #4, North Water Tank, CM
L09	A&B	34.608	118.558	CDMG	Lake Hughes Array #9, Warm Springs
L12	C	34.570	118.560	CDMG	Lake Hughes Array #12, Eliz Lake
L4B	C	34.650	118.477	CDMG	Lake Hughes Array #4B, Camp Mendenhall
LAS	D	33.929	118.260	CDMG	116th St. School, 11610 Stanford Ave., LA
LBG	D	33.768	118.196	CDMG	Long Beach, City Hall Grounds
LBH	D	33.754	118.200	CDMG	Long Beach, Harbor Administration Bldg.
LBL	D	33.840	118.194	CDMG	Long Beach, Rancho Los Cerritos Library
LBN	D	37.106	120.825	CDMG	Los Banos, 18110 W Henry Miller
LBR	D	33.778	118.133	CDMG	Long Beach, Recreation Park
LCN	D	34.063	118.418	CDMG	Cent. City Country Club, LA, North Ground Site
LCS	D	34.062	118.416	CDMG	Cent. City Country Club, LA, South Ground Site
LDR	D	34.274	116.392	CDMG	Landers
LNF	D	34.739	118.214	CDMG	Lancaster, Fox Airfield Grounds
LOB	C	37.001	122.060	CDMG	UC Santa Cruz Lick Observatory
LPK	C	34.109	119.065	CDMG	Point Mugu, Laguna Peak
LRP	C	34.522	117.991	USGS	Littlerock, Post Office
LV1	C	34.594	118.242	CDMG	Leona Valley Array #1
LV2	D	34.595	118.243	CDMG	Leona Valley Array #2
LV3	A&B	34.596	118.243	CDMG	Leona Valley Array #3
LV4	D	34.598	118.242	CDMG	Leona Valley Array #4
LV5	D	34.600	118.241	CDMG	Leona Valley Array #5, Ritter Ranch
LV6	D	34.604	118.244	CDMG	Leona Valley Array #6
MCN	C	34.087	118.693	USGS	Malibu Canyon, Monte Nido Fire Station
MJO	D	35.042	118.377	CDMG	Mojave, Oak Creek Canyon
MJV	D	35.070	118.175	CDMG	Mojave, LAWP Substation, 17031 Sierra Hwy.
MNT	A&B	36.597	121.897	CDMG	Monterey, City Hall
MPK	D	34.288	118.881	CDMG	Moorpark, Ventura County Fire Dept.
MSJ	C	37.530	121.919	CDMG	Mission San Jose, Fremont
MTW	A&B	34.224	118.057	CDMG	Mt. Wilson, CalTech Seismic Station
MVF	C	34.048	116.577	USGS	Morongo Valley, Fire Station
MXC	D	32.618	115.428	IDEI	Mexicali, Casa Flores, SAHOP
NBI	D	33.634	117.902	CDMG	Newport Beach, Irvine Ave. Fire Station
NIL	D	33.239	115.512	CDMG	Niland, Fire Station, 8071 Luxor
NPS	C	33.924	116.543	USGS	North Palm Springs, Post Office
NWH	D	34.390	118.530	CDMG	Newhall, LA County Fire Station
NWK	D	33.915	118.067	BECH	Norwalk, 12400 Imp. Hwy., South Ground Site
OBG	D	34.037	118.178	CDMG	Obregon Park, Los Angeles
ORR	C	34.564	118.642	CDMG	Old Ridge Route, Castaic
OSW	D	37.816	122.314	CDMG	Oakland, Outer Harbor Wharf

Station Code	Site Class	Latitude (°N)	Longitude (°W)	Owner *	Name / Location
PAS	C	34.140	118.120	CIT	Pasadena, CalTech Athenaeum
PCD	A&B	34.334	118.396	CDMG	Pacioma Dam, Downstream
PDL	C	34.578	118.113	USGS	Palmdale, Fire Station
PDS	C	34.077	118.800	CDMG	Point Dume School, Malibu
PGS	D	40.324	124.286	CDMG	Petrolia, General Store
PHN	D	34.145	119.206	CDMG	Port Hueneme, Navy Lab, Bldg. 570
PHT	A&B	37.790	122.429	CDMG	Pacific Heights, 2150 California, San Francisco
PIE	A&B	37.823	122.233	CDMG	Piedmont, Jr. High School Grounds
PKC	C	34.288	118.375	CDMG	Pacoima, Kagel Canyon, 12587 Dexter Park
PLC	C	33.324	116.683	CDMG	Puerta La Cruz, USFS Storage Bldg.
PLS	D	32.790	115.860	USGS	Plaster City
PMG	D	34.113	119.119	CDMG	Point Mugu, Naval Air Station
PPP	C	34.508	117.522	OWNR	Pearblossom, Pumping Plant
PRD	D	33.890	117.641	ACOE	Prado Dam, Downstream
PRS	C	37.792	122.457	CDMG	San Francisco Presidio
PSA	D	33.829	116.501	CDMG	Palm Springs, Airport
PSL	A&B	34.150	118.170	CIT	Pasadena, Old CalTech Seismo Lab
PSW	C	34.136	118.127	USGS	NSMP Pasadena Laboratory, Ground Station
PTB	A&B	37.820	122.520	CDMG	Point Bonita
PTS	C	32.929	115.699	USGS	Parachute Test Site
PVC	A&B	33.746	118.396	CDMG	Rancho Palos Verdes, Crestmont College
PWS	A&B	34.021	116.009	CDMG	Twenty-Nine Palms, Pinto Wye Station
RCH	C	37.935	122.342	CDMG	Richmond, City Hall
RDL	C	40.503	124.100	CDMG	Rio Dell, Painter St. Overpass
RGR	D	34.827	118.265	CDMG	Rosamond, Godde Ranch
RHE	C	33.787	118.356	CDMG	Rolling Hills Estates, Rancho Vista School
RIN	A&B	37.786	122.391	CDMG	Rincon Hill, Fremont & Harrison, San Francisco
RNC	C	34.104	117.574	CDMG	Rancho Cucamonga, Law & Justice Center
ROS	D	34.870	118.206	CDMG	Rosamond, Airport
RVA	C	33.951	117.446	CDMG	Riverside Airport, Maintenance Shop
SAG	C	36.753	121.396	CDMG	Sago South, Cienega Rd., Hollister
SAL	D	36.671	121.642	CDMG	Salinas, John & Work St.
SCP	C	40.026	124.069	CDMG	Shelter Cove, Power Plant Yard
SFG	C	37.806	122.472	USGS	Golden Gate Bridge, Toll Plaza, San Francisco
SFO	D	37.622	122.398	CDMG	San Francisco International Airport
SFY	D	34.236	118.439	CDMG	Arleta, Nordhoff Fire Station
SJB	C	36.846	121.536	CDMG	San Juan Bautista, Fire Station, 24 Polk
SLA	D	37.419	122.205	USGS	Stanford Linear Accelerator Center
SMG	D	34.011	118.490	CDMG	Santa Monica, City Hall Grounds
SNM	D	34.115	118.130	CDMG	San Marino, Southwestern Academy
SOD	C	34.156	117.675	ACOE	San Antonio Dam, Downstream
SPC	C	34.097	118.475	MWD	Sepulveda Canyon, Spillway Building, LA
SPP	C	33.722	118.309	CDMG	San Pedro, Palos Verdes, 1414 W 25th
SSA	A&B	34.231	118.713	DOE	Canoga Park, Santa Susana (ETEC)
SSF	A&B	37.674	122.388	CDMG	South San Francisco, Sierra Point
STG	C	37.255	122.031	CDMG	Saratoga, 14675 Aloha Ave.
SUP	C	32.955	115.823	USGS	Superstition Mountain, Camera Site
SVL	D	37.402	122.024	USGS	Sunnyvale, 1058 Colton Ave.
SYH	D	34.326	118.444	CDMG	Sylmar, County Hospital Parking Lot

Station Code	Site Class	Latitude (°N)	Longitude (°W)	Owner *	Name / Location
TAR	C	34.160	118.534	CDMG	Tarzana, Cedar Hill Nursery
TEM	D	33.496	117.149	CDMG	Temecula, CDF Fire Station
TIB	D	37.806	122.267	CDMG	Title Ins. & Trust Bldg., 1700 Webster, Oakland
TMB	C	35.710	120.170	USGS	Temblor, Cholame-Shandon
TOP	C	34.084	118.599	USGS	Topanga, Fire Station
TPP	D	33.817	116.390	USGS	Thousand Palms, Post Office
TRI	D	37.825	122.373	CDMG	Treasure Island, Naval Base Fire Station
ULA	D	34.068	118.439	CDMG	UCLA Grounds
USB	C	34.422	119.851	CDMG	UC Santa Barbara, Goleta
VCT	D	32.289	115.103	IDEI	Victoria
VHI	D	34.276	119.294	CDMG	Ventura, Holiday Inn, 450 E Harbor Blvd.
VLA	D	34.063	118.463	VA	Brentwood VA Hospital, Los Angeles
VRP	C	34.490	118.320	CDMG	Vasquez Rocks Park
VSP	D	34.249	118.478	VA	Sepulveda VA Hospital, Los Angeles
WDS	C	37.429	122.258	CDMG	Woodside, Fire Station
WSM	D	33.037	115.623	CDMG	Westmoreland, Fire Station
WWT	A&B	33.989	116.655	USGS	Whitewater Canyon, Trout Farm
XLA	D	34.688	118.156	CDMG	Lancaster, Medical Office Bldg., 15th & J
XPO	D	34.056	117.748	CDMG	Pomona, 4th & Locust
YBI	A&B	37.807	122.361	CDMG	Yerba Buena Island, USCG Foghorn Bldg.
YER	D	34.903	116.823	CDMG	Yermo

* ACOE U.S. Army Corps of Engineers
CDMG California Division of Mines and Geology
CIT California Institute of Technology
DOE U.S. Department of Energy
IDEI Instituto de Ingenieria de la Universidad Nacional Autonoma de Mexico
MWD Metropolitan Water District of Southern California
USGS U.S. Geological Survey
VA U.S. Department of Veteran Affairs

APPENDIX B
DATA; PARAMETRIC METHOD

The statistics on normalized phase differences that are used in Chapter 3 are listed in Table B.1. The station code is the same as in Table A.1, where the locations of all the recording stations are tabulated. Source to site distances are taken from:

- Boore et al. (1993, 1994, 1997)
- Chang et al. (1996)

and calculated using information on the seismogenic rupture in:

- Archuleta and Day (1980)
- Bolt et al. (1985)
- Bouchon (1982)
- Chavez et al. (1982)
- Hagerty and Schwartz (1996)
- Hauksson et al. (1993)
- Hauksson and Jones (1995)
- Jones and Hauksson (1988)
- Kanamori and Regan (1982)
- Pacheco and Nabelek (1988)
- Wald et al. (1991)
- Whitcomb et al. (1973).

The parameters in Table B.1 are:

- D: The distance from the site to the vertical projection of the seismogenic rupture on the surface of the Earth.
- μ_L: The mean normalized phase difference for large Fourier amplitudes.
- σ_L^2: The variance of normalized phase difference for large Fourier amplitudes.
- μ_I: The mean normalized phase difference for intermediate Fourier amplitudes.
- σ_I^2: The variance of normalized phase difference for intermediate Fourier amplitudes.
- μ_S: The mean normalized phase difference for small Fourier amplitudes.
- σ_S^2: The variance of normalized phase difference for small Fourier amplitudes.
- wu: The weight of the uniform distribution for small Fourier amplitudes.

Table B.1: Statistics on normalized phase differences that are used in Chapter 3.

Earthquake	Station	*D* (km)	μ_L	σ_L^2	μ_I	σ_I^2	μ_S	σ_S^2	*wu*
Coyote Lake	CYC	1.6	0.63	0.0033	0.63	0.0054	0.65	0.0044	0.009
	G01	9.1	0.61	0.0007	0.62	0.0023	0.63	0.0081	0.027
	G02	7.4	0.61	0.0011	0.62	0.0020	0.62	0.0056	0.018
	G03	5.3	0.60	0.0022	0.60	0.0061	0.62	0.0070	0.009
	G04	3.7	0.58	0.0068	0.59	0.0086	0.63	0.0072	0.009
	G06	1.2	0.63	0.0005	0.63	0.0040	0.64	0.0047	0.044
	HVR	30.0	0.54	0.0134	0.60	0.0245	0.60	0.0475	0.284
	SJB	17.9	0.51	0.0107	0.58	0.0121	0.61	0.0099	0.116
Whittier Narrows	ALF	3.0	0.59	0.0007	0.60	0.0035	0.59	0.0065	0.018
	BHA	22.5	0.51	0.0106	0.52	0.0138	0.56	0.0159	0.089
	CHC	64.4	0.40	0.0096	0.46	0.0233	0.55	0.0383	0.676
	DOW	11.3	0.54	0.0066	0.54	0.0126	0.57	0.0083	0.107
	ECP	10.5	0.59	0.0014	0.58	0.0069	0.61	0.0081	0.071
	FYP	35.5	0.54	0.0025	0.52	0.0160	0.55	0.0221	0.293
	H05	103.9	0.34	0.0088	0.37	0.0274	0.39	0.0269	0.338
	HBL	39.8	0.46	0.0165	0.49	0.0193	0.52	0.0143	0.151
	HSL	20.5	0.50	0.0073	0.53	0.0127	0.55	0.0167	0.116
	IGU	19.4	0.54	0.0032	0.53	0.0077	0.54	0.0093	0.071
	L01	71.7	0.43	0.0153	0.46	0.0211	0.55	0.0249	0.356
	LAS	16.4	0.55	0.0011	0.55	0.0050	0.56	0.0050	0.080
	LBH	30.2	0.44	0.0307	0.52	0.0216	0.56	0.0217	0.107
	LBL	20.9	0.52	0.0056	0.53	0.0085	0.55	0.0117	0.071
	LBR	26.6	0.45	0.0183	0.50	0.0180	0.56	0.0177	0.276
	LCN	27.7	0.50	0.0077	0.52	0.0118	0.55	0.0123	0.080
	LCS	27.5	0.58	0.0066	0.57	0.0170	0.62	0.0157	0.356
	LV5	58.6	0.44	0.0070	0.49	0.0184	0.55	0.0223	0.222
	LV6	59.1	0.51	0.0043	0.53	0.0159	0.57	0.0139	0.231
	MPK	73.9	0.37	0.0087	0.43	0.0348	0.60	0.0492	0.693
	NWH	51.0	0.53	0.0083	0.53	0.0206	0.60	0.0306	0.596
	OBG	5.6	0.58	0.0011	0.57	0.0058	0.57	0.0087	0.044
	ORR	71.5	0.39	0.0076	0.45	0.0336	0.57	0.0416	0.391
	PDS	62.9	0.41	0.0077	0.45	0.0185	0.57	0.0213	0.516
	PKC	32.9	0.51	0.0034	0.53	0.0130	0.55	0.0167	0.258
	RGR	83.8	0.38	0.0040	0.41	0.0202	0.49	0.0302	0.507
	RNC	43.9	0.46	0.0036	0.47	0.0112	0.47	0.0228	0.124
	RVA	56.2	0.48	0.0048	0.46	0.0080	0.48	0.0175	0.187
	SFY	34.1	0.48	0.0084	0.50	0.0138	0.55	0.0185	0.036
	SNM	3.8	0.61	0.0015	0.60	0.0039	0.61	0.0111	0.018
	SYH	40.4	0.45	0.0047	0.48	0.0169	0.53	0.0224	0.213
	TAR	39.3	0.48	0.0027	0.50	0.0064	0.50	0.0080	0.053
	VRP	48.9	0.48	0.0017	0.48	0.0063	0.50	0.0127	0.124
	XLA	67.4	0.41	0.0049	0.42	0.0209	0.49	0.0238	0.267
	XPO	28.0	0.50	0.0054	0.52	0.0140	0.52	0.0158	0.258
Morgan Hill	A01	53.5	0.30	0.0416	0.41	0.0338	0.49	0.0256	0.453
	A1E	50.9	0.46	0.0299	0.51	0.0357	0.55	0.0372	0.667
	AGW	24.4	0.37	0.0654	0.45	0.0292	0.46	0.0313	0.302
	CAP	40.1	0.49	0.0075	0.52	0.0137	0.51	0.0180	0.027
	CLS	24.6	0.51	0.0077	0.53	0.0107	0.55	0.0226	0.231
	CYC	1.0	0.60	0.0004	0.61	0.0019	0.63	0.0049	0.000

Earthquake	Station	*D* (km)	μ_L	σ_L^2	μ_I	σ_I^2	μ_S	σ_S^2	*wu*
Morgan	G01	13.5	0.57	0.0021	0.59	0.0081	0.62	0.0105	0.080
Hill	G02	12.0	0.56	0.0067	0.58	0.0094	0.62	0.0115	0.009
	G03	10.9	0.53	0.0156	0.59	0.0101	0.65	0.0051	0.044
	G04	8.7	0.54	0.0112	0.58	0.0123	0.62	0.0115	0.018
	G06	6.5	0.60	0.0026	0.64	0.0057	0.66	0.0063	0.053
	G07	8.4	0.56	0.0053	0.57	0.0107	0.63	0.0106	0.071
	GIL	13.3	0.60	0.0012	0.59	0.0060	0.62	0.0104	0.098
	HVR	2.4	0.49	0.0086	0.60	0.0125	0.65	0.0113	0.036
	LBN	60.5	0.40	0.0307	0.49	0.0512	0.61	0.0637	0.827
	LOB	46.7	0.55	0.0026	0.56	0.0140	0.55	0.0294	0.231
	MSJ	30.3	0.44	0.0319	0.48	0.0296	0.52	0.0432	0.711
	SFO	70.5	0.33	0.0206	0.41	0.0335	0.40	0.0269	0.480
	SJB	26.4	0.45	0.0255	0.58	0.0192	0.60	0.0347	0.436
Parkfield	C02	6.6	0.59	0.0016	0.58	0.0095	0.61	0.0089	0.022
	C05	9.3	0.50	0.0022	0.51	0.0058	0.54	0.0078	0.000
	C08	13.0	0.54	0.0060	0.56	0.0102	0.58	0.0093	0.022
	TMB	16.1	0.60	0.0019	0.59	0.0050	0.61	0.0035	0.044
North Palm	DSP	1.6	0.59	0.0020	0.60	0.0057	0.62	0.0062	0.089
Springs	H01	59.6	0.49	0.0013	0.49	0.0057	0.49	0.0186	0.053
	H02	53.8	0.59	0.0022	0.58	0.0057	0.57	0.0160	0.133
	H03	48.1	0.63	0.0010	0.64	0.0030	0.63	0.0125	0.107
	H04	43.0	0.51	0.0040	0.51	0.0102	0.51	0.0156	0.187
	H05	39.4	0.50	0.0042	0.50	0.0170	0.51	0.0163	0.071
	H06	35.6	0.50	0.0144	0.52	0.0147	0.50	0.0173	0.133
	H08	27.8	0.54	0.0017	0.54	0.0097	0.57	0.0140	0.089
	H10	21.5	0.60	0.0010	0.59	0.0029	0.60	0.0119	0.107
	HES	70.6	0.39	0.0137	0.42	0.0345	0.44	0.0200	0.329
	INI	43.5	0.43	0.0230	0.51	0.0191	0.56	0.0192	0.196
	JST	22.7	0.51	0.0085	0.54	0.0163	0.59	0.0246	0.160
	LDR	31.4	0.53	0.0044	0.54	0.0089	0.57	0.0129	0.151
	PLC	68.2	0.44	0.0029	0.42	0.0122	0.43	0.0186	0.258
	PSA	12.0	0.52	0.0139	0.57	0.0090	0.60	0.0143	0.071
	RNC	81.0	0.39	0.0415	0.42	0.0341	0.45	0.0272	0.320
	RVA	68.6	0.42	0.0048	0.42	0.0094	0.43	0.0173	0.213
	TEM	69.5	0.40	0.0088	0.44	0.0171	0.49	0.0173	0.267
Imperial	AEP	1.4	0.55	0.0012	0.57	0.0061	0.59	0.0089	0.089
Valley	AGR	1.0	0.50	0.0057	0.52	0.0102	0.55	0.0131	0.222
	BCR	2.6	0.52	0.0053	0.55	0.0057	0.55	0.0130	0.036
	BRA	8.5	0.49	0.0069	0.47	0.0143	0.49	0.0146	0.204
	CAL	23.0	0.44	0.0286	0.44	0.0256	0.47	0.0247	0.169
	CC4	49.0	0.40	0.0101	0.46	0.0317	0.48	0.0376	0.444
	CHU	17.7	0.41	0.0206	0.49	0.0200	0.53	0.0208	0.089
	CMP	23.2	0.42	0.0276	0.47	0.0318	0.48	0.0271	0.204
	CPR	23.5	0.35	0.0569	0.41	0.0461	0.45	0.0227	0.382
	CUC	12.9	0.49	0.0096	0.51	0.0105	0.53	0.0095	0.071
	CXO	10.6	0.50	0.0098	0.50	0.0166	0.51	0.0103	0.107
	DLT	32.7	0.37	0.0782	0.39	0.0365	0.43	0.0198	0.356
	E01	22.0	0.44	0.0155	0.45	0.0150	0.49	0.0114	0.107
	E02	16.0	0.43	0.0017	0.44	0.0147	0.47	0.0122	0.044
	E03	11.2	0.48	0.0042	0.48	0.0154	0.50	0.0089	0.089

Earthquake	Station	*D* (km)	μ_L	σ_L^2	μ_I	σ_I^2	μ_S	σ_S^2	*wu*
Imperial	E04	6.8	0.53	0.0065	0.55	0.0082	0.58	0.0121	0.062
Valley	E05	4.0	0.53	0.0046	0.56	0.0042	0.59	0.0072	0.044
	E06	1.3	0.53	0.0022	0.58	0.0046	0.60	0.0063	0.044
	E07	0.6	0.55	0.0028	0.55	0.0098	0.57	0.0130	0.053
	E08	3.8	0.53	0.0010	0.52	0.0035	0.55	0.0067	0.071
	E10	8.5	0.48	0.0070	0.48	0.0092	0.52	0.0114	0.080
	E11	12.6	0.46	0.0020	0.47	0.0096	0.50	0.0111	0.062
	E12	18.0	0.40	0.0148	0.45	0.0160	0.50	0.0140	0.080
	E13	22.0	0.44	0.0241	0.48	0.0188	0.49	0.0132	0.089
	EDA	5.1	0.52	0.0009	0.52	0.0103	0.56	0.0073	0.044
	ELC	6.2	0.49	0.0070	0.50	0.0117	0.55	0.0087	0.089
	HVP	7.5	0.50	0.0052	0.51	0.0091	0.53	0.0136	0.053
	MXC	8.4	0.56	0.0029	0.57	0.0095	0.57	0.0089	0.151
	NIL	36.0	0.46	0.0172	0.47	0.0240	0.47	0.0278	0.338
	PLS	32.0	0.50	0.0031	0.50	0.0109	0.51	0.0158	0.018
	PTS	14.0	0.44	0.0109	0.48	0.0161	0.52	0.0116	0.116
	SUP	26.0	0.49	0.0008	0.48	0.0087	0.51	0.0105	0.071
	VCT	43.5	0.36	0.0163	0.41	0.0375	0.44	0.0156	0.276
	WSM	15.0	0.48	0.0300	0.49	0.0197	0.54	0.0195	0.178
San	GPK	21.1	0.51	0.0030	0.55	0.0106	0.58	0.0147	0.107
Fernando	L01	23.4	0.55	0.0161	0.56	0.0248	0.61	0.0164	0.222
	L09	20.2	0.64	0.0016	0.63	0.0036	0.63	0.0135	0.107
	L12	17.0	0.63	0.0051	0.61	0.0095	0.61	0.0120	0.089
	PAS	25.7	0.46	0.0081	0.49	0.0085	0.52	0.0128	0.044
	PDL	28.6	0.55	0.0119	0.57	0.0173	0.60	0.0123	0.107
	PPP	37.4	0.58	0.0052	0.58	0.0158	0.60	0.0138	0.204
	PSL	21.9	0.56	0.0056	0.55	0.0126	0.57	0.0117	0.178
	SOD	70.0	0.53	0.0061	0.54	0.0155	0.53	0.0157	0.222
Northridge	ALF	37.2	0.39	0.0100	0.46	0.0231	0.50	0.0190	0.133
	ANB	48.6	0.47	0.0053	0.49	0.0182	0.56	0.0236	0.258
	ANI	73.2	0.39	0.0062	0.42	0.0278	0.41	0.0306	0.320
	ANV	39.4	0.37	0.0099	0.42	0.0254	0.54	0.0238	0.196
	BAD	65.6	0.40	0.0051	0.42	0.0217	0.48	0.0192	0.169
	BHA	30.8	0.42	0.0124	0.47	0.0127	0.48	0.0108	0.044
	CMO	44.3	0.43	0.0437	0.45	0.0253	0.51	0.0286	0.302
	DOW	47.4	0.37	0.0192	0.42	0.0230	0.45	0.0144	0.151
	ELZ	38.1	0.40	0.0041	0.42	0.0149	0.51	0.0197	0.169
	FYP	82.7	0.33	0.0055	0.38	0.0311	0.37	0.0360	0.569
	GPK	24.4	0.49	0.0068	0.53	0.0102	0.56	0.0115	0.124
	HBL	78.3	0.36	0.0339	0.41	0.0269	0.48	0.0364	0.516
	HSL	24.8	0.47	0.0041	0.50	0.0140	0.52	0.0110	0.089
	HUV	73.9	0.38	0.0070	0.44	0.0218	0.44	0.0200	0.267
	IGU	43.1	0.38	0.0186	0.44	0.0229	0.47	0.0131	0.231
	L01	37.7	0.45	0.0129	0.53	0.0240	0.53	0.0149	0.373
	L09	28.4	0.53	0.0008	0.53	0.0104	0.57	0.0090	0.124
	L4B	34.0	0.48	0.0022	0.49	0.0140	0.53	0.0155	0.178
	L04	34.0	0.48	0.0026	0.49	0.0129	0.54	0.0166	0.160
	LAS	42.0	0.40	0.0133	0.42	0.0224	0.41	0.0170	0.178
	LBL	52.7	0.39	0.0413	0.43	0.0288	0.44	0.0172	0.160
	LCN	24.4	0.47	0.0068	0.50	0.0140	0.54	0.0082	0.116

Earthquake	Station	D (km)	μ_L	σ_L^2	μ_I	σ_I^2	μ_S	σ_S^2	wu
Northridge	LNF	53.4	0.43	0.0278	0.43	0.0196	0.48	0.0297	0.338
	LPK	45.7	0.46	0.0061	0.46	0.0169	0.47	0.0129	0.187
	LRP	48.9	0.44	0.0029	0.45	0.0196	0.48	0.0143	0.151
	LV1	38.6	0.48	0.0033	0.51	0.0131	0.55	0.0160	0.107
	LV2	38.6	0.48	0.0029	0.51	0.0158	0.52	0.0223	0.178
	LV3	38.7	0.47	0.0046	0.49	0.0196	0.55	0.0207	0.196
	LV4	38.9	0.45	0.0097	0.47	0.0167	0.54	0.0143	0.169
	LV5	39.2	0.43	0.0114	0.48	0.0207	0.52	0.0170	0.231
	LV6	39.4	0.45	0.0029	0.48	0.0137	0.50	0.0137	0.080
	MCN	27.0	0.49	0.0013	0.50	0.0028	0.52	0.0114	0.098
	MJO	78.0	0.42	0.0050	0.50	0.0298	0.56	0.0218	0.622
	MJV	86.9	0.34	0.0219	0.40	0.0354	0.49	0.0363	0.667
	MPK	28.3	0.47	0.0093	0.51	0.0193	0.51	0.0181	0.107
	MTW	36.9	0.47	0.0036	0.47	0.0148	0.51	0.0143	0.204
	NBI	86.2	0.35	0.0475	0.38	0.0294	0.44	0.0530	0.631
	NWH	8.4	0.56	0.0021	0.56	0.0050	0.57	0.0059	0.018
	NWK	54.1	0.34	0.0180	0.42	0.0259	0.50	0.0166	0.302
	OBG	37.9	0.45	0.0025	0.45	0.0198	0.49	0.0121	0.151
	ORR	24.6	0.49	0.0040	0.51	0.0069	0.51	0.0047	0.044
	PCD	9.3	0.58	0.0008	0.60	0.0020	0.59	0.0125	0.080
	PDS	35.7	0.42	0.0081	0.45	0.0227	0.51	0.0156	0.204
	PHN	56.0	0.43	0.0303	0.44	0.0226	0.47	0.0202	0.213
	PKC	9.3	0.52	0.0088	0.53	0.0124	0.56	0.0134	0.178
	PMG	49.8	0.41	0.0088	0.43	0.0208	0.44	0.0102	0.107
	PRD	86.8	0.30	0.0128	0.36	0.0302	0.41	0.0256	0.356
	PSW	34.5	0.43	0.0053	0.45	0.0158	0.51	0.0197	0.071
	PVC	53.8	0.44	0.0101	0.49	0.0283	0.53	0.0273	0.444
	RHE	50.8	0.42	0.0174	0.45	0.0258	0.48	0.0241	0.400
	RNC	82.9	0.34	0.0249	0.37	0.0232	0.43	0.0270	0.204
	ROS	66.0	0.35	0.0107	0.43	0.0298	0.46	0.0304	0.427
	RVA	99.6	0.48	0.0037	0.48	0.0183	0.49	0.0246	0.311
	SFY	9.5	0.53	0.0109	0.54	0.0123	0.59	0.0086	0.053
	SMG	27.8	0.46	0.0023	0.47	0.0060	0.49	0.0103	0.018
	SNM	35.5	0.46	0.0036	0.46	0.0122	0.47	0.0112	0.142
	SPP	58.5	0.38	0.0071	0.43	0.0219	0.44	0.0293	0.276
	SSA	18.4	0.55	0.0016	0.56	0.0034	0.55	0.0117	0.036
	SYH	7.6	0.56	0.0026	0.57	0.0081	0.60	0.0069	0.036
	TAR	3.0	0.48	0.0030	0.49	0.0058	0.50	0.0064	0.071
	TOP	23.6	0.52	0.0021	0.54	0.0076	0.60	0.0109	0.071
	ULA	23.6	0.49	0.0042	0.51	0.0084	0.54	0.0105	0.107
	USB	114.0	0.49	0.0309	0.55	0.0251	0.60	0.0333	0.409
	VLA	23.7	0.47	0.0051	0.51	0.0121	0.57	0.0119	0.071
	VRP	25.3	0.50	0.0011	0.51	0.0078	0.54	0.0098	0.098
	VSP	9.1	0.53	0.0016	0.53	0.0091	0.56	0.0081	0.053
Loma Prieta	A07	46.5	0.46	0.0146	0.48	0.0206	0.56	0.0177	0.276
	A10	46.6	0.50	0.0140	0.53	0.0215	0.63	0.0256	0.533
	A2E	56.7	0.35	0.0076	0.40	0.0175	0.46	0.0170	0.276
	A3E	56.7	0.45	0.0120	0.47	0.0177	0.51	0.0158	0.213
	AGW	27.0	0.41	0.0139	0.45	0.0175	0.46	0.0156	0.098
	CAP	8.6	0.50	0.0115	0.54	0.0105	0.53	0.0086	0.036

Earthquake	Station	*D* (km)	μ_L	σ_L^2	μ_I	σ_I^2	μ_S	σ_S^2	*wu*
Loma	CFH	83.5	0.41	0.0043	0.45	0.0223	0.57	0.0280	0.427
Prieta	CLS	0.0	0.58	0.0046	0.59	0.0092	0.59	0.0076	0.044
	CYC	21.7	0.53	0.0027	0.52	0.0158	0.55	0.0133	0.196
	DMH	75.9	0.42	0.0026	0.42	0.0159	0.51	0.0353	0.356
	EMV	81.0	0.38	0.0123	0.42	0.0144	0.44	0.0218	0.156
	FMS	42.4	0.38	0.0096	0.43	0.0178	0.46	0.0130	0.111
	G01	10.5	0.60	0.0005	0.60	0.0029	0.61	0.0093	0.018
	G02	12.1	0.56	0.0046	0.57	0.0088	0.60	0.0113	0.053
	G03	14.0	0.54	0.0032	0.56	0.0080	0.60	0.0090	0.044
	G04	15.8	0.51	0.0112	0.52	0.0145	0.56	0.0164	0.071
	G06	19.9	0.54	0.0063	0.56	0.0129	0.60	0.0109	0.151
	G07	24.3	0.51	0.0063	0.52	0.0124	0.54	0.0057	0.080
	GIL	10.9	0.60	0.0005	0.59	0.0037	0.60	0.0102	0.036
	GOF	12.3	0.55	0.0085	0.53	0.0174	0.56	0.0137	0.124
	HAD	25.4	0.47	0.0076	0.51	0.0114	0.56	0.0105	0.022
	HCH	27.8	0.47	0.0067	0.50	0.0138	0.58	0.0113	0.133
	HVR	29.3	0.43	0.0092	0.45	0.0174	0.50	0.0175	0.320
	HWB	57.7	0.35	0.0047	0.38	0.0167	0.45	0.0127	0.213
	LOB	12.5	0.48	0.0027	0.49	0.0108	0.50	0.0123	0.142
	MNT	42.7	0.44	0.0046	0.45	0.0198	0.48	0.0228	0.311
	MSJ	42.0	0.43	0.0131	0.45	0.0225	0.44	0.0122	0.204
	OSW	78.8	0.38	0.0044	0.39	0.0099	0.39	0.0189	0.151
	PHT	80.5	0.39	0.0083	0.40	0.0211	0.45	0.0309	0.480
	PIE	77.2	0.44	0.0071	0.44	0.0099	0.47	0.0268	0.213
	PRS	82.0	0.40	0.0024	0.42	0.0202	0.52	0.0248	0.418
	PTB	87.5	0.43	0.0059	0.45	0.0265	0.57	0.0275	0.587
	RCH	92.0	0.36	0.0102	0.39	0.0151	0.44	0.0252	0.284
	RIN	78.5	0.41	0.0067	0.41	0.0108	0.46	0.0230	0.302
	SAG	34.1	0.48	0.0130	0.52	0.0272	0.59	0.0270	0.356
	SAL	31.4	0.42	0.0211	0.47	0.0170	0.51	0.0208	0.249
	SFG	84.0	0.40	0.0050	0.43	0.0258	0.41	0.0198	0.267
	SLA	35.0	0.44	0.0033	0.44	0.0135	0.49	0.0187	0.089
	SSF	67.6	0.45	0.0028	0.42	0.0072	0.44	0.0184	0.124
	SVL	27.5	0.41	0.0084	0.45	0.0110	0.47	0.0108	0.067
	TIB	76.3	0.34	0.0121	0.45	0.0254	0.43	0.0166	0.222
	TRI	81.5	0.37	0.0031	0.39	0.0090	0.36	0.0143	0.116
	WDS	38.7	0.54	0.0115	0.51	0.0237	0.53	0.0286	0.382
	YBI	79.5	0.42	0.0028	0.40	0.0112	0.45	0.0196	0.302
Petrolia	ERB	1.9	0.57	0.0071	0.54	0.0268	0.56	0.0227	0.302
	ERC	9.8	0.51	0.0043	0.50	0.0212	0.50	0.0159	0.124
	ERF	14.6	0.48	0.0125	0.50	0.0280	0.52	0.0206	0.142
	ERL	17.6	0.46	0.0105	0.51	0.0126	0.52	0.0112	0.062
	ERR	23.9	0.42	0.0132	0.44	0.0209	0.49	0.0147	0.356
	ERU	27.8	0.45	0.0082	0.37	0.0154	0.35	0.0138	0.071
	EUR	35.8	0.42	0.0150	0.45	0.0170	0.47	0.0207	0.356
	FER	10.0	0.48	0.0102	0.52	0.0202	0.52	0.0088	0.169
	FRT	13.7	0.45	0.0125	0.46	0.0331	0.46	0.0217	0.258
	PGS	0.0	0.59	0.0094	0.56	0.0163	0.56	0.0188	0.169
	RDL	12.3	0.53	0.0045	0.52	0.0226	0.54	0.0142	0.062
	SCP	32.6	0.36	0.0294	0.36	0.0340	0.40	0.0362	0.356

APPENDIX C
DATA; METHOD OF ENVELOPES

The statistics on whitened intensity functions that are used in Chapter 4 are listed in Table C.1. The station code is the same as in Table A.1, where the locations of all the recording stations are tabulated. Source to site distances are taken from:

- Boore et al. (1993, 1994, 1997)
- Chang et al. (1996)

and calculated using information on the seismogenic rupture in:

- Archuleta and Day (1980)
- Bolt et al. (1985)
- Bouchon (1982)
- Chavez et al. (1982)
- Hagerty and Schwartz (1996)
- Hauksson et al. (1993)
- Hauksson and Jones (1995)
- Jones and Hauksson (1988)
- Kanamori and Regan (1982)
- Pacheco and Nabelek (1988)
- Wald et al. (1991)
- Whitcomb et al. (1973).

The parameters in Table C.1 are:

- D: The distance from the site to the vertical projection of the seismogenic rupture on the surface of the Earth.
- γ_0: The zeroth moment of the whitened intensity function about the origin (i.e., the area under the whitened intensity function).
- γ_1: The first moment of the whitened intensity function about the origin.
- γ_2: The second moment of the whitened intensity function about the origin.

Table C.1: The whitened intensity moments that are used in Chapter 4.

Earthquake	Station	D (km)	γ_0	γ_1 (sec)	γ_2 (sec^2)
Coyote Lake	CYC	1.6	0.03764	0.1048	0.559
	G01	9.1	0.03755	0.1325	0.941
	G02	7.4	0.03662	0.1240	0.565
	G03	5.3	0.03673	0.1321	0.678
	G04	3.7	0.03727	0.1385	0.821
	G06	1.2	0.03818	0.1118	0.679
	HVR	30.0	0.04462	0.4059	8.684
	SJB	17.9	0.03659	0.1896	1.715
Whittier Narrows	ALF	3.0	0.03630	0.1612	0.941
	BHA	22.5	0.03746	0.2630	2.829
	CHC	64.4	0.03731	0.4957	10.095
	DOW	11.3	0.03810	0.2525	2.386
	ECP	10.5	0.03749	0.1786	1.336
	FYP	35.5	0.03760	0.3296	5.079
	H05	103.9	0.03756	0.5799	10.784
	HBL	39.8	0.03766	0.3919	5.815
	HSL	20.5	0.03740	0.2757	3.063
	IGU	19.4	0.03605	0.2489	2.194
	L01	71.7	0.03879	0.4514	8.104
	LAS	16.4	0.03728	0.2342	1.807
	LBH	30.2	0.03790	0.3468	5.570
	LBL	20.9	0.03673	0.2530	2.263
	LBR	26.6	0.03740	0.3774	5.960
	LCN	27.7	0.03746	0.2937	3.147
	LCS	27.5	0.03827	0.3273	6.309
	LV5	58.6	0.03853	0.3780	5.794
	LV6	59.1	0.03819	0.2989	4.306
	MPK	73.9	0.03803	0.5893	13.103
	NWH	51.0	0.03813	0.4386	8.896
	OBG	5.6	0.03730	0.2011	1.423
	ORR	71.5	0.03846	0.5051	10.422
	PDS	62.9	0.03816	0.4627	8.466
	PKC	32.9	0.03682	0.3326	4.896
	RGR	83.8	0.03743	0.5030	9.049
	RNC	43.9	0.03759	0.3939	5.166
	RVA	56.2	0.03656	0.3827	4.935
	SFY	34.1	0.03779	0.2992	3.383
	SNM	3.8	0.03729	0.1527	0.995
	SYH	40.4	0.03721	0.3717	5.474
	TAR	39.3	0.03671	0.3170	3.157
	VRP	48.9	0.03765	0.3372	3.534
	XLA	67.4	0.03717	0.4287	6.779
	XPO	28.0	0.03731	0.3279	4.082
Morgan Hill	A01	53.5	0.03679	0.5461	10.743
	A1E	50.9	0.03895	0.5231	11.631
	AGW	24.4	0.03753	0.5323	10.516
	CAP	40.1	0.03708	0.3131	3.541
	CLS	24.6	0.03779	0.3229	4.505

Earthquake	Station	D (km)	γ_0	γ_1 (sec)	γ_2 (sec^2)
Morgan Hill	CYC	1.0	0.03777	0.1270	0.552
	G01	13.5	0.03762	0.1690	1.441
	G02	12.0	0.03747	0.1759	1.599
	G03	10.9	0.03779	0.1634	1.661
	G04	8.7	0.03702	0.1809	1.934
	G06	6.5	0.03686	0.1069	1.008
	G07	8.4	0.03787	0.1770	1.807
	GIL	13.3	0.03806	0.1664	1.309
	HVR	2.4	0.03822	0.1684	1.863
	LBN	60.5	0.03870	0.6566	15.778
	LOB	46.7	0.03787	0.3079	4.604
	MSJ	30.3	0.03903	0.5499	12.063
	SFO	70.5	0.03769	0.5670	10.869
	SJB	26.4	0.03770	0.4002	8.190
Parkfield	C02	6.6	0.04705	0.3589	8.737
	C05	9.3	0.03812	0.2759	2.266
	C08	13.0	0.03760	0.1976	1.412
	TMB	16.1	0.04003	0.1863	1.852
North Palm Springs	DSP	1.6	0.03767	0.1563	1.118
	H01	59.6	0.03812	0.3612	4.252
	H02	53.8	0.03785	0.2263	2.243
	H03	48.1	0.04205	0.1527	1.534
	H04	43.0	0.03736	0.3245	3.883
	H05	39.4	0.03697	0.3322	3.917
	H06	35.6	0.03772	0.3323	3.955
	H08	27.8	0.03752	0.2390	2.155
	H10	21.5	0.04068	0.2167	2.813
	HES	70.6	0.03793	0.5038	8.762
	INI	43.5	0.03807	0.3229	4.357
	JST	22.7	0.03852	0.3004	4.767
	LDR	31.4	0.03788	0.2725	2.989
	PLC	68.2	0.03746	0.4484	6.388
	PSA	12.0	0.03858	0.2257	2.273
	RNC	81.0	0.03819	0.4990	8.827
	RVA	68.6	0.03759	0.4547	6.522
	TEM	69.5	0.03760	0.4315	6.745
Imperial Valley	AEP	1.4	0.03801	0.1931	1.261
	AGR	1.0	0.03811	0.2874	2.858
	BCR	2.6	0.03784	0.2467	1.965
	BRA	8.5	0.03782	0.3706	4.490
	CAL	23.0	0.03789	0.4795	7.890
	CC4	49.0	0.03693	0.4178	6.600
	CHU	17.7	0.03738	0.3456	4.527
	CMP	23.2	0.03815	0.4667	7.806
	CPR	23.5	0.03737	0.5432	10.496
	CUC	12.9	0.03778	0.3127	3.270
	CXO	10.6	0.03784	0.3239	3.494
	DLT	32.7	0.03742	0.5517	10.318
	E01	22.0	0.03772	0.4006	5.197
	E02	16.0	0.03717	0.3877	4.546

Earthquake	Station	D (km)	γ_0	γ_1 (sec)	γ_2 (sec^2)
Imperial Valley	E03	11.2	0.03774	0.3396	3.619
	E04	6.8	0.03724	0.2167	1.745
	E05	4.0	0.03721	0.2273	2.148
	E06	1.3	0.03826	0.2011	1.587
	E07	0.6	0.03777	0.2255	1.902
	E08	3.8	0.03730	0.2721	2.238
	E10	8.5	0.03757	0.3229	3.370
	E11	12.6	0.03777	0.3451	3.627
	E12	18.0	0.03778	0.3755	4.708
	E13	22.0	0.03795	0.3731	4.646
	EDA	5.1	0.03762	0.2546	2.106
	ELC	6.2	0.03821	0.2993	2.985
	HVP	7.5	0.03811	0.3016	2.903
	MXC	8.4	0.03859	0.2054	1.537
	NIL	36.0	0.03819	0.4669	8.193
	PLS	32.0	0.03769	0.3004	2.795
	PTS	14.0	0.03726	0.3451	4.106
	SUP	26.0	0.03741	0.3244	3.204
	VCT	43.5	0.03747	0.5291	9.203
	WSM	15.0	0.03793	0.3621	5.222
San Fernando	GPK	21.1	0.03988	0.2465	2.639
	L01	23.4	0.03934	0.2408	3.425
	L04	19.6	0.03907	0.2018	1.913
	L09	20.2	0.04201	0.1411	1.307
	L12	17.0	0.03867	0.1518	1.196
	PAS	25.7	0.03768	0.3235	3.251
	PDL	28.6	0.03870	0.2321	2.641
	PPP	37.4	0.03953	0.2045	1.988
	PSL	21.9	0.03848	0.2523	2.840
	SOD	70.0	0.03780	0.2947	3.251
Northridge	ALF	37.2	0.03825	0.4324	6.402
	ANB	48.6	0.03883	0.4014	7.015
	ANI	73.2	0.03817	0.5231	9.541
	BHA	30.8	0.03851	0.3859	4.646
	CMO	44.3	0.04672	0.6799	16.474
	DOW	47.4	0.03797	0.4864	7.408
	FYP	82.7	0.03793	0.6174	12.575
	HBL	78.3	0.03910	0.6234	13.445
	HSL	24.8	0.03733	0.3042	3.048
	IGU	43.1	0.03851	0.4671	7.216
	L01	37.7	0.03733	0.3585	5.457
	L04	34.0	0.03811	0.3137	3.638
	L09	28.4	0.03825	0.2483	2.244
	L4B	34.0	0.03906	0.3620	4.831
	LAS	42.0	0.03847	0.5065	8.012
	LBG	58.7	0.03859	0.5965	12.197
	LBL	52.7	0.03884	0.5238	8.702
	LCN	24.4	0.03801	0.3130	3.254
	LNF	53.4	0.03822	0.5150	9.566
	LPK	45.7	0.03656	0.3759	4.703

Earthquake	Station	D (km)	γ_0	γ_1 (sec)	γ_2 (sec^2)
Northridge	LV1	38.6	0.03914	0.3474	4.537
	LV2	38.6	0.03880	0.3587	4.880
	LV3	38.7	0.03854	0.3731	5.341
	LV4	38.9	0.03832	0.3578	4.593
	LV5	39.2	0.03804	0.3909	5.721
	LV6	39.4	0.03804	0.3706	4.506
	MJO	78.0	0.03927	0.4673	9.395
	MJV	86.9	0.03749	0.6361	14.424
	MPK	28.3	0.03759	0.3387	4.229
	MTW	36.9	0.03841	0.3472	4.108
	NBI	86.2	0.03907	0.7104	16.557
	NWH	8.4	0.03833	0.2272	1.661
	OBG	37.9	0.03776	0.3925	4.926
	ORR	24.6	0.03880	0.3030	2.672
	PCD	9.3	0.03750	0.1731	1.148
	PDS	35.7	0.03850	0.4080	5.628
	PHN	56.0	0.03810	0.4791	8.256
	PKC	9.3	0.03813	0.2866	3.591
	PMG	49.8	0.03741	0.4401	5.908
	PVC	53.8	0.03828	0.4803	9.032
	RHE	50.8	0.03836	0.4987	9.232
	RNC	82.9	0.03867	0.5476	9.347
	ROS	66.0	0.03809	0.5536	10.743
	RVA	99.6	0.03879	0.4527	7.717
	SFY	9.5	0.03831	0.2202	1.806
	SMG	27.8	0.03761	0.3470	3.557
	SNM	35.5	0.03684	0.3643	4.329
	SPP	58.5	0.03728	0.5139	9.024
	SYH	7.6	0.03798	0.1978	1.647
	TAR	3.0	0.03763	0.3072	2.834
	ULA	23.6	0.03805	0.2822	2.723
	USB	114.0	0.04358	0.5553	14.366
	VHI	62.4	0.03794	0.6571	14.871
	VRP	25.3	0.03805	0.3050	2.892
Loma	A02	47.2	0.04519	0.6247	16.888
Prieta	A07	46.5	0.03882	0.3693	5.677
	A10	46.6	0.03949	0.5221	12.216
	A2E	56.7	0.03832	0.4970	7.943
	A3E	56.7	0.03890	0.4039	5.802
	AGW	27.0	0.03847	0.4462	6.422
	CAP	8.6	0.03818	0.2724	2.393
	CFH	83.5	0.03818	0.4102	6.945
	CLS	0.0	0.03723	0.1782	1.272
	CYC	21.7	0.03743	0.2889	3.387
	DMH	75.9	0.03860	0.4896	8.534
	EMV	81.0	0.03803	0.5588	12.015
	FMS	42.4	0.03824	0.5517	11.798
	G01	10.5	0.03739	0.1640	1.024
	G02	12.1	0.03782	0.1982	1.644
	G03	14.0	0.03781	0.2105	1.636

Earthquake	Station	D (km)	γ_0	γ_1 (sec)	γ_2 (sec^2)
Loma	G04	15.8	0.03765	0.2816	3.247
Prieta	G06	19.9	0.03729	0.2267	2.632
	G07	24.3	0.03762	0.2805	2.664
	GIL	10.9	0.03732	0.1696	1.136
	GOF	12.3	0.03748	0.2649	2.802
	HAD	25.4	0.03760	0.4010	8.736
	HCH	27.8	0.03793	0.4282	9.703
	HSP	28.2	0.04005	0.3833	6.854
	HVR	29.3	0.03829	0.4248	6.581
	HWB	57.7	0.03714	0.4658	6.723
	LOB	12.5	0.03773	0.3212	3.257
	MNT	42.7	0.03777	0.4464	7.097
	MSJ	42.0	0.03804	0.4692	7.432
	OSW	78.8	0.03775	0.4806	7.043
	PHT	80.5	0.03861	0.5420	10.409
	PIE	77.2	0.03870	0.4630	7.405
	PRS	82.0	0.03829	0.4704	8.144
	PTB	87.5	0.03956	0.5001	9.802
	RCH	92.0	0.03698	0.4792	7.810
	RIN	78.5	0.03875	0.4285	6.119
	SAG	34.1	0.03948	0.4367	9.039
	SAL	31.4	0.03784	0.4702	8.674
	SFG	84.0	0.04368	0.6797	16.635
	SLA	35.0	0.03840	0.5392	11.707
	SSF	67.6	0.03778	0.4283	5.625
	STG	11.7	0.03828	0.2904	2.630
	SVL	27.5	0.03895	0.5100	9.806
	TIB	76.3	0.03787	0.4424	6.408
	TRI	81.5	0.03784	0.5061	7.648
	WDS	38.7	0.03922	0.3813	6.317
	YBI	79.5	0.03900	0.4944	7.787
Petrolia	ERB	1.9	0.03828	0.3016	4.037
	ERC	9.8	0.03766	0.3330	3.704
	ERF	14.6	0.03757	0.3273	3.897
	ERL	17.6	0.03739	0.3059	3.040
	ERR	23.9	0.03762	0.3946	5.266
	ERU	27.8	0.03686	0.4882	7.078
	EUR	35.8	0.03830	0.5010	9.013
	FER	10.0	0.03679	0.2949	3.063
	RDL	12.3	0.03796	0.3015	3.480
	SCP	32.6	0.03731	0.5889	11.205
Landers	AMB	68.3	0.04158	0.8813	22.452
	BKR	88.3	0.03855	0.8169	19.526
	BRN	92.4	0.03882	0.8318	20.751
	BRS	37.7	0.03826	0.6832	14.166
	DSP	22.5	0.03796	0.6400	14.807
	FFP	45.4	0.03738	0.6442	13.823
	FTI	65.0	0.03813	0.7585	16.313
	FVR	25.8	0.03765	0.5869	13.071
	H05	69.1	0.03805	0.8063	20.220

Earthquake	Station	D (km)	γ_0	γ_1 (sec)	γ_2 (sec^2)
Landers	H10	51.3	0.03838	0.6584	14.717
	INI	54.9	0.03890	0.6122	14.189
	INO	49.6	0.03756	0.7385	18.783
	JST	11.3	0.03782	0.4625	9.118
	MVF	17.7	0.03856	0.6070	13.136
	NPS	27.7	0.03880	0.7248	17.477
	PLC	95.0	0.03808	0.9418	26.931
	PSA	36.7	0.03818	0.6998	16.761
	PWS	41.9	0.03839	0.6554	14.696
	RVA	95.9	0.03827	0.7817	18.503
	TPP	37.7	0.03759	0.7072	17.390
	WWT	27.6	0.03785	0.7020	16.788
	YER	26.3	0.03812	0.6813	14.626

APPENDIX D
DATA; FOURIER AMPLITUDES

The statistics on Fourier amplitude spectra that are used in Chapter 5 are listed in Table D.1. The station code is the same as in Table A.1, where the locations of all the recording stations are tabulated. Source to site distances are taken from:

- Boore et al. (1993, 1994, 1997)
- Chang et al. (1996)

and calculated using information on the seismogenic rupture in:

- Archuleta and Day (1980)
- Bolt et al. (1985)
- Bouchon (1982)
- Chavez et al. (1982)
- Hagerty and Schwartz (1996)
- Hauksson et al. (1993)
- Hauksson and Jones (1995)
- Jones and Hauksson (1988)
- Kanamori and Regan (1982)
- Pacheco and Nabelek (1988)
- Wald et al. (1991)
- Whitcomb et al. (1973).

The parameters in Table D.1 are:

- D: The distance from the site to the vertical projection of the seismogenic rupture on the surface of the Earth.
- E: The sum of the squared Fourier amplitudes. Note that the values in Table D.1 have not been normalized by N, the order of the Fourier transform.
- M_F: The central frequency parameter.
- V_F: The spectral bandwidth parameter.

Table D.1: The Fourier spectra parameters that are used in Chapter 5.

Earthquake	Station	D (km)	E (g^2)	M_F	V_F
Coyote Lake	CYC	1.6	1194	0.105	0.00433
	G01	9.1	268	0.265	0.03475
	G02	7.4	1705	0.140	0.01369
	G03	5.3	1283	0.134	0.01391
	G04	3.7	1663	0.094	0.00556
	G06	1.2	2275	0.130	0.00481
	HVR	30.0	70	0.122	0.00690
	SJB	17.9	327	0.107	0.00594
Whittier Narrows	ALF	3.0	2901	0.218	0.01686
	BHA	22.5	886	0.168	0.01243
	CHC	64.4	94	0.129	0.00691
	DOW	11.3	771	0.157	0.01967
	ECP	10.5	617	0.256	0.02255
	FYP	35.5	236	0.146	0.00474
	H05	103.9	52	0.277	0.02056
	HBL	39.8	97	0.198	0.01599
	HSL	20.5	530	0.193	0.02117
	IGU	19.4	1119	0.174	0.02236
	L01	71.7	48	0.149	0.01158
	LAS	16.4	2902	0.214	0.01075
	LBH	30.2	286	0.108	0.00906
	LBL	20.9	1223	0.128	0.00871
	LBR	26.6	197	0.142	0.01360
	LCN	27.7	506	0.187	0.01523
	LCS	27.5	214	0.149	0.01085
	LV5	58.6	88	0.178	0.01296
	LV6	59.1	91	0.233	0.02010
	MPK	73.9	113	0.137	0.00569
	NWH	51.0	147	0.141	0.00675
	OBG	5.6	4192	0.222	0.01287
	ORR	71.5	288	0.119	0.00428
	PDS	62.9	82	0.163	0.00987
	PKC	32.9	631	0.165	0.00882
	RGR	83.8	106	0.149	0.00588
	RNC	43.9	128	0.400	0.04841
	RVA	56.2	97	0.313	0.03564
	SFY	34.1	335	0.153	0.01356
	SNM	3.8	994	0.202	0.02754
	SYH	40.4	197	0.167	0.01182
	TAR	39.3	8041	0.160	0.01009
	VRP	48.9	92	0.322	0.03457
	XLA	67.4	154	0.179	0.00957
	XPO	28.0	112	0.224	0.02565
Morgan Hill	A01	53.5	224	0.113	0.00690
	A1E	50.9	61	0.115	0.00795
	AGW	24.4	172	0.066	0.00438
	CAP	40.1	791	0.150	0.00854
	CLS	24.6	317	0.091	0.00445
	CYC	1.0	12816	0.121	0.01236

Earthquake	Station	D (km)	E (g^2)	M_F	V_F
Morgan Hill	G01	13.5	199	0.254	0.02585
	G02	12.0	824	0.164	0.01205
	G03	10.9	1131	0.132	0.01240
	G04	8.7	2567	0.125	0.00682
	G06	6.5	2903	0.105	0.00564
	G07	8.4	684	0.169	0.01153
	GIL	13.3	192	0.317	0.02621
	HVR	2.4	2894	0.095	0.00628
	LBN	60.5	155	0.054	0.00216
	LOB	46.7	85	0.180	0.00866
	MSJ	30.3	48	0.109	0.00943
	SFO	70.5	118	0.120	0.00490
	SJB	26.4	113	0.089	0.00602
Parkfield	C02	6.6	6019	0.068	0.00248
	C05	9.3	2823	0.131	0.00731
	C08	13.0	1019	0.183	0.01718
	TMB	16.1	1497	0.122	0.00403
North Palm Springs	DSP	1.6	3064	0.198	0.01677
	H01	59.6	69	0.367	0.01925
	H02	53.8	149	0.407	0.02474
	H03	48.1	69	0.492	0.06180
	H04	43.0	277	0.167	0.01529
	H05	39.4	424	0.286	0.01770
	H06	35.6	163	0.176	0.02357
	H08	27.8	1176	0.214	0.01744
	H10	21.5	199	0.331	0.03034
	HES	70.6	55	0.231	0.01728
	INI	43.5	167	0.245	0.04500
	JST	22.7	183	0.143	0.00964
	LDR	31.4	247	0.193	0.02050
	PLC	68.2	109	0.398	0.03403
	PSA	12.0	1102	0.250	0.04086
	RNC	81.0	24	0.234	0.03494
	RVA	68.6	52	0.376	0.05018
	TEM	69.5	182	0.140	0.00858
Imperial Valley	AEP	1.4	2812	0.213	0.02633
	AGR	1.0	3170	0.249	0.06979
	BCR	2.6	19999	0.135	0.01157
	BRA	8.5	1478	0.130	0.01476
	CAL	23.0	335	0.114	0.01002
	CC4	49.0	674	0.077	0.00105
	CHU	17.7	3826	0.123	0.01416
	CMP	23.2	1306	0.177	0.01692
	CPR	23.5	4123	0.133	0.01394
	CUC	12.9	3379	0.158	0.02136
	CXO	10.6	2488	0.177	0.01430
	DLT	32.7	9322	0.138	0.01510
	E01	22.0	739	0.257	0.03227
	E02	16.0	3343	0.214	0.01352
	E03	11.2	2296	0.183	0.01511

Earthquake	Station	D (km)	E (g^2)	M_F	V_F
Imperial	E04	6.8	3062	0.091	0.01816
Valley	E05	4.0	5545	0.114	0.02683
	E06	1.3	5851	0.128	0.02917
	E07	0.6	5631	0.056	0.00499
	E08	3.8	5017	0.212	0.03001
	E10	8.5	1879	0.115	0.01460
	E11	12.6	5374	0.141	0.00592
	E12	18.0	1096	0.148	0.01600
	E13	22.0	885	0.171	0.01743
	EDA	5.1	7041	0.131	0.00973
	ELC	6.2	2404	0.071	0.00791
	HVP	7.5	2803	0.140	0.01250
	MXC	8.4	3386	0.212	0.02042
	NIL	36.0	611	0.116	0.00668
	PLS	32.0	189	0.171	0.01049
	PTS	14.0	738	0.136	0.01038
	SUP	26.0	687	0.233	0.01215
	VCT	43.5	648	0.207	0.01585
	WSM	15.0	397	0.085	0.00900
San	GPK	21.1	1223	0.139	0.01870
Fernando	L01	23.4	860	0.081	0.00586
	L09	20.2	510	0.375	0.07290
	L12	17.0	3054	0.216	0.00964
	PAS	25.7	445	0.151	0.02107
	PDL	28.6	1121	0.139	0.01612
	PPP	37.4	508	0.264	0.02046
	PSL	21.9	391	0.206	0.01281
	SOD	70.0	186	0.198	0.01498
Northridge	ALF	37.2	631	0.118	0.00806
	ANB	48.6	97	0.197	0.01595
	ANI	73.2	244	0.190	0.00527
	ANV	39.4	92	0.118	0.00857
	BAD	65.6	864	0.138	0.00371
	BHA	30.8	2231	0.154	0.01433
	CMO	44.3	1263	0.087	0.00529
	DOW	47.4	1838	0.132	0.00715
	ELZ	38.1	807	0.131	0.00609
	FYP	82.7	416	0.122	0.00298
	GPK	24.4	1315	0.155	0.02847
	HBL	78.3	277	0.110	0.00410
	HSL	24.8	3114	0.163	0.01461
	HUV	73.9	832	0.117	0.00447
	IGU	43.1	737	0.118	0.01037
	L01	37.7	370	0.096	0.00696
	L09	28.4	778	0.221	0.01250
	L4B	34.0	126	0.220	0.01662
	L04	34.0	265	0.219	0.01650
	LAS	42.0	1347	0.152	0.00964
	LBL	52.7	521	0.118	0.00737
	LCN	24.4	3920	0.139	0.00820

Earthquake	Station	D (km)	E (g^2)	M_F	V_F
Northridge	LNF	53.4	220	0.102	0.00744
	LPK	45.7	2028	0.120	0.00392
	LRP	48.9	744	0.148	0.00877
	LV1	38.6	212	0.158	0.01415
	LV2	38.6	210	0.164	0.01598
	LV3	38.7	259	0.138	0.01172
	LV4	38.9	299	0.108	0.01254
	LV5	39.2	663	0.122	0.00893
	LV6	39.4	1142	0.158	0.00867
	MCN	27.0	1070	0.366	0.05446
	MJO	78.0	137	0.159	0.00386
	MJV	86.9	90	0.119	0.00510
	MPK	28.3	3118	0.122	0.00422
	MTW	36.9	748	0.234	0.01480
	NBI	86.2	289	0.109	0.00411
	NWH	8.4	14473	0.115	0.00434
	NWK	54.1	287	0.138	0.00878
	OBG	37.9	3708	0.196	0.00908
	ORR	24.6	9255	0.111	0.00511
	PCD	9.3	2431	0.136	0.01549
	PDS	35.7	789	0.137	0.00669
	PHN	56.0	493	0.102	0.00709
	PKC	9.3	5336	0.083	0.00274
	PMG	49.8	2291	0.106	0.00556
	PRD	86.8	444	0.115	0.00488
	PSW	34.5	1144	0.156	0.00992
	PVC	53.8	177	0.152	0.00702
	RHE	50.8	494	0.106	0.00313
	RNC	82.9	147	0.180	0.01810
	ROS	66.0	132	0.134	0.00843
	RVA	99.6	147	0.183	0.00348
	SFY	9.5	5059	0.122	0.01208
	SMG	27.8	9446	0.178	0.01124
	SNM	35.5	766	0.168	0.00988
	SPP	58.5	400	0.115	0.00419
	SSA	18.4	3611	0.275	0.03084
	SYH	7.6	8646	0.089	0.00543
	TAR	3.0	75508	0.173	0.02088
	TOP	23.6	3430	0.180	0.01312
	ULA	23.6	2896	0.235	0.03016
	USB	114.0	488	0.091	0.00311
	VLA	23.7	1565	0.097	0.00596
	VRP	25.3	1058	0.188	0.01638
	VSP	9.1	23155	0.142	0.00828
Loma Prieta	A07	46.5	587	0.097	0.00748
	A10	46.6	854	0.057	0.00178
	A2E	56.7	977	0.126	0.00973
	A3E	56.7	346	0.131	0.00922
	AGW	27.0	1304	0.100	0.00875
	CAP	8.6	7877	0.146	0.01705

Earthquake	Station	D (km)	E (g^2)	M_F	V_F
Loma	CFH	83.5	452	0.054	0.00242
Prieta	CLS	0.0	8536	0.096	0.00580
	CYC	21.7	1547	0.127	0.00732
	DMH	75.9	350	0.101	0.00553
	EMV	81.0	1722	0.058	0.00193
	FMS	42.4	1102	0.137	0.00855
	G01	10.5	5571	0.154	0.01722
	G02	12.1	4082	0.103	0.00969
	G03	14.0	4484	0.155	0.02008
	G04	15.8	3208	0.080	0.00395
	G06	19.9	1480	0.134	0.00604
	G07	24.3	2804	0.135	0.00782
	GIL	10.9	3009	0.187	0.01867
	GOF	12.3	1654	0.103	0.00572
	HAD	25.4	3480	0.078	0.00362
	HCH	27.8	3523	0.051	0.00162
	HVR	29.3	838	0.084	0.00390
	HWB	57.7	927	0.171	0.01226
	LOB	12.5	6782	0.238	0.01494
	MNT	42.7	191	0.168	0.01013
	MSJ	42.0	849	0.156	0.01049
	OSW	78.8	3286	0.064	0.00291
	PHT	80.5	133	0.066	0.00381
	PIE	77.2	160	0.104	0.00839
	PRS	82.0	879	0.075	0.00384
	PTB	87.5	302	0.052	0.00221
	RCH	92.0	547	0.084	0.00560
	RIN	78.5	225	0.113	0.02027
	SAG	34.1	321	0.080	0.00641
	SAL	31.4	800	0.121	0.00862
	SFG	84.0	939	0.066	0.00154
	SLA	35.0	3073	0.098	0.00507
	SSF	67.6	258	0.125	0.01234
	SVL	27.5	2567	0.081	0.00655
	TIB	76.3	401	0.177	0.01922
	TRI	81.5	1197	0.055	0.00198
	WDS	38.7	425	0.078	0.00392
	YBI	79.5	142	0.086	0.00775
Petrolia	ERB	1.9	1938	0.072	0.00278
	ERC	9.8	5228	0.123	0.00848
	ERF	14.6	4412	0.105	0.00364
	ERL	17.6	2353	0.128	0.00904
	ERR	23.9	2107	0.076	0.00419
	ERU	27.8	1694	0.086	0.00413
	EUR	35.8	1094	0.070	0.00401
	FER	10.0	3394	0.071	0.00493
	FRT	13.7	793	0.081	0.00655
	PGS	0.0	12712	0.111	0.01582
	RDL	12.3	5069	0.121	0.00700
	SCP	32.6	1691	0.266	0.01265

Earthquake	Station	D (km)	E (g^2)	M_F	V_F
Landers	AMB	68.3	2447	0.156	0.01346
	BKR	88.3	854	0.129	0.00972
	BRN	92.4	571	0.081	0.00413
	BRS	37.7	731	0.098	0.01056
	DSP	22.5	2177	0.106	0.01087
	FFP	45.4	897	0.195	0.02527
	FTI	65.0	763	0.134	0.01178
	FVR	25.8	3958	0.134	0.00787
	H05	69.1	754	0.214	0.01883
	H10	51.3	223	0.246	0.03082
	INI	54.9	994	0.095	0.01000
	INO	49.6	2093	0.098	0.00506
	JST	11.3	7786	0.084	0.00465
	MVF	17.7	2303	0.084	0.00676
	NPS	27.7	1782	0.160	0.01487
	PLC	95.0	256	0.270	0.01782
	PSA	36.7	1181	0.143	0.02554
	PWS	41.9	346	0.348	0.03852
	RVA	95.9	204	0.249	0.02896
	TPP	37.7	1422	0.123	0.01585
	WWT	27.6	1757	0.231	0.02033
	YER	26.3	2246	0.127	0.01258

APPENDIX E
STATIONS IN THE SMART-1 ARRAY

Table E.1: SMART-1 array station locations (Niazi, 1990).

Station	Longitude (Deg East)	Latitude (Deg. North)	Elevation (meters)
C-00	121.7647	24.6738	6.1
I-01	121.7650	24.6755	5.9
I-02	121.7660	24.6750	5.5
I-03	121.7666	24.6743	6.1
I-04	121.7667	24.6734	6.1
I-05	121.7662	24.6725	6.3
I-06	121.7652	24.6721	6.6
I-07	121.7642	24.6720	6.3
I-08	121.7635	24.6725	6.2
I-09	121.7628	24.6732	7.0
I-10	121.7628	24.6741	7.0
I-11	121.7634	24.6749	6.8
I-12	121.7641	24.6755	6.4
M-01	121.7667	24.6825	5.0
M-02	121.7717	24.6814	4.4
M-03	121.7734	24.6769	4.0
M-04	121.7745	24.6717	4.5
M-05	121.7720	24.6682	3.9
M-06	121.7677	24.6651	4.3
M-07	121.7622	24.6649	5.2
M-08	121.7584	24.6670	7.4
M-09	121.7552	24.6704	10.8
M-10	121.7557	24.6750	7.6
M-11	121.7574	24.6799	7.1
M-12	121.7619	24.6826	5.8
O-01	121.7687	24.6917	5.3
O-02	121.7781	24.6871	4.9
O-03	121.7840	24.6791	3.4
O-04	121.7840	24.6703	2.4
O-05	121.7798	24.6622	3.8
O-06	121.7708	24.6565	4.8
O-07	121.7608	24.6560	7.2
O-08	121.7518	24.6594	18.1
O-09	121.7457	24.6675	9.6
O-10	121.7454	24.6778	13.4
O-11	121.7506	24.6857	9.1
O-12	121.7589	24.6910	6.5
E-01	121.7644	24.6487	5.2
E-02	121.7610	24.6305	9.7

APPENDIX F
THE NORTHRIDGE EARTHQUAKE CASE STUDY; RECORDINGS AND SIMULATIONS

The recording stations used in the 1994 Northridge, California earthquake case study that is described in Chapter 7 are listed in this appendix. The station code is the same as in Table A.1, where the locations of all the recording stations are tabulated. This appendix includes four tables, each containing information on one ground motion intensity parameter:

- Table F.1: Peak ground acceleration.
- Table F.2: Pseudo spectral acceleration corresponding to a natural period of 0.3 seconds.
- Table F.3: Pseudo spectral acceleration corresponding to a natural period of 1.0 seconds.
- Table F.4: Pseudo spectral acceleration corresponding to a natural period of 2.0 seconds.

In each table, the recorded ground motion intensity parameter is reported, along with summary statistics from ten simulations. These summary statistics are:

- The mean.
- The standard deviation.
- The median.
- The standard deviation of the natural logarithm of the ground motion intensity parameter; i.e., the logarithmic standard deviation.

The data that are tabulated in this appendix are presented graphically in Figures 7.2 through 7.5.

Table F.1: Recorded PGA and summary statistics from ten simulated time series.

Station	Recorded PGA (g)	Mean (g)	St.Dev. (g)	Median (g)	Log.St.Dev.
ALF	0.101	0.103	0.007	0.103	0.067
ANB	0.068	0.041	0.006	0.041	0.151
ANI	0.037	0.033	0.005	0.033	0.158
BHA	0.239	0.210	0.020	0.206	0.095
CMO	0.121	0.120	0.015	0.121	0.129
DOW	0.177	0.189	0.028	0.182	0.149
FYP	0.100	0.081	0.009	0.078	0.112
HSL	0.231	0.300	0.075	0.275	0.251
IGU	0.101	0.112	0.012	0.109	0.111
L01	0.077	0.073	0.012	0.076	0.160
L04	0.084	0.076	0.010	0.075	0.131
L09	0.225	0.173	0.023	0.176	0.132
LAS	0.198	0.158	0.015	0.157	0.095
LBL	0.069	0.094	0.016	0.089	0.167
LCN	0.256	0.301	0.026	0.301	0.086
LNF	0.064	0.054	0.005	0.054	0.086
LPK	0.223	0.191	0.020	0.194	0.105
LV1	0.073	0.067	0.005	0.065	0.074
LV2	0.063	0.066	0.008	0.065	0.118
LV3	0.106	0.069	0.009	0.066	0.128
LV4	0.057	0.072	0.008	0.071	0.110
LV5	0.092	0.113	0.015	0.114	0.129
LV6	0.178	0.182	0.023	0.189	0.127
MJO	0.059	0.045	0.007	0.045	0.158
MJV	0.053	0.033	0.003	0.033	0.088
MPK	0.193	0.222	0.026	0.220	0.118
MTW	0.133	0.137	0.014	0.135	0.106
NBI	0.061	0.060	0.008	0.056	0.140
NWH	0.583	0.752	0.105	0.744	0.140
OBG	0.355	0.300	0.030	0.303	0.101
ORR	0.568	0.597	0.096	0.602	0.161
PHN	0.103	0.101	0.015	0.099	0.144
PKC	0.301	0.283	0.033	0.285	0.117
PMG	0.143	0.199	0.019	0.205	0.096
PVC	0.054	0.052	0.005	0.053	0.095
RHE	0.116	0.087	0.009	0.085	0.103
RNC	0.046	0.051	0.006	0.051	0.114
ROS	0.040	0.044	0.006	0.044	0.138
RVA	0.064	0.051	0.010	0.047	0.189
SFY	0.344	0.382	0.051	0.372	0.135
SNM	0.125	0.155	0.020	0.157	0.128
SPP	0.095	0.085	0.011	0.082	0.126
ULA	0.278	0.297	0.024	0.297	0.082
USB	0.069	0.063	0.009	0.064	0.141
VRP	0.140	0.190	0.023	0.188	0.123

Table F.2: Recorded PSA (T = 0.3 sec) and statistics from ten simulated time series.

Station	Recorded PSA (g)	Mean (g)	St.Dev. (g)	Median (g)	Log.St.Dev.
ALF	0.171	0.194	0.027	0.186	0.138
ANB	0.077	0.061	0.020	0.063	0.326
ANI	0.093	0.087	0.009	0.085	0.101
BHA	0.617	0.567	0.089	0.549	0.157
CMO	0.249	0.238	0.023	0.234	0.095
DOW	0.486	0.477	0.049	0.484	0.102
FYP	0.321	0.233	0.018	0.234	0.077
HSL	0.469	0.516	0.093	0.525	0.181
IGU	0.235	0.253	0.021	0.249	0.084
L01	0.211	0.159	0.020	0.155	0.128
L04	0.241	0.195	0.037	0.183	0.188
L09	0.437	0.301	0.053	0.284	0.175
LAS	0.334	0.335	0.059	0.328	0.176
LBL	0.205	0.223	0.019	0.220	0.085
LCN	0.546	0.610	0.071	0.614	0.116
LNF	0.170	0.138	0.017	0.142	0.124
LPK	0.784	0.740	0.080	0.727	0.109
LV1	0.198	0.152	0.029	0.142	0.188
LV2	0.125	0.127	0.021	0.123	0.165
LV3	0.176	0.168	0.020	0.161	0.118
LV4	0.155	0.137	0.017	0.133	0.125
LV5	0.339	0.342	0.045	0.340	0.133
LV6	0.393	0.467	0.055	0.462	0.118
MJO	0.144	0.114	0.016	0.114	0.141
MJV	0.224	0.126	0.017	0.124	0.131
MPK	0.570	0.548	0.071	0.548	0.130
MTW	0.231	0.228	0.029	0.228	0.127
NBI	0.144	0.171	0.024	0.165	0.142
NWH	2.523	2.321	0.330	2.332	0.142
OBG	0.590	0.574	0.096	0.565	0.167
ORR	1.332	1.700	0.216	1.665	0.127
PHN	0.304	0.257	0.038	0.267	0.149
PKC	1.031	1.003	0.100	0.998	0.100
PMG	0.404	0.531	0.046	0.533	0.088
PVC	0.155	0.138	0.016	0.135	0.114
RHE	0.356	0.280	0.033	0.287	0.118
RNC	0.091	0.091	0.014	0.093	0.149
ROS	0.144	0.121	0.011	0.120	0.094
RVA	0.160	0.112	0.012	0.112	0.105
SFY	0.788	0.889	0.122	0.875	0.137
SNM	0.290	0.339	0.054	0.325	0.159
SPP	0.201	0.188	0.032	0.188	0.172
ULA	0.537	0.559	0.077	0.585	0.138
USB	0.165	0.127	0.018	0.125	0.144
VRP	0.247	0.334	0.055	0.354	0.165

Table F.3: Recorded PSA (T = 1.0 sec) and statistics from ten simulated time series.

Station	Recorded PSA (g)	Mean (g)	St.Dev. (g)	Median (g)	Log.St.Dev.
ALF	0.134	0.129	0.022	0.130	0.168
ANB	0.051	0.030	0.007	0.031	0.248
ANI	0.021	0.023	0.002	0.022	0.095
BHA	0.161	0.199	0.026	0.193	0.130
CMO	0.170	0.169	0.018	0.171	0.106
DOW	0.154	0.185	0.022	0.191	0.118
FYP	0.063	0.061	0.007	0.060	0.109
HSL	0.233	0.262	0.034	0.254	0.129
IGU	0.128	0.131	0.014	0.127	0.106
L01	0.168	0.128	0.019	0.126	0.145
L04	0.034	0.034	0.006	0.033	0.170
L09	0.032	0.040	0.005	0.041	0.118
LAS	0.152	0.131	0.018	0.129	0.140
LBL	0.115	0.140	0.017	0.139	0.119
LCN	0.269	0.266	0.020	0.258	0.077
LNF	0.076	0.075	0.009	0.075	0.114
LPK	0.112	0.088	0.015	0.089	0.173
LV1	0.048	0.050	0.006	0.049	0.123
LV2	0.041	0.047	0.008	0.047	0.168
LV3	0.051	0.051	0.009	0.051	0.181
LV4	0.114	0.122	0.014	0.122	0.113
LV5	0.152	0.151	0.025	0.149	0.167
LV6	0.077	0.088	0.012	0.086	0.141
MJO	0.025	0.023	0.005	0.023	0.205
MJV	0.066	0.055	0.008	0.053	0.141
MPK	0.228	0.318	0.039	0.327	0.123
MTW	0.047	0.048	0.009	0.048	0.187
NBI	0.056	0.054	0.008	0.052	0.143
NWH	0.735	0.615	0.059	0.619	0.096
OBG	0.129	0.142	0.021	0.134	0.150
ORR	0.533	0.537	0.094	0.536	0.176
PHN	0.153	0.123	0.010	0.123	0.084
PKC	0.497	0.490	0.056	0.481	0.114
PMG	0.349	0.397	0.020	0.393	0.051
PVC	0.056	0.063	0.005	0.063	0.083
RHE	0.069	0.074	0.011	0.073	0.149
RNC	0.053	0.063	0.009	0.062	0.137
ROS	0.050	0.043	0.005	0.043	0.109
RVA	0.024	0.018	0.002	0.018	0.119
SFY	0.525	0.598	0.050	0.607	0.083
SNM	0.123	0.125	0.009	0.124	0.073
SPP	0.091	0.084	0.006	0.083	0.072
ULA	0.216	0.196	0.039	0.195	0.199
USB	0.101	0.099	0.010	0.097	0.102
VRP	0.205	0.197	0.024	0.196	0.120

Table F.4: Recorded PSA (T = 2.0 sec) and statistics from ten simulated time series.

Station	Recorded PSA (g)	Mean (g)	St.Dev. (g)	Median (g)	Log.St.Dev.
ALF	0.040	0.043	0.009	0.039	0.202
ANB	0.011	0.010	0.002	0.009	0.162
ANI	0.007	0.007	0.001	0.007	0.105
BHA	0.134	0.140	0.015	0.137	0.105
CMO	0.066	0.061	0.007	0.060	0.113
DOW	0.068	0.080	0.010	0.082	0.121
FYP	0.008	0.009	0.002	0.009	0.179
HSL	0.094	0.104	0.015	0.101	0.145
IGU	0.050	0.071	0.011	0.068	0.153
L01	0.029	0.031	0.003	0.031	0.085
L04	0.015	0.021	0.002	0.020	0.094
L09	0.024	0.030	0.004	0.030	0.138
LAS	0.057	0.062	0.006	0.062	0.104
LBL	0.049	0.058	0.006	0.059	0.108
LCN	0.141	0.158	0.019	0.154	0.119
LNF	0.039	0.050	0.005	0.050	0.094
LPK	0.032	0.020	0.003	0.020	0.136
LV1	0.051	0.055	0.003	0.054	0.050
LV2	0.060	0.065	0.004	0.063	0.068
LV3	0.059	0.064	0.004	0.065	0.059
LV4	0.095	0.097	0.006	0.099	0.066
LV5	0.113	0.107	0.009	0.108	0.088
LV6	0.064	0.067	0.005	0.067	0.073
MJO	0.008	0.008	0.001	0.007	0.173
MJV	0.007	0.009	0.001	0.009	0.089
MPK	0.084	0.095	0.013	0.099	0.142
MTW	0.012	0.018	0.002	0.017	0.134
NBI	0.038	0.045	0.004	0.045	0.087
NWH	0.260	0.333	0.033	0.341	0.099
OBG	0.051	0.068	0.007	0.068	0.104
ORR	0.226	0.255	0.020	0.251	0.079
PHN	0.055	0.066	0.006	0.066	0.095
PKC	0.110	0.123	0.018	0.121	0.146
PMG	0.074	0.089	0.010	0.089	0.109
PVC	0.012	0.013	0.002	0.013	0.121
RHE	0.014	0.019	0.002	0.018	0.135
RNC	0.024	0.020	0.003	0.019	0.142
ROS	0.014	0.012	0.001	0.012	0.119
RVA	0.010	0.010	0.001	0.010	0.109
SFY	0.167	0.188	0.021	0.192	0.111
SNM	0.023	0.025	0.004	0.025	0.150
SPP	0.016	0.016	0.001	0.016	0.072
ULA	0.058	0.096	0.009	0.098	0.099
USB	0.031	0.037	0.005	0.038	0.143
VRP	0.051	0.044	0.006	0.042	0.127

REFERENCES

Abrahamson, N.A. (1985). "Estimation of seismic wave coherency and rupture velocity using the SMART 1 strong-motion array recordings." *EERC Report No. UCB/EERC-85/02*. Earthquake Engineering Research Center, University of California, Berkeley, CA, USA.

Abrahamson, N.A., and J.P. Singh (1986). "Importance of phasing of strong ground motion in the estimation of structural response." *Proceedings of the 3rd Conference on Dynamic Response of Structures*, 86-93.

Abrahamson, N.A., and B.A. Bolt (1987). "Array analysis and synthesis mapping of strong seismic motion." in *Strong Motion Synthesis* (B.A. Bolt, ed.). Academic Press, Orlando.

Abrahamson, N.A., B.A. Bolt, R.B. Darragh, J. Penzien, and Y.B. Tsai (1987). "The SMART-1 accelerograph array (1980-1987): a review." *Earthquake Spectra* **3**, 263-287.

Abrahamson, N.A., J.F. Schneider, and J.C. Stepp (1991). "Empirical spatial coherency functions for application to soil-structure interaction analyses." *Earthquake Spectra* **7**, 1-27.

Aki, K. (1968). "Seismic displacements near a fault." *J. Geophys. Res*. **73**, 5359-5376.

Aki, K., and P.G. Richards (1980). *Quantitative Seismology, Theory and Methods*, Vol. I and II. Freeman, San Francisco, CA, USA.

Anderson, J.G., and S.E. Hough (1984). "A model for the shape of the Fourier amplitude spectrum of acceleration at high frequencies." *Bull. Seism. Soc. Am*. **74**, 1069-1993.

Archuleta, R.J., and S.M. Day (1980). "Dynamic rupture in a layered medium: the 1966 Parkfield earthquake." *Bull. Seism. Soc. Am*. **70**, 671-689.

Arias, A. (1970). "A measure of earthquake intensity." in *Seismic Design of Nuclear Power Plants* (edited by R. Hansen), MIT Press, Cambridge, MA, USA, 438-483.

Atkinson, G.M. (1996). "The high-frequency shape of the source spectrum for earthquakes in Eastern and Western Canada." *Bull. Seism. Soc. Am*. **86**, 106-112.

Atkinson, G.M., and D.M. Boore (1995). "Ground-motion relations for eastern North America." *Bull. Seism. Soc. Am*. **85**, 17-30.

Bolt, B.A., C.H. Loh, J. Penzien, Y.B. Tsai, and Y.T. Yeh (1982). "Preliminary report on the SMART 1 strong motion array in Taiwan." *EERC Report No. UCB/EERC-82/13*. Earthquake Engineering Research Center, University of California, Berkeley, CA, USA.

Bolt, B.A., R.A. Uhrhammer, and R.B. Darragh (1985). "The Morgan Hill earthquake of April 24, 1984 – seismological aspects." *Earthquake Spectra* **1**, 407-418.

Boore, D.M. (1983). "Stochastic simulation of high-frequency ground motions based on seismological models of the radiated spectra." *Bull. Seism. Soc. Am*. **73**, 1865-1894.

Boore, D.M. (1986). "Short-period P- and S-wave radiation from large earthquakes: implications for spectral scaling relations." *Bull. Seism. Soc. Am*. **76**, 43-64.

Boore, D.M., W.B. Joyner, and T.E. Fumal (1993). "Estimation of response spectra and peak accelerations from western North American earthquakes: an interim report." *U.S. Geol. Survey Open-File Report 93-509*.

Boore, D.M., W.B. Joyner, and T.E. Fumal (1994). "Estimation of response spectra and peak accelerations from western North American earthquakes: an interim report, part 2." *U.S. Geol. Survey Open-File Report 94-127*.

Boore, D.M., W.B. Joyner, and T.E. Fumal (1997). "Equations for estimating horizontal response spectra and peak acceleration from western North American earthquakes: a summary of recent work." *Seism. Res. Lett*. **68**, 128-153.

Borcherdt, R.D. (1994). "Estimates of site-dependent response spectra for design (methodology and justification)." *Earthquake Spectra* **10**, 617-653.

Bouchon, M. (1982). "The rupture mechanism of the Coyote Lake earthquake of 6 August 1979 inferred from near-field data." *Bull. Seism. Soc. Am*. **72**, 745-757.

Brune, J.N. (1970). "Tectonic stress and the spectra of seismic shear waves from earthquakes." *J. Geophys. Res*. **75**, 4997-5009.

Brune, J.N. (1971). "Correction." *J. Geophys. Res*. **76**, 5002.

BSSC (1994). NEHRP Recommended Provisions for Seismic Regulations for New Buildings. Part I – Provisions. FEMA 222A, Federal Emergency Management Agency.

Campbell, K.W. (1987). "Predicting strong ground motion in Utah." in Assessment of Regional Earthquake Hazards and Risks Along the Wasatch Front, Utah II (edited by P.L. Gori and W.W. Hays). *U.S. Geol. Survey Open-File Report 87-585*, L1-L90.

Chang, S.W., J.D. Bray, and R.B. Seed (1996). "Engineering implications of ground motions from the Northridge earthquake." *Bull. Seism. Soc. Am*. **86**, S270-S288.

Chavez, D., J. Gonzales, A. Reyes, J.N. Brune, F.L. Vernon, R. Simons, L.K. Hutton, P.T. German, and C.E. Johnson (1982). "Main-shock location and magnitude determination using combined U.S. and Mexican data." in The Imperial Valley Earthquake of October 15, 1979. *U.S. Geol. Survey Professional Paper 1254*, 51-54.

Clough, R.W., and J. Penzien (1975). *Dynamics of Structures*. McGraw-Hill, New York, NY, USA.

Conte, J.P., K.S. Pister, and S.A. Mahin (1992). "Nonstationary ARMA modeling of seismic motions." *J. Soil Dyn. and Earthquake Eng*. **11**, 411-426.

Converse, A.M., and A.G. Brady (1992). "BAP: Basic strong-motion accelerogram processing software, version 1.0." *U.S. Geol. Survey Open-File Report 92-296A.*

Der Kiureghian, A. (1996). "A coherency model for spatially varying ground motions." *Earthquake Eng. Struct. Dyn*. **25**, 99-111.

Ellis, G.W., A.S. Cakmak, and J. Ledolter (1987). "Modelling earthquake ground motions in seismically active regions using parametric time series methods." in *Ground Motion and Engineering Seismology* (edited by A.S. Cakmak), Elsevier, Amsterdam, Holland, 551-566.

Hagerty, M.T., and S.Y. Schwartz (1996). "The Cape Mendocino earthquake: broadband determination of source parameters." *J. Geophys. Res*. **101**, 16043-16058.

Hanks, T.C. (1982). "f_{max}." *Bull. Seism. Soc. Am*. **72**, 1867-1879.

Hanks, T.C., and H. Kanamori (1979). "A moment magnitude scale." *J. Geophys. Res*. **84**, 2348-2350.

Hao, H. (1989). "Effects of spatial variation of ground motion on large multiply-supported structures." *Report No. UCB/EERC-89/06,* Earthquake Engineering Research Center, University of California, Berkeley, CA, USA.

Harichandran, R.S., and E.H. Vanmarcke (1984). "Space-time variation of earthquake ground motion." *Research Report R84-12*, Dept. of Civil Engineering, MIT, Cambridge, MA, USA.

Harichandran, R.S., and E.H. Vanmarcke (1986). "Stochastic variation of earthquake ground motion in space and time." *J. Eng. Mech*. **112**, 154-174.

Hartzell, S.H. (1978). "Earthquake aftershocks as Green's functions." *Geophys. Res. Lett*. **5**, 1-4.

Haskell, N.A. (1969). "Elastic displacements in the near-field of a propagating fault." *Bull. Seism. Soc. Am*. **59**, 865-908.

Hauksson, E., L.M. Jones, K. Hutton, and D. Eberhart-Phillips (1993). "The 1992 Landers earthquake sequence: seismological observations." *J. Geophys. Res*. **98**, 19835-19858.

Hauksson, E., and L.M. Jones (1995). "Seismology." in Northridge Earthquake of January 17, 1994 Reconnaissance Report, Volume 1 (edited by J.F. Hall), supplement C to Volume 11 of Earthquake Spectra. *Earthquake Engineering Research Institute Publication 95-03*, EERI, Oakland, CA, USA, 1-12.

Jones, L.M, and E. Hauksson (1988). "The Whittier Narrows, California earthquake of October 1, 1987 – seismology." *Earthquake Spectra* **4**, 43-53.

Joyner, W.B., and D.M. Boore (1981). "Peak horizontal acceleration and velocity from strong-motion records including records from the 1979 Imperial Valley, California, earthquake." *Bull. Seism. Soc. Am*. **71**, 2011-2038.

Joyner, W.B., and D.M. Boore (1988). "Measurement, characterization, and prediction of strong ground motion." in *Earthquake Engineering and Soil Dynamics II – Recent*

Advances in Ground-Motion Evaluation (edited by J.L. Von Thun), ASCE Geotechn. Spec. Publ. No. 20, 43-102.

Kanai, K. (1957). "Semi-empirical formula for the seismic characteristics of the ground." *Univ. Tokyo Bull. Earthquake Res. Inst*. **35**, 309-325.

Kanamori, H., and J. Regan (1982). "Long-period surface waves." in The Imperial Valley Earthquake of October 15, 1979. *U.S. Geol. Survey Professional Paper 1254*, 55-58.

Kanda, J., R. Iwasaki, Y. Ohsaki, T. Masao, Y. Kitada, and K. Sakata (1983). "Generation of simulated earthquake ground motions considering target response spectra of various damping ratios." *Transactions of the 7th International Conference on Structural Mechanics in Reactor Technology*, Vol. K(a), 71-79.

Kasahara, K. (1981). *Earthquake Mechanics*. Cambridge University Press, Cambridge, England, UK.

Kozin, F. (1988). "Autoregressive moving average models of earthquake records." *Prob. Eng. Mech.* **3**, 58-63.

Kubo, T. (1987). "The importance of phase properties in generation of synthetic earthquake strong motions." *Transactions of the 9th International Conference on Structural Mechanics in Reactor Technology*, Vol. K1, 49-54.

Lindgren, B.W. (1976). *Statistical Theory* (3rd edition). Macmillan Publishing Co., New York, NY, USA.

Loh, C.H. (1985). "Analysis of the spatial variation of seismic waves and ground movements from the SMART-1 array data." *Earthquake Eng. Struct. Dyn*. **13**, 561-581.

Madsen, H.O., S. Krenk, and N.C. Lind (1986). *Methods of Structural Safety*. Prentice-Hall, Englewoods Cliffs, NJ, USA.

Marven, C., and G. Ewers (1996). *A Simple Approach to Digital Signal Processing*. John Wiley & Sons, New York, NY, USA.

Matsukawa, K., M. Watabe, N.A. Theofanopulos, and M. Tohdo (1987). "Phase characteristics of earthquake ground motions and those applications to synthetic ones." *Transactions of the 9th International Conference on Structural Mechanics in Reactor Technology*, Vol. K1, 43-48.

McGuire, R.K., A.M. Becker, and N.C. Donovan (1984). "Spectral estimates of seismic shear waves." *Bull. Seism. Soc. Am*. **74**, 1427-1440.

Moehle, J., G. Fenves, R. Mayes, N. Priestley, F. Seible, C.M. Uang, S. Werner, and M. Ascheim (1985). "Highway bridges and traffic management." in Northridge Earthquake of January 17, 1994 Reconnaissance Report, Volume 1 (edited by John F. Hall), supplement C to Volume 11 of Earthquake Spectra. *Earthquake Engineering Research Institute Publication 95-03*, EERI, Oakland, CA, USA, 287-372.

Naraoka, K., and T. Watanabe (1987). "Generation of nonstationary earthquake ground motions using phase characteristics." *Transactions of the 9th International Conference on Structural Mechanics in Reactor Technology*, Vol. K1, 37-42.

Nelder, J.A., and R. Mead (1964). "A simplex method for function minimization." *The Computer Journal* **7**, 308-313.

Newland, D.E. (1993). *An Introduction to Random Vibrations, Spectral and Wavelet Analysis*, 3rd edition. Longman, Essex, England, UK.

Niazi, M. (1990). "Behavior of peak values and spectral ordinates of near-source strong ground motion over the SMART 1 array." *EERC Report No. UCB/EERC-90/17*. Earthquake Engineering Research Center, University of California, Berkeley, CA, USA.

Nigam, N.C. (1982). "Phase properties of a class of random processes." *Earthquake Eng. Struct. Dyn*. **10**, 711-717.

NOAA (1996). *Earthquake Strong Motion CD-ROM Collection*. National Oceanic and Atmospheric Administration, National Environmental Satellite, Data, and Information Service, National Geophysical Data Center, Boulder, CO, USA.

Ohsaki, Y. (1979). "On the significance of phase content in earthquake ground motions." *Earthquake Eng. Struct. Dyn*. **7**, 427-439.

Oliviera, C.S. (1985). "Variability of strong ground motion characteristics obtained in SMART-1 array." *Proceedings of the 12th Regional Seminar on Earthquake Engineering*, Halkidiki, Greece.

Pacheco, J., and J. Nabelek (1988). "Source mechanisms of three moderate California earthquakes of July 1986." *Bull. Seism. Soc. Am*. **78**, 1907-1929.

Papageorgiou, A.S., and K. Aki (1983). "A specific barrier model for the quantitative description of inhomogeneous faulting and the prediction of strong ground motion. Part I. Description of the model." *Bull. Seism. Soc. Am*. **73**, 693-722.

Park, S., and S. Elrick (1998). "Predictions of shear-wave velocities in southern California using surface geology." *Bull. Seism. Soc. Am*. **88**, 677-685.

Priestley, M.B. (1967). "Power spectral analysis of non-stationary processes." *J. Sound and Vibration* **6**, 86-97.

Reiter, L. (1990). *Earthquake Hazard Analysis – Issues and Insight*. Columbia University Press, New York, NY, USA.

Rice, S.O. (1944). "Mathematical analysis of random noise." *Bell Syst. Techn. J*. **23**, 282-332.

Sabetta, F., and A. Pugliese (1996). "Estimation of response spectra and simulation of nonstationary earthquake ground motions." *Bull. Seism. Soc. Am*. **86**, 337-352.

Sadigh, K., C.Y. Chang, J.A. Egan, F. Makdisi, and R.R. Youngs (1997). "Attenuation relationships for shallow crustal earthquakes based on California strong motion data." *Seism. Res. Lett*. **68**, 180-189.

Seed, H.B., C. Ugas, and J. Lysmer (1976). "Site-dependent spectra for earthquake-resistant design." *Bull. Seism. Soc. Am*. **66**, 221-243.

Shinozuka, M., and G. Deodatis (1988). "Stochastic process models for earthquake ground motion." *Prob. Eng. Mech*. **3**, 114-123.

Sigbjörnsson, R., G.I. Baldvinsson, H. Thráinsson, S. Ólafsson, G.Th. Gardarsdóttir, and Ó Thórarinsson (1994). "On seismic hazard in Iceland – a stochastic simulation approach." *Proceedings of the 10th European Conference on Earthquake Engineering*, A.A. Balkema, Rotterdam, 111-116.

Somerville, P.G. (1997). "Engineering characteristics of near fault ground motion." *Proceedings of the SMIP97 Seminar on Utilization of Strong-Motion Data*, 9-28.

Somerville, P.G., N.F. Smith, R.W. Graves, and N.A. Abrahamson (1997). "Modification of empirical strong ground motion attenuation relations to include the amplitude and duration effect of rupture directivity." *Seism. Res. Lett*. **68**, 199-222.

Spudich, P., and S.H. Hartzell (1985). "Predicting earthquake ground-motion time-histories." in Evaluating Earthquake Hazards in the Los Angeles Region – An Earth-Science Perspective (edited by J.I. Ziony). *U.S. Geol. Survey Professional Paper 1360*, 249-261.

Suzuki, S., and A.S. Kiremidjian (1988). "A stochastic ground motion forecast model with geophysical considerations." *The John A. Blume Earthquake Engineering Center Report No. 88*, Stanford University, Stanford, CA, USA.

Sveshnikov, A.A. (1968). *Problems in Probability Theory, Mathematical Statistics and Theory of Random Functions*, translated from Russian by Richard A. Silverman. Dover, New York, NY, USA.

Tajimi, H. (1960). "A statistical method of determining the maximum response of a building structure during an earthquake." *Proc. 2nd World Conf. Earthquake Eng*., Vol. II, 781-798.

Tinsley, J.C., and T.E. Fumal (1985). "Mapping Quaternary sedimentary deposits for aerial variations in shaking response." in Evaluating Earthquake Hazards in the Los Angeles Region – An Earth-Science Perspective (edited by J.I. Ziony). *U.S. Geol. Survey Professional Paper 1360*, 101-126.

Wald, D.J., D.V. Helmberger, and T.H. Heaton (1991). "Rupture model of the 1989 Loma Prieta earthquake from the inversion of strong-motion and broadband teleseismic data." *Bull. Seism. Soc. Am*. **81**, 1540-1572.

Wald, D.J., and T.H. Heaton (1994). "A dislocation model of the 1994 Northridge, California earthquake determined from strong ground motions." *U.S. Geol. Survey Open-File Report 94-278*.

Westermo, B. (1992). "The synthesis of strong ground motion accelerograms from existing records." *Earthquake Eng. Struct. Dyn*. **21**, 743-756.

Whitcomb, J.H., C.R. Allen, J.D. Garmany, and J.A. Hileman (1973). "San Fernando earthquake series, 1971; focal mechanisms and tectonics." *Rev. of Geophys. and Space Phys.* **11**, 693-730.

Winterstein, S. (1991). “Nonlinear effects on ship bending in random seas.” *Technical Report No. 91-2032*, Det Norske Veritas, Høvik, Norway.

Zembaty, Z., and S. Krenk (1993). “Spatial seismic excitations and response spectra.” *J. Eng. Mech*. **119**, 2449-2460.